

School of Molecular and Life Sciences

Exploring the Chemistry of Lanthanoid β -Triketonate Complexes

Laura Abad Galán

**This thesis is presented for the Degree of
Doctor of Philosophy
of
Curtin University**

July 2018

Declaration

To the best of my knowledge and belief this thesis contains no material previously published by any other person except where due acknowledgment has been made.

This thesis contains no material which has been accepted for the award of any other degree or diploma in any university.

Signature:

A handwritten signature in black ink, consisting of a stylized, cursive script that is difficult to decipher. It appears to be written over a horizontal line.

Date: 02/07/18



“Great things are done by a series of small things brought together”- Vincent Van Gough

Abstract

This investigation explores the design, synthesis and characterisation of new β -triketonate lanthanoid complexes. Their structural and photophysical properties were studied in detail to better comprehend the unexplored β -triketone molecules as ligands for f -metal ions and iridium.

Chapter 1 provides an overview of the fundamental photophysical aspects of luminescent lanthanoid metal complexes and in particular, for the well-studied β -diketonate complexes and the novel β -triketonate analogues. Chapter 2 report efforts to explore the differences in luminescence of β -triketonate complexes with respect to structurally comparable β -diketonate complexes using tribenzoylmethane (**tbmH**, **L1H**) and 1,10-phenanthroline as an ancillary ligand for $\text{Ln}^{3+} = \text{Eu}^{3+}, \text{Er}^{3+}$ and Yb^{3+} . The photophysical studies, in the solid-state and solution, revealed similar performance of both families of complexes. These results suggested that structural features must be taken into account when designing lanthanoid complexes. Therefore, the work described in Chapter 3 was proposed to expand the family of the previously reported tetranuclear assemblies ($[\text{Ln}(\text{AeHOEt})(\mathbf{L1})_4]_2 \text{Ln}^{3+}/ \text{Ae}^+ = \text{Eu}^{3+}, \text{Gd}^{3+}, \text{Tb}^{3+}, \text{Dy}^{3+}, \text{Ho}^{3+}, \text{Er}^{3+}, \text{Yb}^{3+}; \text{Ae}^+ = \text{Na}^+, \text{K}^+, \text{Rb}^+$) by incorporation of caesium atoms and the use of a new β -triketone molecule in ethanolic medium: tri(4-methylbenzoyl)methane (**mtbmH**, **L2H**). Unique polymeric structures of formula $[\{\text{Ln}(\text{Cs})(\mathbf{L1})_4\}_2]_n$ and $[\{\text{Ln}(\text{Cs})(\mathbf{L2})_4\}_2]_n$, for $\text{Ln}^{3+} = \text{Eu}^{3+}, \text{Er}^{3+}$ and Yb^{3+} , presenting bright visible and NIR emission, were isolated instead. Chapter 4 covers research designed to assess the reproducibility of the coordination polymer synthesis by using other alkaline bases such as RbOH. Indeed the isolation of isomorphous complexes with formula $[\{\text{Ln}(\text{Rb})(\mathbf{L2})_4\}_2]_n$ for $\text{Ln}^{3+} = \text{Eu}^{3+}$ and Nd^{3+} was achieved, giving the first example of a β -triketonate Nd^{3+} complex. Indeed, the fact that analogous structures were found for Eu^{3+} and Nd^{3+} , offered the possibility to prepare mixed-metal complexes achieving effective lanthanoid-lanthanoid energy transfer to the $4f^*$ of Nd^{3+} . In Chapters 3 and 4, two structures involving a possible *in situ* retro-Claisen condensation reaction were observed for both **L1H** and **L2H**. Thus, a detailed study of the β -triketone stability with respect to the retro-Claisen condensation was performed and is reported in Chapter 5. Four new ligands were synthesised: tris(3,5-dimethylbenzoyl)methane (**dmtbmH**, **L3H**), tris(4-ethylbenzoyl)methane (**ettbmH**, **L4H**), tris(4-butylbenzoyl)methane (**butbmH**, **L5H**) and *t*-tris(4-*tert*-butylbenzoyl)methane (**t-butbmH**, **L6H**) with the aim of exploring the impact of alkyl substituents on complexation and reactivity of the triketonate ligands. A total of 11 more metal complexes that showed retro-Claisen condensation reactivity were found involving both precursor molecules, benzoate, and β -diketonate. Chapter 6 describes, a synthetic method designed to enable synthesis of β -triketonate complexes under conditions

where the ligand is stable, by avoiding alcohol solvents. Mononuclear species with formula $[\text{Ln}(\mathbf{tnm})_3(\text{DMSO})_2]$ ($\text{Ln}^{3+} = \text{Nd}^{3+}, \text{Eu}^{3+}, \text{Gd}^{3+}$ and Yb^{3+}) were isolated, where **tnm** (**L7H**) is tris(2-naphthoyl)methane, a new more highly conjugated β -triketone. The study of the emission properties of the NIR-emitting complexes of this family found them to have the longest lifetimes encountered in any of these systems, and with higher quantum yields than the majority of the diketonate complexes found in the literature including perfluorinated systems and being only surpassed by full deuterated species. Finally in Chapter 7, β -diketones and triketones were used as ancillary ligands for iridium and their structural and photophysical properties studied, showing bright emission in the solid state.

Symbols and Abbreviations

Δ	Change	A3	N1,N2-bis(pyridin-2-ylmethyl)ethane-1,2-diamine
τ_R	Radiative Lifetime	Ae	Alkali Element
Φ_{Ln}^L	Overall Quantum Yield	acac	Acetylacetonate
Φ_{Ln}^L	Intrinsic Quantum Yield	AIE	Aggregation Induced Emission
Φ_{PL}	Photoluminescence Quantum Yield	bath	Bathophenanthroline
Φ_{sens}	Sensitisation Efficiency	BDTH	2Z,2'Z)-1,1'-(thiophene-2,5-diyl)bis(4,4,4-trifluoro-3-hydroxybut-2-en-1-one)
ϵ	Molar Absorptivity	BET	Back Energy Transfer
η	Refractive Index	bga	6-Phenyl-1,3,5-triazine-2,4-diamine
λ_{exc}	Excitation Wavelength	bpy	2,2'-Bipyridine
λ_{em}	Emission Wavelength	bpm	2,2'-Bipyrimidine
ν	Frequency	BPTZ	3,6-Di(pyridin-2-yl)-1,2,4,5-tetrazine
τ_{obs}	Observed Lifetime	BTTH	1,1'-([2,2'-Bithiophene]-5,5'-diyl)bis(4,4,4-trifluorobutane-1,3-dione)
A1	4,4'-Dimethoxy-2,2'-bipyridine	Car-dbm	1-(4-(4aH-Carbazol-9(4bH,8aH,9aH)-yl)phenyl)-3-phenylpropane-1,3-dione
A2	Diethyl 1,10-phenanthroline-4,7-dicarboxylate	CCDC	Cambridge Crystallographic Data Centre

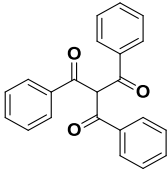
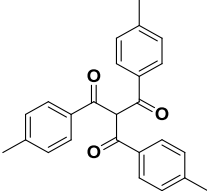
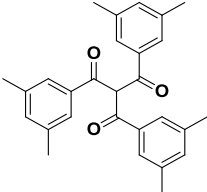
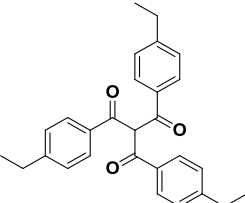
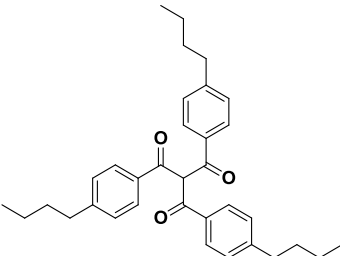
Cbo-dbm	1-(4-(4-(4aH-Carbazol-9(4bH,8aH,9aH)-yl)butoxy)phenyl)-3-phenylpropane-1,3-dione	D4H	1,3-Bis(perfluorophenyl)propane-1,3-dione
CNPD	1-(9-Ethyl-9H-carbazol-3-yl)-3-(naphthalen-2-yl)propane-1,3-dione	D5H	Trifluoro-1-phenylbutane-1,3-dione
CTPD	1-(9-Ethyl-9H-carbazol-3-yl)-3-(thieno[3,2-b]thiophen-2-yl)propane-1,3-dione	D6H	Heptafluoro-1-hydroxy-1-phenylhex-1-en-3-one
c.p.s	Counts per Second	D7H	Heptafluoro-1-hydroxy-1-phenylhex-1-en-3-one
CShM	Continuous Shape Measures	D8H	Tridecafluoro-1-hydroxy-1-phenylhex-1-en-3-one
CT	Charge Transfer	D9H ₄	1,1'-(((2-((4-(4,4,4-Trifluoro-3-hydroxybut-2-enoyl)phenoxy)methyl)-2-((4-(4,4,4-trifluoro-3-oxobutanoyl)phenoxy)methyl)propane-1,3-diyl)bis(oxy))bis(4,1-phenylene))bis(4,4,4-trifluorobutane-1,3-dione)
D1H	Pentafluoro-1-(perfluorophenyl)pentane-1,3-dione	D10H	(Z)-1-(7-(Diphenylamino)-9,9-diethyl-9H-fluoren-3-yl)-4,4,4-trifluoro-3-hydroxybut-2-en-1-one
D2H	Heptafluoro-1-(perfluorophenyl)hexane-1,3-dione	D11H	Trifluoro-1-(5-hydroxy-3-methyl-1-phenyl-1H-pyrazol-4-yl)ethanone
D3H	Pentadecafluoro-1-(perfluorophenyl)decane-1,3-dione	D12H	N,N-Dimethyl-3-nitro-3-oxopropanamide

D13H	5-Hydroxy-3-methyl-1-phenyl-1H-pyrazol-4-yl)(phenyl)methano	hH	Hexane-2,4-dione
Daf	5H-cyclopenta[1,2-b:5,4-b']dipyridin-5-one	hfaaH	Hexafluoroacetylacetone
dbmH	Dibenzoylmethane	hfpvr	Heptafluoro-1-(thiophen-2-yl)hexane-1,3-dione
dbso	(Sulfinylbis(methylene))dibenzene	hfthH	Heptafluoro-1-hydroxy-1-(thiophen-2-yl)hex-1-en-3-one
DCM	Dichloromethane	IC	Internal Conversion
dmhH	2,6-Dimethylheptane-3,5-dione	ILCT	Intraligand Charge Transfer
DMSO	Dimethylsulfoxide	IR	Infrared
dpso	Sulfinyldibenzene	IRF	Instrumental Response
ED	Electric Dipole	ISC	Intersystem Crossing
ET	Energy Transfer	k_{nr}	Non-radiative Rate Constant
EtOH	Ethanol	k_r	Radiative Rate Constant
F	Fluorescence	L	Luminescence
Fc	Ferrocene	LC	Ligand Centred
fodH	Heptafluoro-2,2-dimethyloctane-3,5-dione	LLCT	Ligand-to-ligand Charge Transfer
fhdH	Decafluoroheptane-2,4-dione	LMCT	Ligand-to-metal Charge Transfer
FRET	Forster Resonance Energy Transfer	Ln	Lanthanoid
FT-IR	Fourier Transform Infrared	LUMO	Lowest Unoccupied Molecular Orbital

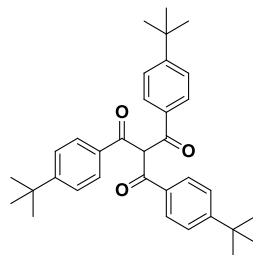
FWHM	Full-width at half-maximum	RT	Room Temperature
MC	Metal Centred	S ₀	Ground State
MeOH	Methanol	S ₁	Lowest Excited Singlet State
MLCT	Metal-to-ligand charge transfer	S _n	Excited Singlet State
MO	Molecular Orbital	SOC	Spin Orbit Coupling
m.p.	Melting Point	TA	Transient Absorption
nbmH	1-(4-(Tert-butyl)phenyl)-3-(naphthalen-2-yl)propane-1,3-dione	T ₁	Lowest Triplet State
ndH	Nonane-2,4-dione	T _n	Triplet State
nfthH	Tridecafluoro-1-(thiophen-2-yl)hexane-1,3-dione	tfacH	Trifluoroacetylacetone
NIR	Near Infrared	tfnbH	Trifluoro-1-(naphthalen-2-yl)butane-1,3-dione
NMR	Nuclear Magnetic Resonance	tfiH	Trifluoro-1-(3-hydroxy-1H-inden-2-yl)ethanone
odH	Heptane-2,4-dione	THF	Tetrahydrofuran
OLED	Organic Light Emitting Device	t-ONBH	1-(4-(5-(4-(Tert-butyl)phenyl)-1,3,4-oxadiazol-2-yl)phenyl)-3-(naphthalen-2-yl)propane-1,3-dione
P	Phosphorescence	tmhd	2,2,6,6-Tetramethylheptane-3,5-dione
pfndH	Pentadecafluoro-1-(naphthalen-2-yl)decane-1,3-dione	tmpH	Trifluorotrimethylacetone
phen	1,10-Phenanthroline	tppo	Triphenylphosphine oxide

R1	6'-(Pyridin-2-yl)-2,2':4',2''-terpyridine	tptz	6'-(Pyridin-2-yl)-2,2':4',2''-terpyridine
tpy	2,2':6',2''-terpyridine	UV	Ultraviolet
ttaH	thenoyltrifluoroacetone	VR	Vibrational Relaxation

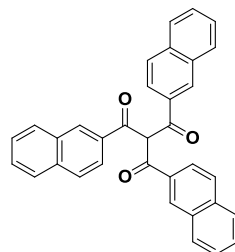
List of compounds

<i>Abbreviation</i>	<i>Compound</i>
	Ligands
L1H (tbmH)	
L2H (mtbmH)	
L3H (dmtbmH)	
L4H (ettbmH)	
L5H (butbmH)	

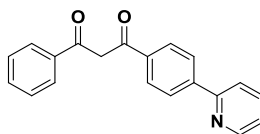
L6H (*t*-butbmH)



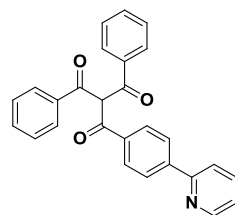
L7H (tnmH)



L8H (pydbmH)

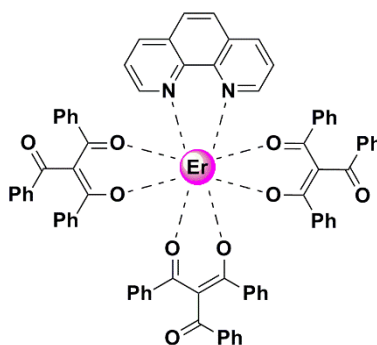


L9H (pytbmH)

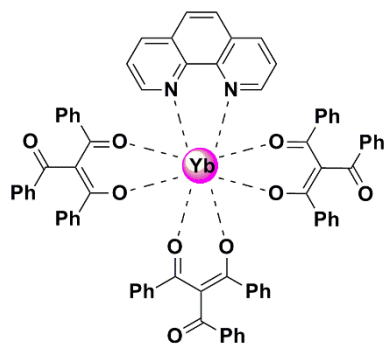


Lanthanoid Complexes

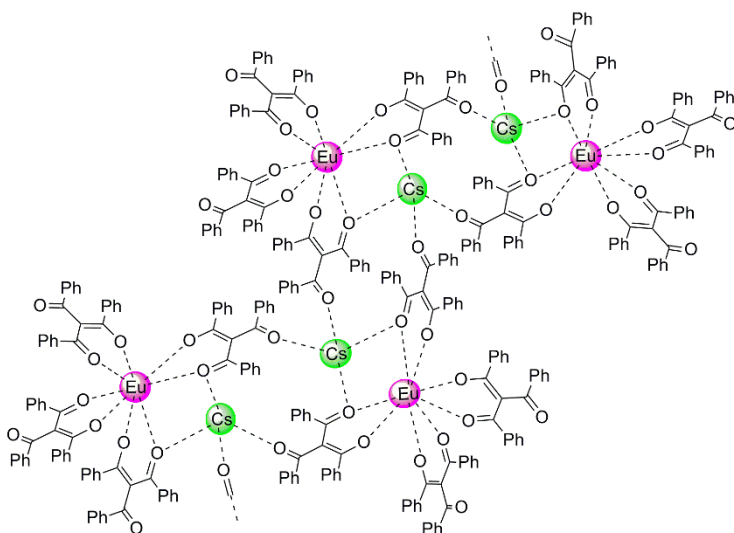
C1 [Er(**tbm**)₃(phen)]



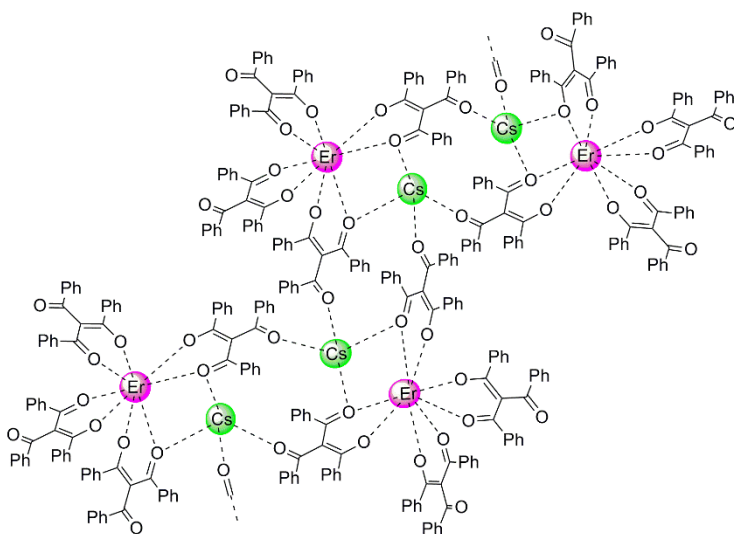
C2 [Yb(**tbm**)₃(phen)]



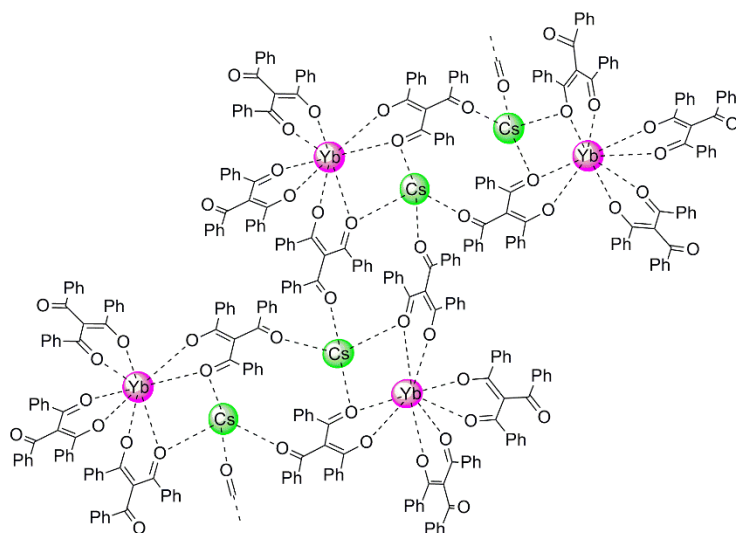
C3 [Eu(Cs)(**tbm**)₄]_n



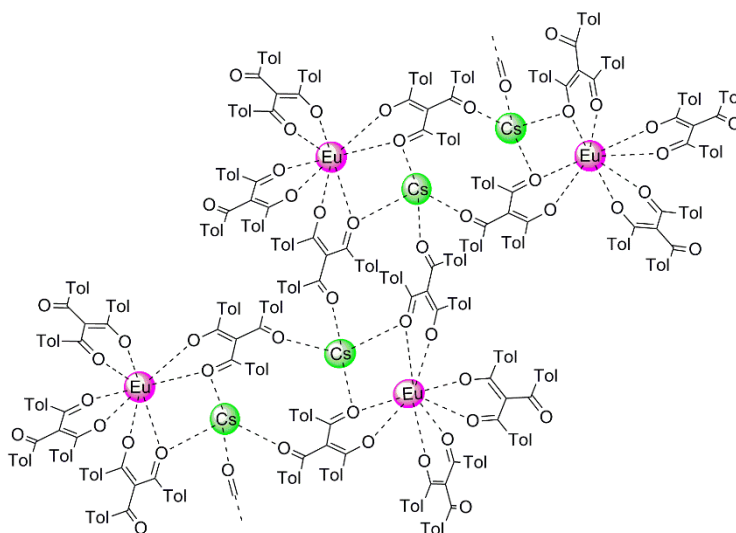
C4 [Er(Cs)(**tbm**)₄]_n



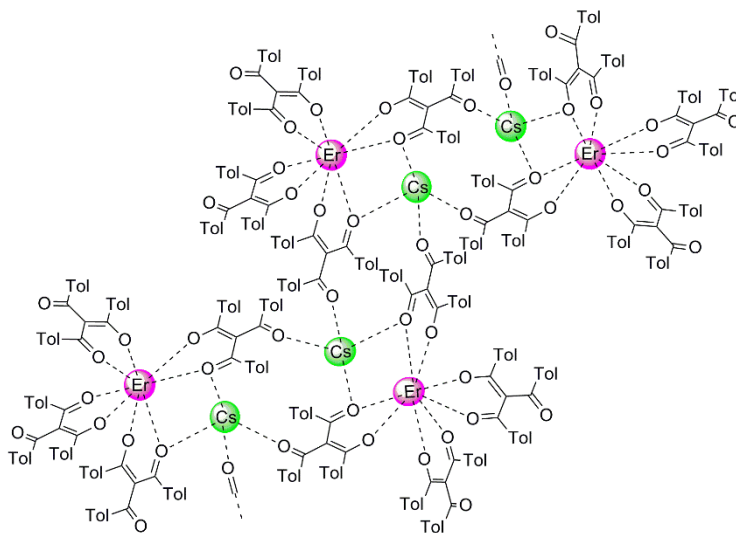
C5 [Yb(Cs)(**tbm**)₄]_n



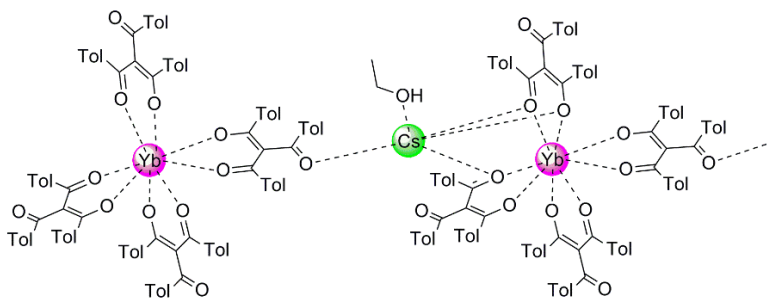
C6 [Eu(Cs)(**mtbm**)₄]_n



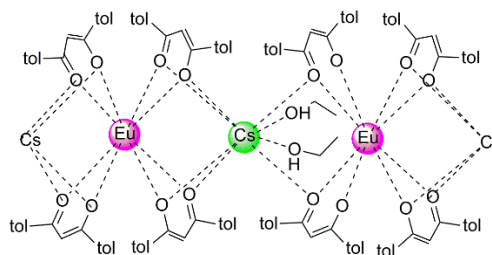
C7 [Er(Cs)(**mtbm**)₄]_n



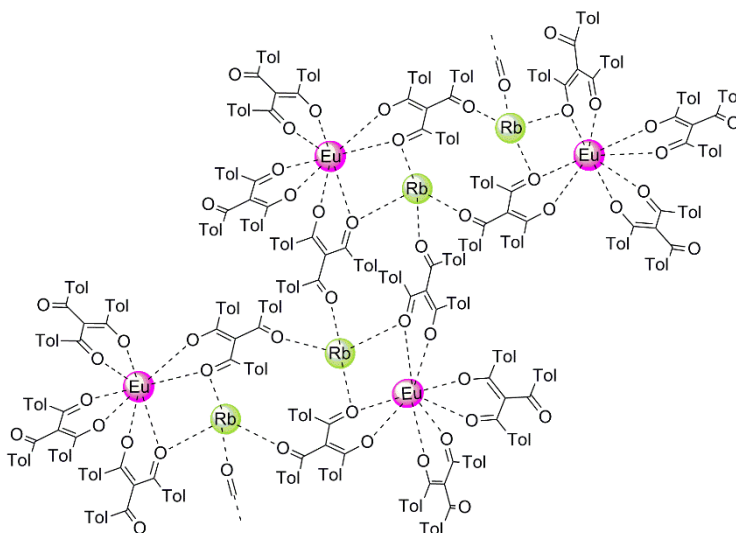
C8 [Yb(Cs·HOEt)(**mtbm**)₄]_n



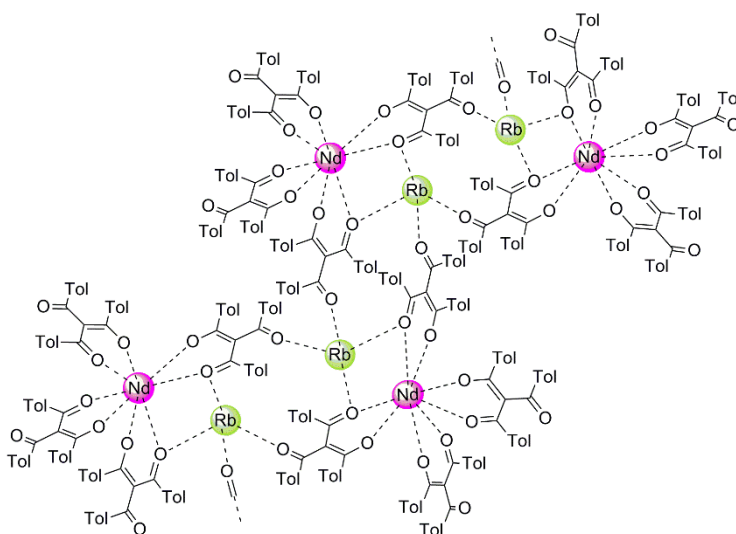
C9 [Eu(Cs·2HOEt)(**mdbm**)₄]_n



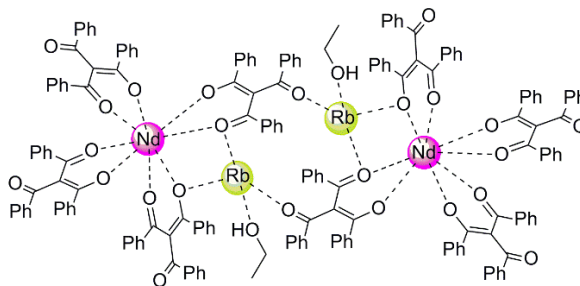
C10 [Eu(Rb)(**mtbm**)₄]_n



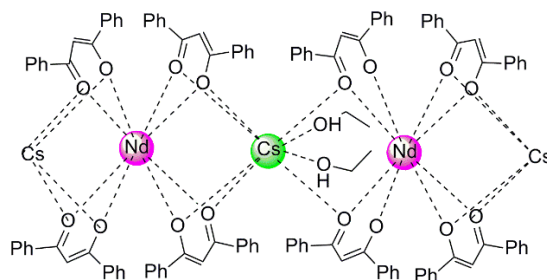
C11 [Nd(Rb)(**mtbm**)₄]_n



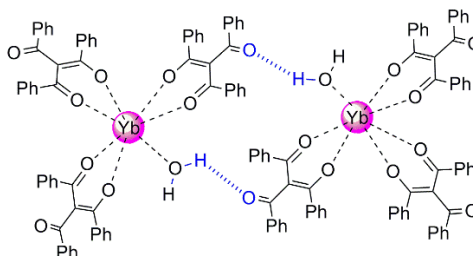
C12 [Nd(Rb)(**tbm**)₄]₂



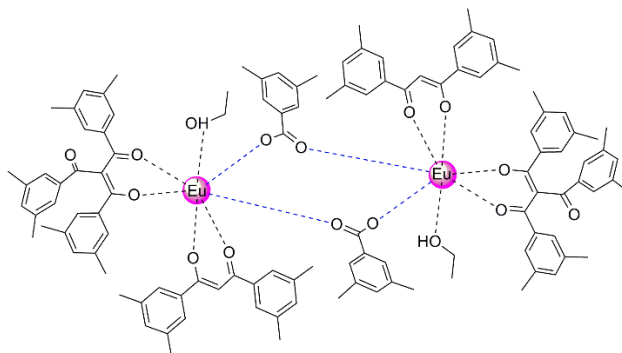
C13 [Nd(Cs·2HOEt)(**dbm**)₄]_n



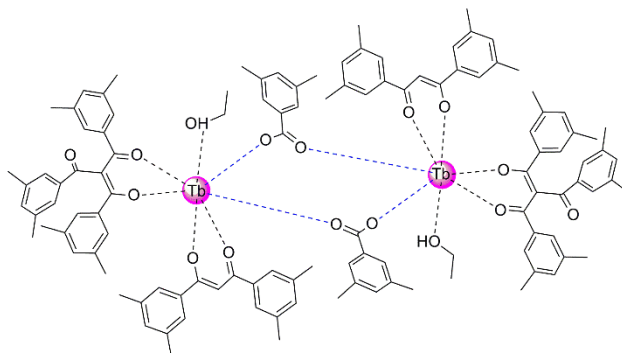
C14 [Yb(**mtbm**)₃(OH₂)₂]₂



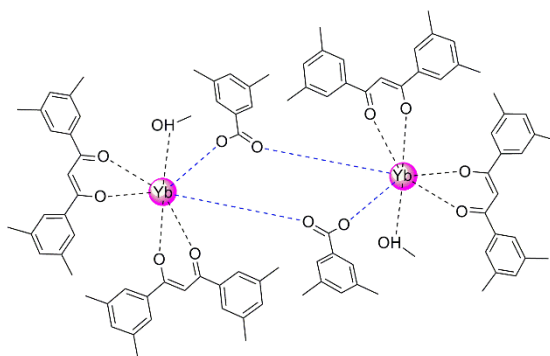
C15 [Eu(μ-dmba)(dmdbm)(**dmtbm**)(HOEt)]₂



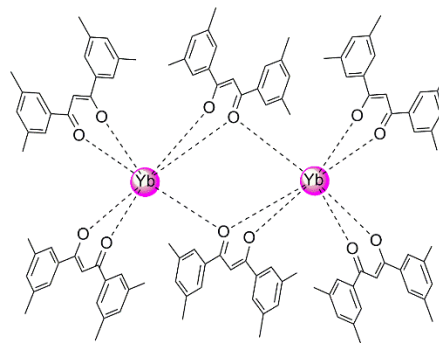
C16 [Tb(μ-dmba)(dmdbm)(**dmtbm**)(HOEt)]₂



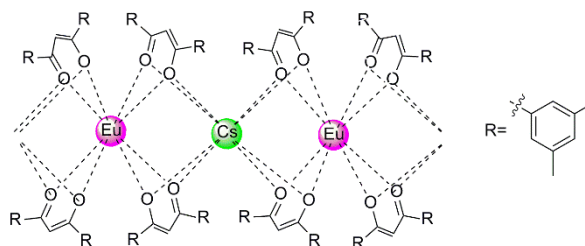
C17 [Yb(μ -
dmmba)(**dmdbm**)(OHMe)]₂



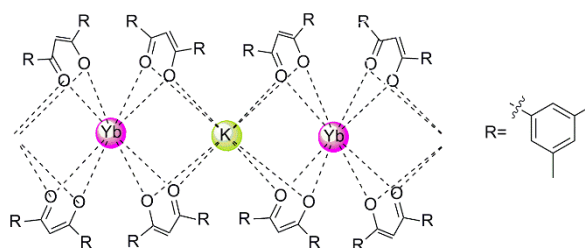
C18 [Yb(μ -dmdbm)(**dmdbm**)₂]₂



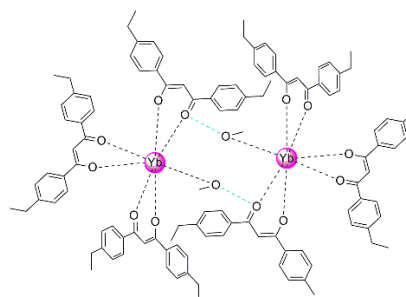
C19 [Eu(**dmdbm**)₄(Cs)]_n



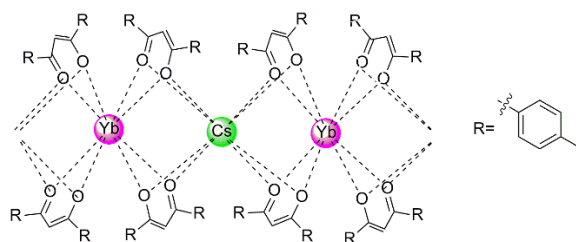
C20 [Yb(**dmdbm**)₄(K)]_n



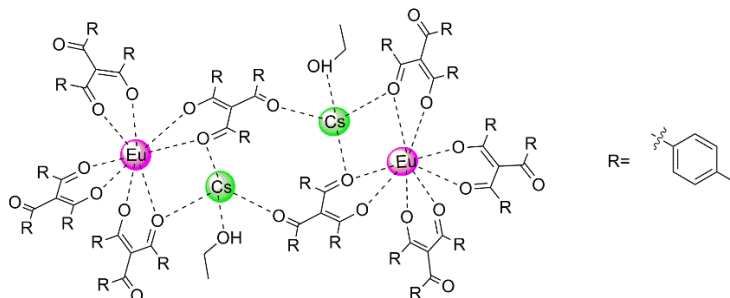
C21 [Yb(**etdbm**)₃(HOMe)]



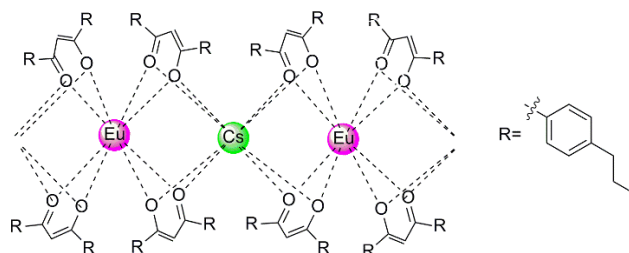
C22 [Yb(etdbm)₄(Cs)]_n



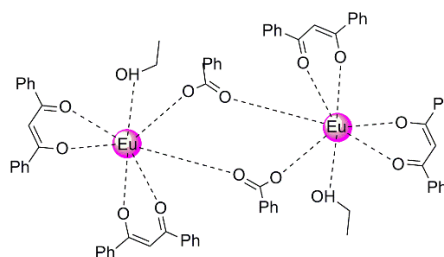
C23 [Eu(ettbm)₄(Cs·HOEt)]₂



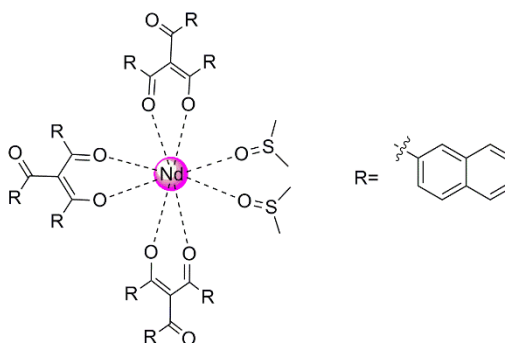
C24 [Eu(budbm)₄(Cs)]_n



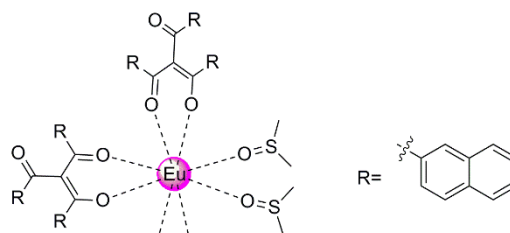
C25 [Eu(μ-*mba*)(mdbm)(OHEt)]₂



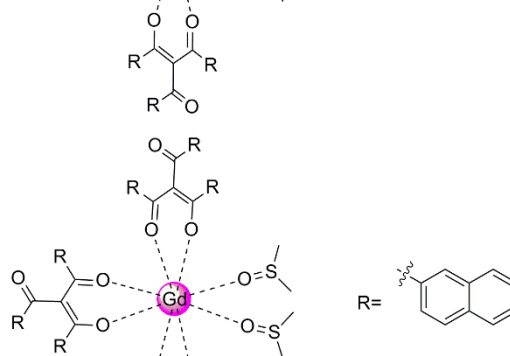
C26 [Nd(tbm)₃(DMSO)₂]



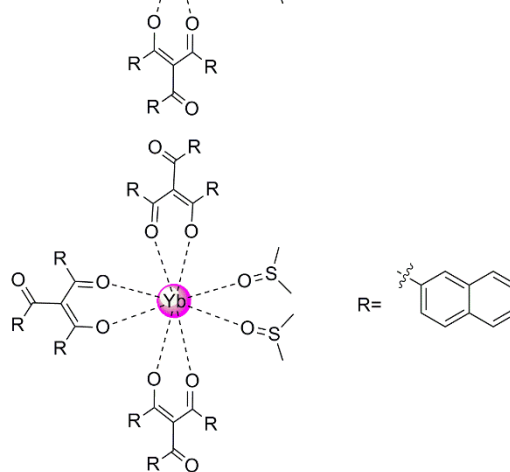
C27 [Eu(**tbm**)₃(DMSO)₂]



C28 [Gd(**tbm**)₃(DMSO)₂]

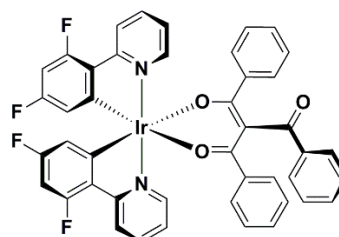


C29 [Yb(**tbm**)₃(DMSO)₂]

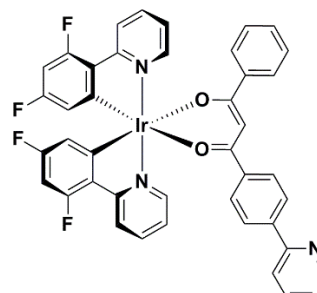


Iridium Complexes

C30 [Ir(dFppy)₂(**tbm**)].

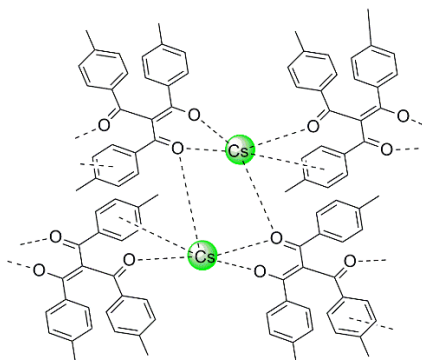


C31 [Ir(dFppy)₂(**pydbm**)].



Others

[Cs(**mtbm**)₄]



Acknowledgements

“I am [also] among those who think that science has great beauty” (Marie Curie, 1937) and my PhD project was not to be an exception. During these three years I have discovered the magnificent beauty of the lanthanoid properties and for that I need to thank all the people who directly or indirectly brought me into this chemistry.

Firstly, I thank my supervisors Assoc. Prof. Massimiliano Massi and Prof. Mark I. Ogden for giving me this opportunity and for their knowledge and guidance throughout this journey. I also thank my co-supervisor Prof. Eli Zysman-Colman for his tireless supervision during this time and for his help during my research stay in St Andrews.

I thank Dr. Evan G. Moore at the University of Queensland for the Transient Absorption measurements and the useful discussions about lanthanoid photophysics that made me think in different perspectives and learn from every word he pronounced. I thank Assoc. Prof. Stefano Stagni, for his help with the erbium emission measurements. Big thank you to Alexandre Sobolev and Prof. Brian Skelton at University of Western Australia and Dr. David Cordes at University of St Andrews, for all the crystal structure analysis which represent a big percentage of the work presented here.

I am thankful to all my colleagues from Curtin University who made this time so enjoyable. In particular, I thank Dr. Brodie Reid for being my mentor because our two theses together will be a beautiful two fascicle story. Thanks also to all my colleagues from the University of St Andrews who made my stay unforgettable.

I thank you my family and friends back in Spain for their encouragement to persuade my dream of doing a PhD even if that would mean living thousands of kilometres away. Finally, I deeply thank Alejandro, because this thesis would not have been possible without him. Because chemistry was, is and will always be between us.

Table of Contents

Abstract	i
Symbols and Abbreviations	iii
List of compounds	ix
Acknowledgements	xix
Table of Contents	xxi
Chapter 1 Introduction	1
1.1 Introductory Remarks	1
1.2 Electronic Properties	2
1.2.1 Electronic Configuration of Free Ions	2
1.2.2 Ligand-field Effects	4
1.3 Absorption Spectra	5
1.3.1 Absorption of Light	5
1.3.2 Selection Rules	6
1.4 Emission Spectra	6
1.4.1 Excited States	7
1.4.2 Sensitisation Mechanism	8
1.4.3 Energy Transfer	9
1.4.4 Non-radiative Decay	11
1.4.5 Charge Transfer States	13
1.4.6 Efficiency of the Sensitisation Process	14
1.5 Lanthanoid β -Diketonate Based Complexes	16
1.5.1 Overview	16
1.5.2 NIR Emitters	18
1.5.3 Visible Emitters	22
1.6 β -Triketonate Based Complexes	23
1.7 Scope	25

Chapter 2	Effect of β -Triketonate on the Lanthanoid Photophysical Properties.....	27
2.1	Introduction	27
2.2	Synthesis.....	27
2.3	X-Ray Diffraction	28
2.3.1	Shape Analysis	30
2.4	Photophysical Properties	32
2.4.1	Europium Complexes	34
2.4.2	Ytterbium Complexes.....	39
2.4.3	Erbium Complexes	44
2.5	Conclusion.....	45
Chapter 3	β -Triketonate Assemblies Incorporating Caesium Cations	47
3.1	Introduction	47
3.2	Synthesis.....	47
3.2.1	Ligand.....	47
3.2.2	Lanthanoid Assemblies.....	49
3.3	X-ray diffraction Studies	51
3.3.1	Shape Analysis	55
3.4	Photophysical Properties	56
3.4.1	Europium Assemblies.....	57
3.4.2	Ytterbium Assemblies	59
3.4.3	Erbium Assemblies.....	62
3.5	Transient Absorption.....	63
3.6	Conclusion.....	68
Chapter 4	Neodymium Assemblies; Antenna Effect and Lanthanoid-lanthanoid Sensitisation	69
4.1	Introduction	69
4.2	Synthesis.....	69
4.3	X-ray Diffraction	71
4.3.1	Shape Analysis	76

4.4	Photophysical Properties	77
4.4.1	Europium Assemblies	78
4.4.2	Neodymium Assemblies.....	79
4.4.3	Mixed Lanthanoid Assemblies	80
4.5	Conclusions	84
Chapter 5	Stability of β -Triketones in Solution.....	87
5.1	Introduction	87
5.2	Synthesis	87
5.2.1	Ligands	87
5.2.2	Lanthanoid Assemblies	89
5.3	NMR Studies	92
5.4	X-Ray Diffraction Studies.....	98
5.4.1	Products of the Reaction of dmtbmH with Lanthanoids	98
5.4.2	Products of the Reaction of ettbmH with Lanthanoids.....	101
5.4.3	Products of the Reaction of butbmH and t-butbmH with Lanthanoids	102
5.4.4	Products of the Reaction of mtbmH with Lanthanoids	103
5.4.5	Shape Analysis.....	104
5.5	Photophysical Properties	106
5.5.1	Europium Assemblies	109
5.5.2	Ytterbium Assemblies	112
5.6	Conclusions	113
Chapter 6	DMSO Solvated Complexes.....	115
6.1	Introduction	115
6.2	Synthesis	115
6.2.1	Ligand	115
6.2.2	Lanthanoid Assemblies	117
6.3	X-Ray Diffraction Studies.....	118
6.3.1	Shape Analysis.....	119
6.4	Photophysical Properties	120

6.4.1	Europium Emission	122
6.4.2	Ytterbium and Neodymium Emission	124
6.5	Conclusions	128
Chapter 7	Iridium Complexes Using β -Ketonates as Ancillary Ligands	129
7.1	Introduction	129
7.2	Synthesis.....	134
7.2.1	Ligands	134
7.2.2	Complexes	137
7.3	X-Ray diffraction Studies	139
7.4	UV-VIS Studies	140
7.5	Electrochemistry	141
7.6	Photophysical Properties	144
7.7	Conclusions	152
Chapter 8	Conclusion and Future Work	153
Chapter 9	Experimental	157
9.1	General Procedures	157
9.2	Photophysical Measurements	157
9.3	Transient Absorption Measurements.....	159
9.4	Electrochemical Measurements	160
9.5	Synthetic Procedures	161
9.5.1	Synthesis of Ligands.....	161
9.5.2	Synthesis of the Lanthanoid Complexes.....	164
9.6	X-Ray Crystallography.....	171
Chapter 10	References.....	179
Appendix	202

Chapter 1 Introduction

1.1 Introductory Remarks

Lanthanoids were discovered in 1794 by Johan Gadolin but it was not until 1901 that their optical properties had practical applications. In fact, the discovery of the bright emitting phosphor $\text{Y}_2\text{O}_3:\text{Eu}^{3+}$ at the beginning of the 20th century is still in use nowadays. Thanks to their optic and magnetic properties, lanthanoids have contributed enormously towards the development of advanced materials and technologies, including catalysis, magnets, electronic devices, telecommunication systems, lasers, wind and solar energy conversion materials as well as medical applications.¹⁻⁹

While visible emitters such as Sm^{3+} (orange), Eu^{3+} (red), Tb^{3+} (green) and Sm^{3+} (yellow) have been widely studied and are still under investigation for light emitting devices (LEDs) and organic light emitting devives (OLEDs),¹⁰⁻¹² the near infrared (NIR) region is nowadays much in demand in the biomedical area, as light has its maximum depth of penetration in tissue in this spectral region.^{1,3,4,13-17} However, NIR emitters such as Nd^{3+} , Er^{3+} and Yb^{3+} also find applications in telecommunication, optical signalling and night vision technology.^{1,13}

Much of the effort is now focused on the development of highly luminescent lanthanoid-based compounds. Indeed, one of the most studied sensitisers is the bis-chelating β -diketonate molecule. Since the first examples reported in the early 1960s,¹⁸⁻²¹ these complexes have received much interest mainly because of the versatility of this ligand and the stability of the complexes formed.²²⁻²⁵ In contrast, β -triketonate ligands were surprisingly unexplored until 2014 when the first structural characterised example was reported by Reid *et al.*²⁶ A robust family of tetranuclear assemblies was subsequently described.²⁷ Interestingly, the photophysical properties of the NIR complexes were found to be much improved in comparison to the β -diketonate analogues.

The aim of the research presented in this thesis, was to extend the family of β -triketonate based lanthanoid complexes in order to reveal their structural characteristics, as well as to quantitatively characterise their emission properties in realtion to their structure.

1.2 Electronic Properties

1.2.1 Electronic Configuration of Free Ions

The lanthanoid series comprises the elements with atomic number of 57-71 (Ln= La-Lu) in the periodic table. The elemental electronic configuration of the lanthanoids is $[\text{Xe}]4f^n6s^2$ ($n=0-14$), with the exception of lanthanum, cerium, gadolinium and lutetium with configuration $[\text{Xe}]4f^{n-1}5d^16s^2$.²⁸ Their most stable oxidation state is +3 with electronic configuration $[\text{Xe}]4f^n$. However, some lanthanoids are relatively stable at oxidation states +2,²⁹⁻³³ such as Nd^{2+} , Sm^{2+} , Eu^{2+} and Yb^{2+} or even +4 (Ce^{4+}).³⁴⁻³⁷ The 4f orbitals have inner orbital character as a consequence of shielding by the comparatively radially extended 5s and 5p subshells. Additionally, the 4f orbitals are poorly shielded and thus experience strongly the increasing nuclear charge of the xenon core, causing the atomic radius of the lanthanoids to decrease.²⁸ This phenomenon is commonly known as the *lanthanoid contraction* and explains some aspects of the particular chemical and spectroscopic behaviour of the lanthanoid cations.^{38,39}

According to Pauli's exclusion principle, two electrons in the same atom cannot be described by the same set of quantum numbers. Therefore, every 4f electron is described by its four specific quantum numbers. For the lanthanoids, the principal quantum number (n) is equal to 4 and the orbital angular momentum quantum number (l) is 3, referring to the shape of the f orbitals. Each electron is then associated with one of the seven 4f orientations, described by the magnetic quantum number (m_l), and a spin quantum number of +1/2 or -1/2 (m_s). The n electrons for a specific electronic configuration can then be distributed in different combinations following the formula:

$$\frac{(4l + 2)!}{n! (4l + 2 - n)!} = \frac{14!}{n! (14 - n)!} \text{ when } l = 3$$

These combinations are energetically degenerate in the absence of any other interactions apart from electron nuclear attractions. However, electronic repulsions and spin-orbit coupling generate splitting of the ground state electronic configuration into different energy levels, otherwise known as microstates, which are described by new quantum numbers: total spin angular momentum quantum number (S), total orbital angular momentum (L), and the coupling of the spin and the angular momenta, spin-orbit coupling quantum number (J) where:

$$L = \sum_i l_i \quad S = \sum_i s_i \quad J = |L + S|$$

A set of microstates is called a spectroscopic term, which is generally written as $^{2S+1}L_J$. The term representing the lowest energy level, known as the ground state, can be found following Hund's rules:

Rule 1: Largest total spin number (S)

Rule 2: Largest orbital angular momentum (L)

Rule 3: Largest J if electron shell is more than half filled, smallest J if electron shell is less than half filled.

A complete energy level diagram, showing the ground and excited states of all the trivalent lanthanoid ions is displayed in Figure 1.1

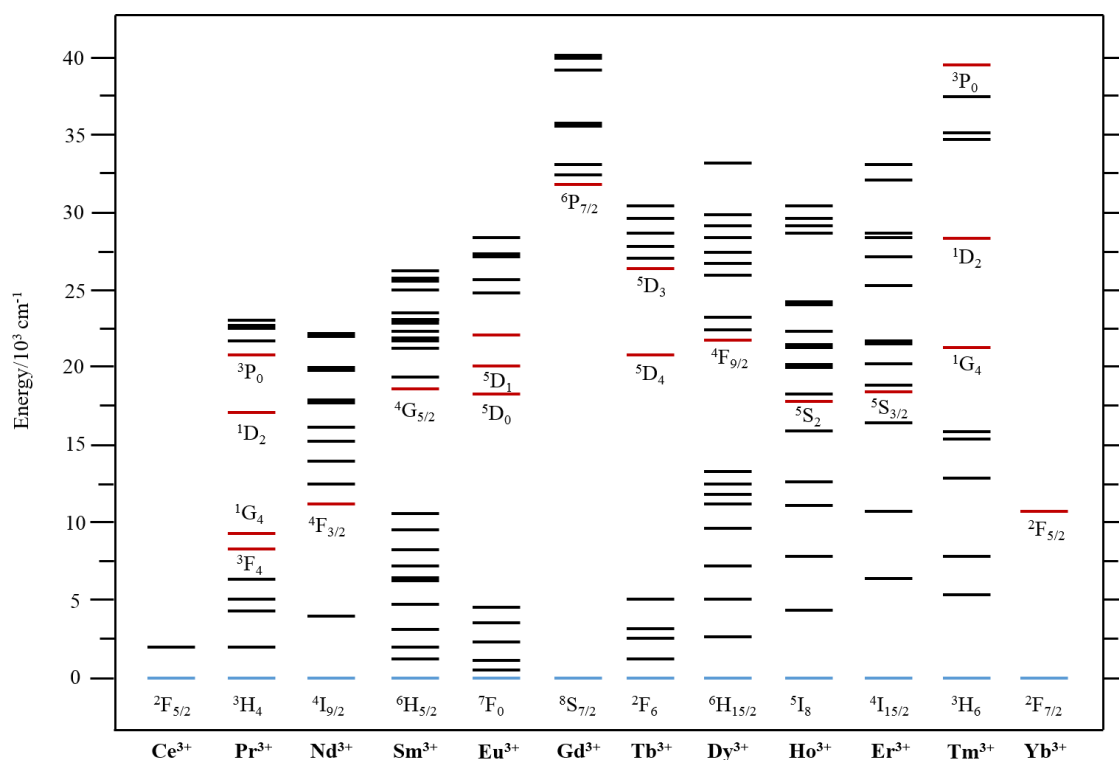


Figure 1.1 Energy levels of the trivalent lanthanoids. Ground states being emphasised in blue and emitting excited states in red. Energy values taken from trivalent lanthanoid aquo ions.⁴⁰

1.2.2 Ligand-field Effects

Although it has been stated that 4f electrons are inner core and are shielded from their environment, their limited interaction with the surrounding ligands nevertheless affects the spherical symmetry of the orbitals, resulting in splitting of the spectroscopic levels into $2J+1$ states. This perturbation results in energy level splitting of 10^2 cm^{-1} at the most, being therefore, generally considered negligible in comparison with electronic repulsions or spin-orbit coupling with splitting of 10^4 cm^{-1} .⁴¹ However, in the case of ions with odd number of electrons (Kramer's ions) the $2J+1$ are two fold degenerate, creating what is commonly known as Kramer's doublets.⁴²⁻⁴⁴

Examples of the splitting of the 4f energy states for Eu^{3+} (even number of electrons) and Yb^{3+} (odd number of electrons) are given in Figure 1.2 and Figure 1.3.

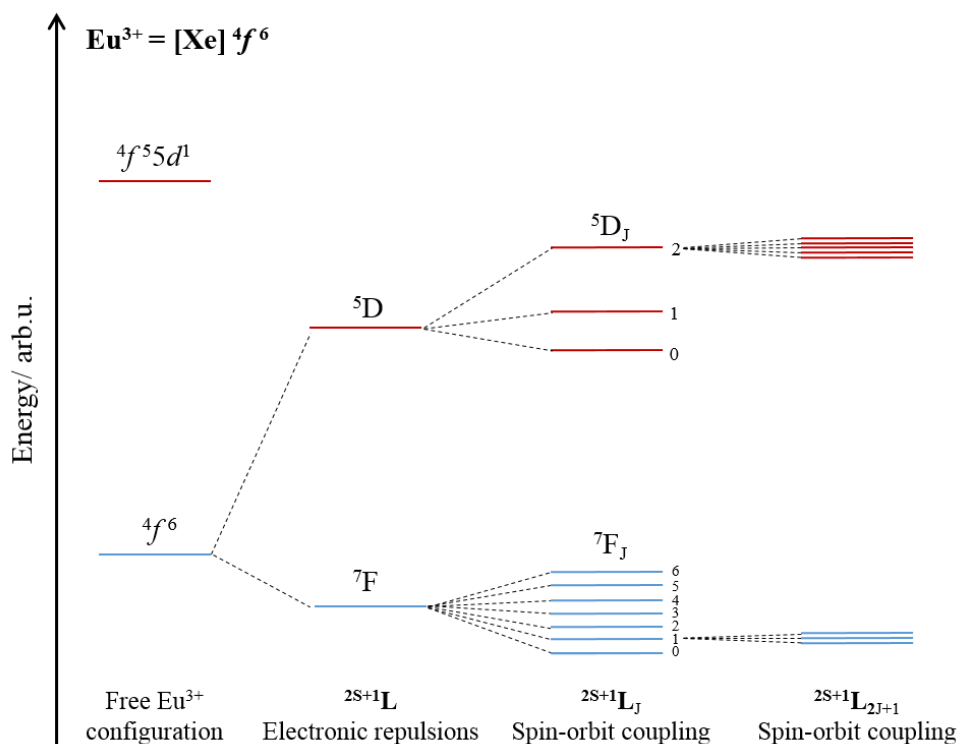


Figure 1.2 Effect of the perturbation on the electronic configuration of Eu^{3+} .

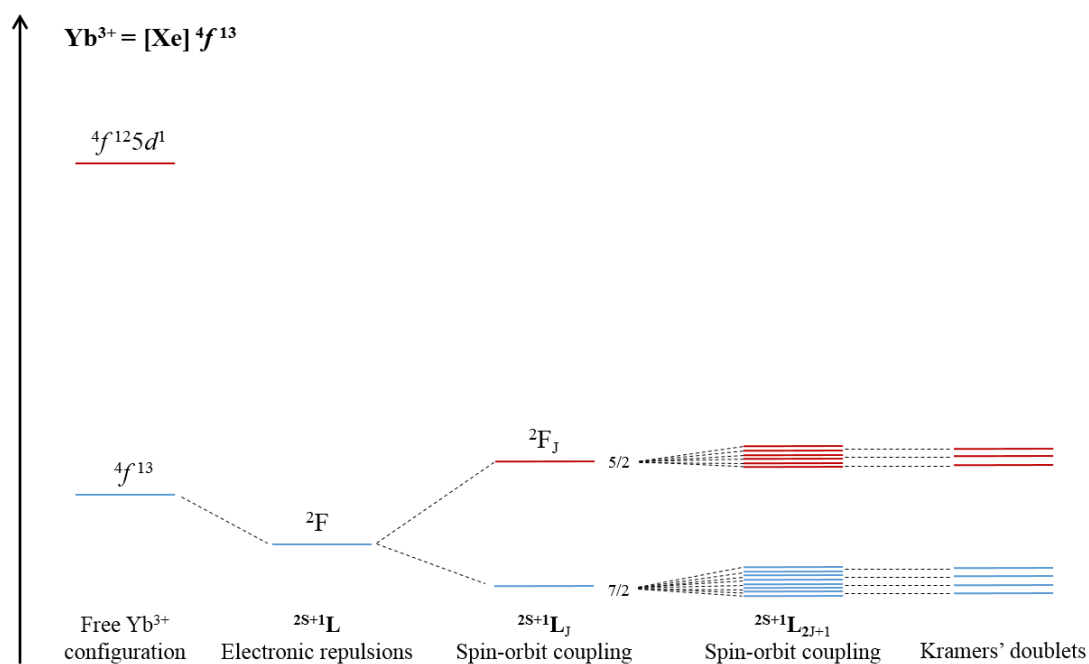


Figure 1.3 Effects of the perturbations on the electronic configuration of Yb^{3+} .

1.3 Absorption Spectra

1.3.1 Absorption of Light

In the process of photoluminescence, absorption of light by matter must always occur before any type of emission occurs. The absorption of light by a molecule dissolved in solution is described by the Beer-Lambert law, Equation 1.1:

$$A = \log \frac{I_0}{I} = \epsilon bc \quad (1.1)$$

Where I_0 is the intensity of the incident light, I is the intensity of the transmitted radiation, b is the optical path length, c is the concentration of the solution and ϵ is the molar absorptivity, which describes the ability for the chromophore to absorb light at a specific wavelength.

When the light hits the sample, the molecules get excited from the ground state to higher energy excited states. Absorbance within the $4f$ shell occurs due to the interaction of the electromagnetic radiation with the f electrons. These transitions can therefore be classified according to their character as electric (ED) or magnetic dipole transitions (MD) with odd and even parity, respectively. The probability of these transitions is determined by the selection rules, discussed in Section 1.2.2.

1.3.2 Selection Rules

The selection rules are based on the symmetry, overlap and multiplicity of the states involved in the transition and can be simplified as the spin rule and parity, or Laporte rule.

The spin rule states that the spins of the ground and excited states must remain constant for a transition to be allowed. As can be seen in the energy level diagram (Figure 1.1) many lanthanoid ground and excited states have a change in spin and therefore are strictly forbidden. However, in the presence of heavy atoms such as the lanthanoids, this rule can be relaxed. In these cases the electron spin interacts with the magnetic vector produced from the orbit resulting in what is commonly known as spin-orbit coupling (SOC). Strong SOC effects favour the mixing of spin states allowing transitions with different multiplicity.⁴⁵

The parity or Laporte rule states that for an optical transition to be allowed, the parity between ground and excited state must change. Since f orbitals have odd symmetry (ungerade), the pure ED transitions (odd parity) are forbidden and only pure MD transitions (even parity) are allowed by the Laporte rule. However, many f-f transitions are activated from the interaction of both ED and MD components with the electrons and can be modified depending on the symmetry in which the lanthanoid is located. Therefore, the transitions would not be purely $u \rightarrow u$ and the parity rule can be relaxed.⁴⁶ In fact, some ED transitions display a large dependence on the coordination environment due to mixing of their electronic states with those of the ligand field. These transitions are denoted *hypersensitive* and their intensity can be enhanced up to 200 times depending on the environment. This phenomenon was proposed by Schaffer and Jorgensen in 1958 who explained how a reduction of the electron repulsion and therefore, expansion in the metal orbitals is caused by the interaction with the orbital clouds of the ligands.⁴⁷ This effect was called the *nephelauxetic effect* or cloud-expanding.

Although it has been shown that *f-f* transitions can be partially allowed by relaxation of the selection rules, their absorption cross section is very low and high intensity sources are required. Thus, their emission needs to be promoted via a sensitizer or antenna with higher molar absorptivity.

1.4 Emission Spectra

All the lanthanoids with the exception of La^{3+} and Lu^{3+} are luminescent, covering the entirety of the spectrum, from UV (Gd^{3+}) to visible (Pr^{3+} , Sm^{3+} , Eu^{3+} , Tb^{3+} , Dy^{3+} and Tm^{3+}) and near infrared (Pr^{3+} , Nd^{3+} , Ho^{3+} , Er^{3+} and Yb^{3+}). Some of the lanthanoid ions are considered fluorescent, when their emission is from a singlet excited state ($\Delta S=0$), while others are

phosphorescent, when their spin multiplicity changes upon emission ($\Delta S \neq 0$). In general, their f-f transitions are sharp and unaffected by the environment since 4f orbitals do not participate much in binding ligands (see Section 1.1.2). The emission of light via f-f transitions is gained via ED or MD and the selection rules are equal to those already described for the absorption.

1.4.1 Excited States

After the absorption of light, molecules will become excited at a higher energy electronic levels, where the position of the nuclei remains unchanged, following the Franck-Condon principle.⁴⁸ This principle states that electronic transitions between two vibrational energy levels will be more likely to happen when the overlap between the two vibrational wavefunctions is significant. After the molecule is excited, two different options are possible for its relaxation to the ground state: radiative and non-radiative pathways.

Non-radiative decays include every process of relaxation that does not involve emission of light. Kasha's rule states that the absorption of light will be followed by the excited molecule relaxing to the lowest singlet state (S_1) via internal conversions (IC).⁴⁹ From here, molecules can relax back to the ground state, via further IC processes, or to one with different multiplicity via a process called inter-system crossing (ISC). Although ISC is considered forbidden by the selection rules, it can be facilitated due to spin-orbit coupling effects in the presence of heavy metals, commonly known as the heavy atom effect. The non-radiative decay rates are in part governed by the energy gap law, which states, in simple terms, that the smaller the energy gap between two states, the greater the non-radiative decay rates (k_{nr}).

In contrast, radiative decays involve relaxation processes with spontaneous emission of light. From the lowest excited state, in a similar manner as the non-radiative decay, the molecules can further relax to a state with the same spin multiplicity (fluorescence) or to one involving a change in spin (phosphorescence).

The processes taking place after electronic excitation of molecules due to the absorption of light are normally presented in a Jablonski diagram (see Figure 1.4).

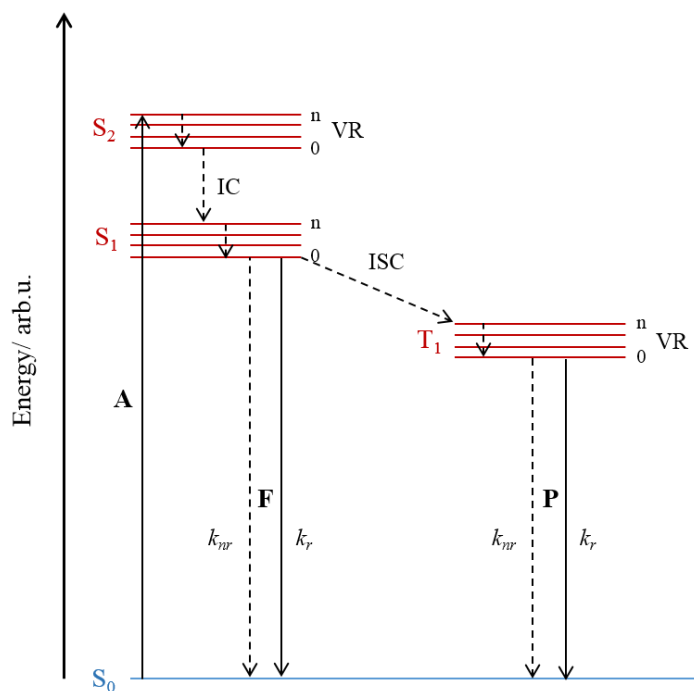


Figure 1.4 Jablonski diagram showing the processes of absorption (A), vibrational relaxation (VR), internal conversion (IC), intersystem crossing (ISC), fluorescence (F) and phosphorescence (P). k denotes rates of radiative (r) and non-radiative (nr) decays.

1.4.2 Sensitisation Mechanism

Due to the forbidden nature of the $f-f$ transitions and therefore, low absorptivity, efficient excitation pathways are necessary. The first description of lanthanoid sensitisation was reported by Weissman in 1942 where the $4f^*$ excited state emission was promoted by energy transfer from an organic chromophore. This process is commonly known as the *antenna effect* and consists of the use of a sensitising molecule (antenna) with higher molar absorptivity that can then be involved in energy transfer to the metal centre. The process, illustrated in Figure 1.5, starts with the absorption of light by the antenna molecule, which leads to a singlet state (S_n). Due to the presence of a lanthanoid ion, intersystem crossing is facilitated, leading to population of a long lived triplet state (T_1) that can transfer the energy to the emissive lanthanoid excited state ($4f^*$).

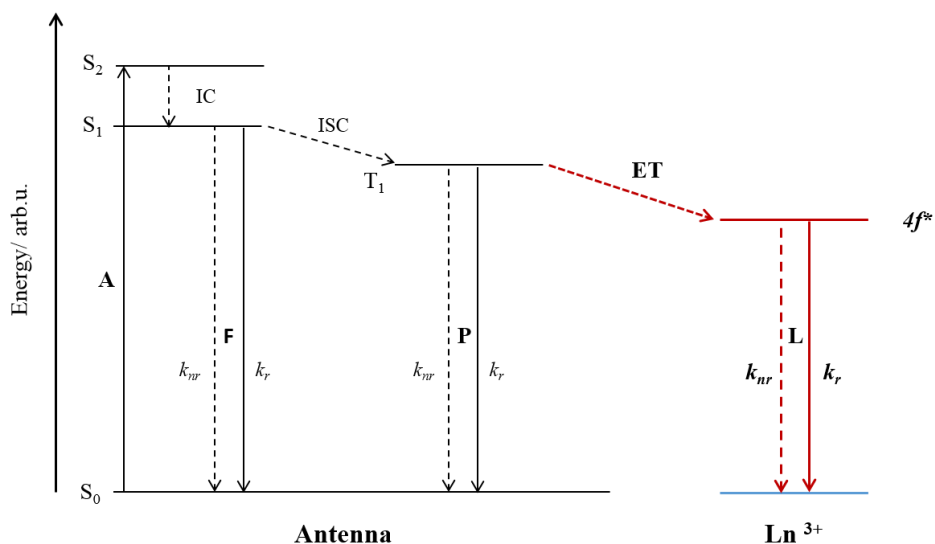


Figure 1.5 Jablonski diagram showing the antenna effect involving the processes of absorption (A), vibrational relaxation (VR), internal conversion (IC), intersystem crossing (ISC), antenna fluorescence (F), antenna phosphorescence (P), energy transfer (ET) and lanthanoid luminescence(L) where k denotes rates of radiative (r) and non-radiative (nr) decays.

Although it is normally assumed that energy transfer occurs from the triplet state of the organic molecules due to an effective intersystem crossing,⁵⁰ there are a few examples reported where the energy is transferred directly from the singlet state^{51–55}.

1.4.3 Energy Transfer

As discussed before, in the sensitisation process the energy absorbed by the antenna must then be transferred to the lanthanoid ion. This process can be achieved by three possible mechanisms, involving a double electron exchange (Dexter energy transfer), a virtual photon by dipole-dipole exchange (Förster energy transfer) or the lesser known dipole-multipole mechanism. In this chapter only the Dexter and Förster mechanisms will be covered. However, it is important to point out that dipole-multipole mechanisms can contribute greatly to the energy transfer process.⁵⁶

The Dexter mechanism was first proposed by Dexter in 1945.⁵⁷ It involves a double exchange of electrons between donor and acceptor as shown in Figure 1.6. For this process to occur there should be an overlap of the electronic wavefunctions between donor and acceptor, which generally requires overlap of the orbitals involved. Therefore, donor and acceptor must sit relatively close in distance ($<10\text{\AA}$). The rate of Dexter energy transfer (k_{ET}^D) can be expressed following Equation 1.2.

$$k_{ET}^D = \frac{2\pi}{h} V_0^2 J_D \exp\left(-\frac{2R_{DA}}{L}\right) \quad (1.2)$$

where h is Plank's constant, R_{DA} is the distance between donor and acceptor, L is the sum of van der Waals radius, J_D is the Dexter overlap integral and V_0 is the electronic coupling matrix element between the donor and acceptor at the contact distance.

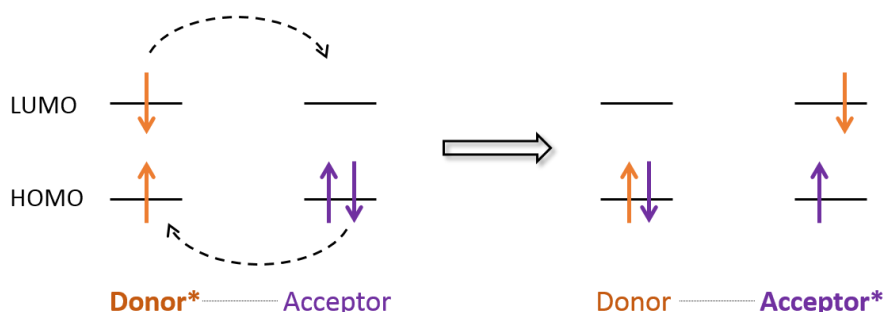


Figure 1.6 Representation of Dexter energy transfer mechanism.

On the other hand, the Förster mechanism was first proposed in 1948 and it is also known as the coulombic or dipole-dipole mechanism.⁵⁸ This mechanism involves the migration of a virtual photon from an excited donor to an acceptor molecule as illustrated in Figure 1.7. It, therefore, requires the overlap between the emission bands of the donor with the absorption bands of the acceptor. Moreover, it does not require physical contact between donor and acceptor and can occur over much longer distances. The rate of Förster energy transfer (k_{ET}^F) is given by Equation 1.3:

$$k_{ET}^F = k_o \left(\frac{R_0}{R} \right)^6 \quad (1.3)$$

where k_o is the rate of spontaneous deactivations of the excited donor, R_o is the Förster radius defined as the distance at which 50% of the excited state is transferred, and R is the distance between donor and acceptor.

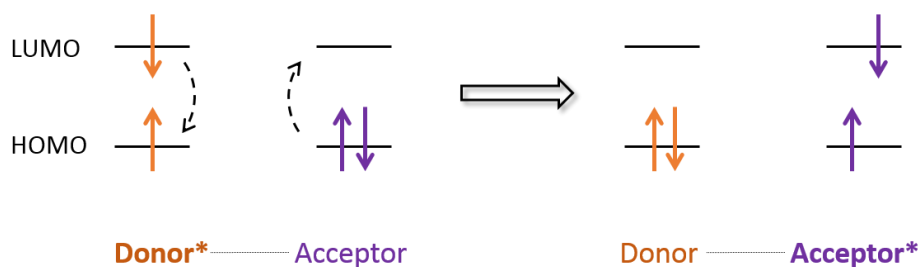


Figure 1.7 Representation of Forster energy transfer mechanism.

In the case of the lanthanoid ions, energy transfer is generally accepted to occur following Förster mechanisms due to the poor overlap between the 4f orbitals with the orbitals of the ligands. However, because Eu^{3+} and Yb^{3+} are easily reduced, Dexter mechanisms can also be possible.^{59,60}

1.4.4 Non-radiative Decay

The lanthanoid sensitisation process is often deactivated to some degree by non-radiative processes, including back energy transfer (BET) to the antenna triplet state, concentration quenching and multiphonon relaxation enhanced by the ligand or solvent molecules. These pathways of quenching generally lead to an increase of the non-radiative rates with the result of overall low emission efficiencies of sensitisation. The three main non radiative quenching mechanisms of the lanthanoid excited states are represented in Figure 1.8.

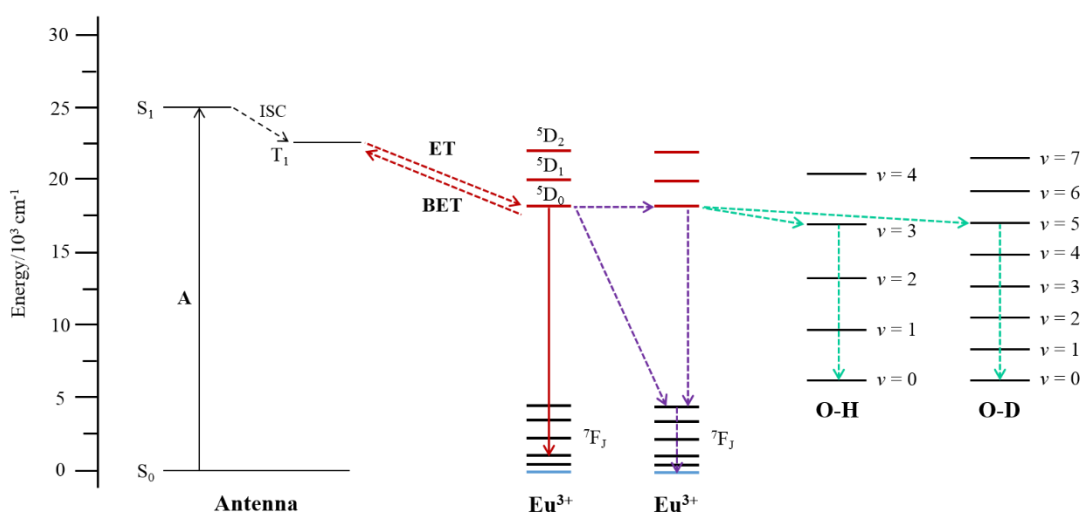


Figure 1.8 Simplified sensitisation and quenching of Eu^{3+} excited states via back energy transfer (red trace, BET), lanthanoid-lanthanoid cross-relaxation (purple trace) and multiphonon relaxation (green trace).

1.4.4.1 Back Energy Transfer

Triplet states play an important role in either the sensitisation process, as explained in Section 1.3.2, or quenching processes, if the energy of the antenna triplet state lies close in energy to the lanthanoid excited states. In fact, it has been reported that an energy difference of 2,500 cm^{-1} is required to provide efficient energy transfer from the ligand to the metal ion and minimise the probability of back energy transfer (BET).⁶¹

1.4.4.2 Lanthanoid-lanthanoid Cross Relaxation Quenching

Concentration quenching usually refers to all types of quenching between lanthanoid ions at high concentrations of Ln^{3+} . Although there are different models for concentration quenching,⁶² cross-relaxation is usually accepted as the general term when the energy is transferred between identical Ln^{3+} with multiple energy levels.⁶³ Therefore, this terminology should be used cautiously for the lanthanoids containing one unique excited state, such as Yb^{3+} .

Lanthanoid to lanthanoid energy transfer is facilitated when the lanthanoid ions lie close in distance, generally taken to be less than 8 Å.^{64,65} For longer distances the f - f energy transfer has been found to be ligand-mediated.^{66,67}

Although this type of energy transfer is normally considered as a quenching pathway there is one example that showed how energy transfer between Tb^{3+} centres actually inhibits BET and promotes the emission properties of the clusters.⁶⁸ In fact, it can also be utilised as a sensitisation mechanism when it involves two different lanthanoids.⁶⁹⁻⁷⁶

1.4.4.3 Multiphonon Relaxation

Lanthanoid excited states can also be quenched by molecular vibrations from the ligands or solvents around the lanthanoid ions. In particular, overtones of high-energy vibrations of groups such as O-H, N-H and to a lesser extent C-H, can efficiently quench the lanthanoid luminescence. Multiphonon relaxation follows the energy gap law and, therefore, the greater the energy gap between the emissive state and the highest sublevel of the ground state, the less likely quenching will occur. This is because the number of phonons needed to bridge the energy gap is higher.⁴¹ An example for Eu^{3+} is given in Figure 1.8, where the energy gap between the $^5\text{D}_0$ and $^7\text{F}_6$ is approximately 12,000 cm^{-1} . As an O-H bond has a vibrational energy of 3600 cm^{-1} , three vibrational quanta are required to effectively quench the Eu^{3+} emissive state.^{77,78} In contrast, the bond O-D with a vibrational energy of 2200 cm^{-1} would require five vibrational quanta to relax the $^5\text{D}_0$ state and therefore, this process is less efficient.⁷⁷ The energy gap law for the some lanthanoid ions with respect to the vibrational energy of the bond O-H is illustrated in Table 1.1.

Table 1.1 Number of phonons required for efficient multiphonon relaxation quenching of the Ln³⁺ emissive states.

Ln ³⁺	States involved	ΔE (cm ⁻¹)	n• phonons	
			O-H	O-D
Gd	⁸ S _{7/2} ← ⁶ P _{7/2}	32100	9	14-15
Tb	² F ₀ ← ⁵ D ₄	14800	4	7
Eu	⁷ F ₆ ← ⁵ D ₀	12200	3-4	5-6
Yb	² F _{7/2} ← ² F _{5/2}	10300	3	4-5
Er	⁴ I _{15/2} ← ⁴ I _{13/2}	6600	2	3
Nd	⁴ I _{15/2} ← ⁴ F _{3/2}	5400	1-2	2-3

Because NIR-emitting lanthanoid ions have the smallest energy gap they are the most affected by multiphonon relaxation. In fact, it has been demonstrated that C-H oscillators within a sphere of 20 Å from the lanthanoid centre can efficiently quench Er³⁺ and Nd³⁺.^{79,80} Therefore, special effort must be made in the design of the NIR emitters, where the main strategy to minimise this type of quenching so far is by deuteration or perfluorination (see Section 1.4.2).

1.4.5 Charge Transfer States

Although energy transfer from π - π^* states is the most common sensitisation pathway in funnelling energy to an excited lanthanoid state, sensitisation via charge transfer states (CT) is also possible. There are three main different types of CT states: ligand centred CT states, commonly known as intraligand charge transfer (ILCT), ligand-to-metal CT states (LMCT)⁸¹ or metal-to-ligand CT states (MLCT) originating from transitions involving the metal.

The role of an ILCT highly depends on its energy and relative to the energy of the excited state of the lanthanoid involved.^{6,81} It can act as the main donor state⁸²⁻⁸⁵ or as a quencher^{86,87} when its energy level is above or too close to the excited emitting lanthanoid state, respectively.

LMCT states are present mainly for Eu³⁺ and Yb³⁺ complexes as they are more easily reduced. In the case of Eu³⁺, these states have a strong quenching effect when lying below 25,000 cm⁻¹.^{88,89} In contrast, favourable contribution is found when the LMCT is located at higher energies.⁹⁰ In the case of Yb³⁺, some examples of LMCT state acting as efficient donors have also been reported.⁹¹⁻⁹⁴

Finally, MLCT states from d-block metal complexes can also be used as sensitisers. In fact, there are numerous examples of efficient sensitisation from metal complexes such as those based on ruthenium(II), rhenium(I) and iridium(III) amongst others.⁹⁵⁻¹⁰⁶ However, when

targeting Eu^{3+} and Tb^{3+} , due to the close proximity between the MLCT and the lanthanoid emissive states, energy transfer is often not efficient.^{107–109}

1.4.6 Efficiency of the Sensitisation Process

Two important parameters characterise the emission of light from the lanthanoid emissive states; the lifetime of the excited state (τ) and the photoluminescence quantum yield (Φ).

The observed lifetime (τ_{obs}) is the time required for the excited state to decay to 1/e or 36.8% of its original population, as a combination of the probabilities of the radiative and non-radiative decays. Observable lifetimes can easily be measured by experimental methods.

$$\tau_{\text{obs}} = \frac{1}{k_r + k_{nr}} \quad (1.4)$$

In contrast, the radiative lifetime (τ_r) describes the depopulation of the emissive state in the absence of non-radiative decays.

$$\tau_r = \frac{1}{k_r} \quad (1.5)$$

The radiative decays are not constant values for a given lanthanoid ion; they define a specific excited state in a given coordination environment. Also, radiative decays depend on the refractive index of the media and their value can be changed depending on the ligands or solvent used. Therefore, their experimental determination is much more difficult. However, there are two cases where the radiative decays can be calculated:

- a) The absorption spectrum of the excited emissive state is known. One common example is Yb^{3+} due the simplicity of its luminescence transition involving a unique excited state and the ground level (${}^2\text{F}_{7/2} \leftarrow {}^2\text{F}_{5/2}$). In this case, radiative decay can be calculated following Equation 1.6.

$$\frac{1}{\tau_r} = 2303 \times \frac{8\pi c n^2 \check{\nu}^2 (2J+1)}{N_A (2J'+1)} \int \varepsilon(\check{\nu}) d\check{\nu} \quad (1.6)$$

Where N_A is the Avogadro's number (6.023×10^{23} molecules/mol) and J and J' are the quantum number for the ground and excited state, respectively.

- b) Eu^{3+} where the radiative decay can be calculated following Equation. 1.7 due to the magnetic dipole nature of its ${}^7\text{F}_1 \leftarrow {}^5\text{D}_0$ transition⁴⁶.

$$\frac{1}{\tau_r} = A_{MD,o} n^3 \left(\frac{I_T}{I_{MD}} \right) \quad (1.7)$$

Where $A_{MD,o}$ is the spontaneous emission probability of the ${}^7\text{F}_1 \leftarrow {}^5\text{D}_0$ transition with a constant value of 14.65 s^{-1} , I_T/ I_{MD} is the ratio of the total integrated area to the magnetic dipole transition of the Eu^{3+} emission spectrum⁵¹ and n is the refractive index of the medium, considered 1.5 in the solid state.¹¹⁰

The photoluminescence quantum yield (Φ) is the ratio of the number of emitted photons to the number of photons absorbed and therefore, describes the efficiency of the whole sensitisation process. For the lanthanoid ions two different values of quantum yield are normally calculated. The intrinsic quantum yield (Φ_{Ln}^{Ln}) describes the contribution of radiative decay from the lanthanoid excited states, taking into account the radiative and non-radiative rates, following Equation 1.8:

$$\Phi_{Ln}^{Ln} = \frac{k_r}{k_r + k_{nr}} = \frac{\tau_{obs}}{\tau_R} \quad (1.8)$$

As the intrinsic quantum yield depends directly on the radiative decay, this value is difficult to estimate. However, the overall quantum yields (Φ_{Ln}^L), which describes the overall efficiency of sensitised emission, can be obtained experimentally with the use of an integrating sphere or by dilute method.¹¹¹

The two different quantum yields are related according to equation 1.9:

$$\Phi_{Ln}^L = \Phi_{ISC} \times \Phi_{ET} \times \Phi_{Ln}^{Ln} = \Phi_{sens} \times \Phi_{Ln}^{Ln}$$

The efficiency of energy transfer (Φ_{ET}) and intersystem crossing (Φ_{ISC}) combined are defined by the sensitisation efficiency (Φ_{sens}).

1.5 Lanthanoid β -Diketonate Based Complexes

1.5.1 Overview

Different antenna ligands have been explored for the sensitisation of the lanthanoid emission. These range from simple organic molecules^{112–118} to macrocyclic ligands.^{119–125} Lanthanoid β -diketonate complexes are one of the most popular and investigated complexes. Since the first example was synthesised in 1897 by Urbain¹²⁶, these complexes have been explored because of their multiple applications; from solvent-solvent extraction processes in the 1960s, to NMR shift reagents in the 1980s, to electroluminescent materials in organic light emitting diodes (OLEDs) in recent times.

β -Diketones are 1,3-diketones where the two carbonyl groups are separated by one central carbon atom (α -C). Alkyl groups, fluorinated alkyl groups or aromatic and heteroaromatic groups, can act as substituents on the carbonyl function, opening up a versatile family of molecules (Figure 1.9 and Figure 1.10).^{127,128}

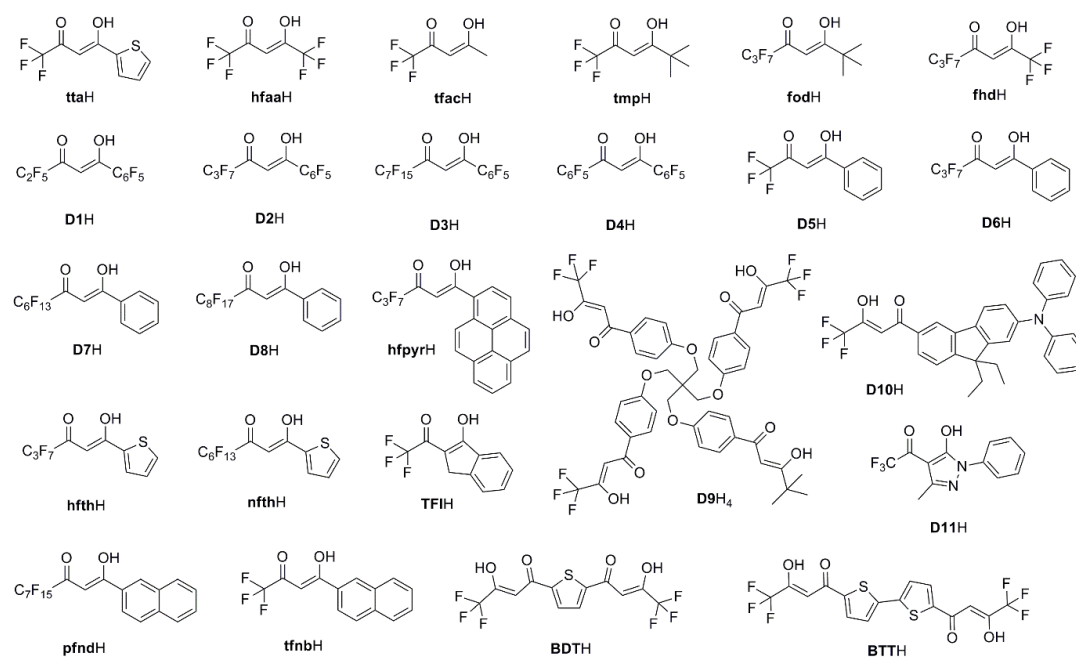


Figure 1.9 Selection of fluorinated β -diketonates.

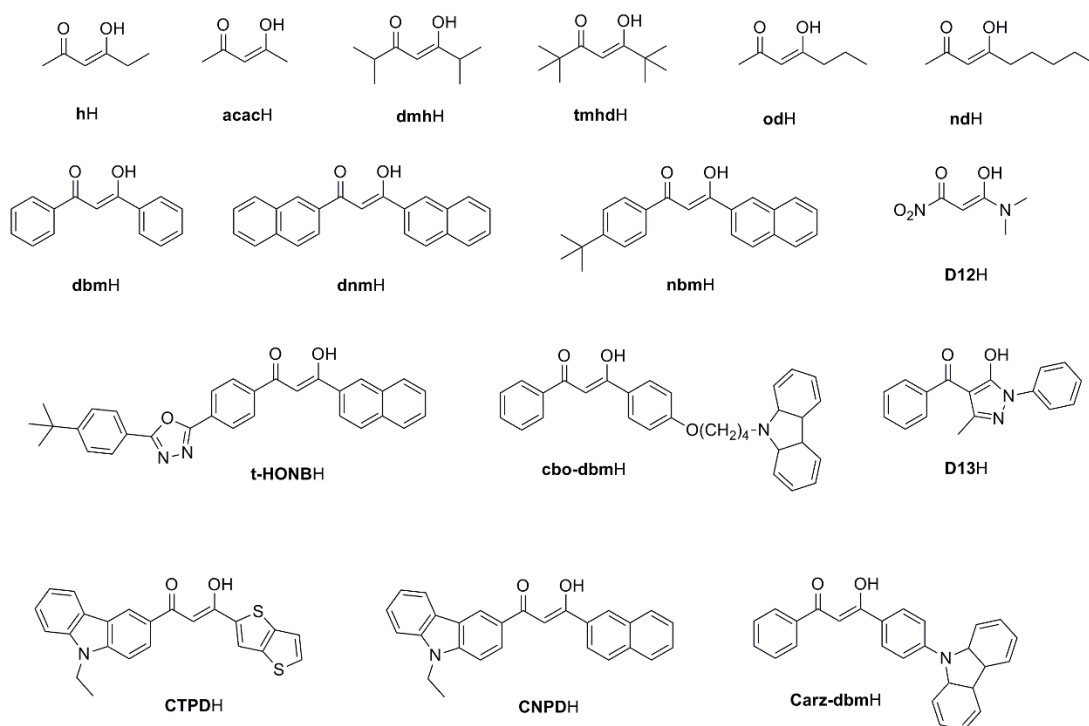


Figure 1.10 Selection of non-fluorinated β -diketones.

These molecules exhibit keto-enol tautomerism in solution that is influenced by the nature of the substituents on the dicarbonyl system, the solvent and the temperature (see Figure 1.11).

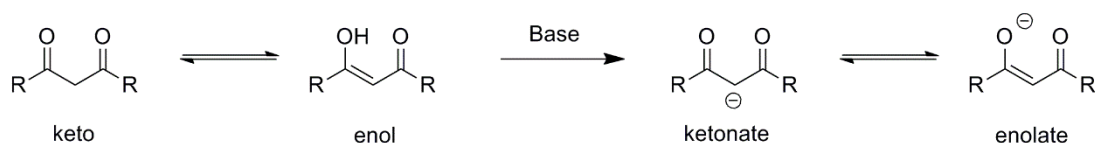


Figure 1.11 Keto-enol tautomerism of β -diketones and β -diketonates after deprotonation.

β -Diketonates are bis-chelating ligands giving mostly three types of complexes: tris complexes, tetrakis complexes and Lewis-base adducts of tris complexes. While unsolvated tris-complexes have a six-coordinate lanthanoid ion,^{129,130} most of the β -diketonate-based complexes are eight coordinate where molecules of solvent or Lewis bases, such as 1,10-phenanthroline (phen) or 2,2'-bipyridine (bpy), complete the coordination sphere (see Figure 1.12)^{74,131–136}. The tetrakis-complexes arrange four β -diketonates ligands around the lanthanoid ion forming anionic complexes with formula $R[Ln(\beta\text{-diketonate})_4]$, where R is an organic or inorganic cation.^{137–141}

The main β -diketonate based complexes emitting in the visible and the NIR regions will be assessed from a photophysical perspective in the next sections.

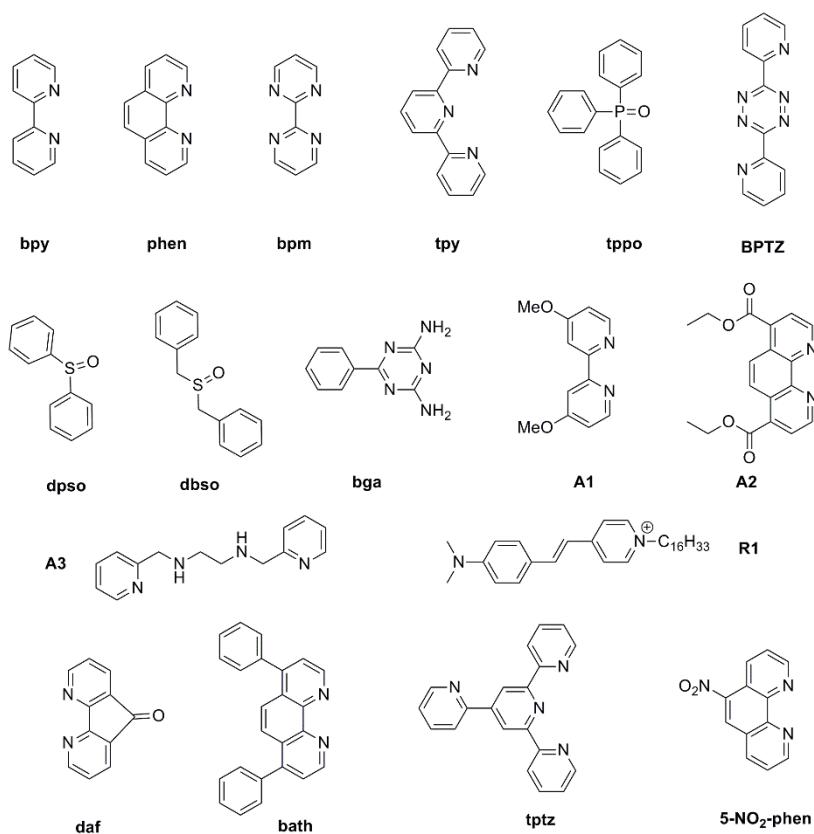


Figure 1.12 A selection of ancillary ligands used to complete the coordination sphere in lanthanoid β -diketonate complexes.

1.5.2 NIR Emitters

Lanthanoid complexes exhibiting NIR emission have been used in applications for fibre-optic communication as well as night vision technology, NIR-OLEDs and biomedical probes.^{10,13,81,83,84,142–147}

In this section, β -diketonate complexes of Nd^{3+} , Er^{3+} and Yb^{3+} will be reviewed, focussing on reports that include quantitative data such as quantum yields and lifetimes. Because overall quantum yield data in the NIR range remain scarce due to the low availability of fully equipped instruments for the NIR range, intrinsic quantum yields will also be considered.

The NIR-emitting lanthanoids Nd^{3+} , Er^{3+} and Yb^{3+} are characterised by relatively short excited state lifetimes given their spin-allowed transition and their tendency to be readily quenched. More than fifty papers have been published in the last couple of decades presenting β -diketonate-based lanthanoid complexes emitting in the near infrared region. Two main strategies on the design of β -diketonates have been followed for improving the photophysical properties of the complexes. The first one emphasises removing high-energy vibrators such as C-H or O-H by deuteration and fluorination or the use of an extra generally neutral ligand,

80,148–172 while the second one focuses on lowering the energy of the donor states to facilitate the energy transfer to the f^* states.^{173–184} A list of the corresponding photophysical data for these complexes is provided in Table A1-A3 while the most pertinent results are summarised in Tables 1.2-1.4

Altogether, the best Yb^{3+} complex was obtained by Tsvirko *et al.* in 2001 for the complex with formula $[\text{Yb}(\mathbf{tta}\text{-}\mathbf{D})_3(\text{DMSO-}d^6)_n]$ in $\text{DMSO-}d^6$ with an overall quantum yield of 6.1%.¹⁵⁰ In this report the influences of the additional neutral ligand and the deuteration of the proton in the α -C position of the β -diketonate were studied, suggesting an improvement for the cited complex with respect to the $[\text{Yb}(\mathbf{tta})_3(\text{OH}_2)_2]$, $[\text{Yb}(\mathbf{tta})_3(\text{phen})]$ and $[\text{Yb}(\mathbf{tta})_3(\text{DMSO-}d^6)_n]$ with quantum yields of 0.12%, 1.6% and 2.14%, respectively. However, deuteration techniques are expensive and not widely accessible and therefore, other complexes have been suggested since then. Two good examples are the complexes $[\text{Yb}(\mathbf{hfaa})_3(\text{bpy})]$ ¹⁶⁶ and $[\text{Yb}(\mathbf{hfpvr})_3(\text{bath})]$ ¹⁸⁴ with overall quantum yields of 3.3% and 3.08%, respectively (see Table 1.2).

Table 1.2 Selected Yb^{3+} emitting systems published recently (1999-2017).

Complex	Sample	$\tau_{\text{obs}}/\mu\text{s}$	$\Phi_{\text{Ln}}^{\text{Ln}}(\%)$	$\Phi_{\text{Ln}}^{\text{L}}(\%)$	Ref
$[\text{Yb}(\mathbf{tta}\text{-}\mathbf{D})_3(\text{DMSO-}d^6)_n]$	$\text{DMSO-}d^6$	71.8	-	6.1 ^b	150
$[\text{Yb}(\mathbf{hfaa})_3(\text{bpy})]$	CHCl_3	47	-	3.3 ^d	166
$[\text{Yb}(\mathbf{hfpvr})_3(\text{bath})]$	Powder	13.45	0.67 ^a	3.08 ^b	184
$[\text{Yb}(\mathbf{D9})](\text{NBu}_4)$	Powder	12.3	-	2.6 ^b	178
$[\text{Yb}(\mathbf{tta})_3(\text{dpsO})]$	CHCl_3	-	-	2.40 ^d	169
$[\text{Yb}(\mathbf{tta})_3(\text{DMSO-}d^6)_n]$	$\text{DMSO-}d^6$	27.3	-	2.14 ^b	150
$[\text{Yb}(\mathbf{tta})_3(\text{tppo})]\text{H}_2\text{O}$	CHCl_3	-	-	1.92 ^d	168
$[\text{Yb}(\mathbf{tta})_3(\text{phen})]$	Toluene	15.8	-	1.6 ^b	150
	Toluene	10.4	-	1.10 ^b	148
$[\text{Yb}(\mathbf{hftH})_3(\text{phen})]$	Powder	14.7	-	-	153
	Toluene	-	-	1.28 ^c	
$[\text{Yb}(\mathbf{D11})_3(\text{bipy})]$	MeCN	16.17	1.35 ^a	1.12 ^d	183

^a Assuming literature τ_{R} of 2 ms.⁶ ^b Measured with an integrating sphere. ^c Calculated following diluted methods with $[\text{Yb}(\mathbf{tta})_3(\text{phen})]$ as reference ($\Phi_{\text{Ln}}^{\text{L}}=1.1\%$).¹⁴⁸ ^d Calculated following diluted methods with $[\text{Yb}(\mathbf{tta})_3(\text{H}_2\text{O})_2]$ as reference ($\Phi_{\text{Ln}}^{\text{L}}=0.35\%$).¹⁴⁸

In the case of Er^{3+} the same strategies have been followed, however, highly luminescent complexes have not been found. Although the value of the lifetime has been improved recently to even values of 106 μs after deuteration at the α -C position of the β -diketonate, the sensitisation efficiency remains especially poor and therefore the overall quantum yields remain low. Their poor emissive properties make their photophysical quantification almost impossible and only a few papers have indeed reported values of quantum yield in the range of 0.01-0.1 % (See Table 1.3). Noteworthy examples are $[\text{Er}(\mathbf{D12})_3(\text{phen})]$, $[\text{Er}(\mathbf{CNPD})_3(\text{tpy})]$ and particularly $[\text{Er}(\mathbf{D10})_3(\text{DMSO})_n]$ with sensitisation via an ILCT state in the visible for the latest complex.^{176,177,180}

Table 1.3 Selected Er^{3+} emitting systems published recently (1999-2017).

Complex	Sample	$\tau_{\text{obs}}/\mu\text{s}$	$\Phi_{\text{Ln}}^{\text{Ln}}$ (%)	$\Phi_{\text{Ln}}^{\text{L}}$ (%)	Ref
$[\text{Er}(\mathbf{D10})_3(\text{phen})]$	THF	2.5	-	0.11 ^b	180
$[\text{Er}(\mathbf{hfth})_3(\text{phen})]$	Powder	2.73	-	-	153
	Toluene	-	-	0.019 ^c	
$[\text{Er}(\mathbf{CNPD})_3(\text{tpy})]$	MeCN	1.44	-	-	177
	Powder	-	-	0.008 ^d	
$\text{Cs}[\text{Er}(\mathbf{hfaa-D})_4]$	Powder	106	-	-	80
$[\text{Er}(\mathbf{hfaa})_3(\text{TPPO})_2]$	Powder	60.8	0.43 ^a	-	154
$[\text{Er}(\mathbf{D12})_3(\text{DMSO})_n]$	DMSO	DMSO	-	-	176

^a Assuming literature τ_R of 14 ms.¹⁸⁵ ^b Calculated following diluted methods with 9,10-diphenylanthracene as reference ($\Phi = 95\%$).¹⁸⁶ ^c Calculated following diluted methods with $[\text{Yb}(\text{tta})_3(\text{phen})]$ as reference ($\Phi_{\text{Ln}}^{\text{L}} = 1.1\%$).¹⁴⁸ ^d Measured with an integrating sphere.

Something similar occurs for Nd^{3+} with slightly higher quantum yields in the range of 0.01-1.0%. The complex with the highest quantum yield was reported in 2016 by George *et al.* with values of lifetimes and quantum yields of 6.16 μs and 1.07%, respectively.¹⁸⁴ Simultaneous energy transfer from singlet and triplet states of the ligand were found in the $[\text{Nd}_2(\mathbf{BDT})_3(\text{DMSO})_6]$ thereby achieving reasonable quantum yields of almost 0.5%.¹⁵³

These reports present multiple methods to calculate intrinsic and overall quantum yields. As explained in Section 1.3.6, intrinsic quantum yields depend on radiative decays that are not easily calculated by experimental methods. Therefore, the majority of the research groups use reference values. However, as can be noted in Tables 1.2-4 the reference values used are not always the same. For example, for Nd^{3+} two main values are commonly used: 0.25 ms and 0.42 ms.^{6,187} Consequently, intrinsic quantum yields should be compared with extreme care.

On the other hand, overall quantum yields calculated by absolute methods such as an integration sphere are considerably more reliable. Unfortunately, only a few laboratories are equipped with the necessary instrumentation for quantum yield measurements in the NIR. Hence, dilute methods by comparison with a reference in solution are often the preferred option. The reference is normally [Yb(tta)₃(OH)₂] or [Yb(tta)₃(phen)] in toluene. These complexes were first reported in 1999 by Meshkova *et al.*¹⁴⁸ with overall quantum yields values of 0.35% and 1.1%, respectively. However, only a couple of years later, the same group suggested new values of 0.12% and 1.6%¹⁵⁰, respectively. Both values are still being used at present.

Table 1.4 Selected Nd³⁺ emitting systems published recently (1999-2017).

Complex	Sample	$\tau_{\text{obs}}/\mu\text{s}$	$\Phi_{\text{Ln}}^{\text{Ln}}$ (%)	$\Phi_{\text{Ln}}^{\text{L}}$ (%)	Ref
[Nd(hfpyr) ₃ (bath)]	Powder	6.16	2.28 ^a	1.07 ^d	184
[Nd ₂ (BDT) ₃ (DMSO) ₆]	DMSO	-	-	0.49 ^e	153
[Nd(D4) ₃]	THF- <i>d</i> ⁸	4.5	1.70 ^b	0.42 ^d	149
[Nd(D12) ₃ (phen)]	THF	1.6	-	0.09 ^f	180
[Nd(hfaa) ₃ (bpy)]	CHCl ₃	1.5	-	0.19 ^e	166
[Nd(CTPD) ₃ (tpy)]	MeCN	0.95	-	-	177
	Powder	-	-	0.1 ^d	
[Nd(hftth) ₃ (bipy)]	Powder	1.27	-	-	153
	Toluene	-	-	0.072 ^g	
[Nd(D13) ₃ (bipy)]	MeCN	5.34	1.27 ^a	0.068 ^e	183
[Nd(D10) ₃ (DMSO) _n]	DMSO	1.2	0.29 ^c	0.008 ^d	176

^a Assuming literature τ_{R} of 0.25 ms.¹⁸⁷ ^b Measured with an integrating sphere after direct excitation. ^c Assuming literature τ_{R} of 0.42 ms.⁶ ^d Measured with an integrating sphere. ^e Calculated following diluted methods with [Yb(tta)₃(OH)₂] as reference ($\Phi_{\text{Ln}}^{\text{L}}=0.35\%$).¹⁴⁸ ^f Calculated following diluted methods with 9,10-diphenylanthracene as reference ($\Phi=0.95\%$).¹⁸⁶ ^g Calculated following diluted methods with [Yb(tta)₃(phen)] as reference ($\Phi_{\text{Ln}}^{\text{L}}=1.1\%$).¹⁴⁸

Although improved photophysical properties of the β -diketonate lanthanoid complexes have been achieved in the last decade, these complexes are still not as efficient as those with β -diphosphinate ligands, which show particularly long lifetimes of 1.1 ms, 741 μs and 44 μs for Yb³⁺, Er³⁺ and Nd³⁺, respectively.¹³³

1.5.3 Visible Emitters

Visible emitter lanthanoid complexes have been extensively investigated due to their applicability in many fields such as organic light emitting diodes (OLEDs) as well as probes for biomedical applications.^{1,2,5,10,84,188,189}

The photophysical properties of the visible lanthanoid β -diketonate complexes have been extensively investigated^{160,161,171,180,190–199} and summarised in recent reviews.^{200,201} Therefore, this chapter will only include the most relevant examples for Eu^{3+} in the context of this work.

A large library of β -diketonates and ancillary ligands are also found for visible emitters. A selected list of them are presented in Figure 1.13.

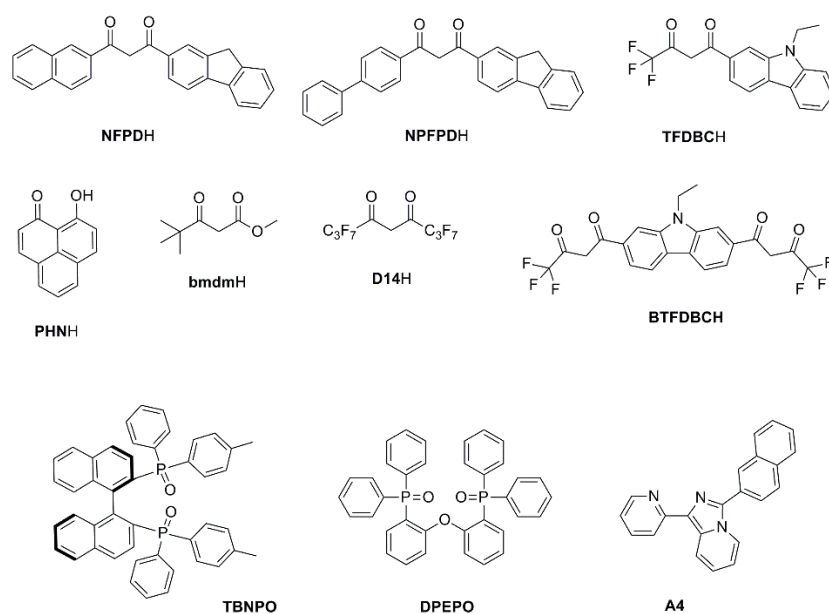


Figure 1.13 Selection of β -diketonates and ancillary ligands used for Eu^{3+} emissive complexes.

As can be seen in Table 1.5, quantum yields for these complexes are much higher than the NIR emitters. This is because the f^* states of Eu^{3+} are less affected by high energy vibrational modes and lie much closer to the donor excited states, achieving high values of quantum yields of up to 80%. One of the most studied ligands is the **ttaH** (2-thenoyltrifluoroacetone) where by changing the ancillary ligand present in the complex the photophysical properties can be improved.^{166,191,195–197} One relevant example is the complex reported by Van Deun *et al.* where visible sensitisation was achieved with the use of a modified β -diketonate, 9-hydroxyphenal-1-one (**PHNH**).²⁰² Unfortunately, poor quantum yields and lifetime values were detected in this case probably due to the presence of solvent molecules attached to the lanthanoid ions.

Table 1.5 Selected Eu^{3+} emitting systems published recently (1999-2017).

Complex	Sample	$\tau_{\text{obs}}/\mu\text{s}$	$\Phi_{\text{Ln}}^{\text{Ln}}(\%)$	$\Phi_{\text{Ln}}^{\text{L}}(\%)$	Ref
[Eu(tta) ₃ (dbso) ₂]	Solid	260	-	85 ^b	196
{Eu(dbm) ₆ } ₂ (μ -A3)	MeOH	523	-	75 ^d	171
[Eu(tta) ₃ (TPPO) ₂]	Solid	500	-	73 ^b	191
[Eu(tta) ₃ (DPEPO)]	DCM	1,010	81 ^a	70 ^e	197
[Eu(tta) ₃ (bpy)]	Solid	932	-	45 ^b	166
	CHCl ₃	929	-	48 ^c	
[Eu(BPFDP) ₃ (TBNPO)]	Solid	877	71 ^a	43 ^b	193
[Eu(NFPD) ₃ (TBNPO)]	Solid	790	73 ^a	28 ^b	193
[Eu(bmdm) ₃ (TPPO)]	Solid	450	55 ^a	-	194
[Eu(TFDBC) ₃ (phen)]	Solid	323	-	28 ^e	203
[Eu(TFDBC) ₃ (phen)]	Solid	106	-	10 ^e	203
[Eu(tta) ₃ (A4)]	CHCl ₃	200	-	7	195
[Eu(PHN) ₃ (OH ₂)(DMF)]	THF	10	-	0.5 ^e	202

^a Value of τ_{R} calculated from emission spectrum.⁴⁶ ^b Obtained following diffuse reflectance methods.²⁰⁴ ^c Obtained following dilute methods using quinine sulfate as reference ($\Phi=54.6\%$).²⁰⁵ ^d Obtained following dilute methods using [Ru(bpy)₃]Cl₂ as reference ($\Phi=2.8\%$).²⁰⁶ ^e Measured with an integrating sphere.

1.6 β -Triketonate Based Complexes

β -Triketones are derived from β -diketones by substituting an extra acyl group in the α -C position. In contrast to β -diketones, β -triketones are surprisingly under-explored. Indeed, although the first example was reported in 1960¹⁸, until recently only two further reports could be found in the literature involving the tribenzoylmethane molecule.^{19,207} However, none of these reports presented the structural characterisation of the complexes. It was not until 2014 when the first example of a fully characterised β -triketonate based-Ln³⁺ complex was presented by the Massi group (see Figure 1.14).²⁶ The coordination mode was found to be via only two of the carbonyl groups in a bidentate chelate giving tetranuclear assemblies of formula [Ln(Ae·HOEt)(**tbm**)₄], for Ae= Na⁺, K⁺ and Rb⁺. The tetranuclear assembly was

preserved throughout almost the whole lanthanoid series, for $\text{Ln}^{3+} = \text{Eu}^{3+}, \text{Gd}^{3+}, \text{Tb}^{3+}, \text{Dy}^{3+}, \text{Ho}^{3+}, \text{Er}^{3+},$ and Yb^{3+} .^{27,208}

These systems were not soluble in organic solvent and not stable in ethanolic and methanolic solutions and therefore, their photophysical properties were investigated only in the solid state.

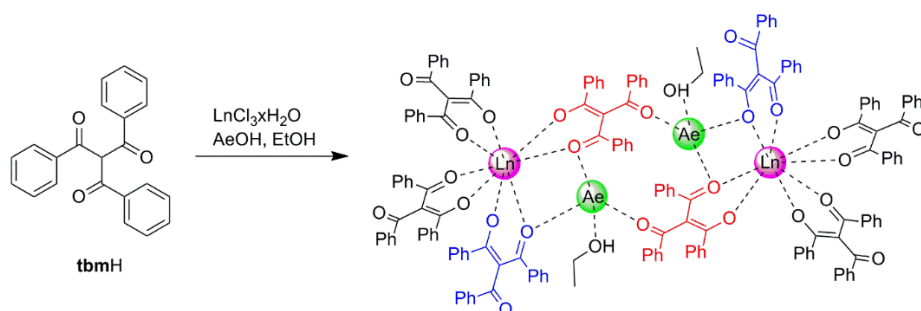


Figure 1.14 Synthetic pathway for the synthesis of $[\text{Ln}(\text{Ae}\cdot\text{HOEt})(\text{tbm})_4]$.

Excited state lifetimes and intrinsic quantum yields of the tetranuclear assemblies containing Yb^{3+} and Er^{3+} were found to exceed the performance of β -diketonates complexes in the solid state except for perfluorinated or deuterated systems (see Table 1.6). The improvement of the luminescence performance seemed to be related to the removal of the α -CH, minimising the multiphonon relaxation quenching. However, these reports did not include overall quantum yields, which would be ideal to identify the sensitisation efficiency of these systems.

Eu^{3+} was the only visible emission lanthanoid ion efficiently sensitised by the **tbm** molecule because its excited triple state ($\sim 20,700 \text{ cm}^{-1}$)²⁶ lies lower than the $^5\text{D}_4$ of Tb^{3+} . In contrast, it is of sufficient energy to sensitise the $^5\text{D}_4$ state of Eu^{3+} ($\sim 17,200 \text{ cm}^{-1}$). The lifetime values were found to be in the range of 500-540 μs with overall quantum yields of 35-37%. These values show similar performance to β -diketonates complexes, suggesting that multiphonon relaxation do not substantially quench the excited level of Eu^{3+} as has been previously suggested.⁶

Table 1.6 Selected photophysical data for [Ln(Ae-HOEt)(t**bm**)₄] in the solid state.

Complex	$\tau_{\text{obs}}/\mu\text{s}$	$\Phi_{\text{Ln}}^{\text{Ln}}$ (%)	$\Phi_{\text{Ln}}^{\text{L}}$ (%)
[Yb(Na·HOEt)(t bm) ₄]	37.0	3.1 ^a	-
[Yb(K·HOEt)(t bm) ₄]	46.7	3.9 ^a	-
[Yb(Rb·HOEt)(t bm) ₄]	44.4	3.8 ^a	-
[Er(Na·HOEt)(t bm) ₄]	4.8	0.7 ^a	-
[Er(K·HOEt)(t bm) ₄]	5.0	0.8 ^a	-
[Er(Rb·HOEt)(t bm) ₄]	5.8	0.9 ^a	-
[Eu(Na·HOEt)(t bm) ₄]	500	50 ^b	35 ^c
[Eu(K·HOEt)(t bm) ₄]	520	50 ^b	37 ^c
[Eu(Rb·HOEt)(t bm) ₄]	540	53 ^b	36 ^c

^a Assuming literature τ_{R} of 2 ms for Yb³⁺ and 0.66 for Er³⁺.⁶ ^b Value of τ_{R} calculated from emission spectrum ^c Measured with an integrating sphere.

1.7 Scope

In a review of the literature relating to the lanthanoid complexes, a lack of quantitative luminescence data has been identified for the NIR emitters in particular. Therefore, this investigation will seek to develop an improved method for the measurements of near infrared quantum yields. This method will be used to provide the necessary data to better understand the sensitisation efficiency of the complexes studied. There are also only a few reports of β -triketone assemblies. Therefore, attempting to form new structures and investigate their photophysical properties will be a major component of this research. Chapter 2 will discuss the use of an integrating sphere with two different detectors, visible and NIR, for the calculation of NIR-overall quantum yields. This chapter will also make a direct comparison between analogous tris(β -diketonate) and tris(β -triketone) lanthanoid monomers in order to evaluate the impact of the removal of the α -CH bond on the photophysical properties. Chapter 3 will describe a new family of lanthanoid coordination polymers formed by using CsOH as the base in the complexation reaction, characterised using X-ray diffraction studies and luminescence properties. Chapter 4 will focus on the sensitisation of Nd³⁺ assemblies, not previously reported, via Eu³⁺ donor states. Chapter 5 will report work exploring the stability of a new library of β -triketones and structurally analyse the complexes formed. Chapter 6 will

show a new family of soluble and stable β -triketones complexes in non-coordinating organic solvents with improved NIR photophysical properties. Finally, Chapter 7 will describe investigation of the ability of β -triketones to coordinate to an iridium(III) centre as an ancillary ligand, giving an example of aggregation induced emission (AIE).

Chapter 2 Effect of β -Triketonate on the Lanthanoid Photophysical Properties

Major aspects of the work presented in this chapter have been published:

L. Abad Galán, B. L. Reid, S. Stagni, A. N. Sobolev, B. W. Skelton, E. G. Moore, G. S. Hanan, E. Zysman-Colman, M. I. Ogden and M. Massi, *Dalt. Trans*, 2018, 47, 7956-7964

2.1 Introduction

This chapter will cover the synthesis of new monomeric β -triketonate complexes containing tribenzoylmethanide (**tbm**) and 1,10-phenanthroline (phen) ligands ($[\text{Ln}(\text{phen})(\text{tbm})_3]$, Ln = Er³⁺ and Yb³⁺), along with the analogous previously reported dibenzoylmethanide (**dbm**) complexes $[\text{Ln}(\text{phen})(\text{dbm})_3]$ and $[\text{Eu}(\text{phen})(\text{tbm})_3]$. Fortunately, in this case, similarities in composition and structure between the β -diketonate and β -triketonate complexes were found, making it possible to compare their photophysical properties. The monomeric complexes were studied by absorption and emission spectroscopies. Furthermore, an adapted relative method was followed for the calculation of the overall quantum yields for the NIR emitters, providing full characterisation of their photophysical properties. The results show only a small enhancement for the NIR β -triketonate-based complexes, suggesting that structural and composition factors must be considered to explain the remarkable properties of the previously reported tetranuclear complexes of tribenzoylmethanide.^{27,209}

2.2 Synthesis

Tribenzoylmethane (**tbmH**, **L1H**) was synthesised according to a literature procedure,²⁰⁹ whereby dibenzoylmethane (**dbmH**) was made to react with benzoyl chloride and NaH in dry diethyl ether. The spectroscopic data of the synthesised **tbmH** matched those previously reported (see Section 7.5.1.2).²⁶

The $[\text{Ln}(\text{phen})(\text{tbm})_3]$ complexes for Ln³⁺ = Er³⁺ and Yb³⁺ (**C1-C2**) were prepared by the addition of **tbmH**, phen, and hydrated LnCl₃ with triethylamine to hot ethanol following a similar procedure already reported for Eu³⁺ (see Figure 2.1).²¹⁰ After filtration, slow evaporation of the solvent resulted in the formation of suitable crystals for X-ray diffraction for the $[\text{Ln}(\text{phen})(\text{tbm})_3]$ (Ln³⁺ = Er³⁺, Yb³⁺). The formulation of the resulting solids was confirmed by elemental analysis and IR spectroscopy.

The previously reported $[\text{Ln}(\text{phen})(\text{dbm})_3]$ for $\text{Ln}^{3+} = \text{Eu}^{3+}, \text{Er}^{3+}$ and Yb^{3+} complexes were prepared following a slightly modified procedure¹²⁷. Reaction of **dbmH**, phen, and hydrated LnCl_3 with triethylamine in ethanol at 50°C resulted in pale yellow solids which were filtered, washed with ethanol and dried *in vacuo*. The compositions of the solids were confirmed by means of IR and elemental analysis.

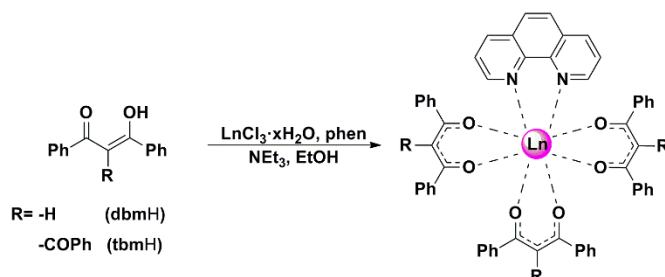


Figure 2.1 Reaction scheme for the preparation of $[\text{Ln}(\text{phen})(\text{dbm})_3]$ and $[\text{Ln}(\text{phen})(\text{tbm})_3]$ ($\text{Ln} = \text{Eu}^{3+}, \text{Er}^{3+}, \text{Yb}^{3+}$ complexes).

2.3 X-Ray Diffraction

The $[\text{Ln}(\text{phen})(\text{tbm})_3]$ ($\text{Ln}^{3+} = \text{Er}^{3+}, \text{Yb}^{3+}$) complexes are isostructural and analogous to the previously reported $[\text{Eu}(\text{phen})(\text{tbm})_3]$.²¹⁰ These complexes crystallise as a triclinic structure in the *P1* space group (see Figure 2.2). The Ln^{3+} cations are eight-coordinate by six O atoms from three **tbm** ligands and two N atoms from the coordinated phen molecule. The coordination geometry is best described as a distorted square antiprism. A supramolecular dimer, situated about an inversion centre, is formed through π -stacking²¹¹ of phen ligands of two complexes, with a distance of $\sim 3.3 \text{ \AA}$ between the π -stacked planes of the phen ligands and of $\sim 3.6 \text{ \AA}$ between centroids (see Figure 2.2). These interactions result in a $\text{Ln}\cdots\text{Ln}$ distance of $\sim 9.2 \text{ \AA}$ (see Table 2.1), a distance which suggests that direct energy transfer between the two Ln^{3+} ions should be minimal.⁶⁴

The $[\text{Ln}(\text{phen})(\text{dbm})_3]$ ($\text{Ln} = \text{Eu}^{3+}, \text{Er}^{3+}, \text{Yb}^{3+}$) crystal structures have been previously reported in the literature.^{127,134,212} Similarly to the $[\text{Ln}(\text{phen})(\text{tbm})_3]$ complexes, the Ln^{3+} ion is coordinated by six O atoms from three **dbm** ligands and two N atoms from the coordinated phen molecule. Unlike the **tbm** series, the **dbm** complexes are not isomorphous. Nevertheless, the $\text{Ln}\cdots\text{Ln}$ distances are greater than 9 \AA in all of these complexes and thus cross relaxation pathways are not expected to influence one series of complexes more than the other in the solid state.

Table 2.1 Selected bond lengths (Å) and intermetallic distances for [Ln(phen)(**tbm**)₃].

	[Eu(phen)(tbm) ₃]	[Er(phen)(tbm) ₃]	[Yb(phen)(tbm) ₃]
Ln(1)-N(421)	2.583(1)	2.510(4)	2.495(2)
Ln(1)-N(411)	2.602(1)	2.545(4)	2.523(2)
Ln(1)-O(11)	2.330(1)	2.260(3)	2.252(2)
Ln(1)-O(12)	2.372(1)	2.306(3)	2.287(2)
Ln(1)-O(21)	2.333(1)	2.282(3)	2.254(2)
Ln(1)-O(22)	2.367(1)	2.305(3)	2.295(2)
Ln(1)-O(31)	2.394(1)	2.342(3)	2.322(2)
Ln(1)-O(32)	2.338(1)	2.287(3)	2.261(2)
phen-phen	3.292(3)	3.253(7)	3.256(4)
Centroid-Centroid	3.602	3.598	3.588
Ln(1)-Ln(1)*	9.2508(6)	9.2357(6)	9.2141(6)

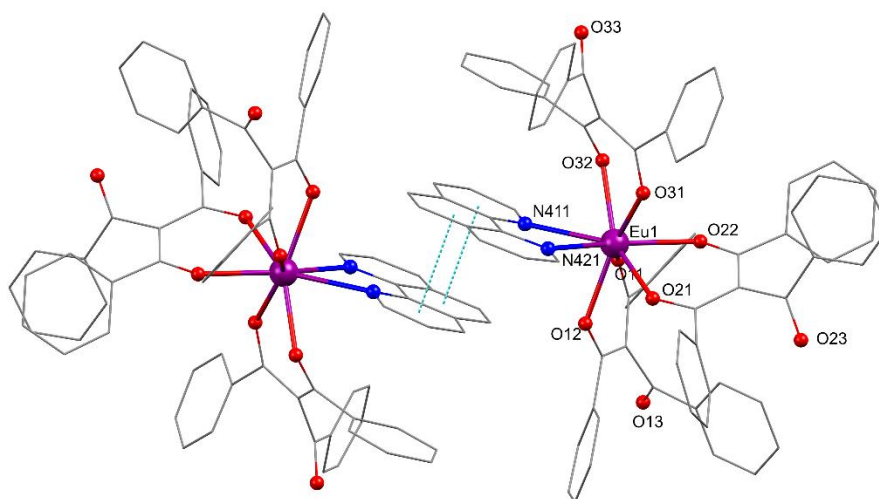


Figure 2.2 Representation of the X-ray crystal structure of [Eu(phen)(**tbm**)₃], emphasising the supramolecular dimer formed by phen π - π stacking interactions between centro-symmetrically related molecules, where centroids are marked with blue spheres. Hydrogen atoms have been omitted for clarity.

Most importantly for this study, the coordination sphere of the complexes of each lanthanoid cation is quite similar. Overlaying the primary coordination sphere structures²¹³ for the **dbm** and **tbm** complexes of each metal gave root-mean-square deviation (RMSD) for the overlay and the maximum distance between two equivalent atoms. These values and the overlaid structures are shown in Figure 2.3.

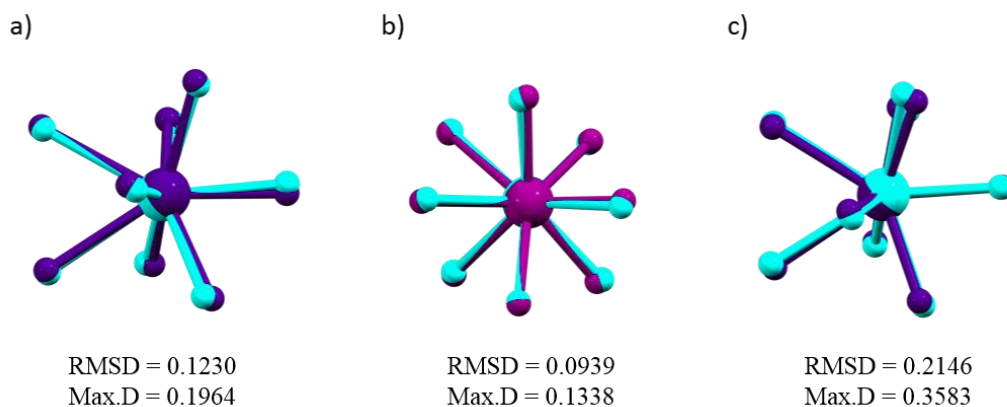


Figure 2.3 First coordination sphere overlay for complexes a) $[Eu(phen)(t\mathbf{bm})_3]/[Eu(phen)(d\mathbf{bm})_3]$, b) $[Er(phen)(t\mathbf{bm})_3]/[Er(phen)(d\mathbf{bm})_3]$ and c) $[Yb(phen)(t\mathbf{bm})_3]/[Yb(phen)(d\mathbf{bm})_3]$.

2.3.1 Shape Analysis

Spatial arrangement of the lanthanoid coordination sphere plays a major role in their luminescence properties. Therefore, the coordination sphere geometry of every complex presented herein will be assessed so as to estimate how variations on the geometry could affect the emission spectra. This study will be accomplished by the use of the Shape Version 2.1 software developed by Alvarez *et al.*²¹⁴ The software is based on the calculation of continuous shape measurements (CShM) proposed by Avnir *et al.* following Equation 2.1.²¹⁵

$$CShM(P) = \min \frac{\sum_{i=1}^N |Q_i - P_i|^2}{\sum_{i=1}^N |Q_i - Q_0|^2} 100 \quad (2.1)$$

Where P, the given polyhedron with a set of N atoms and characterised by its position vectors Q_i , is compared with the position vector of the ideal polyhedron's vertices (P_i) and the position vector of the geometrical centre of P (Q_0). The minimum of every possible pair of vertices between the ideal and the given polyhedron, leaving the metal atom in the centre, are taken in consideration. Following this definition, when the given polyhedron is identical to the reference the $CShM(P)$ value would be 0.

Therefore, the software Shape Version 2.1 provides an evaluation of how much a given structure deviates from an ideal shape.²¹⁶⁻²¹⁹ However, this is not its only feature. The software offers as well the possibility to compare a given crystal structure with two different ideal polyhedra and determines which of them best describes its geometry by taking the lowest CShM value.²¹⁸ This is represented in Shape Maps, where the CShM values for the two ideal geometries are represented as coordinates on an x- and y- axis (see Figure 2.3). These maps present as well a trace corresponding to the lowest energy interconversion pathway (LEIP) between the two ideal polyhedra.

In the case of the $[\text{Ln}(\text{phen})(\mathbf{t}\mathbf{b}\mathbf{m})_3]$ and $[\text{Ln}(\text{phen})(\mathbf{d}\mathbf{b}\mathbf{m})_3]$, the two closest polyhedral geometries are triangular dodecahedron and square antiprism, respectively (see Figure 2.4 and Table 2.2).

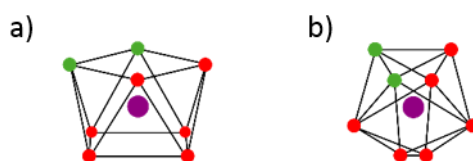


Figure 2.4 Representation of the ideal square antiprism (a) and triangular dodecahedron (b) geometries.

From the Shape map (see Figure 2.5), it becomes evident that all the species have a coordination geometry best described as distorted square antiprism with the exception of $[\text{Yb}(\text{phen})(\mathbf{d}\mathbf{b}\mathbf{m})_3]$ which is closer to triangular dodecahedron.

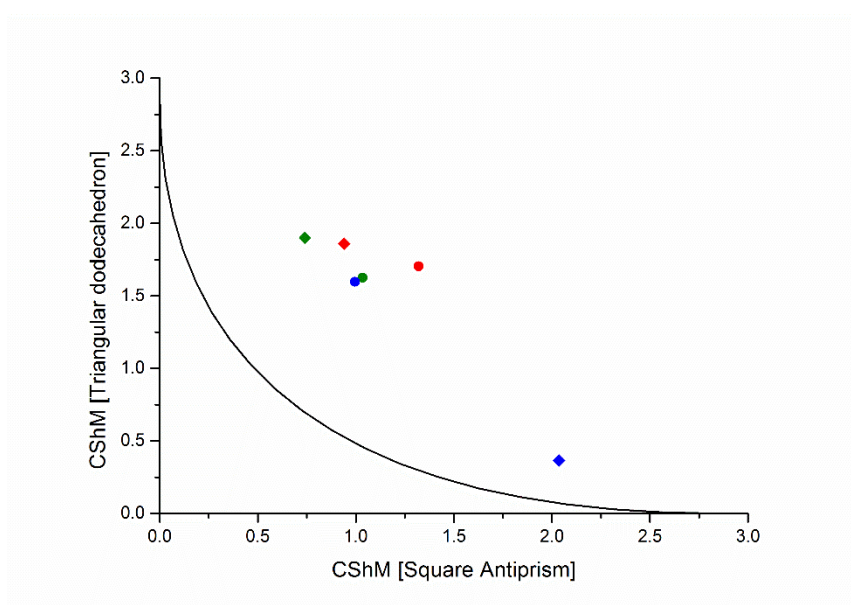


Figure 2.5 Shape Map representing the CshM values of the $[\text{Ln}(\text{phen})(\mathbf{t}\mathbf{b}\mathbf{m})_3]$ (dots) and $[\text{Ln}(\text{phen})(\mathbf{d}\mathbf{b}\mathbf{m})_3]$ (rhomboids) for Eu^{3+} (red), Er^{3+} (green) and Yb^{3+} (blue).

The CShM values for both families of complexes were found via the Shape Version 2.1 software using the atomic coordinates provided by Mercury software from the crystal structures of the new $[\text{Ln}(\text{phen})(\mathbf{t}\mathbf{b}\mathbf{m})_3]$ ($\text{Ln} = \text{Yb}^{3+}$ and Er^{3+}) and previously reported $[\text{Eu}(\text{phen})(\mathbf{t}\mathbf{b}\mathbf{m})_3]$ ²¹⁰ and $[\text{Ln}(\text{phen})(\mathbf{d}\mathbf{b}\mathbf{m})_3]$ ^{127,134,212} ($\text{Ln} = \text{Eu}^{3+}$, Yb^{3+} and Er^{3+}) complexes (see Table 2.2).

Table 2.2 CShM values for the [Ln(phen)(**tbm**)₃] and [Ln(phen)(**dbm**)₃] complexes for Ln = Eu³⁺, Yb³⁺ and Er³⁺.

Complex	SAPR-8	TTD-8
[Eu(phen)(tbm) ₃]	1.32	1.70
[Eu(phen)(dbm) ₃]	0.94	1.86
[Yb(phen)(tbm) ₃]	0.996	1.59
[Yb(phen)(dbm) ₃]	2.036	0.36
[Er(phen)(tbm) ₃]	1.035	1.62
[Er(phen)(dbm) ₃]	0.74	1.93

These results are consistent with the coordination sphere overlay, with the Yb pair of complexes showing the greatest difference in structure.

2.4 Photophysical Properties

The photophysical properties for [Ln(phen)(**tbm**)₃] (Ln = Eu³⁺, Yb³⁺ and Er³⁺) including excited state lifetime decays (τ_{obs}), calculated radiative lifetime decays (τ_{R}), intrinsic photoluminescence quantum yields ($\Phi_{\text{Ln}}^{\text{Ln}}$), overall photoluminescence quantum yields ($\Phi_{\text{Ln}}^{\text{L}}$), and sensitisation efficiency (η_{sens}) are summarised in Tables 1.2-1.4 at the beginning of each section.

The energies of the ³ π - π^* excited states of the **dbm**, **tbm** and phen have been previously reported, being estimated at the 0-phonon transition from the phosphorescence of the Gd³⁺ complexes at 77K. These energies were found at 20,350 cm⁻¹, 20,704 cm⁻¹ and 21,050 cm⁻¹ for **dbm**¹⁹, **tbm**^{175,209} and phen^{220,221}, respectively. Gd³⁺ complexes are commonly used for finding the energy of the ligand triplet state because the intersystem crossing is favoured, as a result of the heavy atom effect, but energy transfer to the lanthanoid centre is not accessible, due to the high energy level of the **f* of Gd³⁺. These ³ π - π^* states are of high enough energy to sensitise metal-centred emission from Eu³⁺, Er³⁺ and Yb³⁺. The similarities between the excitation spectra and the absorption profiles of the **tbm/dbm** ligands and phen ligands support the conclusion that the emission from the lanthanoid cations originates through sensitisation from the coordinated ligands. Given the large difference between the energy of the ³ π - π^* and ²F_{5/2} excited state of Yb³⁺ (~10,200 cm⁻¹), energy transfer in this case could be mediated by a ligand-to-metal charge transfer state (LMCT).⁹¹ In the case of Eu³⁺, energy transfer will usually occur to the ⁵D₀ (~17,200 cm⁻¹) or ⁵D₁ (~19,000 cm⁻¹) states.²⁸ Sato and Wada have reported that for efficient funnelling of the energy to the ⁵D₁ state, an energy

difference of $1,500\text{ cm}^{-1}$ is sufficient.²²² Therefore in our systems, energy transfer is likely to occur to both excited states. Finally, in the case of Er^{3+} , energy transfer will take place via high energy excited states which will later relax non-radiatively to the ${}^4\text{I}_{13/2}$ emissive state ($\sim 6,500\text{ cm}^{-1}$).

The measurements were performed on neat solids or with the complexes dispersed within a transparent PMMA matrix following a previously reported procedure,¹²³ where the polymer monolith was loaded by addition of the corresponding complex in a *ca.* 10^{-3} M acetonitrile solution. The obtained data were also compared with measurements performed in *ca.* 10^{-5} M dichloromethane solutions at room temperature and at 77 K . Dichloromethane was used as a non-coordinating solvent as the structure was not preserved in polar coordinating solvents such as ethanol, probably due to ligand exchange. As can be seen in Figure 2.6, when the same 10^{-5} M ethanolic solution was measured fresh and after an hour, the emission profile is no longer structured and the lifetime is shortened, probably due to a mixture of species present in solution.

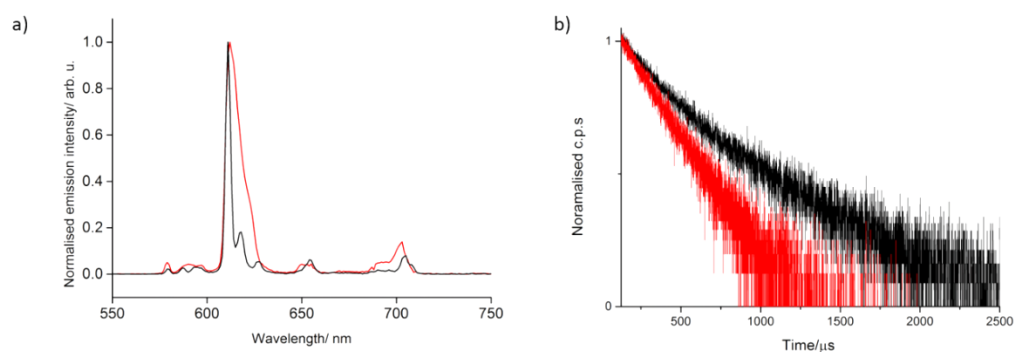


Figure 2.6 Normalised emission (a) and excited lifetime decay (b) plots for $[\text{Eu}(\text{phen})(\text{tbm})_3]$ in EtOH fresh solution (black trace) and after an hour (red trace) at room temperature.

The photophysical properties of $[\text{Er}(\text{phen})(\text{tbm})_3]$ were only studied in the solid state as this complex was almost non-emissive in solution at room temperature.

2.4.1 Europium Complexes

Table 2.3 Photophysical data for [Eu(phen)(*dbm*)₃] and [Eu(phen)(*tbm*)₃] complexes.

Complex	Sample	τ_{obs} (μs)	τ_{R} (μs)	$\Phi_{\text{Ln}}^{\text{Ln}}$ (%)	$\Phi_{\text{Ln}}^{\text{L}}$ (%)	Φ_{sens} (%)
[Eu(phen)(<i>tbm</i>) ₃]	Powder	550	1030	53	45 ^a	85
	DCM (RT)	124	1080	12	0.6 ^b	5
	DCM glass (77K)	554	990	56	-	-
	PMMA	433	1009	43	-	-
[Eu(phen)(<i>dbm</i>) ₃]	Powder	484	960	50	55 ^a	~100
	DCM (RT)	120	843	14	1.3 ^b	10
	DCM glass (77K)	673	989	68	-	-
	PMMA	462	956	48	-	-

^a quantum yield measured with an integrating sphere; ^b quantum yield in dichloromethane solution relative to [Ru(*bpy*)₃]Cl₂ in water ($\Phi_{\text{ref}}=2.8\%$).²²³

The emission spectrum of [Eu(phen)(*tbm*)₃] in the solid state is in agreement with that found in the literature²¹⁰, displaying the five characteristic Eu³⁺ emission bands attributed to ⁷F_J←⁵D₀ (*J* = 0-4) transitions in the region of 580-750 nm (see Figure 2.7). The low intensity ⁷F₀←⁵D₀ band has a full-width at half-maximum (FWHM) of 35 cm⁻¹, indicative of one unique emitting species.⁴⁶ The ⁷F₁←⁵D₀ transition is split into three easily distinguishable bands, two of which are very close in energy. This splitting is inherent with a local Eu³⁺ symmetry lower than *D*_{2d}.⁴⁶ This is consistent with the observed splitting in the ⁷F₂←⁵D₀ band and the high integral ratio (13.5) of this band with respect to the ⁷F₁←⁵D₀. Low symmetry is observed as well in the crystal structure where the ideal square antiprismatic geometry is distorted, with the symmetry lowered due to the *N*-donor ligand.

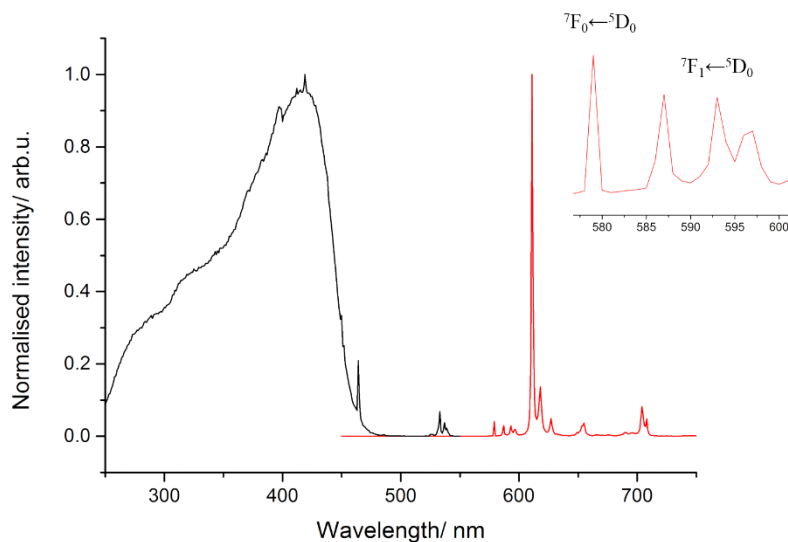


Figure 2.7 Normalised excitation (black) and emission (red) ($\lambda_{exc}=350$ nm) plots of $[\text{Eu}(\text{phen})(\text{dbm})_3]$ in the solid state. Inset: highlight of the peaks corresponding to the ${}^7F_J \leftarrow {}^5D_0$ ($J=0, 1$) transitions.

The emission spectrum for the $[\text{Eu}(\text{phen})(\text{dbm})_3]$ in the solid state is likewise in agreement with that found in the literature, showing the five characteristic Eu^{3+} bands associated with the ${}^7F_J \leftarrow {}^5D_0$ ($J = 0-4$) transitions (see Figure 2.8). The ${}^7F_0 \leftarrow {}^5D_0$ band has a FWHM of 27 cm^{-1} , which again indicates the presence of only one unique emitting Eu^{3+} centre. The ${}^7F_1 \leftarrow {}^5D_0$ transition is split in two different bands because of the crystal field effects. The splitting of the band is lower than for $[\text{Eu}(\text{phen})(\text{tbn})_3]$, revealing higher symmetry in this case, which is in agreement with the results found with the shape analysis, where the $[\text{Eu}(\text{phen})(\text{dbm})_3]$ complex is less distorted from square antiprismatic geometry compared to the analogous complexes bound to **tbn** (see Section 2.3.1).²¹⁴

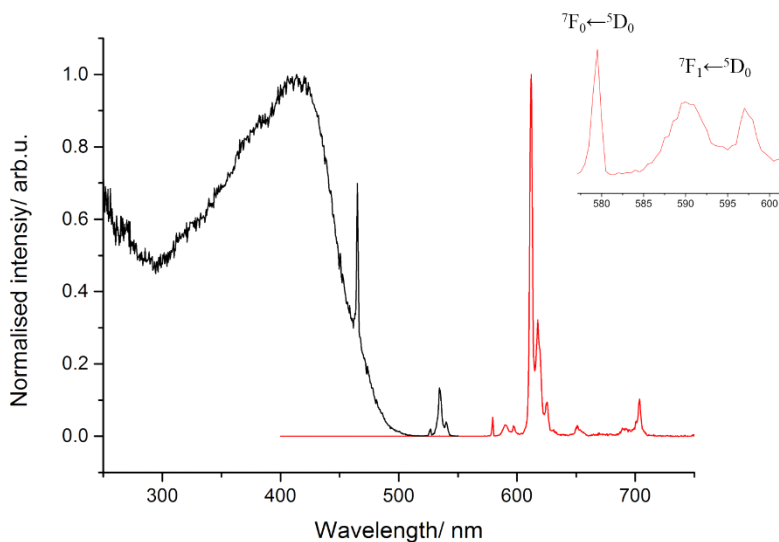


Figure 2.8 Normalised excitation (black) and emission (red) ($\lambda_{exc}=350$ nm) plots of $[\text{Eu}(\text{phen})(\text{dbm})_3]$ in the solid state. Inset: highlight of the peaks corresponding to the ${}^7F_J \leftarrow {}^5D_0$ ($J=0, 1$) transitions.

The $[\text{Eu}(\text{phen})(\text{dbm})_3]$ excited state decay was found to be monoexponential, giving an excited state lifetime (τ_{obs}) value of 0.55 ms. The radiative decay (τ_{R}) could be estimated from the emission spectrum to be 1.03 ms. From these data, the intrinsic quantum yield ($\Phi_{\text{Ln}}^{\text{Ln}}$) was calculated to be 53%. The overall quantum yield was measured to be 45% by an absolute method using an integrating sphere, leading to a sensitisation efficiency (η_{sens}) of 82%. This value is slightly improved in comparison to our previous report on the assemblies that involved only **tbm** ligands ($\sim 70\%$),²⁷ and thus may be due to more efficient sensitisation *via* the phen ligand upon excitation at 350 nm. The values of τ_{obs} , τ_{R} , and $\Phi_{\text{Ln}}^{\text{Ln}}$ for the $[\text{Eu}(\text{phen})(\text{dbm})_3]$ were found to be very similar to the **tbm** complex at 0.48 ms, 0.96 ms and 50%, respectively, with an overall quantum yield ($\Phi_{\text{Ln}}^{\text{Ln}}$) of 55% and a virtually quantitative sensitisation efficiency, within experimental error, associated with the quantum yield measurement. These data indicate that the introduction of the extra ketone group at the α -carbon of the β -diketonate does not significantly affect the emission behaviour for Eu^{3+} complexes, and the photophysical properties for the β -diketonate and β -triketonate complexes are comparable. This is not surprising as the α -CH bond is not an efficient quencher of the 5D_0 excited state.

As both systems behave similarly across every medium, and the data for the $[\text{Eu}(\text{phen})(\text{dbm})_3]$ are in agreement with those in the literature,¹²⁷ only the photophysical properties of the $[\text{Eu}(\text{phen})(\text{tbm})_3]$ complexes will be discussed in detail from here on (see Figures A1-2).

The emission properties of $[\text{Eu}(\text{phen})(\text{tbm})_3]$ in PMMA were studied in order to assess any possible contribution of energy migration between Eu^{3+} centres in the neat solid (see Figure

2.99). A slightly different splitting of emission bands were found when compared to the solid state probably because of a different geometry of the ligands around the lanthanoid centre in the dispersed medium. The values of τ_{obs} , τ_{R} , and $\Phi_{\text{Ln}}^{\text{Ln}}$ are 0.43 ms, 1.09 ms, and 43%, respectively. These data show similar values to those in neat solids, suggesting that concentration quenching does not affect the solid-state emission properties.

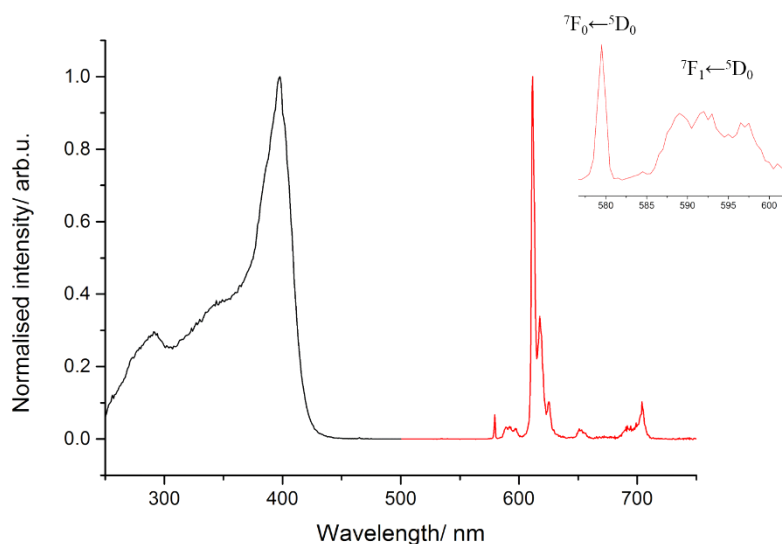


Figure 2.9 Normalised excitation (black) and emission (red) ($\lambda_{\text{exc}}=350$ nm) plots of $[\text{Eu}(\text{phen})(\text{tbm})_3]$ in PMMA. Inset: highlight of the peaks corresponding to the ${}^7\text{F}_J \leftarrow {}^5\text{D}_0$ ($J=0, 1$) transitions.

The $[\text{Eu}(\text{phen})(\text{tbm})_3]$ complex in dichloromethane solution at room temperature shows characteristic emission from the $\text{Eu}^{3+} {}^5\text{D}_0$ state, similar to the spectrum observed in PMMA (see Figure 2.10). All the emission lines were less defined due to higher degrees of freedom of the ligands in solution at room temperature. However, when the solution formed a glass at 77 K, the emission structure was similar to that observed in PMMA with no significant changes. The FWHM of the ${}^7\text{F}_0 \leftarrow {}^5\text{D}_0$ transition are 82 cm^{-1} and 26 cm^{-1} at room temperature and 77 K, respectively. In the frozen glass, the ${}^7\text{F}_1 \leftarrow {}^5\text{D}_0$ transition is split into three bands, two of them very close in energy comparable to the dispersed medium.

Excited state lifetime decays (τ_{obs}) of $[\text{Eu}(\text{phen})(\text{tbm})_3]$ in dichloromethane solution were measured to be 0.12 ms and 0.55 ms at room temperature and 77 K, respectively. The radiative decay (τ_{R}), the intrinsic ($\Phi_{\text{Ln}}^{\text{Ln}}$) and overall quantum yield ($\Phi_{\text{Ln}}^{\text{L}}$) at room temperature were determined to be 1.08 ms, 12% and 0.58%, which leads to a sensitisation efficiency (η_{sens}) of 5%. These data are consistent with those reported for $[\text{Eu}(\text{phen})(\text{dbm})_3]$ in dichloromethane solution, suggesting similar behaviour of both systems in solution. The significantly short lifetimes found at room temperature with respect to the 77K may be explained by a more

efficient vibrational quenching of the 5D_0 excited state favoured due to a higher configurational lability in solution. The reduction of the overall quantum yield, in comparison to that in the solid state, is suggestive of a poor sensitisation efficiency of the ketonates in solution as has been previously suggested.¹²⁷

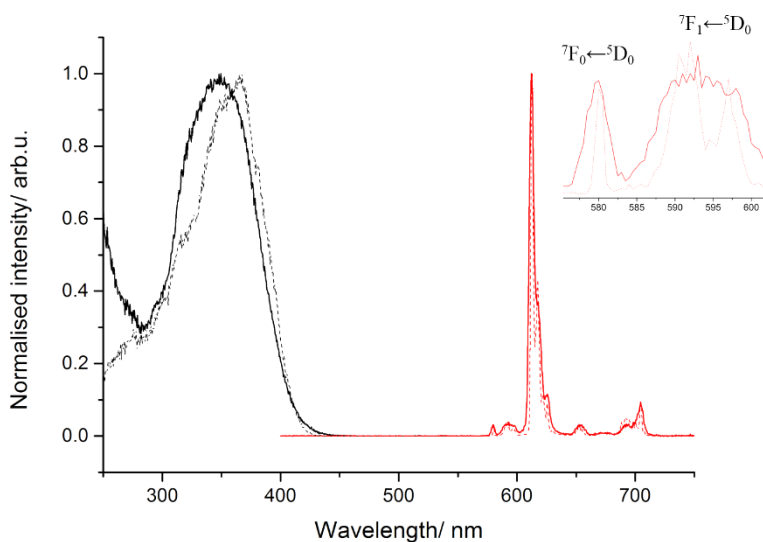


Figure 2.10 Normalised excitation (black) and emission (red) ($\lambda_{exc}=350$ nm) plots of $[Eu(phen)(tbn)_3]$ in $10^{-5}M$ DCM at room temperature (solid line) and 77K (dashed line). Inset: highlight of the peaks corresponding to the $^7F_J \leftarrow ^5D_0$ transitions.

These results demonstrate that both β -diketonate and β -triketonate systems behave similarly in all the conditions studied (see comparison in Figure 2.11), thereby confirming that the α -CH bond is not an efficient quencher of the 5D_0 excited state. However, the poor emission properties of both systems in solution, in comparison with the neat solids, suggest efficient quenching processes taking place and poor sensitisation properties of these ketonates.

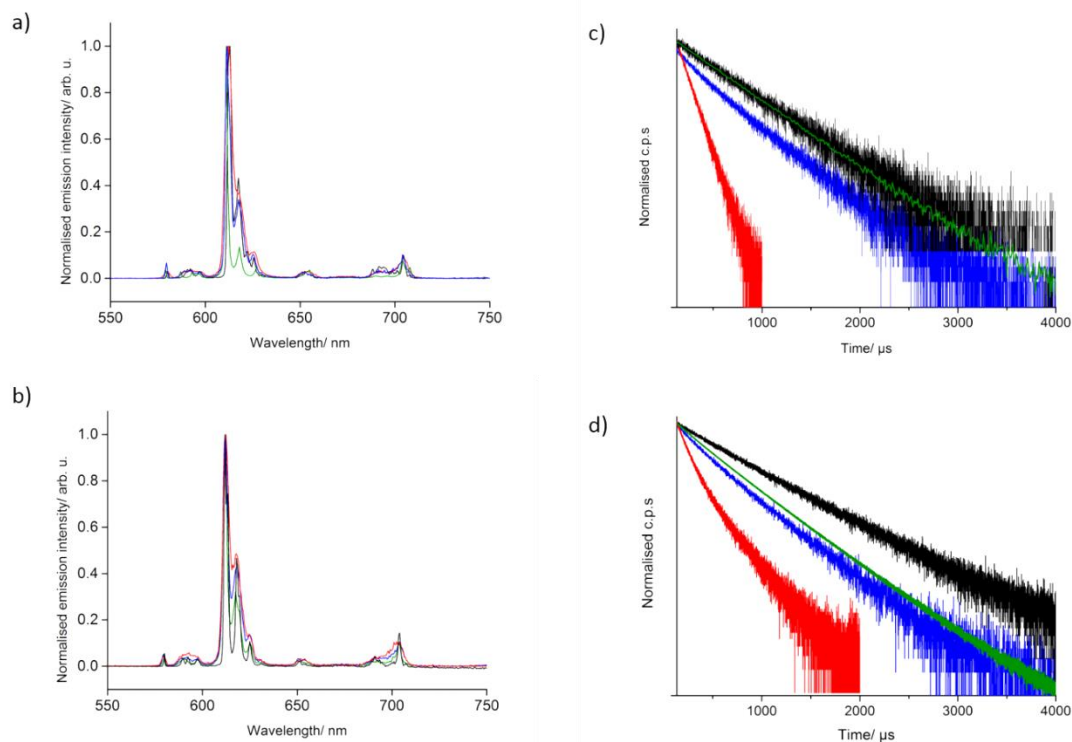


Figure 2.11 Normalised emission intensity ($\lambda=350$ nm) and excited lifetime decays plots of $[\text{Eu}(\text{phen})(\text{tbm})_3]$ (a,c) and $[\text{Eu}(\text{phen})(\text{dbm})_3]$ (b,d) in solid state (green trace), DCM solution (10^{-5}M) (red trace), 77K (black trace) and PMMA (blue trace).

2.4.2 Ytterbium Complexes

Table 2.4 Photophysical data for $[\text{Yb}(\text{phen})(\text{tbm})_3]$ and $[\text{Yb}(\text{phen})(\text{dbm})_3]$ complexes.

Complex	Sample	τ_{obs} (μs)	$\Phi_{\text{Ln}}^{\text{L}}$ (%)
$[\text{Yb}(\text{phen})(\text{tbm})_3]$	Powder	15.9	3.64 ^a
	DCM (RT)	18.0	1.16 ^b
	DCM glass (77K)	16.0	-
	PMMA	16.7	-
$[\text{Yb}(\text{phen})(\text{dbm})_3]$	Powder	11.3	2.91 ^a
	DCM (RT)	12.9	0.87 ^b
	DCM glass (77K)	9.7	-
	PMMA	10.7	-

^a quantum yield measured with an integrating sphere. ^b quantum yield in dichloromethane solution relative to $[\text{Yb}(\text{phen})(\text{TTA})_3]$ in toluene ($\Phi_{\text{Ln}}^{\text{L}}=1.6\%$).¹⁵⁰

The emission spectrum of the $[\text{Yb}(\text{phen})(\text{tbm})_3]$ complex in the solid state shows characteristic NIR emission from the ${}^2\text{F}_{7/2} \leftarrow {}^2\text{F}_{5/2}$ (see Figure 2.12) This transition is split into four main bands at 976, 1011, 1029 and 1043 nm due to crystal field effects. The splitting of

the ${}^2F_{7/2} \leftarrow {}^2F_{5/2}$ transition in the case of the $[\text{Yb}(\text{phen})(\mathbf{t}\mathbf{b}\mathbf{m})_3]$ is slightly different with three main bands at 976, 1007 and 1039 nm (see Figure A.3) This may be due to different degrees of distortion between the two coordination spheres, which were the largest differences observed amongst the three pairs of complexes. This is also in line with the results found in the shape analysis study where it was shown that $[\text{Yb}(\text{phen})(\mathbf{t}\mathbf{b}\mathbf{m})_3]$ is best described as a distorted square antiprism, while the best description of the geometry for $[\text{Yb}(\text{phen})(\mathbf{d}\mathbf{b}\mathbf{m})_3]$ is a distorted triangular dodecahedron (see Figure 2.5).

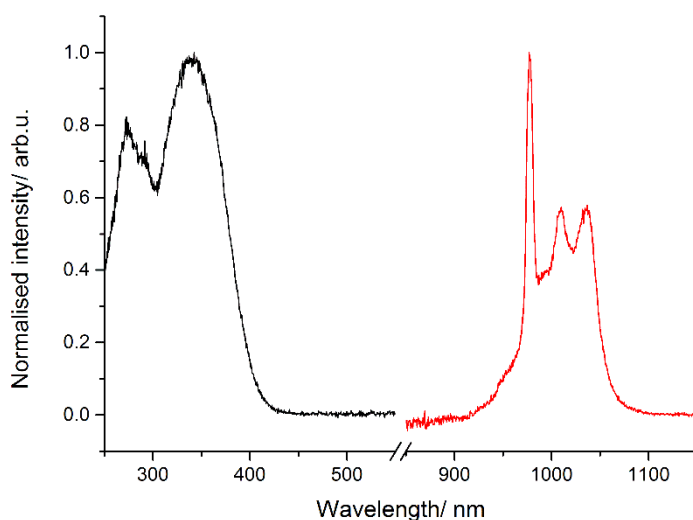


Figure 2.12 Normalised excitation (black) and emission (red) ($\lambda_{\text{exc}}=350$ nm) plots of $[\text{Yb}(\text{phen})(\mathbf{t}\mathbf{b}\mathbf{m})_3]$ in the solid state.

The observed lifetimes decays (τ_{obs}) for $[\text{Yb}(\text{phen})(\mathbf{t}\mathbf{b}\mathbf{m})_3]$ and $[\text{Yb}(\text{phen})(\mathbf{d}\mathbf{b}\mathbf{m})_3]$ complexes in the solid state were fitted to monoexponential functions, giving values of 15.9 and 11.3 μs , respectively. The excited state lifetime is slightly higher in the case of the $[\text{Yb}(\text{phen})(\mathbf{t}\mathbf{b}\mathbf{m})_3]$. Overall quantum yields ($\Phi_{\text{Ln}}^{\text{L}}$) were measured with the help of an integrating sphere using two different detectors: visible and NIR. In order to do so, $[\text{Yb}(\text{phen})(\mathbf{t}\mathbf{t}\mathbf{a})_3]$ with $\Phi_{\text{Ln}}^{\text{L}}=1.6\%$,¹⁵⁰ was used as a reference to calibrate the system. The value of $\Phi_{\text{Ln}}^{\text{L}}$ for the previous reported complex, $[\text{Yb}(\text{phen})(\mathbf{d}\mathbf{b}\mathbf{m})_3]$ in toluene was found to be 0.62%, in accordance with the literature value of 0.59%.¹⁵⁰ The $\Phi_{\text{Ln}}^{\text{L}}$ of the $[\text{Yb}(\text{phen})(\mathbf{t}\mathbf{b}\mathbf{m})_3]$ and $[\text{Yb}(\text{phen})(\mathbf{d}\mathbf{b}\mathbf{m})_3]$ in the solid state were determined to be 3.64 and 2.91%, respectively, showing a small enhancement for the $\mathbf{t}\mathbf{b}\mathbf{m}$ complex due to reduction of non-radiative decay pathways.²⁰⁹

As for the Eu^{3+} complexes, the photophysical properties of the $[\text{Yb}(\text{phen})(\mathbf{t}\mathbf{b}\mathbf{m})_3]$ and $[\text{Yb}(\text{phen})(\mathbf{d}\mathbf{b}\mathbf{m})_3]$ in PMMA were studied (see Figure 2.13 and A.4, respectively). The emission spectrum of $[\text{Yb}(\text{phen})(\mathbf{t}\mathbf{b}\mathbf{m})_3]$ shows emission from the ${}^2F_{7/2} \leftarrow {}^2F_{5/2}$ transition with

a slightly different splitting of the band due to small differences in the coordination sphere . The values of observed lifetimes decay (τ_{obs}) are similar to the ones found in the solid state.

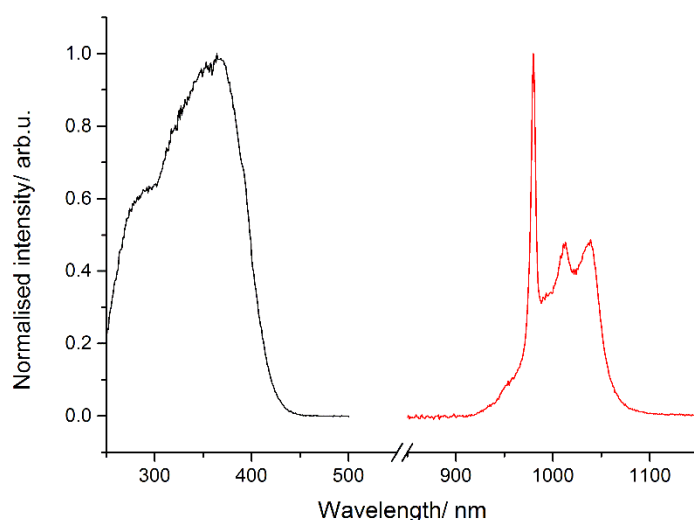


Figure 2.13 Normalised excitation (black) and emission (red) ($\lambda_{\text{exc}}=350$ nm) plots of $[\text{Yb}(\text{phen})(\text{tbn})_3]$ in PMMA.

The $[\text{Yb}(\text{phen})(\text{tbn})_3]$ and $[\text{Yb}(\text{phen})(\text{dbm})_3]$ complexes in dichloromethane solution at room temperature and at 77 K show characteristic emission from the ${}^2\text{F}_{5/2}$ state with a similar splitting to the spectra observed in PMMA (see Figure 2.14). The frozen matrix, in contrast, do not present emission in the 930-960 nm region corresponding to emission from hot bands, because these states are not accessible at 77K (see Figure 2.15). The observed lifetime decays (τ_{obs}) were fitted to monoexponential functions with values of 18.0 and 12.9 μs , respectively. The overall quantum yield ($\Phi_{\text{Ln}}^{\text{I}}$) of the $[\text{Yb}(\text{phen})(\text{tbn})_3]$ and $[\text{Yb}(\text{phen})(\text{dbm})_3]$ at room temperature were determined to be 1.16 and 0.87%, respectively, by the dilute method using $[\text{Yb}(\text{phen})(\text{tta})_3]$ as the reference.¹⁵⁰ The values of the quantum yields are slightly lower than in the solid state probably due to a less efficient sensitisation process, as was seen to a greater degree for the Eu^{3+} complexes. These data suggest that energy migration between the lanthanoid centres does not affect the photophysical properties of the complexes in the neat solids.

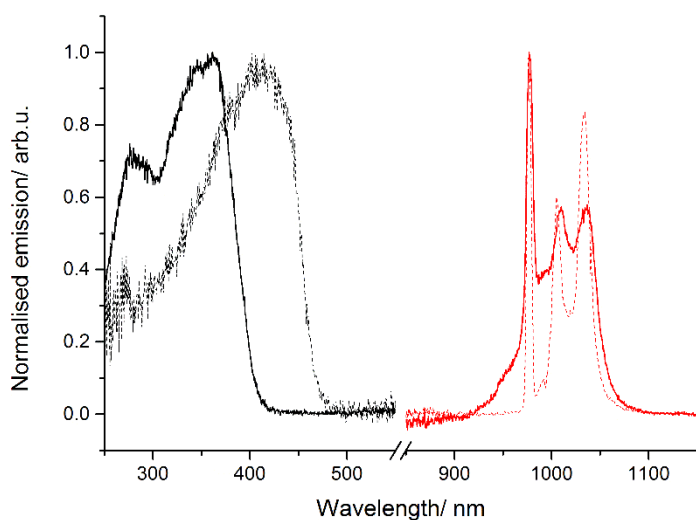


Figure 2.14 Normalised excitation (black) and emission (red) ($\lambda_{exc}=350$ nm) plots of $[Yb(phen)(tbn)_3]$ in $10^{-5} M$ DCM at room temperature (solid line) and 77K (dashed line).

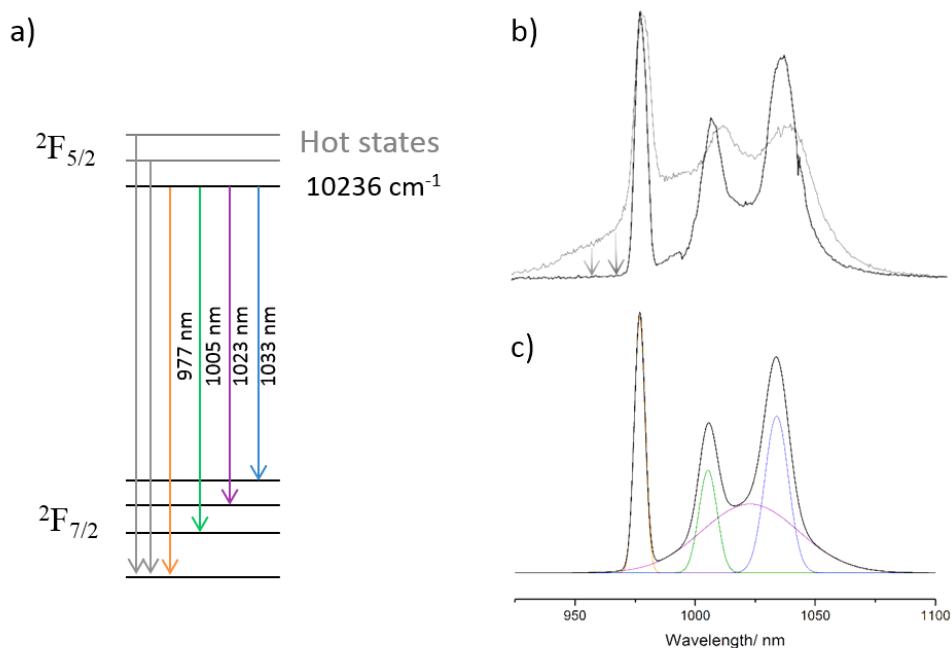


Figure 2.15 Relation between the energy levels of the Yb^{3+} represented in the Jablonski diagram (a) and the emission spectra (b) in an acetonitrile solution at room temperature (grey trace) and 77K (black trace). The emission spectrum was fit ($R^2=0.997$) to a series of overlaying Gaussians (c), using the software OriginPro 9.64, where the black trace represents the total fitting, and orange, green, purple and blue curves show the transitions at 977nm, 1005 nm, 1023 nm and 1033 nm, respectively.

These results indicate that the additional ketone group at the α -carbon of the β -diketone has an effect on the emission behaviour for Yb^{3+} complexes, and the photophysical properties for

the β -triketonate complexes are slightly enhanced (see comparison in Figure 2.16). This is not surprising because the α -CH bond is an efficient quencher of the $^2F_{5/2}$ excited state. However, the values found for the monomeric species do not rival the photophysics of the previously reported tetranuclear assemblies. This suggests that more specific structure and/or composition details play a major role in their unusual photophysical properties, rather than the β -triketonate ligand alone making a fundamental difference compared to β -diketonate analogues.

Finally, if the radiative lifetime is assumed to be 1200 μ s, which is the standard for Yb^{3+} diketonate complexes,¹⁵⁰ the intrinsic quantum yield for $[Yb(phen)(\mathbf{tbm})_3]$ and $[Yb(phen)(\mathbf{dbm})_3]$ in the solid state would be 1.3% and 0.9%, respectively. Both of these values are lower than the respective overall quantum yields, which suggests that the radiative lifetime is therefore, shorter than 1.2 ms in both systems. These results highlight the importance of considering the new modified method for the measurement of NIR-overall quantum yields and the low reliability of intrinsic quantum yields calculated via standard radiative lifetimes.

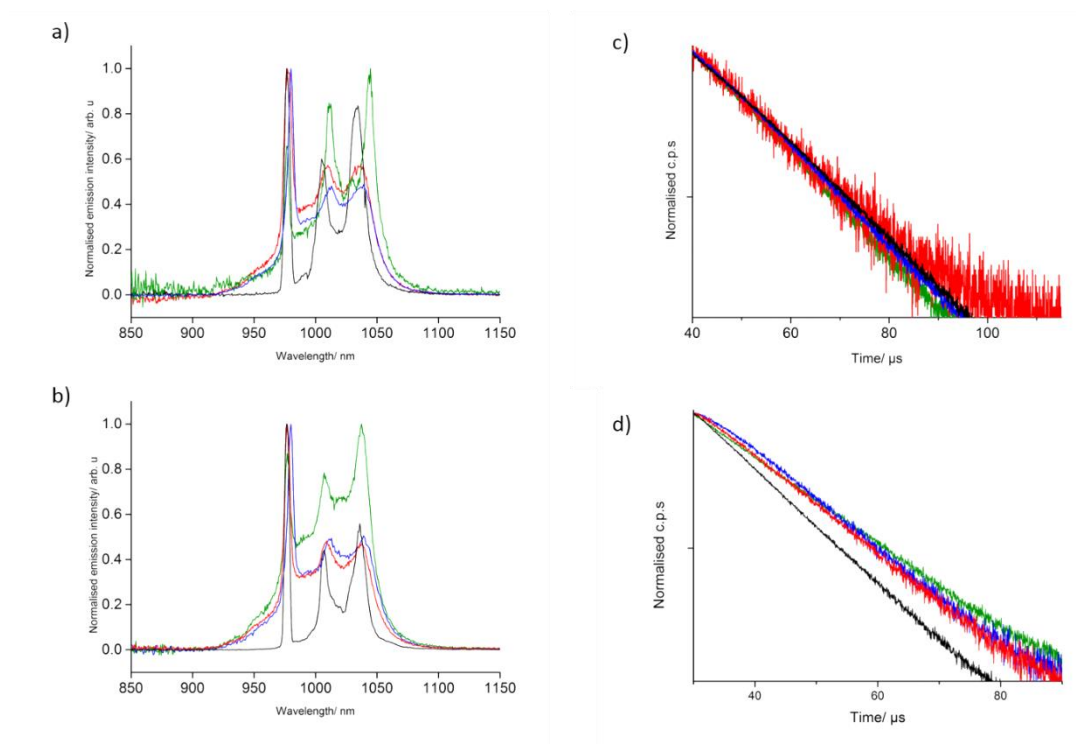


Figure 2.16 Normalised emission intensity ($\lambda_{exc}=350$ nm) and excited lifetime decay plots of $[Yb(phen)(\mathbf{tbm})_3]$ (a,c) and $[Yb(phen)(\mathbf{dbm})_3]$ (b,d) in solid state (green trace), DCM solution (10-5M) (red trace), 77K (black trace) and PMMA (blue trace).

2.4.3 Erbium Complexes

Table 2.5 Photophysical data for [Er(phen)(**tbm**)₃] and [Er(phen)(**dbm**)₃] complexes in the solid state.

Complex	τ_{obs} (μs)	τ_{R} (μs)	$\Phi_{\text{Ln}}^{\text{Ln}}$ (%)
[Er(phen)(dbm) ₃]	1.8	660 ^a	0.27
[Er(phen)(tbm) ₃]	3.2	660 ^a	0.48

^a Literature τ_{R} for Er^{3+} ⁶

The emission spectra of both [Er(phen)(**tbm**)₃] and [Er(phen)(**dbm**)₃] in the solid state display NIR emission from the ${}^4\text{I}_{15/2} \leftarrow {}^4\text{I}_{13/2}$ transition in the $\lambda_{\text{PL}}=1420$ to 1620 nm range (Figure 2.17). The structure of the emission band varies slightly from both complexes due to relatively different crystal field effects evidenced by shape analysis.

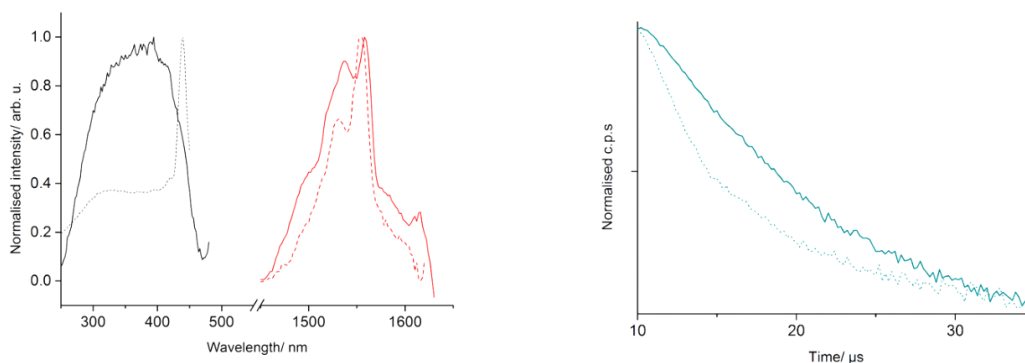


Figure 2.17 Normalised excitation (black)-emission (red) ($\lambda_{\text{exc}}=350$ nm) and excited lifetime decay (green) plots of [Er(phen)(**tbm**)₃] (solid line) and [Er(phen)(**dbm**)₃] (dashed line).

The observed emission decays for both complexes, [Er(phen)(**tbm**)₃] and [Er(phen)(**dbm**)₃], in the solid state were fitted to a monoexponential function, with the lamp component of the decay removed, giving values of 1.8 and 3.2 μs , respectively. The solid-state radiative decay for the Er^{3+} complexes is assumed to be 660 μs .⁶ With this in consideration, the intrinsic quantum yield could be calculated to be 0.48% and 0.27%, respectively.

As these complexes are poorly emissive, their photophysical properties in PMMA and dichloromethane solutions were not measured.

2.5 Conclusion

This chapter has presented new mononuclear eight-coordinate Er^{3+} and Yb^{3+} complexes with tribenzoylmethanide (**tbm**) and phenanthroline (phen) ligands, of the general formula $[\text{Ln}(\text{phen})(\text{tbm})_3]$. This work has focussed on a direct comparison with the analogous $[\text{Ln}(\text{phen})(\text{dbm})_3]$ complexes, in order to better understand the effect on the photophysical properties of the replacement of the α -CH in β -diketonates with an additional ketone functional group to give β -triketonates.

The emission profiles, excited state lifetimes and quantum yields for the Eu^{3+} complexes revealed similar behaviour for both systems. Particularly short lifetimes were found in solution, suggestive of efficient deactivation pathways of the excited states via non-radiative decay. On the other hand, a small enhancement was observed for Yb^{3+} moving from the **dbm** to the **tbm** system, probably because of reduced multiphoton quenching. However, these values do not rival the photophysical properties of the previously reported assemblies,^{27,209,224} suggesting that simply replacing β -diketonates with β -triketonate ligands in similar complex structures is not likely to enhance the photophysical properties of the complex. The remarkable properties of the tetranuclear assemblies presumably are linked to other factors that arise from their structure and composition. Finally, the development of an adapted method was employed for the calculation of NIR overall quantum yields, making possible to comprehensively characterise the photophysical properties of these complexes.

Chapter 3 β -Triketonate Assemblies Incorporating Caesium Cations

Major aspects of this chapter have been published:

L. Abad Galán, B. L. Reid, S. Stagni, A. N. Sobolev, B. W. Skelton, M. Cocchi, J. M. Malicka, E. Zysman-colman, E. G. Moore, M. I. Ogden and M. Massi, *Inorg. Chem.*, 2017, **56**, 8975–8985.

3.1 Introduction

The previous chapter described how structural factors, and not only the removal of the proton of the α -C of the **tbmH** molecule, have a direct effect on the NIR photophysical properties. Therefore, further study on the structures of the assemblies is needed. This chapter will focus on the synthesis of lanthanoid assemblies incorporating Cs^+ as the alkali cation. Furthermore, this investigation was expanded by using the new ligand tri(4-methylbenzoyl)methane (**mtbmH**) alongside the previously employed tribenzoylmethane (**tbmH**). Studying **mtbmH** is an initial step towards establishing how chemical modifications of the ligand might influence the specific structure of the species obtained. The resulting assemblies were investigated by absorption and emission spectroscopy to characterise their photophysical properties. Additional transient absorption experiments have been conducted to further elucidate the detailed sensitisation pathways that characterise lanthanoid species bound to β -triketone ligands.

3.2 Synthesis

3.2.1 Ligand

The **mtbmH** (**L2H**) ligand was synthesised in an analogous fashion to the **tbmH** molecule²⁰⁹ by forming the di(4-methylbenzoyl)methane first, followed by cross-Claisen condensation with 4-methylbenzoyl chloride. The reagents and conditions used are given in Figure 3.1.

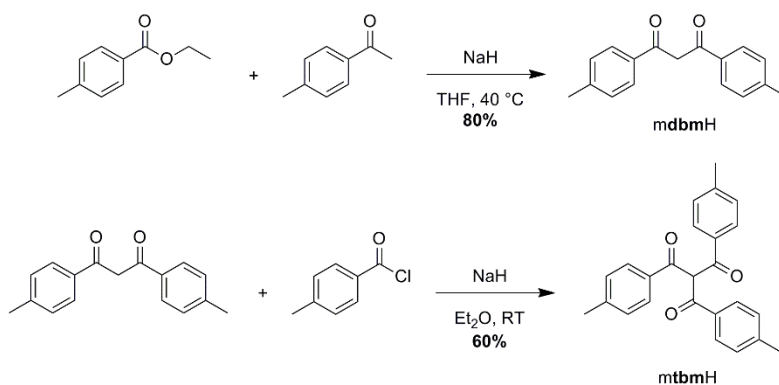


Figure 3.1 Synthetic scheme for the preparation of *mtbmH*.

The **mtbmH** was characterized by melting point, IR, $^1\text{H-NMR}$, $^{13}\text{C-NMR}$ and elemental analysis (see Experimental section). The melting point was found to be 233-234 °C, lying much higher than the precursor **mdbmH** (126-127 °C)²²⁵, which indicates the likely presence of a new species. The IR spectrum displays a sharp peak at 1685 cm^{-1} , suggesting the presence of a carbonyl stretch shifted from the **mdbmH** precursor. Finally, the $^1\text{H-NMR}$ in $\text{DMSO-}d_6$ revealed three peaks in the aromatic region between 7.3 ppm and 8.0 ppm (see Figure 3.2). The splitting pattern and peak positions are consistent with the proposed product. The singlet at 7.95 ppm corresponds to the proton situated at the $\alpha\text{-C}$ position, suggesting that the major species present is the keto tautomer as this peak would not be present in the case of the enol tautomer. The pair of doublets at 7.35 ppm and 7.89 ppm of integrated ratios 6:6 are assigned to the phenyl protons in *meta* and *ortho* position, respectively. The peak in the aliphatic region at 2.38 ppm, which has an integration of 9, is assigned to the methyl groups situated in the *para* position to the carbonyl group.

The keto-enol tautomerism is an equilibrium affected by the nature of the solvent and the β -triketone substituents.²²⁵ Small peaks at 7.28 ppm, 7.83 ppm and 8.06 ppm were observed which are associated with small traces, less than 3%, of the enol tautomer.

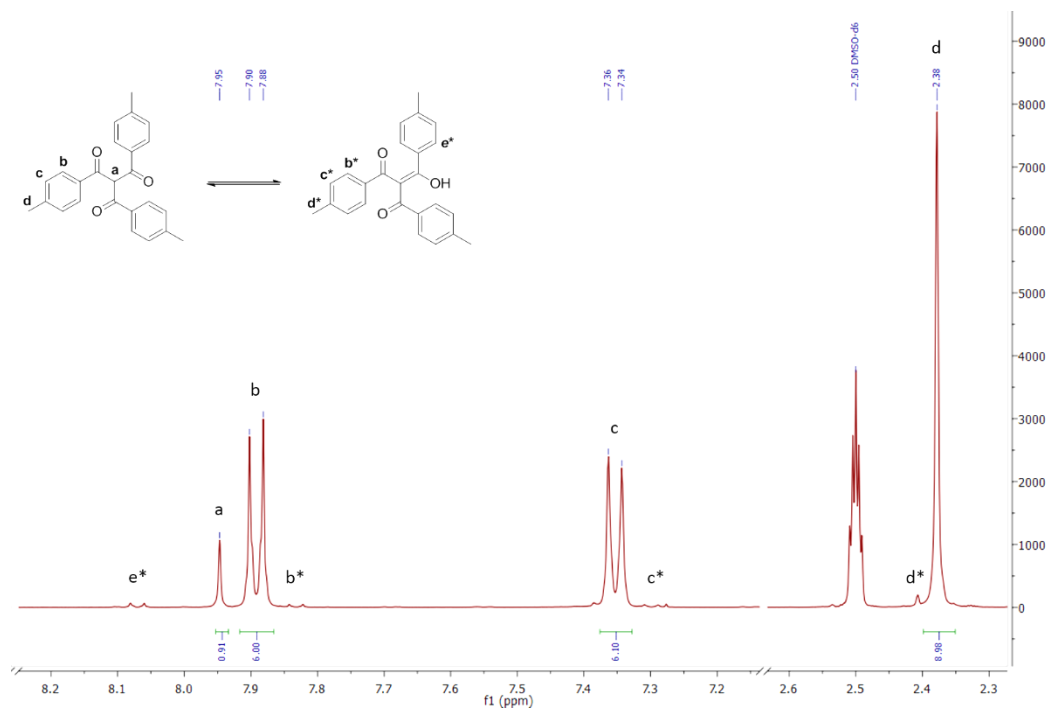


Figure 3.2 Portion of the $^1\text{H-NMR}$ spectrum of *mtbmH* in DMSO-d_6 .

3.2.2 Lanthanoid Assemblies

Following the same methodology used for the preparation of discrete tetranuclear $[\text{Ln}(\text{Ae}\cdot\text{HOEt})(\mathbf{tbm})_4]_2$ ($\text{Ae}^+ = \text{Na}^+, \text{K}^+, \text{Rb}^+$) assemblies,²⁷ one equivalent of hydrated LnCl_3 ($\text{Ln}^{3+} = \text{Eu}^{3+}, \text{Er}^{3+}, \text{and Yb}^{3+}$) was made to react with four equivalents of either **tbmH** or **mtbmH** in the presence of four equivalents of CsOH in ethanol (see Figure 3.3). In general, slow evaporation of the solvent over several days resulted in the deposition of crystals suitable for X-ray diffraction. The formulation of all the isolated species was further confirmed by elemental analysis and IR spectroscopy. In particular, the former revealed the presence of various degrees of solvation, which is typical for these bimetallic $\text{Ln}^{3+}/\text{Ae}^+$ assemblies.²⁷

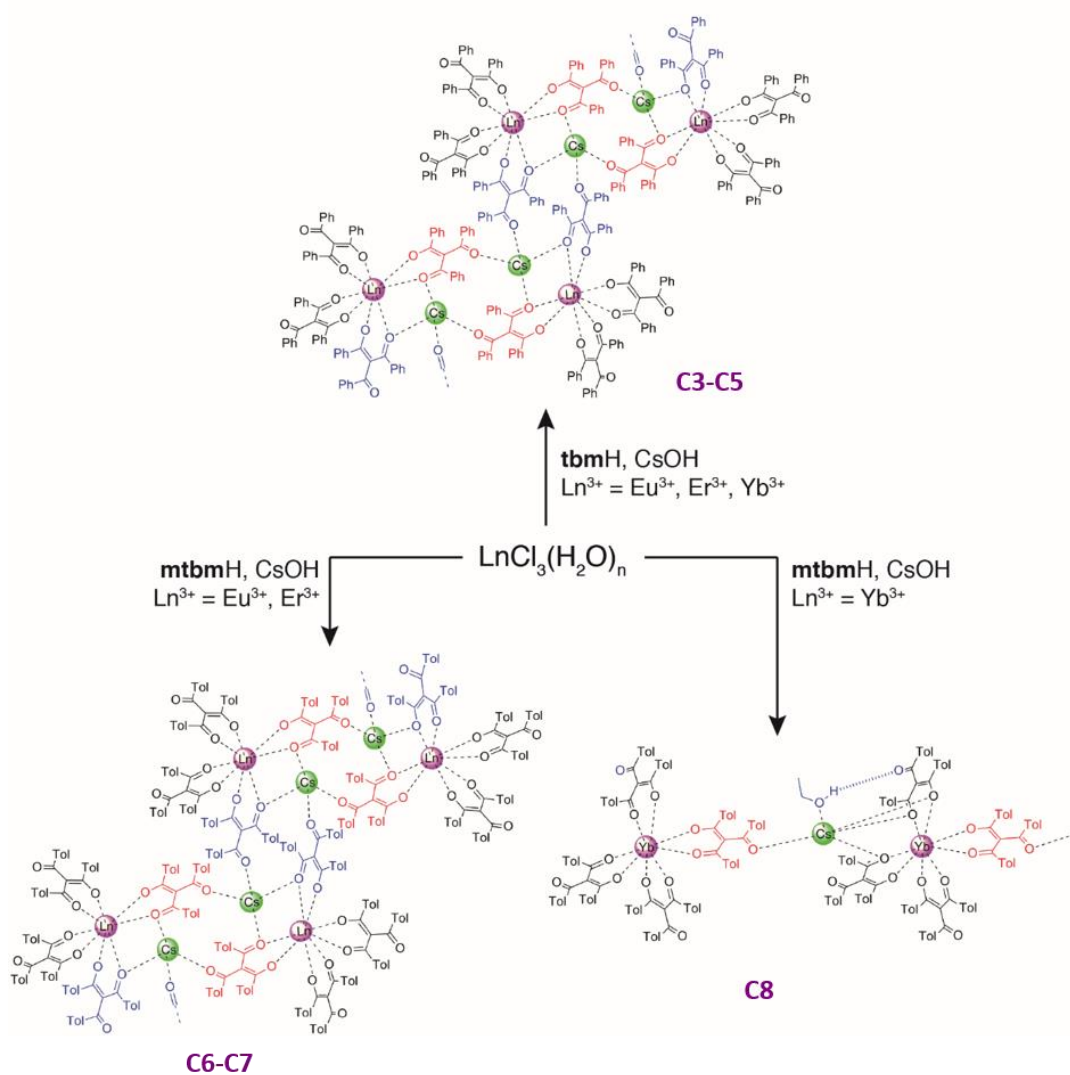


Figure 3.3 Summary of the isolated assemblies according to reaction conditions.

Structural characterisation revealed the formation of unique coordination polymers with formulation $\{[\text{Ln}(\text{Cs})(\text{tbm})_4]_2\}_n$ (**C3-C5**) for $\text{Ln}^{3+} = \text{Eu}^{3+}$, Er^{3+} , and Yb^{3+} or $\{[\text{Ln}(\text{Cs})(\text{mtbm})_4]_2\}_n$ (**C6-C7**) for $\text{Ln}^{3+} = \text{Eu}^{3+}$ and Er^{3+} , upon reaction of LnCl_3 with CsOH and either **tbmH** or **mtbmH** (see Figure 3.3). In each case, the repeating unit of these polymeric species was found to be a tetranuclear assembly analogous to the previously reported species obtained when the alkali metal was Na^+ , K^+ , or Rb^+ .^{27,209} On the other hand, reaction of YbCl_3 with **mtbmH** and CsOH yielded a different coordination polymer that was identified as $[\text{Yb}(\text{Cs}\cdot\text{HOEt})(\text{mtbm})_4]_n$ (**C8**) (see Figure 3.3). In this case, the repeating unit can be more appropriately described as mononuclear Yb^{3+} complexes linearly bridged by Cs^+ cations.

Notably, when analysing crystals obtained from the reaction of hydrated EuCl_3 and **mtbmH**, a second product was also identified by the presence of crystals having a different morphology with respect to those belonging to $\{[\text{Eu}(\text{Cs})(\text{mtbm})_4]_2\}_n$. This by-product was identified as a linear polymer where mononuclear Eu^{3+} complexes bearing di(4-methylbenzoyl)methanide ligands (**mdbm**) were linked by Cs^+ cations, $[\text{Eu}(\text{Cs}\cdot 2\text{HOEt})(\text{mdbm})_4]_n$ (**C9**). This arrangement is analogous to a previously published structure formed by lanthanoid cations and dibenzoylmethanide.²²⁶ The presence of this species seems to indicate possible retro-Claisen reactivity of the triketonate ligands in the alkaline reaction conditions, with formation of the analogous diketonate species. This hypothesis is supported by the fact that the $^1\text{H-NMR}$ spectrum of the purified ligand **mtbmH** prior to the metal complexation experiments does not show the presence of **mdbmH**.

3.3 X-ray diffraction Studies

The repeating units of the three $\{[\text{Ln}(\text{Cs})(\text{tbn})_4]_2\}_n$ polymers with $\text{Ln}^{3+} = \text{Eu}^{3+}$, Er^{3+} , and Yb^{3+} are analogous to previously reported $\text{Ln}^{3+}/\text{Ae}^+$ assemblies.^{27,209} A $\text{Ln}^{3+}/\text{Cs}^+$ dimer is formed by two Ln^{3+} and two Cs^+ metal centres surrounded by eight anionic triketonates (see Figure 3.4). Each Ln^{3+} ion is eight-coordinate, with the four **tbn** ligands binding in a bidentate mode. The third O-keto atoms of two of the ligands, O(23, 43), are not involved in any contact, one O-keto atom, O(33), bridges to a Cs^+ ion to form the dimer, and the fourth, O(13), bridges to a neighbouring Cs^+ forming the polymeric structure. In the previously reported dimeric structures,²⁷ this last position in the coordination sphere of the Ae^+ cation was occupied by the O atom of an ethanol molecule. Here, an EtOH molecule is found in the lattice, with a hydrogen bond formed with the keto O(43) atom. The remainder of the coordination sphere of the Cs^+ comprises three μ -O atoms (one each from ligands 1-3) bridging to the Ln^{3+} cation.

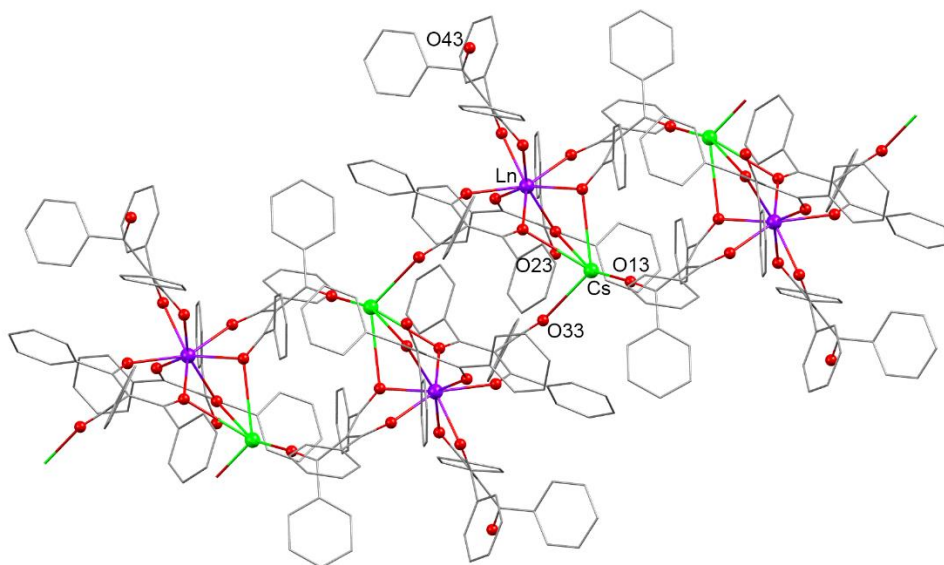


Figure 3.4 Representation of the X-ray crystal structure of $\{[\text{Ln}(\text{Cs})(\text{t}\mathbf{b}\mathbf{m})_4]_2\}_n$, $\text{Ln}^{3+} = \text{Eu}^{3+}, \text{Er}^{3+}, \text{Yb}^{3+}$. Hydrogen atoms are omitted for clarity.

The structures of the two $\{[\text{Ln}(\text{Cs})(\mathbf{m}\mathbf{t}\mathbf{b}\mathbf{m})_4]_2\}_n^{+}$ polymers, with $\text{Ln}^{3+} = \text{Eu}^{3+}$ and Er^{3+} , are unsolvated and structurally similar to the **tbm** coordination polymers (see Figure 3.5). The tetranuclear $\text{Ln}^{3+}/\text{Ae}^+$ dimeric assembly is again observed, with the polymeric structure formed by coordination to the Cs^+ cations. The specifics of these bridging interactions between the tetranuclear assemblies do differ. Comparing the two Eu^{3+} polymeric structures, in the **mtbm** system, the closest approaches between aromatic rings and the Cs^+ cations occur within the tetranuclear assembly ($\text{Cs}\cdots\text{C}(216, 316)$, 3.324, 3.521; $\text{Cs}\cdots\text{centroid}(2,3)$, 3.926, 4.257 Å), consistent with an attractive interaction.^{227,228} In contrast, the closest such approaches occur *between* the tetranuclear assemblies in the **tbm** polymers ($\text{Cs}\cdots\text{C}(115)$, 3.580 Å; $\text{Cs}\cdots\text{centroid}$, 3.542 Å). This results in a $\text{Cs}^+\cdots\text{Cs}^+$ distance between linked tetranuclear assemblies of 7.332 Å in the **tbm** system, compared to 8.168 Å in the **mtbm** system.

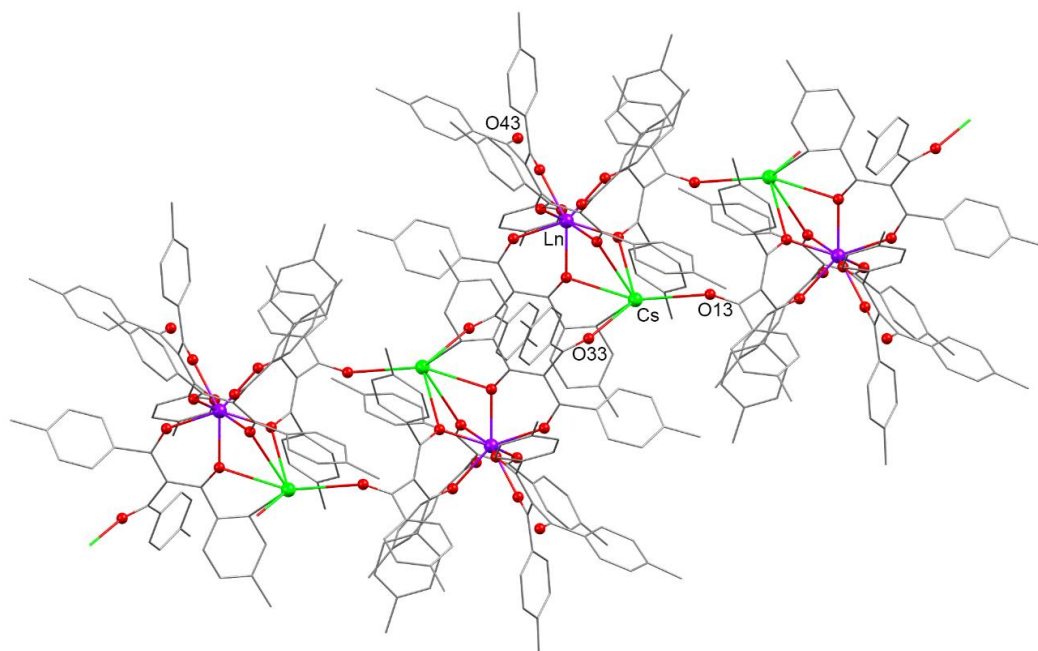


Figure 3.5 Representation of the X-ray crystal structure of $\{[Ln(Cs)(\mathbf{mtbm})_4]_2\}_n$, $Ln^{3+} = Eu^{3+}, Er^{3+}$. Hydrogen atoms are omitted for clarity.

The $[Yb(Cs)(\mathbf{mtbm})_4]_n$ polymer crystallised as a significantly different structure (see Figure 3.6). This species comprises of one Yb^{3+} and one Cs^+ that are counter balanced by four anionic **mtbm** ligands. Each Yb^{3+} is octacoordinated and bound to four ligands in a bidentate mode. The third keto-O atoms on three of the ligands are not coordinated, while the fourth, O(13), is bridging to the Cs^+ cation. The bridging interaction also involves a close approach with the second ring of the first ligand, with a $Cs^+ \cdots$ centroid distance of 3.473 Å. The remainder of the coordination sphere of the Cs^+ cation includes three μ -O atoms bridging to Yb^{3+} (one from ligand 2, two from ligand 4) and a molecule of ethanol, which presents a hydrogen-bond interaction with keto-O(43) atom ($O(1) \cdots O(43)$, 2.838 Å).

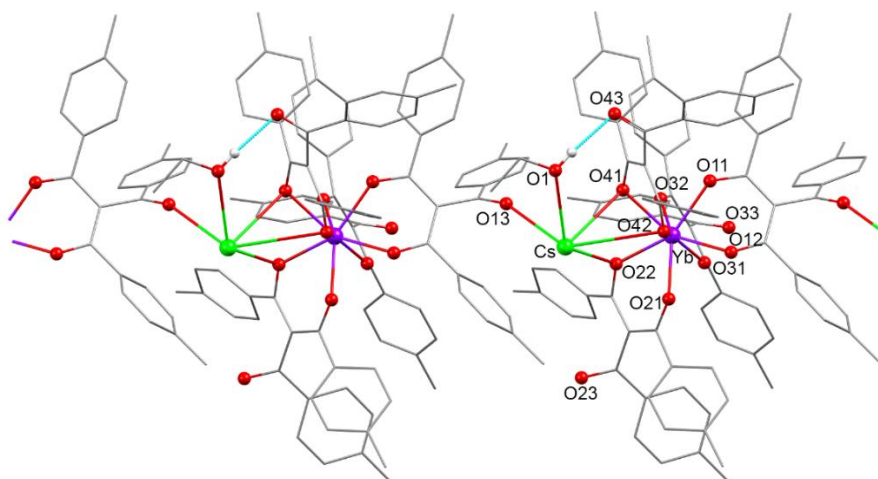


Figure 3.6 Representation of the X-ray crystal structure of $[\text{Yb}(\text{Cs})(\text{mtbm})_4]_n$. Hydrogen atoms are omitted for clarity. The hydrogen bonding interaction is highlighted with a light blue line.

The $[\text{Eu}(\text{Cs})(\text{EtOH})_2(\text{mdbm})_4]_n$ species (see Figure 3.7) presumably formed due to retro-Claisen reaction of **mtbm** in the presence of CsOH and hydrated EuCl_3 , is a coordination polymer analogous to previous reports. Each subunit comprises one octacoordinate Eu^{3+} and one Cs^+ counterbalanced by four deprotonated ligands. The Cs^+ is coordinated to two molecules of solvent and six $\mu\text{-O}$ atoms bridging to the Eu^{3+} .

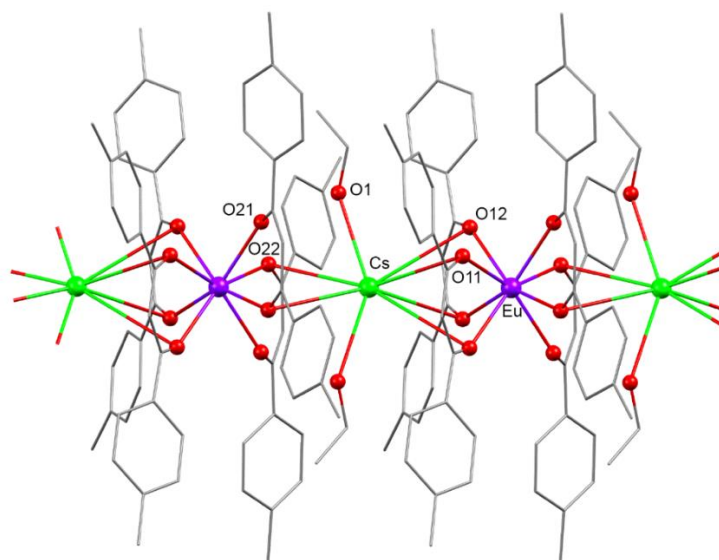


Figure 3.7 Representation of the X-ray crystal structure of $[\text{Eu}(\text{Cs})(\text{EtOH})_2(\text{mdbm})_4]_n$. Hydrogen atoms are omitted for clarity.

3.3.1 Shape Analysis

The coordination sphere of the assemblies was assessed using the Shape analysis version 2.1 software as explained in Chapter 2. Each complex was studied against the 13 ideal eight-coordination polyhedra, the complexes of which being best described either as square antiprism (SAPR-8) or triangular dodecahedron (TDD-8) (see Figure 3.8).

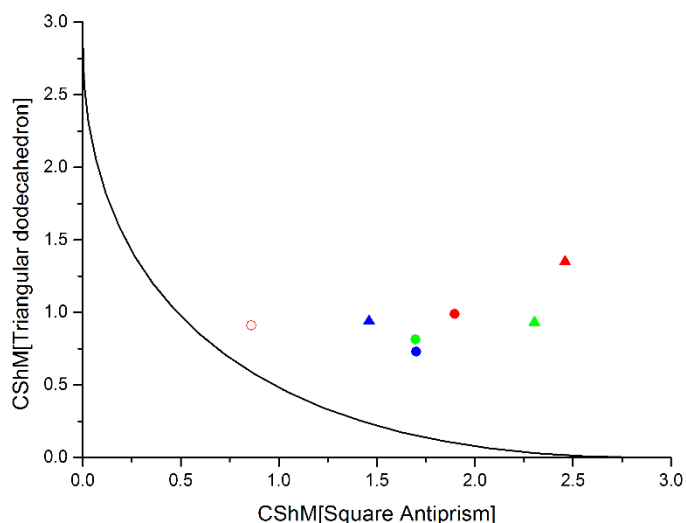


Figure 3.8 Shape Map representing the CshM values of the $\{[Ln(Cs)(\mathbf{tbm})_4]_2\}_n$ (dots), $\{[Ln(Cs)(\mathbf{mtbm})_4]_2\}_n$, $[Yb(Cs)(\mathbf{mtbm})_4]_n$ (triangles) and $[Eu(Cs)(EtOH)_2(\mathbf{mdbm})_4]_n$ (circle) complexes for Eu^{3+} (red), Er^{3+} (green) and Yb^{3+} (blue).

Table 3.1 CShM values for complexes **C3-C9** for $Ln = Eu^{3+}$, Yb^{3+} and Er^{3+} .

Complex	TTD-8	SAPR-8
C3 $\{[Eu(Cs)(\mathbf{tbm})_4]_2\}_n$	0.99	1.90
C6 $\{[Eu(Cs)(\mathbf{mtbm})_4]_2\}_n$	1.35	2.46
C4 $\{[Er(Cs)(\mathbf{tbm})_4]_2\}_n$	0.81	1.70
C7 $\{[Er(Cs)(\mathbf{mtbm})_4]_2\}_n$	0.93	2.30
C5 $\{[Yb(Cs)(\mathbf{tbm})_4]_2\}_n$	0.73	1.70
C8 $[Yb(Cs)(\mathbf{mtbm})_4]_n$	0.94	1.46
C9 $[Eu(Cs)(EtOH)_2(\mathbf{mdbm})_4]_n$	0.91	0.86

As observed, all the complexes are best described as distorted triangular dodecahedra with the exception of $[Eu(Cs)(EtOH)_2(\mathbf{mdbm})_4]_n$, which is closer to square antiprism.

3.4 Photophysical Properties

The photophysical data, which include excited state lifetime decay (τ_{obs}), calculated radiative decay (τ_{R}), intrinsic photoluminescence quantum yield ($\Phi_{\text{Ln}}^{\text{Ln}}$), overall photoluminescence quantum yield ($\Phi_{\text{Ln}}^{\text{L}}$), and calculated sensitisation efficiency (η_{sens}), are reported in Tables 3.2-3.4 at the beginning of each section.

The emission properties were recorded in the solid state as it has been previously demonstrated that these assemblies do not persist in polar coordinating solvents and are generally insoluble in non-polar solvents.²⁷ This was also found to be the case for species bound to the **mtbm** ligand, as the substitution with a simple methyl group does not appear to be sufficient to impart solubility in common non-coordinating solvents. In each case, the emission of the various species originates as a consequence of the antenna effect, an argument that is supported by the broad excitation spectra that are analogous to the corresponding absorption profiles of the **tbm** and **mtbm** ligands. The absorption spectra of **mtbmH/tbm** is very similar to the **tbmH/tbm**, with main absorption bands at 260 nm and 350 nm attributed to π - π^* transitions²⁶ (see Figure 3.9). This suggests that the addition of the methyl group should not have a significant effect on the sensitisation of lanthanoids.

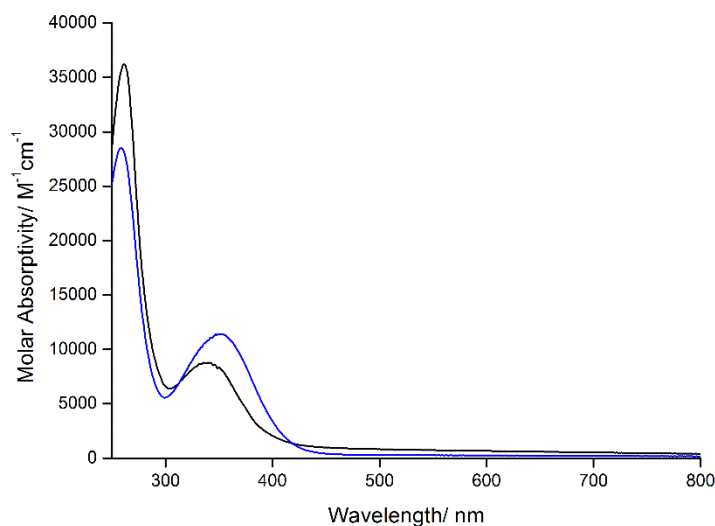


Figure 3.9 Absorption profiles of **mtbmH** (black trace) and **mtbm** (excess of KOH, blue trace) at 298K in $10^{-5}M$ ethanol.

The triplet states of **tbm** and **mtbm** were found to be approximately the same and in the range $21,500$ - $20,500 \text{ cm}^{-1}$ (0-phonon transition at 465-488 nm) based on measurements of the phosphorescence emission at 77 K of their corresponding Gd^{3+} complexes in ethanol glass

(see Figure 3.10).¹¹⁵ The energy of the triplet state is therefore high enough to sensitise emission from the excited states of Eu^{3+} , Er^{3+} , and Yb^{3+} (the latter possibly *via* charge transfer excited states).^{91,98}

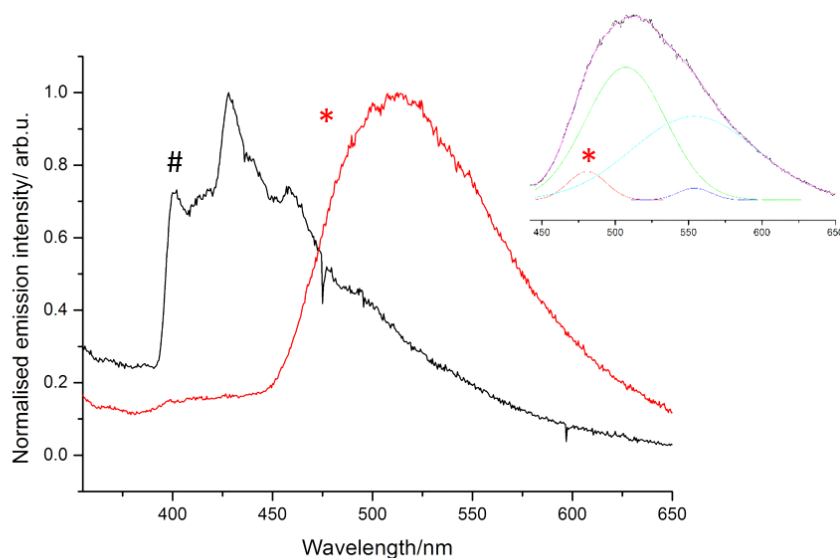


Figure 3.10 Emission of ligand *mtbmH* (black trace) and *mtbm* in the presence of excess of Gd^{3+} and triethylamine (red trace). The # and * symbols indicate de 0-phonon transitions for the singlet and triplet excited states, respectively.

3.4.1 Europium Assemblies

Table 3.2 Photophysical data for the Eu^{3+} complexes in the solid state.

Complex	τ_{obs} (μs)	τ_{R} (ms)	$\Phi_{\text{Ln}}^{\text{Ln}}$ (%)	$\Phi_{\text{Ln}}^{\text{L}}$ (%) ^a	Φ_{sens} (%)
$\{[\text{Eu}(\text{Cs})(\text{tbn})_4]_2\}_n$	355	0.660	54	31	57
$\{[\text{Eu}(\text{Cs})(\text{mtbn})_4]_2\}_n$	424	0.798	53	37	64

^a measured with the use of an integrating sphere.

The emission spectra of $\{[\text{Eu}(\text{Cs})(\text{tbn})_4]_2\}_n$ and $\{[\text{Eu}(\text{Cs})(\text{mtbn})_4]_2\}_n$ are very similar and show the characteristic Eu^{3+} -centred line-like bands in the region 580-750 nm corresponding to the ${}^7\text{F}_J \leftarrow {}^5\text{D}_0$ ($J = 0-4$) transitions (see Figure 3.11). The ${}^7\text{F}_0 \leftarrow {}^5\text{D}_0$ peak appears narrow (full-width at half-maximum smaller than $\approx 30 \text{ cm}^{-1}$), albeit of very weak intensity, indicating that the emission originates in each case from a unique Eu^{3+} , and in agreement with the fact that the two Eu^{3+} cations in each assembly unit are related by an inversion centre.^{6,27,46}

The magnetic-dipole allowed transition, ${}^7F_1 \leftarrow {}^5D_0$, appears to be split into two bands in the case of $\{[\text{Eu}(\text{Cs})(\mathbf{tbm})_4]_2\}_n$ and into three bands (with two being quasi-degenerate) for $\{[\text{Eu}(\text{Cs})(\mathbf{mtbm})_4]_2\}_n$. This trend suggests slightly different degrees of distortion between the two coordination spheres,⁴⁶ which is supported by the results found in the shape analysis study where $\{[\text{Eu}(\text{Cs})(\mathbf{mtbm})_4]_2\}_n$ is more distorted than $\{[\text{Eu}(\text{Cs})(\mathbf{tbm})_4]_2\}_n$ with respect to an ideal triangular dodecahedron.³⁸ Slight differences can also be observed in the splitting of the hypersensitive ${}^7F_2 \leftarrow {}^5D_0$ peaks.

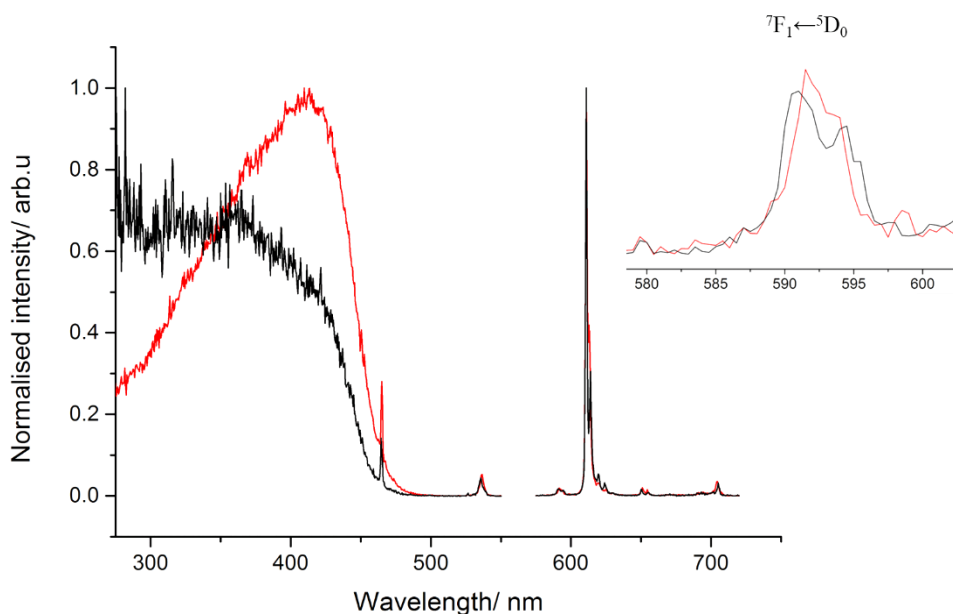


Figure 3.11 Normalised excitation and emission ($\lambda_{exc}=350$ nm) plot for $\{[\text{Eu}(\text{Cs})(\mathbf{tbm})_4]_2\}_n$ (red trace) and $\{[\text{Eu}(\text{Cs})(\mathbf{mtbm})_4]_2\}_n$ (black trace) in the solid state at 298K. Inset: highlight of the peaks corresponding to the ${}^7F_1 \leftarrow {}^5D_0$ transition.

Excited state lifetime decay values (τ_{obs}) were measured to be 355 μs and 424 μs for $\{[\text{Eu}(\text{Cs})(\mathbf{tbm})_4]_2\}_n$ and $\{[\text{Eu}(\text{Cs})(\mathbf{mtbm})_4]_2\}_n$, respectively. In both cases, the decays were satisfactorily fitted with monoexponential functions (see Figure 3.12).

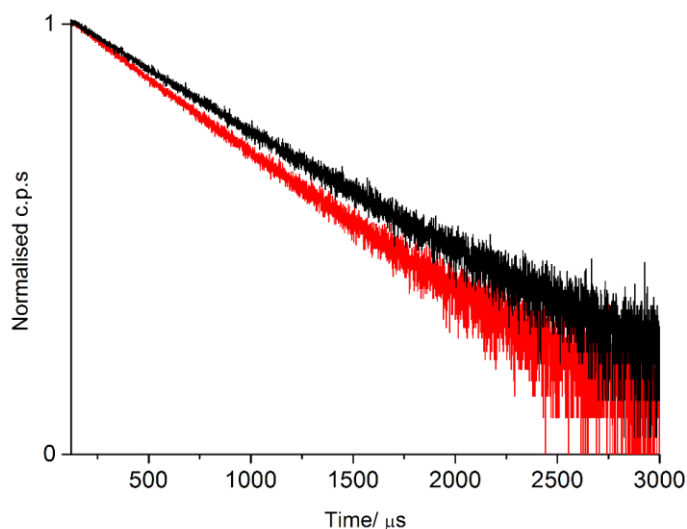


Figure 3.12 Lifetime decays at 612nm ($\lambda_{exc}=350$ nm) of the $\{[Eu(Cs)(\mathbf{tbm})_4]_2\}_n$ (red trace) and $\{[Eu(Cs)(\mathbf{mtbm})_4]_2\}_n$ (black trace) in the solid state at 298K.

From the emission spectra, the value of the radiative lifetimes could be estimated at 660 and 798 μs for $\{[Eu(Cs)(\mathbf{tbm})_4]_2\}_n$ and $\{[Eu(Cs)(\mathbf{mtbm})_4]_2\}_n$, respectively. The overall quantum yields of the compounds were measured with values of 0.51 and 0.57 for $\{[Eu(Cs)(\mathbf{tbm})_4]_2\}_n$ and $\{[Eu(Cs)(\mathbf{mtbm})_4]_2\}_n$, respectively. From these data, the intrinsic quantum yields, as a ratio of τ_{obs}/τ_R , could be calculated at 0.54 and 0.53, providing information on the sensitisation efficiency for the **tbm** (0.57) and **mtbm** ligand (0.64).

Taken together, the photophysical data for the two Eu^{3+} species indicate that in these complexes energy transfer from the **tbm** and **mtbm** ligands is quite efficient and in line with the previously reported Eu^{3+} assemblies obtained with Na^+ , K^+ , and Rb^+ .²⁷

3.4.2 Ytterbium Assemblies

Table 3.3 Photophysical data for the Yb^{3+} complexes in the solid state.

Complex	τ_{obs} (μs)	τ_R (ms)	Φ_{Ln}^{Ln} (%)	Φ_{Ln}^L (%) ^b	Φ_{sens} (%)
$\{[Yb(Cs)(\mathbf{tbm})_4]_2\}_n$	46	1.2 ^a	4	4.5	-
$[Yb(Cs)(\mathbf{mtbm})_4]_n$	19	1.2 ^a	1	2	-

^a literature τ_R for Yb^{3+} , ^b measured with the use of an integrating sphere.

Characteristic NIR emission from both $\{[\text{Yb}(\text{Cs})(\text{t**bm**)_4]_2\}_n$ and $[\text{Yb}(\text{Cs}\cdot\text{HOEt})(\text{m**tbm**)_4]_n$ was observed in the 900-1100 nm region, corresponding to the spin-allowed ${}^2\text{F}_{7/2} \leftarrow {}^2\text{F}_{5/2}$ transition (see Figure 3.13). This transition is split into four main bands due to crystal field effects and shows emission from hot bands as a shoulder in the 930-960 nm region.⁷ As in the previous cases, slight differences in the fine splitting of the band are ascribed to a variable degree of distortion for the two Yb^{3+} centres.²¹⁴

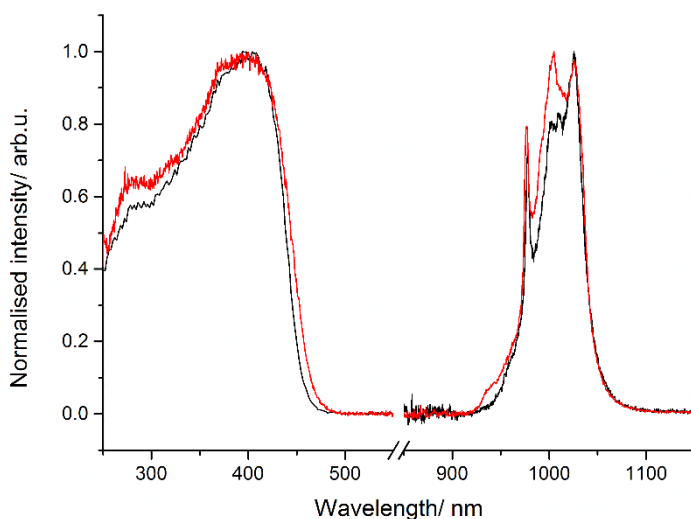


Figure 3.13 Normalised excitation and emission ($\lambda_{\text{exc}}=350$ nm) plot for $\{[\text{Yb}(\text{Cs})(\text{t**bm**)_4]_2\}_n$ (red trace) and $[\text{Yb}(\text{Cs}\cdot\text{HOEt})(\text{m**tbm**)_4]_n$ (black trace) in the solid state at 298K..

The observed lifetime decays τ_{obs} were fitted to a monoexponential function and give values of 46 and 19 μs for $\{[\text{Yb}(\text{Cs})(\text{t**bm**)_4]_2\}_n$ and $[\text{Yb}(\text{Cs}\cdot\text{HOEt})(\text{m**tbm**)_4]_n$, respectively (see Figure 3.14). If the radiative lifetime is assumed to be 1200 μs (which is the standard assumption for Yb^{3+} diketonate complexes, but experimental data are known to range between 500 and 1200 μs),^{6,64,229} the complexes would have intrinsic quantum yield values of 4% and 1%, respectively.

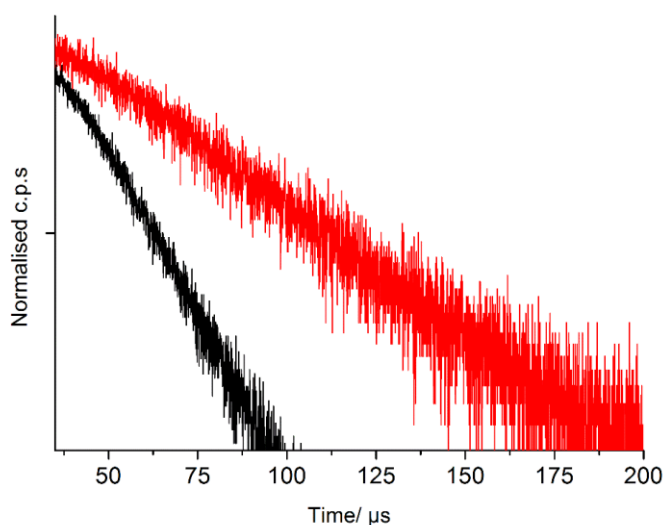


Figure 3.14 Lifetime decays at 980 nm ($\lambda_{exc}=350$ nm) of the $\{[Yb(Cs)(\mathbf{tbm})_4]_2\}_n$ (red trace) and $\{[Yb(Cs)(\mathbf{mtbm})_4]_2\}_n$ (black trace) in the solid state at 298K.

The value of τ_{obs} for $\{[Yb(Cs)(\mathbf{tbm})_4]_2\}_n$ is still relatively high compared to Yb^{3+} diketonate compounds ($4-5 \mu s$)¹³² and it is analogous to the previously reported series of Yb^{3+}/Ae^+ ($Ae^+ = Na^+, K^+, \text{ and } Rb^+$) assemblies.²⁷ This new result suggests that the presence of the molecule of ethanol coordinated to Ae^+ in the tetranuclear assemblies is not a dominant factor for non-radiative deactivation of the ${}^2F_{5/2}$ excited state of Yb^{3+} . Interestingly, the $[Yb(Cs \cdot HOEt)(\mathbf{mtbm})_4]_n$ species has a similar composition to the tetranuclear assemblies, but its excited state lifetime is halved. Based on the previous consideration, it might be excluded that the shorter value of τ_{obs} for $[Yb(Cs \cdot HOEt)(\mathbf{mtbm})_4]_n$ will be due to multiphonon relaxation caused by the molecule of ethanol coordinated to the Cs^+ cation. Given that energy migration is unlikely due to the distance between Yb^{3+} centres,²²⁹ the difference in excited state lifetime decays could be caused by a shorter value of τ_R for $[Yb(Cs \cdot HOEt)(\mathbf{mtbm})_4]_n$.

However, as it has been explained in the previous chapter, the most accurate way to calculate the quantum yield for the NIR emitters is with the use of an integrating sphere. Following the same home modified procedure, overall quantum yields were calculated to be 4.5% and 2%, respectively. These data suggest that the radiative decay in both cases is shorter than the literature-assumed 1.2 ms, considering that overall quantum yields must be lower than intrinsic quantum yields. Apart from a shorter value of radiative decay, a lower sensitisation efficiency is found for the \mathbf{mtbm} complex which suggests that structural factors have an impact on the NIR photophysical properties. These results are consistent with the results described in Chapter 2.

3.4.3 Erbium Assemblies

Table 3.4 Photophysical data for the Er^{3+} complexes in the solid state.

Complex	τ_{obs} (μs)	τ_{R} (ms)	$\Phi_{\text{Ln}}^{\text{Ln}}$ (%)
$\{[\text{Er}(\text{Cs})(\text{tbm})_4]_2\}_n$	7	0.66 ^a	1
$\{[\text{Er}(\text{Cs})(\text{mtbm)_4]_2\}_n$	7	0.66 ^a	1

^a Literature τ_{R} for Er^{3+}

The emission spectra of both $\{[\text{Er}(\text{Cs})(\text{t**b**m})_4]_2\}_n$ and $\{[\text{Er}(\text{Cs})(\text{m**t**b**m**)_4]_2\}_n$ show the characteristic Er^{3+} -based NIR emission in the 1450-1650 nm spectral region. This peak is attributed to the spin-allowed ${}^4\text{I}_{15/2} \leftarrow {}^4\text{I}_{13/2}$ transition (see Figure 3.15). The peak appears structured as a consequence of the crystal field effect exerted by the ligands.¹³¹ The fine structure of the splitting is slightly different, which is ascribed to a different degree of distortion in the coordination sphere around the Er^{3+} centres in the two species (see Figure 3.15).³⁸

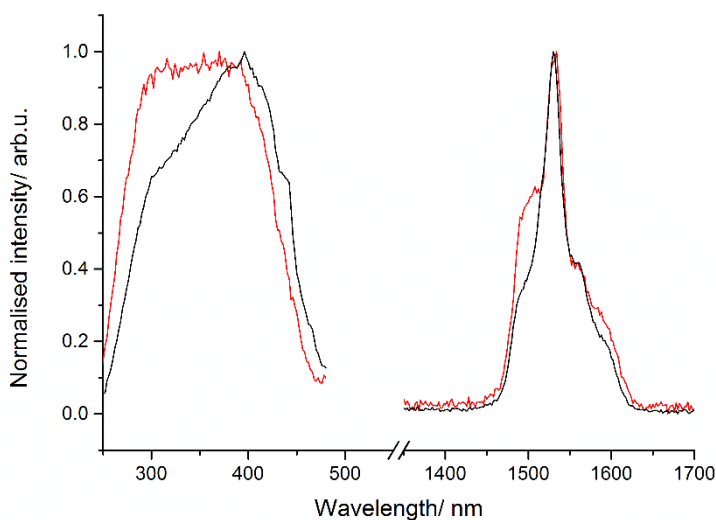


Figure 3.15 Normalised excitation and emission ($\lambda_{\text{exc}}=350$ nm) plot for $\{[\text{Er}(\text{Cs})(\text{t**b**m})_4]_2\}_n$ (red trace) and $\{[\text{Er}(\text{Cs})(\text{m**t**b**m**)_4]_2\}_n$ (black trace) in the solid state at 298K.

The values of τ_{obs} were measured to be 7 μs for both $\{[\text{Er}(\text{Cs})(\text{t**b**m})_4]_2\}_n$ and $\{[\text{Er}(\text{Cs})(\text{m**t**b**m**)_4]_2\}_n$. Both decay profiles were satisfactorily fitted by monoexponential

functions after deconvolution from instrumental response (see Figure 3.16). This value provides an estimation of the intrinsic quantum yield Φ_{Ln}^{Ln} of 0.01.

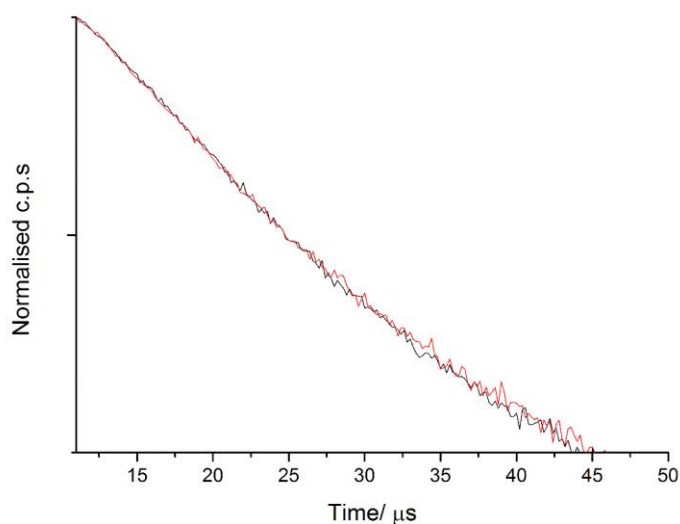


Figure 3.16 Lifetime decays at 1550 nm ($\lambda_{exc}=350$ nm) of the $\{[Er(Cs)(\mathbf{tbm})_4]_2\}_n$ (red trace) and $\{[Er(Cs)(\mathbf{mtbm})_4]_2\}_n$ (black trace) in the solid state at 298K.

As in the case of the previously published assemblies bearing Er^{3+} and Na^+ , K^+ , or Rb^+ ,²⁹ τ_{obs} is longer than the average excited state lifetime values for Er^{3+} diketonate species (1-2 μs), and within the range of Er^{3+} species that have complexes with perfluorinated and deuterated ligands (6-11 μs at 58-98% α -deuteration).^{79,131} However, overall quantum yields could not be measured due to poor emissive properties.

3.5 Transient Absorption

To gain a more detailed insight into the kinetics involved in the sensitisation process for the triketonate ligands, transient absorption (TA) measurements on the femtosecond timescale were also performed. Previous TA measurements have proven useful in understanding the excited state properties for diketonate species.²³⁰⁻²³³ As noted earlier, the tetranuclear assemblies do not persist in polar coordinating solvents,²⁷ so these measurements had to be performed using simpler model complexes. To that end, solutions of the **tbm** and **mtbm** ligands were prepared using a K_2CO_3 -saturated EtOH solution as the solvent, in order to ensure deprotonation of the ligand in solution. To these solutions, a large molar excess (>10 eq.) of the $Ln^{3+} = Gd^{3+}$, Eu^{3+} , Yb^{3+} , or Er^{3+} cation was added using trifluoromethanesulfonate

salts. Complexation was confirmed using UV-Vis spectroscopy, which showed a shift in the absorption peak maxima to *ca.* 340 nm. The formation of the lanthanoid complexes was assumed to be 1:1 ($[\text{Ln}(\mathbf{tbm})(\text{OH}_2)_x]^{2+}$ and $[\text{Ln}(\mathbf{mtbm})(\text{OH}_2)_x]^{2+}$) given the large excess of metal ion added.

Table 3.5 Summary of excited state properties determined by fs-TA spectroscopy.

Complex	τ_1 ($S_1 \rightarrow S_n$)	$k_{\text{obs-S1}}$	τ_2 ($T_1 \rightarrow T_n$)	$k_{\text{obs-T1}}$	$k_{\text{EET-T1}}$	$\Phi_{\text{EET-T1}}$
	(ps)	(s^{-1})	(ps)	(s^{-1})	(s^{-1})	(%)
$[\text{Gd}(\mathbf{tbm})]^{2+}$	15.3	6.54×10^{10}	961	1.04×10^9	-	-
$[\text{Gd}(\mathbf{mtbm})]^{2+}$	20.1	4.98×10^{10}	2076	4.82×10^8	-	-
$[\text{Yb}(\mathbf{tbm})]^{2+}$	2.4	4.17×10^{11}	28.4	3.52×10^{10}	3.42×10^{10}	97.0
$[\text{Yb}(\mathbf{mtbm})]^{2+}$	4.4	2.27×10^{11}	72.0	1.39×10^{10}	1.34×10^{10}	96.5
$[\text{Er}(\mathbf{tbm})]^{2+}$	7.2	1.39×10^{11}	37.4	2.67×10^{10}	2.57×10^{10}	96.1
$[\text{Er}(\mathbf{mtbm})]^{2+}$	5.4	1.85×10^{11}	36.5	2.74×10^{10}	2.69×10^{10}	98.2
$[\text{Eu}(\mathbf{tbm})]^{2+}$	5.1	1.96×10^{11}	-	-	-	-
$[\text{Eu}(\mathbf{mtbm})]^{2+}$	4.3	2.33×10^{11}	-	-	-	-

The resulting TA spectra for the Gd^{3+} complexes of **tbm** and **mtbm** are shown in Figure 3.177. The excited state difference spectra (ΔOD) at early time delays reveal a negative ground state bleach (GSB) signal at wavelengths less than 380 nm and a positive excited state absorption (ESA) peak centred at *ca* 400 nm, with the latter decaying rapidly to form a broader feature centred at *ca* 650 nm, which subsequently decays. The corresponding kinetic plots for the observed ΔOD dynamics integrated over 10 nm data intervals from 350 to 650 nm are shown in Figure 3.177, and these data were globally fit to a biexponential decay function of the form;

$$I_{(t)} = A_1 \exp^{-1/\tau_1(t)} + A_2 \exp^{-1/\tau_2(t)} \quad (3.1)$$

where $I_{(t)}$ is the intensity of the transient absorption data at time (t), τ_1 and τ_2 are the observed lifetimes, and A_1 and A_2 are pre-exponential scaling factors. The best fits to the experimental data are shown in Figure 3.17, and resulting lifetimes are summarised in Table 3.5, together with the Decay Associated Difference Spectra (DADS) shown in Figure 3.17.

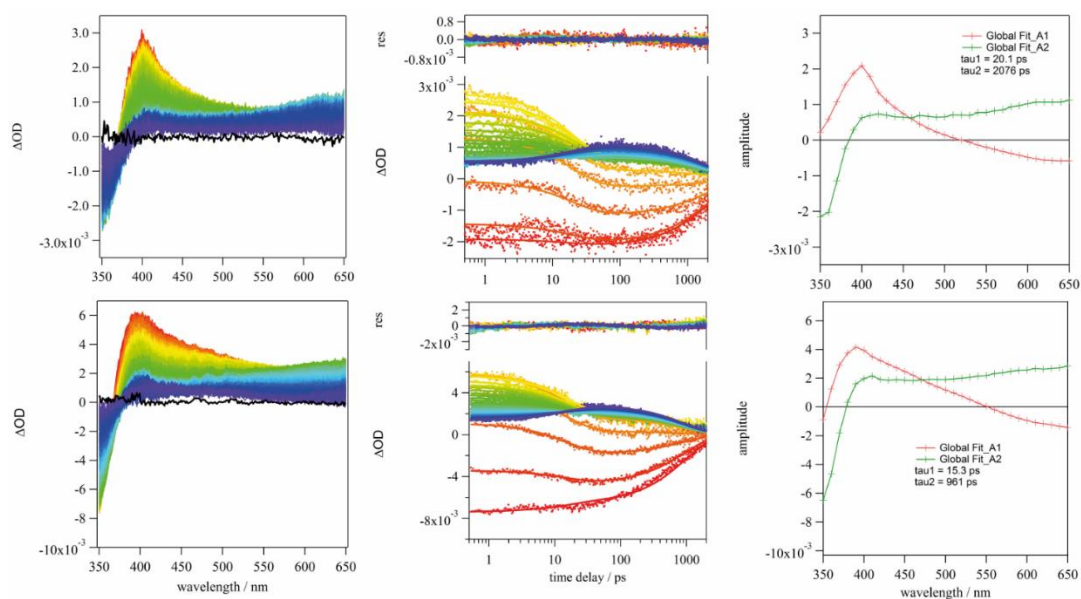


Figure 3.17 TA spectra (left) of Gd^{3+} complexes of **mtbm** (top) and **tbm** (bottom), along with corresponding decay kinetic plots (middle) and Decay Associated Difference Spectra (right).

Notably, the data for the Gd^{3+} complexes of **tbm** and **mtbm** are very similar, which is not surprising given their similar chemical structures. For both complexes, a fast decay component ($\tau_1 = 15\text{--}20$ ps) at *ca* 400 nm (positive DADS signal) is matched by a fast rise at *ca* 650 nm (negative DADS signal). Hence, these spectral features may be assigned to decay of the initially populated S_1 excited state to form the T_1 excited state *via* ISC, with subsequent decay of the T_1 state on the nanosecond timescale leading to ground state recovery.

Corresponding data for the remaining $Ln^{3+} = Yb^{3+}$, Eu^{3+} , and Eu^{3+} , complexes of the **tbm** and **mtbm** ligands were also collected (see Figures 3.18–3.20, respectively). For the Yb^{3+} and Er^{3+} complexes, the spectra obtained are again very similar, and yielded excellent fits to a biexponential decay model. As summarised in Table 3.5, the evaluated decay lifetimes for both the S_1 and T_1 excited states of these complexes are shorter than those for the corresponding Gd^{3+} complexes, indicating efficient ISC and energy transfer to the corresponding $4f^*$ accepting states.

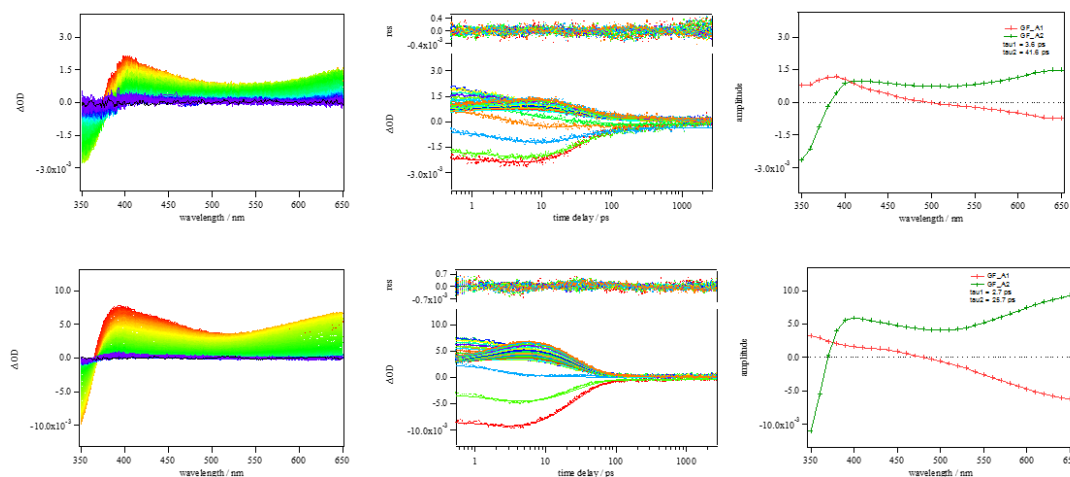


Figure 3.18 TA spectra (left) of Yb^{3+} complexes of *mtb* (top) and *tbm* (bottom), along with corresponding decay kinetic plots (middle) and Decay Associated Difference Spectra (right).

Using the Gd^{3+} complexes as model compounds, and assuming the other radiative and non-radiative decay pathways will be equivalent for the Ln^{3+} complexes, we are able to calculate the rate of electronic energy transfer from the excited T_1 state ($k_{\text{EET-T}_1}$) and hence the efficiencies for this triplet-mediated sensitisation pathway ($\Phi_{\text{EET-T}_1}$), which are summarised in Table 3.5. The calculated rate constants are on the order of $\sim 10^{10} \text{ s}^{-1}$, and reveal that both the *tbm* and *mtbm* ligands are efficient sensitisers, with $\Phi_{\text{EET-T}_1}$ values of $\geq 96\%$.

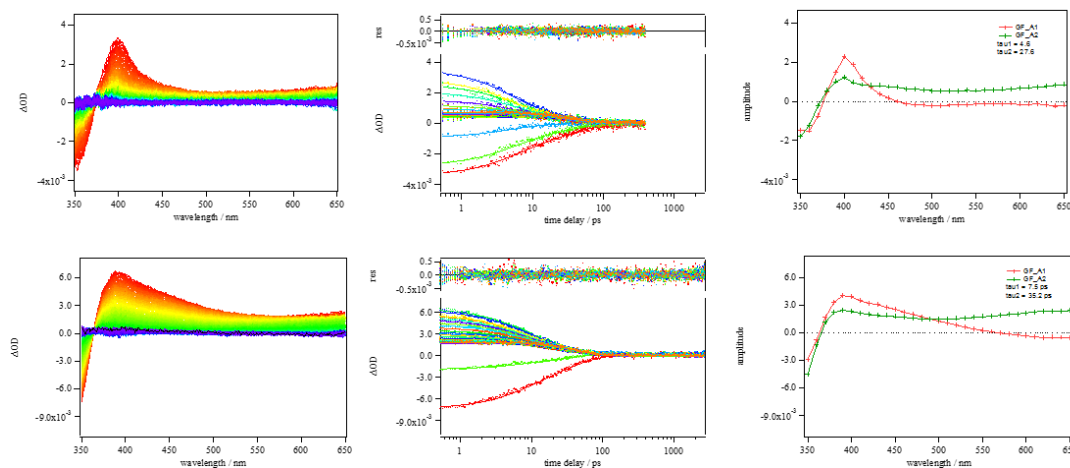


Figure 3.19 TA spectra (left) of Er^{3+} complexes of *mtbm* (top) and *tbm* (bottom), along with corresponding decay kinetic plots (middle) and Decay Associated Difference Spectra (right).

For the corresponding Eu^{3+} complexes, a close analysis of the TA spectra revealed a very interesting result. For both the *tbm* and *mtbm* ligands, while the initial ΔOD spectra obtained

at early time delays were similar to the other complexes, the broader spectral feature appearing at *ca* 650 nm due to $T_1 \rightarrow T_n$ excited state absorption was clearly absent, and in both cases the observed TA kinetics were more accurately represented by a monoexponential decay function of the form;

$$I(t) = A_1 \exp^{-t/\tau_1(t)} \quad (3.2)$$

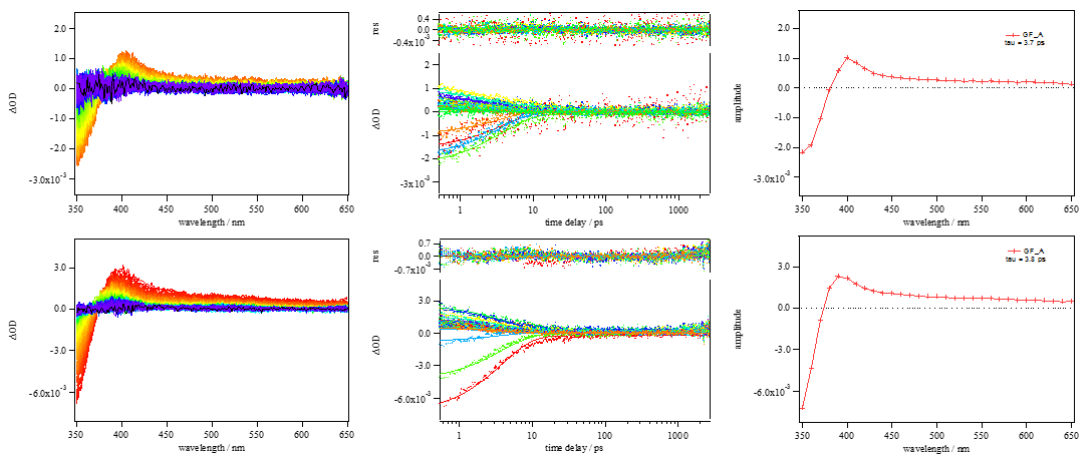


Figure 3.20 TA spectra (left) of Eu^{3+} complexes of *mtbm* (top) and *tbm* (bottom), along with corresponding decay kinetic plots (middle) and Decay Associated Difference Spectra (right).

The lack of an observed $T_1 \rightarrow T_n$ signal suggests that ISC to form the excited T_1 state may be less efficient for these complexes, and furthermore that either a singlet mediated energy transfer pathway and/or a competing ligand-to-metal charge transfer (LMCT) pathways, involving the formation of reduced Eu^{2+} , may play an important role in the sensitisation of Eu^{3+} observed using these ligands. This result is in line with recent reports that have highlighted the importance of the LMCT state in sensitized Eu^{3+} luminescence.^{2,6,46} However, it should also be recognized that the situation may differ in the isolated solid $\{[\text{Ln}(\text{Cs})(\text{tbm})_4]_2\}_n$ and $\{[\text{Ln}(\text{Cs})(\text{mtbm})_4]_2\}_n$ coordination polymers, since differences in the redox potential (and hence LMCT excited state energies) would be expected when comparing the tetranuclear assemblies in the solid state and the analogous simple model complexes in solution.

3.6 Conclusion

This work has focused on the synthesis of bimetallic assemblies composed of Ln^{3+} cations (Eu^{3+} , Er^{3+} , and Yb^{3+}), Cs^+ cations and triarylmethanide ligands. The ligands of choice were tribenzoylmethanide (**tbmH**) and tri(4-methylbenzoyl)methanide (**mtbmH**). In the case of Eu^{3+} and Er^{3+} , structural assemblies were obtained that are analogous to the previously reported study when Na^+ , K^+ , and Rb^+ were used as alkali element cations. However, in the present work these assemblies are the repeating units of one-dimensional polymers. These units are linked through the Cs^+ cations binding to the O atoms of the triketonate ligands. The only exception to this series was the structure obtained by combining Yb^{3+} , Cs^+ , and tri(4-methylbenzoyl)methanide. In this case, the repeating unit of the linear polymer was represented by mononuclear Yb^{3+} complexes bridged together *via* coordination of Cs^+ cations. The photophysical properties were investigated by means of absorption, emission and transient absorption spectroscopy. In particular, for Er^{3+} and Yb^{3+} , the transient absorption data reveal efficient and fast energy transfer from the triplet excited state of the ligand after ISC. On the other hand, the transient absorption data for Eu^{3+} seems to suggest an alternative energy transfer pathway, either occurring directly *via* the ligand singlet state or through the population of an intermediate LMCT state. The emission profiles, excited state lifetime and quantum yield data for the Eu^{3+} species confirms efficient sensitisation and relatively high quantum yields, with values in line with previously reported Eu^{3+} diketonate complexes. On the other hand, the NIR emission of Er^{3+} and Yb^{3+} highlights rather elongated excited state lifetimes with respect to analogous diketonate species, similar to those previously observed for assemblies of these elements, tribenzoylmethanide, and Na^+ , K^+ , or Rb^+ . The calculation of Yb^{3+} overall quantum yields indicates shorter values of radiative decays than 1.2 ms (the generally accepted value for Yb^{3+}). This result calls attention to limitations in the use of intrinsic quantum yields. Indeed, they must be looked at carefully or avoided when the calculation of radiative decays cannot be performed experimentally.

Chapter 4 Neodymium Assemblies; Antenna Effect and Lanthanoid-lanthanoid Sensitisation

Major aspects of the work presented in this chapter have been published:

L. Abad Galán, A. N. Sobolev, B. W. Skelton, E. Zysman-Colman, M. I. Ogden and M. Massi. *Dalton Trans.*, 2018, Accepted Manuscript.

4.1 Introduction

As shown in Chapter 3, β -triketonate based assemblies present improved photophysical properties for Yb^{3+} and Er^{3+} compared to similar β -diketonate complexes^{26,27}. In contrast, Nd^{3+} assemblies were not isolated and therefore, their luminescence properties remain unknown. Furthermore, as shown in Section 1.4.2, quantitative photophysical data for Nd^{3+} are scarce.

In this chapter, the first Nd^{3+} β -triketonate based complexes will be reported using both, **tbmH** and **mtbmH**, as the ligands. The synthesis and crystal structures of the resulting assemblies will be presented, showing analogous composition to the previously reported tetranuclear assemblies^{26,27} and Cs-polymers (see Chapter 3), respectively. The photophysical properties of the assemblies were studied via two different sensitisation pathways: energy transfer from the triplet state of the ligand, and from the $^5\text{D}_0$ of Eu^{3+} , giving to the best of our knowledge, the first example of a coordination polymer with effective lanthanoid-lanthanoid energy transfer to the $4f^*$ of Nd^{3+} .

4.2 Synthesis

The **tbmH** (**L1H**) and **mtbmH** (**L2H**) molecules were synthesised as described in Section 3.2.²⁶ Following a similar procedure to that previously employed for the preparation of $\{[\text{Ln}(\text{Cs})(\text{tbm})_4]_2\}$ ($\text{Ln}^{3+} = \text{Eu}^{3+}, \text{Er}^{3+}, \text{Yb}^{3+}$) and $\{[\text{Ln}(\text{Cs})(\text{mtbm})_4]_2\}_n$ ($\text{Ln}^{3+} = \text{Eu}^{3+}, \text{Er}^{3+}$) (see Section 3.2), one equivalent of hydrated LnCl_3 ($\text{Ln}^{3+} = \text{Eu}^{3+}, \text{Nd}^{3+}$) was reacted with four equivalents of **mtbmH** and four equivalents of RbOH in ethanol. Slow evaporation of the solvent resulted in the formation of suitable crystals for X-Ray diffraction revealing the formation of coordination polymers with formula $\{[\text{Ln}(\text{Rb})(\text{mtbm})_4]_2\}_n$ where $\text{Ln}^{3+} = \text{Eu}^{3+}$

(**C10**), Nd^{3+} (**C11**) (see Figure 4.1). The $\text{Eu}^{3+}/\text{Nd}^{3+}$ mixed assemblies were synthesised in a similar fashion to the $\{[\text{Ln}(\text{Rb})(\text{mtbm})_4]_2\}_n$ except for the use of mixtures of hydrated EuCl_3 and NdCl_3 in molar ratios of Nd^{3+} to Eu^{3+} of 0.25 (**C10a**), 0.50 (**C10b**), and 0.75 (**C10c**) (see Figure 4.1).

Analogous studies were attempted with CsOH and NdCl_3 in order to assess the effect of a different alkaline base in the mixed systems. However, only the caesium-containing coordination polymer $[\text{Cs}(\text{mtbm})]_n$ was isolated.²²⁴

When the same procedure was followed for the hydrated NdCl_3 and **tbmH** with RbOH or CsOH , the formation of assemblies with formula $[\text{Nd}(\text{Rb})(\text{tbm})_4]_2$ and $[\text{Nd}(\text{Cs}\cdot 2\text{HOEt})(\text{dbm})_4]_n$ were found, respectively (see Figure 4.1). The $[\text{Nd}(\text{Rb})(\text{tbm})_4]_2$ (**C12**) complex presents a similar structure to the previously reported tetranuclear assemblies.²⁷ In contrast, the isolation of the $[\text{Nd}(\text{Cs}\cdot 2\text{HOEt})(\text{dbm})_4]_n$ (**C13**) linear polymer shows the second example of a possible *in situ* retro-Claisen condensation reaction of **tbmH** in the presence of CsOH and hydrated NdCl_3 resulting in the formation of a β -diketonate complex similar to previously reported examples.²²⁴ The hypothesis that the triketonate ligands undergo a retro-Claisen condensation reaction under these reaction conditions will be considered in Chapter 5.

Finally, when the same procedure was attempted with YbCl_3 , a dimeric structure was crystallised with formula $[\text{Yb}(\text{mtbm})_3(\text{OH}_2)_2]_2$ (**C14**). Due to difference in composition and symmetry of this structure in comparison with the polymeric species of complexes **10** and **11**, Yb^{3+} was not investigated for the purpose of *f-f* sensitisation.

The compositions of the isolated species were further confirmed by elemental analysis and IR spectroscopy.

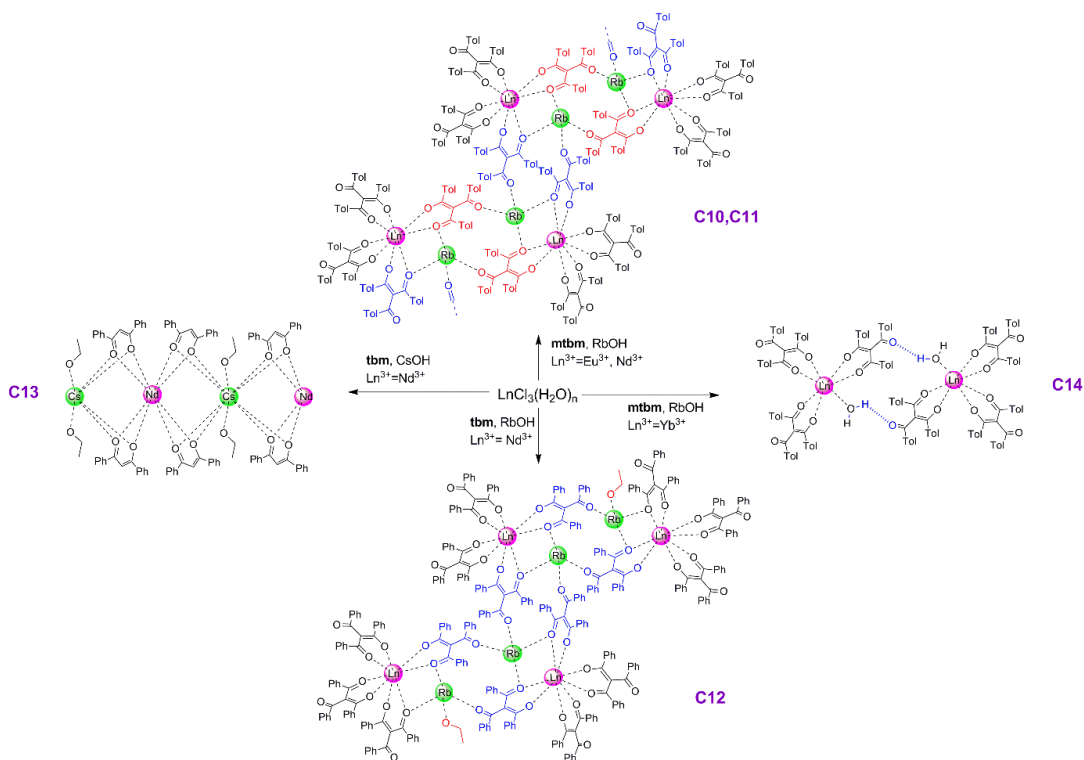


Figure 4.1 Summary of the isolated assemblies according to reaction conditions.

4.3 X-ray Diffraction

The structures of the two $\{[\text{Ln}(\text{Rb})(\text{mtbm})_4]_2\}_n$ for Eu^{3+} (**C10**) and Nd^{3+} (**C11**) complexes are isomorphous and structurally similar to the Cs-based polymers with formula $\{[\text{Ln}(\text{Cs})(\text{mtbm})_4]_2\}_n$ ($\text{Ln}^{3+}=\text{Eu}^{3+}, \text{Er}^{3+}$) (see Section 3.3). The units formed of two Ln^{3+} , two Rb^+ metal centres and eight **mtbm** ligands are analogous to the previously reported tetranuclear assemblies.²⁰⁹ The Ln^{3+} is eight coordinated, with four **mtbm** ligands coordinated by two of the O-keto atoms in a bidentate mode. In this case, the third O-keto of two of the ligands are linked to Rb^+ cations, forming the tetranuclear assembly and the polymer, respectively (see Figure 4.2).

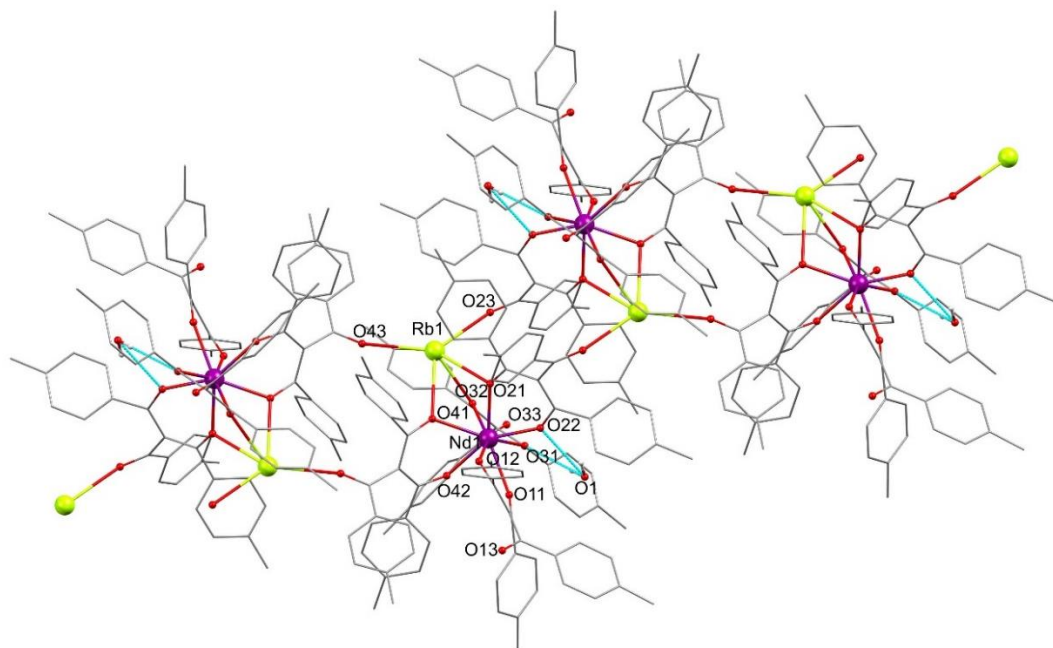


Figure 4.2 Representation of the X-Ray structure of $\{[Nd(Rb)(\mathbf{mtbm})_4]_2\}_n$, where hydrogens have been omitted for clarity except for the solvent H_2O molecule.

Here, a H_2O molecule is found in the lattice with two hydrogen bonds formed with two keto O(22) and O(31). Intermolecular interactions between chains are present between two methyl groups (C327-C327) and the free keto oxygen lone pair and a phenyl ring (O13-C325 and O33-C132) with distances shorter than 3.3\AA in every case. Although these kinds of forces are not commonly seen, previous examples have been suggested in literature.^{234,235} These interactions bring two lanthanoid centres between chains relatively close, with distances of 15.314\AA and 14.938\AA for Nd^{3+} and Eu^{3+} , respectively (see Figure 4.3 and Table 4.2)

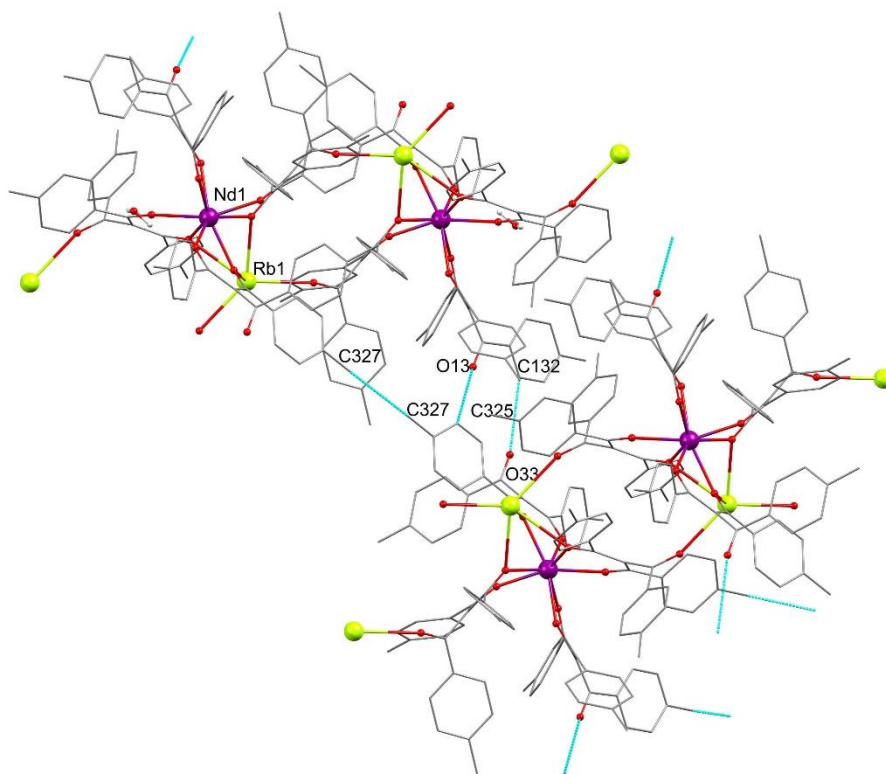


Figure 4.3 Representation of the X-ray crystal structure of $[\{Nd(Rb)(\mathbf{mtbm})_4\}_n]$ where intermolecular interactions have been highlighted and the hydrogen atoms are omitted for clarity.

The structure of the $[Nd(Rb \cdot HOEt)(\mathbf{tbm})_4]_2$ (**C12**) is isomorphous to the previously published tetranuclear assemblies (see Figure 4.4) where the units are formed by two Nd^{3+} ions, two Rb^+ and eight **tbm** molecules coordinated in a bidentate mode.

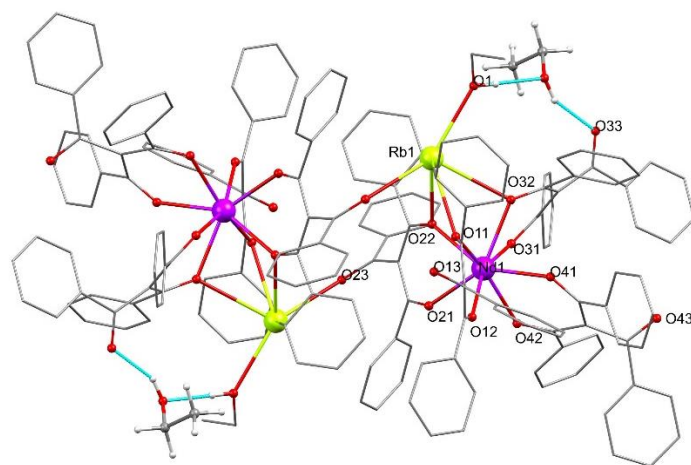


Figure 4.4 Representation of the X-Ray structure of $[Nd(Rb)(\mathbf{tbm})_4]_2$, where hydrogens have been omitted for clarity except for the solvent EtOH molecule.

Table 4.1 Selected bond lengths (Å) and intermetallic distances for complexes C10-C12

	C10 {[Eu(Rb)(mtbm) ₄] ₂] _n	C11 [Nd(Rb)(mtbm) ₄] ₂] _n	C12 [Nd(Rb·HOEt)(tbn) ₄] ₂
Ln-O	2.404(3)-2.327(2)	2.444(2)-2.362(2)	2.450(2)-2.390(2)
Ae-O	2.983(2)-2.816(2)	2.989(2)-2.817(2)	3.051(2)-2.822(2)
Ae(1)-Ae(2)	8.1196(5)	8.1312(5)	8.3053(6)
Ae(1)-Ae(2')	8.7992(5)	8.8013(5)	-
Ln(1)-Ln(2)	9.4915(5)	9.5391(5)	8.9836(5)
Ln(1)-Ln(2')	11.0901(6)	11.0929(5)	13.8915(6)
Ln(1)-Ae(1)	4.0944(4)	4.1044(4)	4.1342(4)
Ln(1)-Ae(2)	8.145(5)	8.8169(5)	7.5993(6)
Ae(2)-Ln(1')	8.8149(5)	8.2087(5)	-
Ln(1)-Ln(1*)	14.9383(7)	14.9907(5)	14.0539(5)

*'subsequent units and * different chain*

The [Nd(Cs·2HOEt)(**dbm**)₄]_n (**C13**) complex crystallises as a linear polymer where Nd(**dbm**)₄⁻ units are linked by Cs⁺ cations analogously to the previously reported [{Nd(Cs)(**dbm**)₄]_n,²⁷ with the difference of two molecules of EtOH directly coordinated to the Cs⁺ cation (see Figure 4.5).

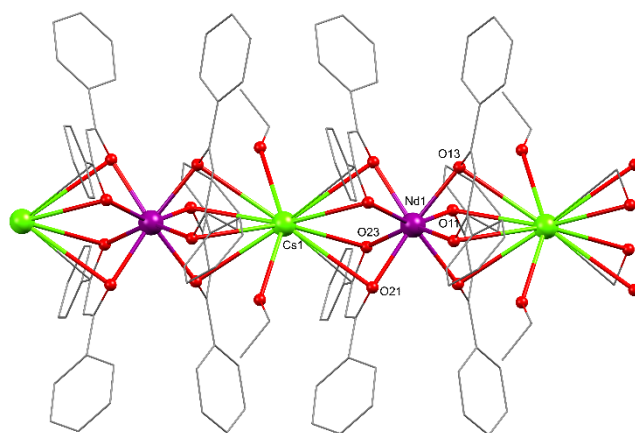


Figure 4.5 Representation of the X-ray crystal structure of [Nd(Cs·2HOEt)(**dbm**)₄]_n where the hydrogen atoms are omitted for clarity.

The $[\text{Yb}(\text{mtbm})_3(\text{OH}_2)_2]_2$ (**C14**) complex crystallises as a dimer formed by a hydrogen bond between the water coordinated to one Yb^{3+} centre and the uncoordinated oxygen atom O(13), with a distance of 1.84(2) Å (see Figure 4.6).

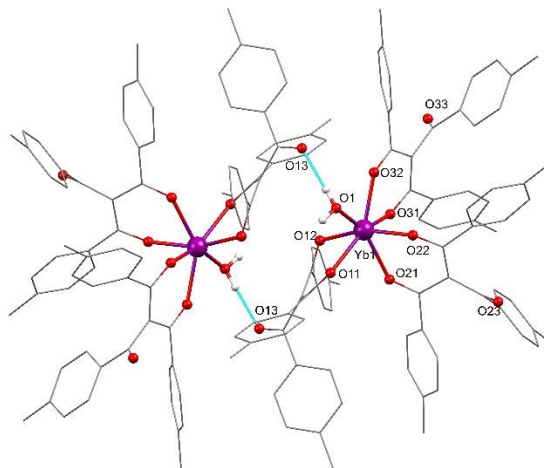


Figure 4.6 Representation of the X-ray crystal structure of $[\text{Yb}(\text{mtbm})_3(\text{OH}_2)_2]_2$ where the hydrogen atoms are omitted for clarity with the exception of the molecule of water.

Finally the $[\text{Cs}(\text{mtbm})]_n$ structure can be defined as a one-dimensional polymer parallel to the a-axis. Each Cs^+ atom is bound to four carbonyl oxygen atoms and one phenyl ring from three different molecules (see Figure 4.7). Each **mtbm** molecule acts as a bridge between to different Cs^+ atoms with a bidentate coordination through two of the carbonyl oxygen atoms or one oxygen and one phenyl ring.

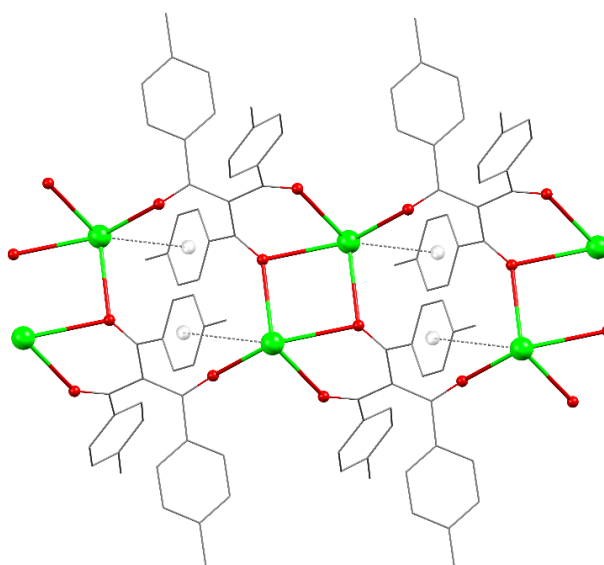


Figure 4.7 Representation of the X-ray crystal structure of $[\text{Cs}(\text{mtbm})]_n$ where the hydrogen atoms are omitted for clarity.

4.3.1 Shape Analysis

The shape analysis has been carried out considering the degree of distortion with respect to square antiprism and triangular dodecahedron for the eight coordinated complexes **C10-C13** (see Figure 4.8)

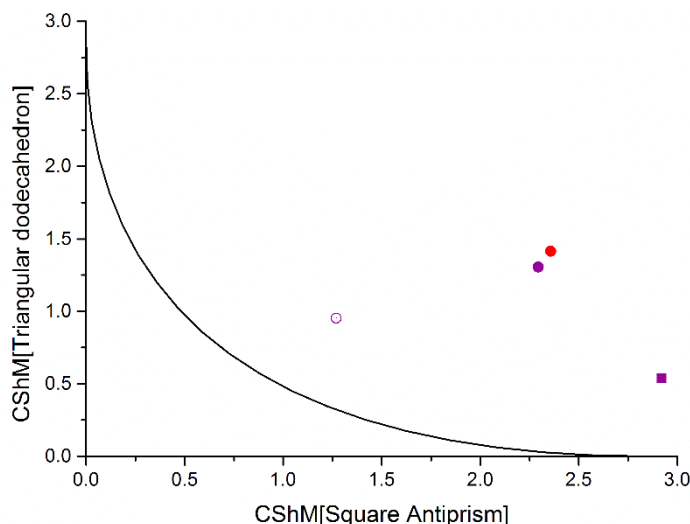


Figure 4.8 Shape Map representing the CshM values of the $\{[Ln(Rb)(\mathbf{tbm})_4]_2\}_n$ (dots), $[Nd(Rb)(\mathbf{tbm})_4]_2$ (square) and $[Nd(Cs\cdot 2HOEt)(\mathbf{dbm})_4]_n$ (circle) complexes for Eu^{3+} (red) and Nd^{3+} (purple).

Complexes **C10** and **C11** have a really similar geometry being best describes as distorted triangular dodecahedron. Complex **C12** is also best described as triangular dodecahedron however, the degree of distortion is remarkably smaller in a similar manner to the previously reported analogous Rb^+ assemblies.²⁷

Table 4.2 CShM values for complexes **C10-C13** for $Ln^{3+} = Eu^{3+}$ and Nd^{3+} .

Complex	TTD-8	SAPR-8
$\{[Eu(Rb)(\mathbf{mtbm})_4]_2\}_n$	1.415	2.357
$\{[Nd(Rb)(\mathbf{mtbm})_4]_2\}_n$	1.306	2.295
$[Nd(Rb)(\mathbf{tbm})_4]_2$	0.539	2.921
$[Nd(Cs\cdot 2HOEt)(\mathbf{dbm})_4]_n$	0.951	1.269

The shape analysis was also performed for the seven coordinate complex **C13**, according to 7 ideal seven-coordinated polyhedral, being best defined as a highly distorted pentagonal bipyramid with CShM value of 2.52 (see Figure 4.9). The CShM values for the other geometries were higher than 4.8. Therefore, shape maps were not illustrative in this case.

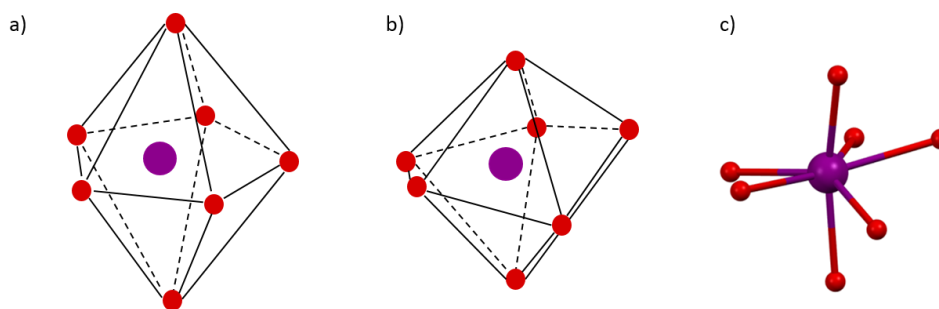


Figure 4.9 Representation of ideal pentagonal bipyramid (a), coordination polyhedron of Yb^{3+} (b) for the first coordination sphere of from $[\text{Yb}(\text{mtbm})_3(\text{OH}_2)_2]_2$ (c).

4.4 Photophysical Properties

The photophysical data for complexes **C10-12** and mixed lanthanoid complexes **C10a-c**, including excited state lifetime decay (τ_{obs}), calculated radiative decay (τ_{r}), intrinsic photoluminescence quantum yield ($\Phi_{\text{Ln}}^{\text{Ln}}$), overall photoluminescence quantum yield ($\Phi_{\text{Ln}}^{\text{L}}$), and calculated sensitisation efficiency (η_{sens}), are reported in Table 4.3

The emission properties were recorded in the solid state due to the low stability of the complexes in polar solvents and poor solubility in nonpolar solvents as previously reported.²⁰⁹

Table 4.3 Photophysical data for the complexes **C10-C12** in the solid state

Complex	λ_{em} (nm)	τ_{obs} (μs)	τ_{r} (ms)	$\Phi_{\text{Ln}}^{\text{Ln}}$ (%)	$\Phi_{\text{Ln}}^{\text{L}^a}$ (%)	Φ_{Sens} (%)	k_{ET} (s^{-1})	τ_{ET} (s)	Φ_{ET} (%)
C10	612	507	0.86	59	31	52	-	-	-
C11	1060	11	0.27 ^b	4.2	1.34	32	-	-	-
C10_a	612	335	0.681	49	17.5	35	$1.0 \cdot 10^3$	$9.87 \cdot 10^{-4}$	34
	1060	8.7	0.27 ^b	3.1	0.23	7			
C10_b	612	183	0.46	40	6.55	16	$3.5 \cdot 10^3$	$2.86 \cdot 10^{-4}$	64
	1060	11.0	0.27 ^b	4.1	0.74	18			
C10_c	612	143	0.54	27	1.44	5	$5.0 \cdot 10^3$	$1.99 \cdot 10^{-4}$	72
	1060	8.7	0.27 ^b	3.2	0.44	14			
C12	1060	8.8	0.27 ^b	3.3	0.58	17	-	-	-

^a quantum yield measured with the use of an integrating sphere ^b literature value for Nd^{3+} .¹⁸⁴

As shown before, the energy of the **mtbm** and **tbm** triplet states ($21,140 \text{ cm}^{-1}$ and $20,704 \text{ cm}^{-1}$)^{209,224} are sufficiently high in order to sensitise the $^5\text{D}_0$ ($\sim 17,200 \text{ cm}^{-1}$) of Eu^{3+} , the $^2\text{F}_{5/2}$

($\sim 10,200\text{ cm}^{-1}$) of Yb^{3+} and the ${}^4\text{I}_{13/2}$ ($\sim 6,566\text{ cm}^{-1}$) of Er^{3+} . Therefore, energy transfer to the ${}^4\text{F}_{3/2}$ ($\sim 11,260\text{ cm}^{-1}$) state of Nd^{3+} is also expected. In fact, each emission spectrum shown herein is the result of an effective antenna effect supported by the broad excitation spectra which matches with the absorption profile of the corresponding ligands.

4.4.1 Europium Assemblies

The emission spectrum of $\{[\text{Eu}(\text{Rb})(\text{mtbm})_4]_2\}_n$ (**C10**) shows the characteristic Eu^{3+} emission bands attributed to the ${}^7\text{F}_J \leftarrow {}^5\text{D}_0$ ($J=0-4$) region 580-820 nm (see Figure 4.10). The ${}^7\text{F}_0 \leftarrow {}^5\text{D}_0$ transition is strictly forbidden by the selection rules and is only observable for low symmetry complexes. The lack of this band in our system suggests a higher symmetry than C_{nv} , C_n or C_s . The magnetic dipole-allowed band (${}^7\text{F}_1 \leftarrow {}^5\text{D}_0$) is split into two sublevels inherent to tetragonal crystal fields. This is in agreement with the splitting of the hypersensitive band (${}^7\text{F}_2 \leftarrow {}^5\text{D}_0$) in four sublevels. The splitting of the main transitions is in accordance with the shape analysis which suggests that the local symmetry of the Eu^{3+} cation is best described as a distorted triangular dodecahedron.

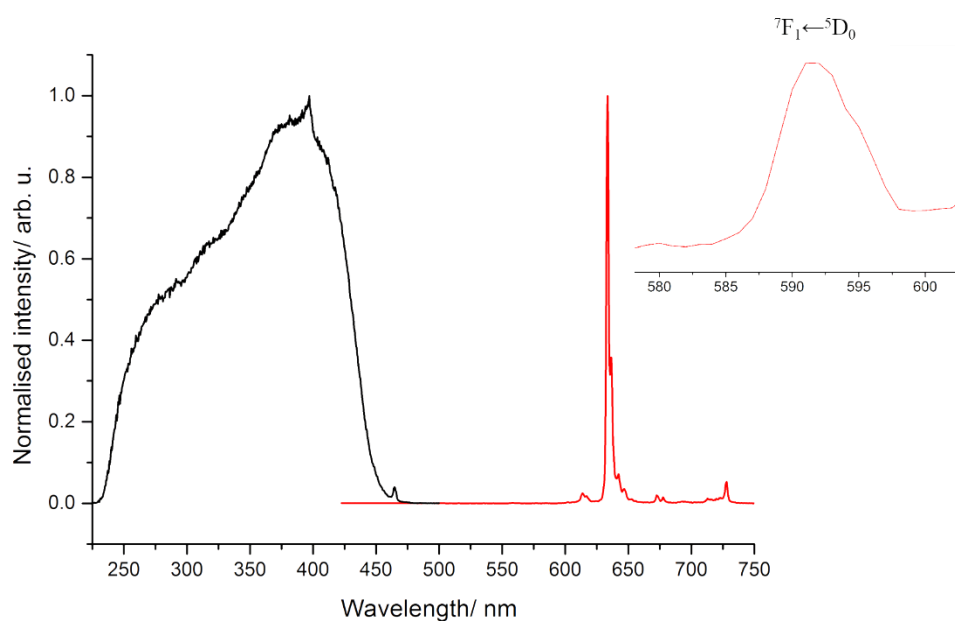


Figure 4.10 Normalised excitation (black) and emission ($\lambda_{exc}=350\text{ nm}$) (red) of $\{[\text{Eu}(\text{Rb})(\text{mtbm})_4]_2\}_n$ in the solid state. Inset: highlight of the peaks corresponding to the ${}^7\text{F}_1 \leftarrow {}^5\text{D}_0$ transition.

4.4.2 Neodymium Assemblies

The emission spectrum of $\{[\text{Nd}(\text{Rb})(\text{mtbm})_4]_2\}_n$ (**C11**) shows the characteristic Nd^{3+} emission bands from the ${}^4\text{I}_J \leftarrow {}^4\text{F}_{3/2}$ ($J = 9/2, 11/2, 13/2$) with maxima at 910, 1060 and 1350 nm, respectively (see Figure 4.11). These bands are structured as a consequence of the crystal field effect from the ligands. The excited state decay was measured to be 11 μs after deconvolution from instrumental response. This value of τ_{obs} is relatively high in comparison to the previously reported β -diketonate compounds^{21,28} and of the same order of magnitude as highly conjugated systems.^{51,173}

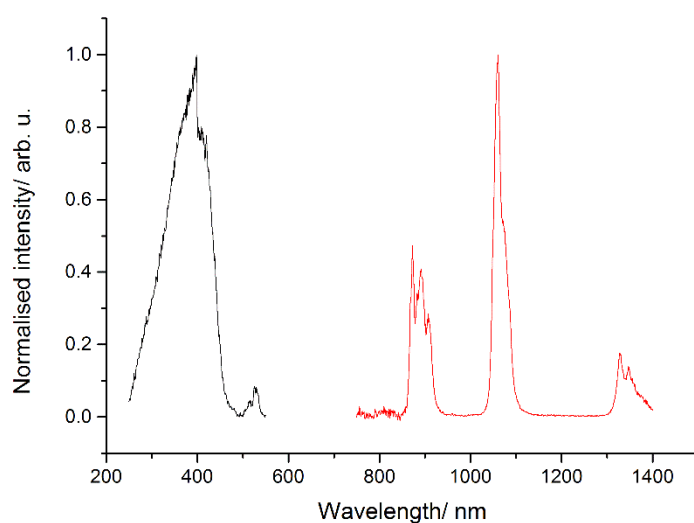


Figure 4.11 Normalised excitation (black) and emission ($\lambda_{\text{exc}} = 350 \text{ nm}$) (red) of $\{[\text{Nd}(\text{Rb})(\text{mtbm})_4]_2\}_n$ in the solid state.

Although it is known that the radiative decay for Nd^{3+} ranges from 0.2 to 0.5 ms,⁶ a standard value¹⁸⁴ of 0.27 ms is generally accepted for the Nd^{3+} complexes in the solid state. The intrinsic quantum yield can therefore be estimated to 4.2%. The overall quantum yield, following the modified integrating sphere method previously explained in Section 2.4.2, was found to be 1.34%, which implies a sensitisation efficiency of 32%. This value of the quantum yield is, to the best of our knowledge, the highest found for Nd^{3+} β -diketonate based complexes, followed by $[\text{Nd}(\text{hfpvr})_3(\text{bath})]$ (see Figure 1.9), with an overall quantum yield of 1.07% in the solid (see Section 1.4.2).¹⁸⁴ These data suggest that reducing non-radiative decay pathways due to the removal of the C-H bond is an effective way to enhance the photophysical properties of the Nd^{3+} emitters, similarly to Yb^{3+} and Er^{3+} (see Section 3.4).

The emission spectrum of $[\text{Nd}(\text{Rb}\cdot\text{HOEt})(\mathbf{tbm})_4]_2$ (**C12**) shows the three characteristic Nd^{3+} bands from the ${}^4\text{I}_J \leftarrow {}^4\text{F}_{3/2}$ ($J = 9/2, 11/2, 13/2$) similarly to complex $[\text{Nd}(\text{Rb}\cdot\text{HOEt})(\mathbf{tbm})_4]_2$ (**C11**) (see Figure 4.12). The values of lifetime (τ_{obs}), intrinsic quantum yield (Φ^{Ln}) and overall quantum yield (Φ^{Ln}) were found to be 8.85 μs , 3.3% and 0.58%, respectively. The main difference with complex **C11** arises from a lower overall quantum yield, maintaining the values of lifetime and intrinsic quantum yields, which suggests that the sensitisation process from **tbm** to the $4f^*$ accepting states of Nd^{3+} is not as efficient as in the **mtbm** based complexes.

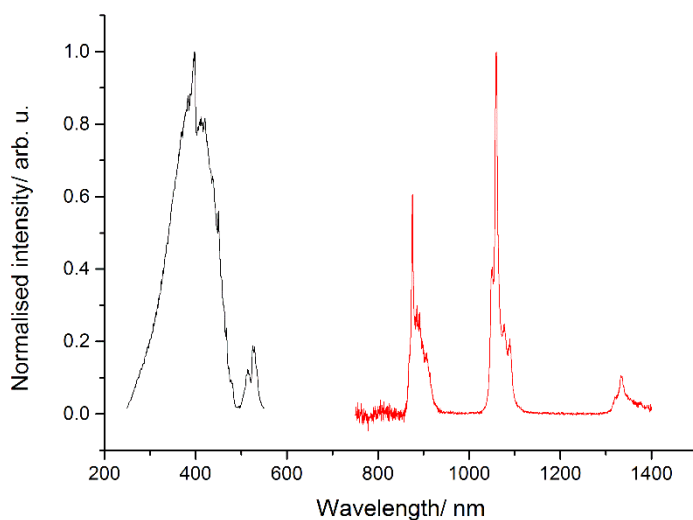


Figure 4.12 Normalised excitation (black) and emission ($\lambda_{\text{exc}}=350$ nm) (red) of $[\text{Nd}(\text{Rb})(\mathbf{tbm})_4]_2$ in the solid state.

4.4.3 Mixed Lanthanoid Assemblies

As the structures for Eu^{3+} and Nd^{3+} are isomorphous, $\{[\text{Ln}(\text{Rb})(\mathbf{mtbm})_4]_2\}_n$ mixtures of both lanthanoids were prepared (**C10a**, **C10b**, **C10c**) in order to assess sensitisation of the ${}^4\text{F}_{3/2}$ of Nd^{3+} via the ${}^5\text{D}_0$ of Eu^{3+} as has been previously proposed (see Figure 4.13).^{237–239,240} Even though, the structure found for Yb^{3+} showed a difference composition, mixed Eu^{3+} and Yb^{3+} complexation reactions were attempted. Unfortunately, single crystals were not isolated and therefore, the photophysical studies were not investigated.

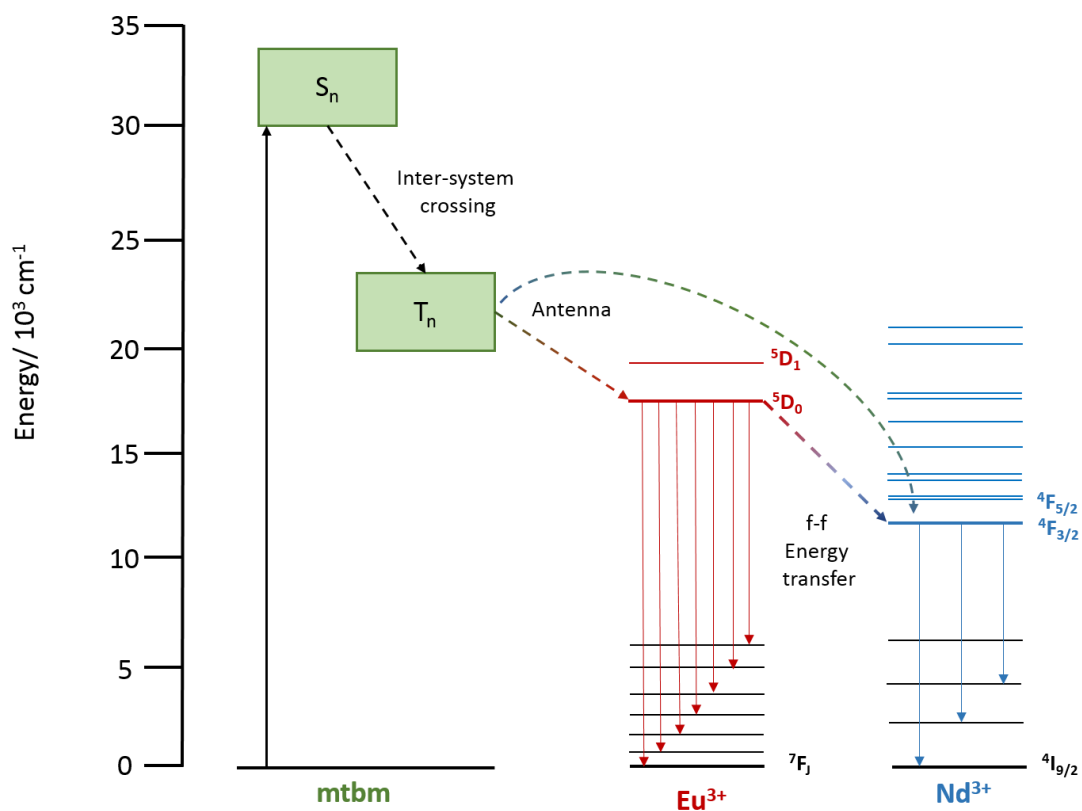


Figure 4.13 Simplified energy level diagram to show energy transfer occurring from the *mtbm* ligand to the lowest $4f^*$ state for the mixed complexes $\{[Eu_{1-x}Nd_x(Rb)(mtbm)_4]_2\}_n$.

The emission spectra of the mixed complexes show the characteristic emission bands from the ${}^7F_J \leftarrow {}^5D_0$ ($J=0-4$) of Eu^{3+} in the visible region (580-820 nm) and the ${}^4I_1 \leftarrow {}^4F_{3/2}$ ($J=9/2, 11/2, 13/2$) Nd^{3+} bands in the NIR region (850 -1400 nm) with identical splitting in comparison with the pure complexes **C10** and **C11**, respectively (see Figures 4.14 and Figure 4.15, respectively). This suggests that the structure is preserved with the mixed lanthanoid complexes.

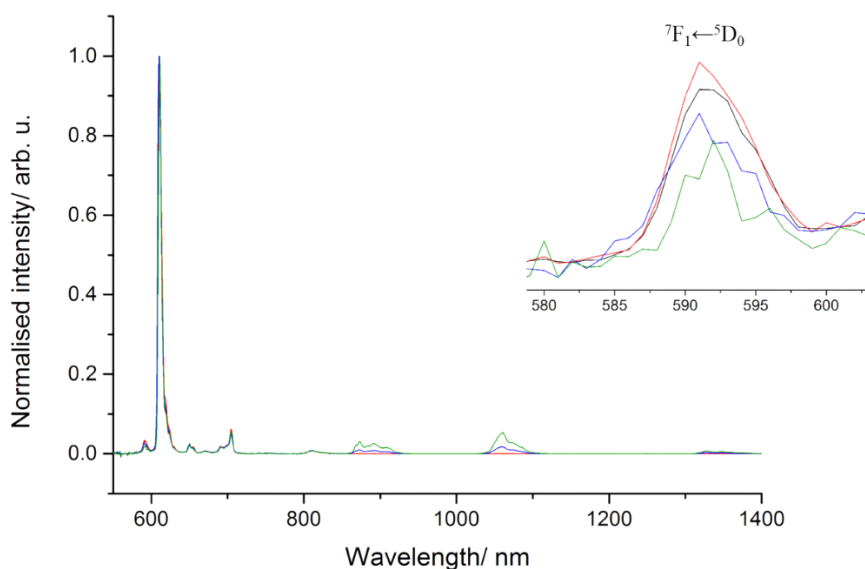


Figure 4.14 Whole emission spectra ($\lambda_{exc}=350$ nm) comparison for complexes **C10** (black trace), **C10a** (red trace), **C10b** (blue trace) and **C10c** (green trace) in the solid state.

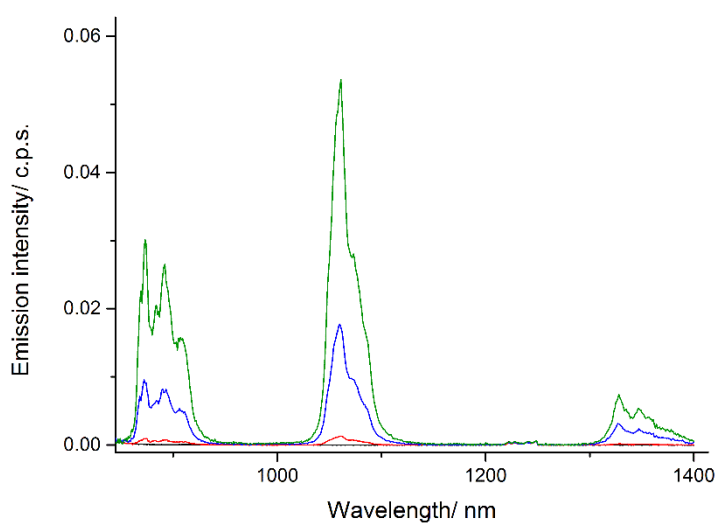


Figure 4.15 Emission spectra ($\lambda_{exc}=350$ nm) comparison for complexes **C10** (black trace), **C10a** (red trace), **C10b** (blue trace) and **C10c** (green trace) in the solid state.

The intensity of the Nd^{3+} emission bands increases when the molar ratio of Nd^{3+} is higher (see Figure 4.15). The lifetime of the excited state of Eu^{3+} is shortened as the amount of Nd^{3+} increases, from 507 μs for **10** to 335 μs , 183 μs and 143 μs for **C10a**, **C10b** and **C10c**, respectively (see Figure 4.17). From these numbers, the rate of energy transfer (k_{ET}) and

quantum efficiency of energy transfer (Φ_{ET}) can be calculated according to the following equations:

$$k_{\text{ET}} = \frac{1}{\tau_{\text{q}}} - \frac{1}{\tau_{\text{u}}} \quad (4.1)$$

$$\Phi_{\text{ET}} = 1 - \frac{\tau_{\text{q}}}{\tau_{\text{u}}} \quad (4.2)$$

where τ_{q} and τ_{u} are the $^5\text{D}_0$ decay lifetime of Eu^{3+} in the presence or absence of the quencher (Nd^{3+}), respectively. Therefore, the highest quantum efficiency can be calculated to be 72% for complex **10c**. Overall quantum yields were measured, and were found to decrease with values for Eu^{3+} of 17.5%, 6.55% and 1.44% for complexes **C10a**, **C10b** and **C10c**, respectively (see Table 4.3). In the case of Nd^{3+} , both lifetime and overall quantum yield values seem to be negatively altered by the presence of Eu^{3+} . These results indicate possible quenching of the $^4\text{F}_{3/2}$ of Nd^{3+} by the $^7\text{F}_J$ of Eu^{3+} as previously suggested in literature.²³⁸ However, the ratio of this energy transfer was calculated to be only 20% which is probably the main difference with previous Eu/Nd coordination compounds where no Nd^{3+} emission was observed.

Typically, energy transfer between lanthanoid centres is considered limited to distances longer than 9 Å due to slow energy migration.⁶² In fact, if a purely dipole-dipole exchange mechanism is considered, the donor-acceptor distance can be calculated to be 7.7 Å following equation 1.3 (see Section 1.3.3), for a quantum efficiency of energy transfer (Φ_{ET}) of 0.72 for complex **C11**. However, in our system, the shortest distance between two lanthanoid centres is 9.5 Å. Therefore, the sensitisation to *f states of Nd^{3+} from the $^5\text{D}_0$ of Eu^{3+} for complexes **C10a-c** may be ligand mediated.^{66,241}

For control experiments, equimolar mechanically-ground mixtures of **10** and **11** were studied, and similar emission spectra to the pure Eu^{3+} and Nd^{3+} complexes were obtained, respectively (see Figure 4.16). The lifetime of the $^5\text{D}_0$ of Eu^{3+} was found to be 356 μs (see Figure 4.17), shorter than the Eu^{3+} lifetime for complex **C10**, suggesting that there is energy transfer between chains that may occur via intermolecular interactions. In fact, molecular interaction between chains can be observed in the crystal structures (see Figure 4.3).

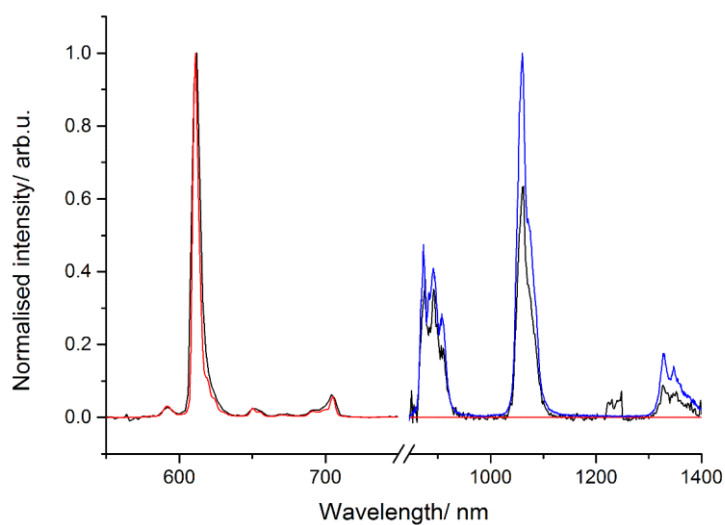


Figure 4.16 Emission spectra ($\lambda_{exc}=350\text{nm}$) comparison for complexes **C10** (red trace), **C11** (blue trace) and grounded mixture **C10 + C11** (black trace) in the solid state.

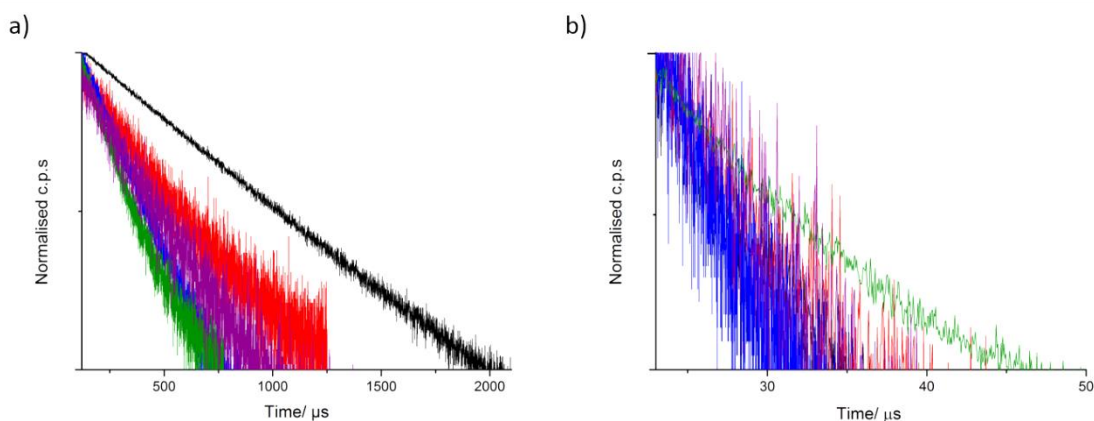


Figure 4.17 Lifetime decay at 612 nm ($\lambda_{exc}=350\text{ nm}$) (Eu^{3+}) (a) and 1060 nm ($\lambda_{exc}=350\text{ nm}$) (Nd^{3+}) (b) for complexes **C10** (black trace, a), **C11** (black trace, b), **C10a** (red trace), **C10b** (blue trace), **C10c** (green trace) and **C10 + C11** (purple trace) in the solid state at 298 K.

4.5 Conclusions

In this chapter, the study of β -triketonate-based lanthanoid complexes has been extended to Nd^{3+} , presenting new examples of tetranuclear assemblies ($[\text{Nd}(\text{Rb}\cdot\text{HOEt})(\text{t}\mathbf{b}\mathbf{m})_4]_2$) and coordination polymers with formula $\{[\text{Nd}(\text{Rb})(\text{mt}\mathbf{b}\mathbf{m})_4]_2\}_n$. The fact that isomorphous structures were found for the **mtbm** and Ln^{3+} ($\{[\text{Ln}(\text{Rb})(\text{mt}\mathbf{b}\mathbf{m})_4]_2\}_n \text{Ln}^{3+}=\text{Eu}^{3+}, \text{Nd}^{3+}$), opened up the possibility to synthesise mixed lanthanoid complexes with the aim of achieving f - f energy transfer. Indeed, an example of a mixed **mtbm** lanthanoid coordination polymer with

efficient sensitisation from the 5D_0 of Eu^{3+} to the $^4F_{3/2}$ of Nd^{3+} was formulated. The emission studies of the pure and mixed complexes show particularly good photophysical properties in the case of Nd^{3+} via both mechanisms; standard antenna and *f-f* sensitisation.

Chapter 5 Stability of β -Triketones in Solution

Major aspects of the work presented in this chapter have been published:

L. Abad Galán, A. N. Sobolev, E. Zysman-Colman, M. I. Ogden and M. Massi. *ChemRxiv*, Pre-print: <https://doi.org/10.26434/chemrxiv.6448253.v1>

5.1 Introduction

In previous chapters, two cases of a possible *in situ* retro-Claisen condensation reaction were found to occur for both **tbmH** and **mtbmH** molecules, suggesting low stability of the β -triketones in ethanolic solutions (see Chapter 4 and 3, respectively). In this chapter, four new β -triketone molecules with different substituents are presented in order to assess the effect on the retro-Claisen condensation reactivity: **dmtbmH** (tris(3,5-dimethylbenzoyl)methane), **ettbmH** (tris(4-ethylbenzoyl)methane), **butbmH** (tris(4-butylbenzoyl)methane) and **t-butbmH** (tris(4-*tert*-butylbenzoyl)methane). Assuming that the structures of the preferentially crystallised species are solubility-dependent, the modification of the substituents may have an impact on products isolated from the reaction mixture. With the aim to find new condensation products, changes in the synthetic conditions were attempted with the use of different solvents (methanol and ethanol) and different alkali salts (KOH, CsOH). Three new different families of complexes were found where one, two or three of the retro-Claisen condensation products coordinated to the lanthanoid cations. These results show how the lability of lanthanoids leads to the isolation of different complexes in the presence of a dynamically changing set of ligands. Additional solid-state photophysical studies were conducted to elucidate the effect of the composition and structure on their emission properties.

5.2 Synthesis

5.2.1 Ligands

The new **dmtbmH** (**L3H**), **ettbmH** (**L4H**), **butbmH**(**L5H**) and **t-butbmH**(**L6H**) molecules were synthesised following the procedure previously reported for **tbmH** and **mtbmH**, where the corresponding β -diketone was reacted with the required benzoyl chloride (see Figure 5.1).

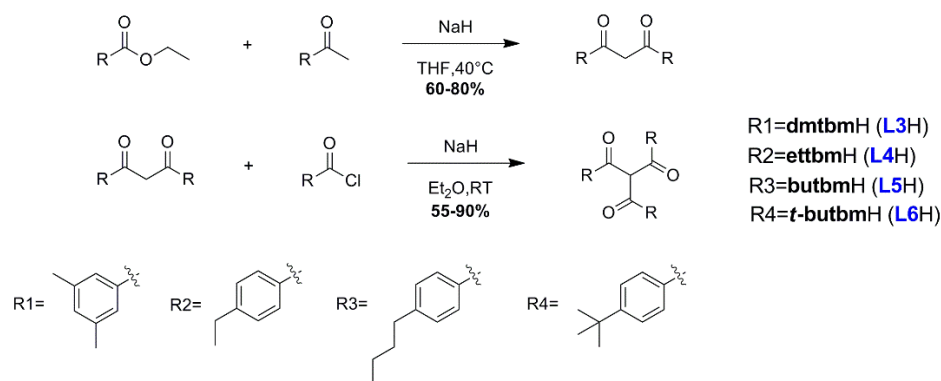


Figure 5.1 Synthetic scheme for the preparation of **L3H-L6H**.

The four new molecules were characterised by $^1\text{H-NMR}$ and $^{13}\text{C-NMR}$ spectroscopy, melting point and elemental analyses (see Experimental section). Melting points were found to be 194–196 °C, 210–212 °C, 260–262 °C and 267–269 °C for **L3H** to **L6H**, respectively, each being higher than the corresponding β -diketones. In every case, a peak in the IR spectrum at around 1700 cm^{-1} was observed, shifted from the precursors ($1500 - 1600\text{ cm}^{-1}$)²⁴², which is suggestive of the presence of a different carbonyl stretch. Finally, the $^1\text{H-NMR}$ and $^{13}\text{C-NMR}$ in CDCl_3 showed the presence of the keto tautomer for all the ligands except for the **dmtbmH** molecules where small traces of enol tautomer was also found at 7.70 ppm (see Figure 5.2).

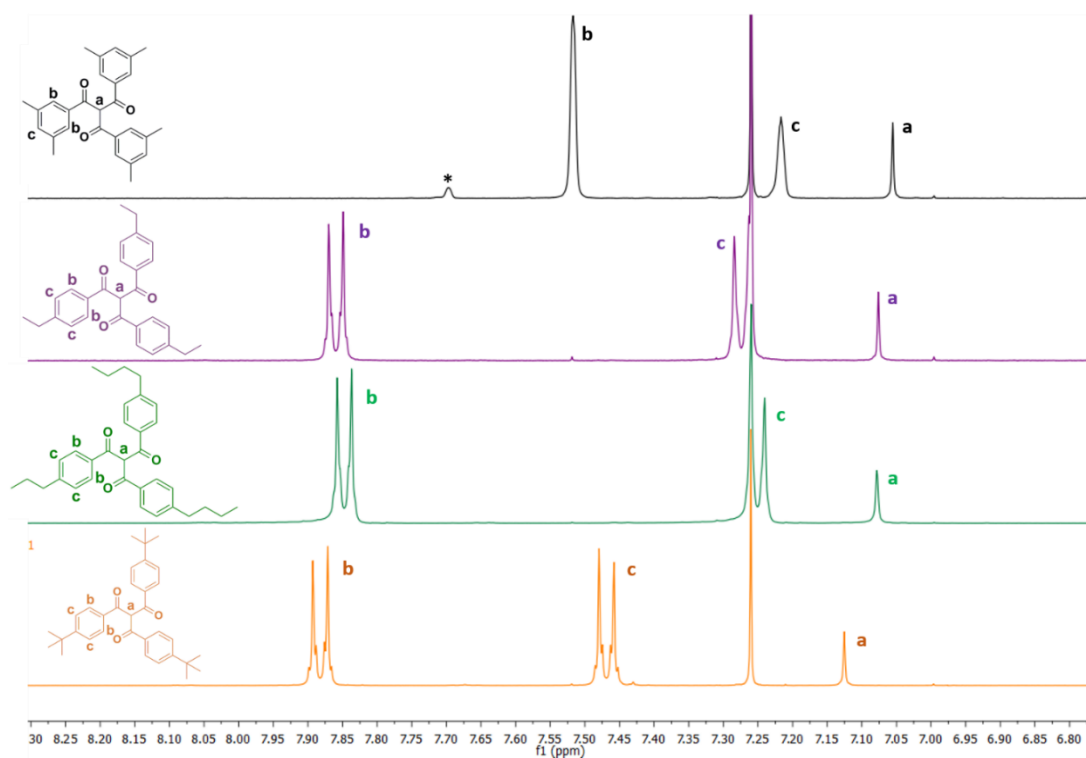


Figure 5.2 Portion of the $^1\text{H-NMR}$ spectrum of **dmtbmH** (black trace), **ettbmH** (purple trace), **butbmH** (green trace) and ***t*-butbmH** (orange trace), where * highlights the presence of the enolate.

5.2.2 Lanthanoid Assemblies

The **dmtbmH**, **ettbmH**, **butbmH** and *t*-**butbmH** molecules were synthesised following the procedure previously reported for **tbmH** and **mtbmH**.²⁶ The ligands **dmtbmH** (**L3H**), **ettbmH** (**L4H**), **butbmH** (**L5H**) and *t*-**butbmH** (**L6H**) were each made to react with hydrated LnCl₃ (Ln³⁺ = Eu³⁺, Tb³⁺, Yb³⁺) in the presence of AeOH (Ae⁺ = K⁺, Cs⁺) in polar solvents (ethanol or methanol). In each case, species containing products of the retro-Claisen condensation reaction of the triketonate molecules were isolated from these reactions. The isolated complexes were identified by X-ray diffraction along with IR spectroscopy. Elemental analysis confirmed the composition of the bulk samples, albeit with differing degrees of solvation, as has been reported for analogous structures.²⁷

The two β -triketone retro-Claisen condensation products are the associated β -diketonate and benzoate anions formed probably via alcoholysis (see Figure 5.3)²⁴³. However water could also be a potential nucleophile as previously noted.²⁴⁴ Consequently, three potential ligands can be present in the complexation mixture: β -triketones, β -diketonates and benzoates.

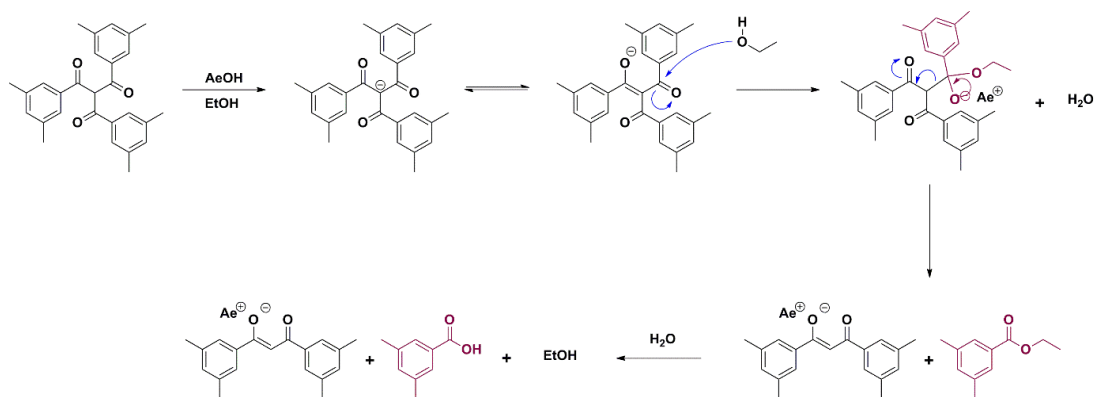


Figure 5.3 Possible mechanism for the retro-Claisen condensation through alcoholysis of the β -triketones.

In the case of **dmtbmH**, the isolated complexes can be classified in three distinct families depending on the number of different species directly coordinated to the lanthanoid centre (see Figure 5.4):

- Three species (3S): [Ln(μ -dmba)(**dmdbm**)(**dmtbm**)(HOEt)]₂, where Ln³⁺ = Eu³⁺ (**C15**), Tb³⁺ (**C16**)
- Two species (2S): [Yb(μ -dmba)(**dmdbm**)₂(HOMe)]₂ (**C17**)
- One species (1S): [Yb(μ -dmdbm)(**dmdbm**)₂]₂ (**C18**), [Ln(**dmdbm**)₄(Ae)]_n where Ln³⁺ = Eu³⁺, Yb³⁺, Ae⁺ = Cs, K (**C19**, **C20**)

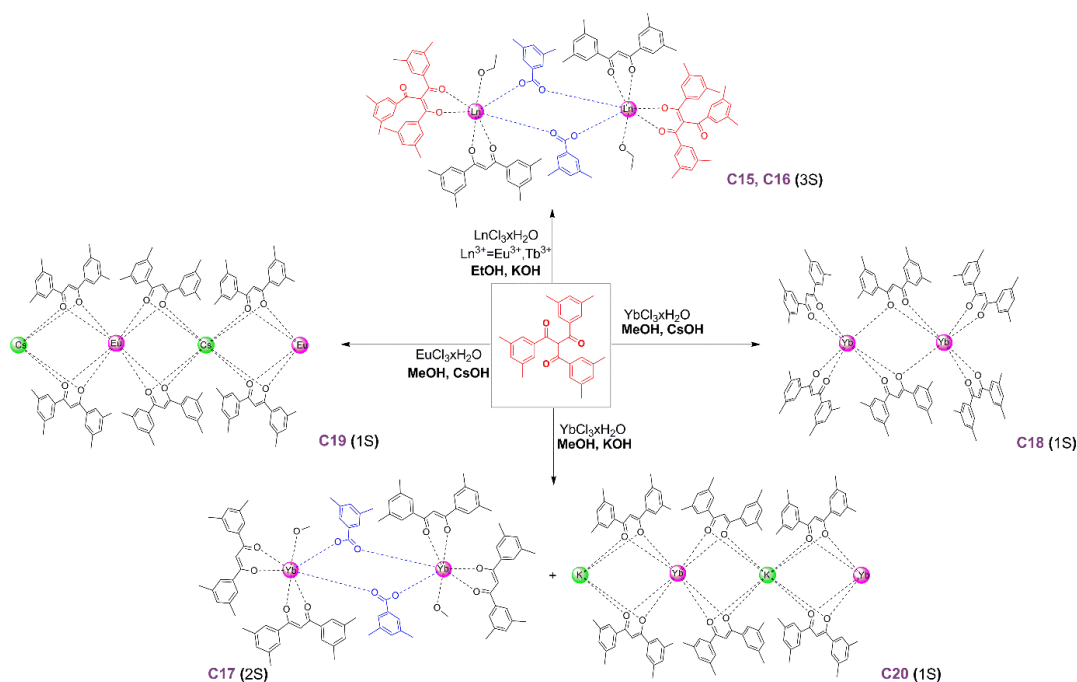


Figure 5.4 Summary of the isolated assemblies according to reaction conditions for the *dmtbmH* molecule.

Similar behaviour was found for the *ettbmH* ligand with the isolated complexes confirming retro-Claisen condensation reactivity; $[\text{Yb}(\text{etdbm})_3(\text{HOME})]$ (C21), $[\text{Yb}(\text{etdbm})_4(\text{Cs})]_n$ (C22). Furthermore, one structure was identified to contain only the unreacted β -triketonate ligand, $[\text{Eu}(\text{ettbm})_4(\text{Cs} \cdot \text{HOEt})_2]$ (C23), following the formula previously reported for the tetranuclear assemblies (see Figure 5.5).²⁷ This is the first example of a Cs-containing discrete tetranuclear assembly found during studies of the β -triketonates. Previous caesium-based complexes were polymeric with formula $\{[\text{Ln}(\text{L})_4(\text{Cs})]_2\}_n$, with $\text{L} = \text{tbm}$ and mtbm and $\text{Ln}^{3+} = \text{Eu}^{3+}, \text{Er}^{3+}$ and Yb^{3+} (see Section 3.3). Therefore, the isolation of the tetranuclear assembly for **L4** (*ettbm*) may suggest that steric hindrance caused by the elongation of the alkane chain prevents the formation of the polymeric structures.

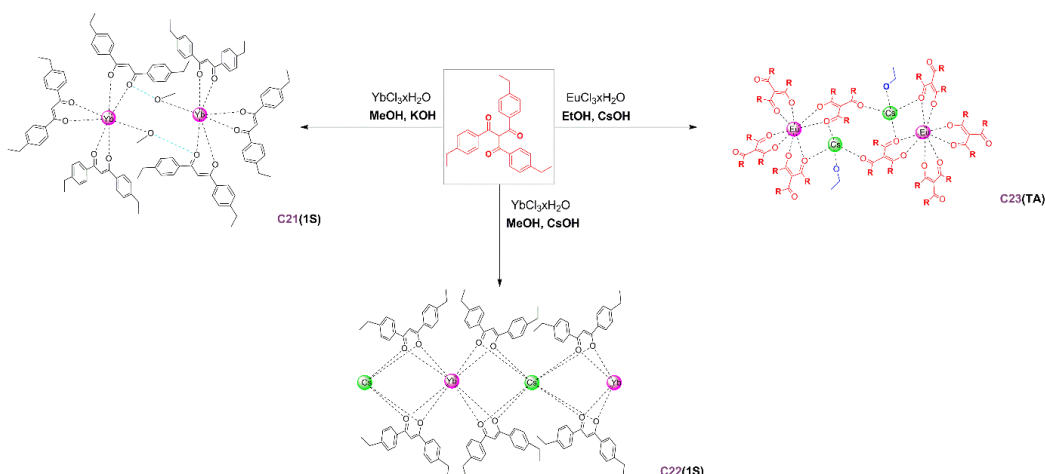


Figure 5.5.-Summary of the isolated assemblies according to reaction conditions for the *etbmH* molecule.

When analogous complexation reactions were carried out for the **butbmH** and *t*-**butbmH** molecules, only one crystalline material could be isolated (see Figure 5.6), $[\text{Eu}(\text{butbm})_4(\text{Cs})]_n$ (**C24**), suggesting higher solubility of the complexes formed in polar solvents such as ethanol and methanol. Therefore, less polar solvents were tested. Unfortunately, when one equivalent of $\text{Ln}(\text{NO}_3)_3 \cdot \text{DMSO}_n$ ($\text{Ln}^{3+} = \text{Eu}^{3+}, \text{Yb}^{3+}$) was reacted with four equivalents of the *t*-**butbmH** in the presence of four equivalents of potassium *tert*-butoxide in acetonitrile, only the *t*-**butbmH** molecule crystallised.

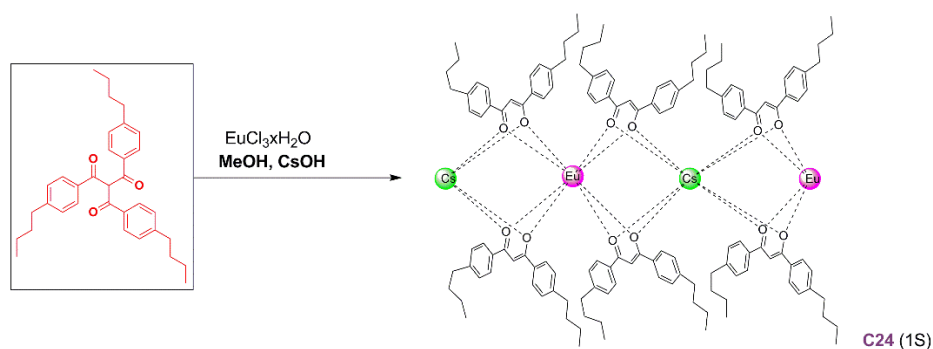


Figure 5.6 Summary of the isolated assemblies according to reaction conditions for the *butbmH* molecule.

According to these results, methanol seems to enhance the retro-Claisen condensation reactivity of the β -triketones as more structures containing these products were found in comparison to ethanol, where the majority of the cases include unreacted triketonates.

5.3 NMR Studies

The stability of the β -triketonate molecules, including **tbmH** and **mtbmH** previously presented, in basic methanolic conditions were studied by ^1H NMR. The different solutions, prepared in *d*-methanol by addition of the correspondent β -triketonate and 1 equivalent of KOH (10^{-2} M), were monitored by ^1H -NMR every 24 hours. In every case, mixtures of β -triketonates and β -diketonates, in both tautomeric forms, and their correspondent benzoates could be detected in solution over time, resulting in convoluted spectra.

When **tbmH** was dissolved under basic conditions in *d*-methanol, only the β -triketonate keto form at 7.62 (6H) ppm and \sim 7.25 (9H) ppm and traces of the enolate tautomer at 7.80 ppm and \sim 7.35 ppm were found (see Figure 5.7). However, after one day the same solution started presenting the β -diketonate enolate aromatic peaks at 8 ppm and \sim 7.5 ppm tautomer according to the literature.²⁴⁵ The peaks for the formed benzoate may lie below the signals of the other species.²⁴⁶

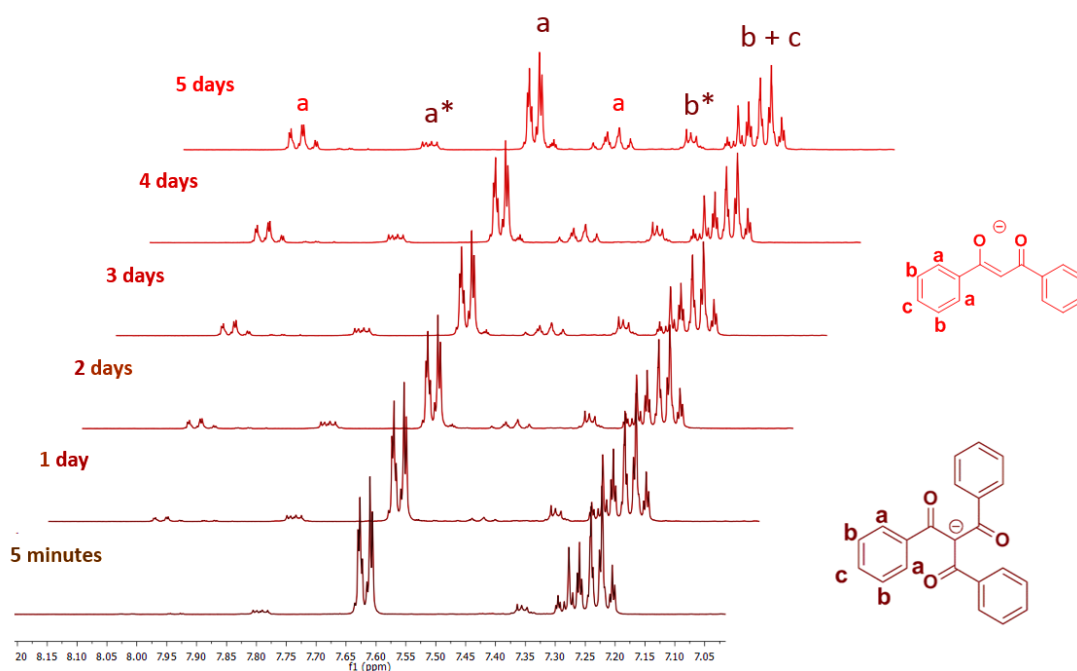


Figure 5.7 ^1H NMR of the **tbmH** molecule and one equivalent of KOH over 5 days in *d*-MeOH.

In the case of **mtbmH**, the β -triketonate in keto form was found at 7.52 (6H) ppm, 7.05 (9H) ppm and 2.28 (9H) ppm in fresh solution (see Figure 5.8). Small peaks of the β -diketonate enolate form were also observed at 7.82 (6H) ppm 7.22 (9H) and 2.37 (9H) that seem to slowly increase in intensity over the time.²²⁵ Moreover, after one day, new peaks at 7.91, 7.32 and 2.39 ppm were observed and assigned to the analogous benzoate.²⁴⁷

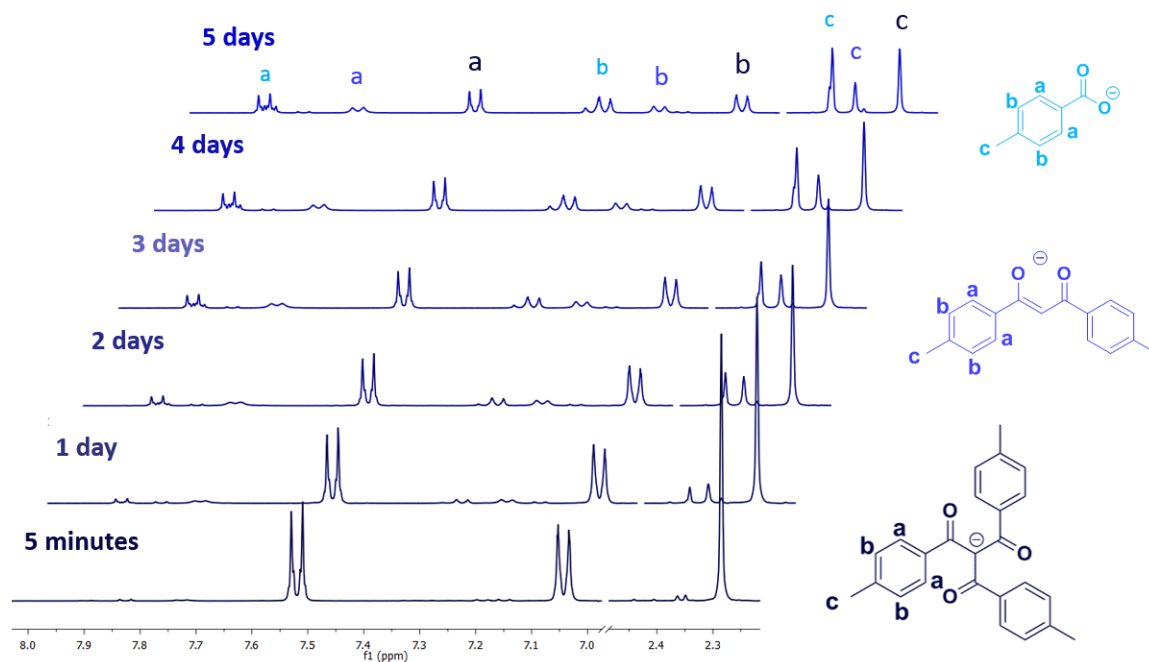


Figure 5.8 ^1H NMR of the **mtbmH** molecule and one equivalent of KOH over 5 days in *d*-MeOH.

The **dmtbmH** molecule presented a high percentage of β -diketonate in fresh solution. As can be seen in Figure 5.9, the resonance of the starting material were found at 7.1 (6H), 6.82 (3H) and 2.14 (18H) ppm, while the correspondent β -diketonate and the analogue benzoate were found shifted at higher ppm.^{248,249} Small traces of enolate and ketone tautomer for the triketonate and diketonate were also found, assigned in Figure 5.9 as * and # respectively. This molecule presents the highest percentage of β -diketonate in fresh solution, which is in accordance with the crystal structures where the **dmtbmH** ligand showed the maximum number of retro-Claisen species.

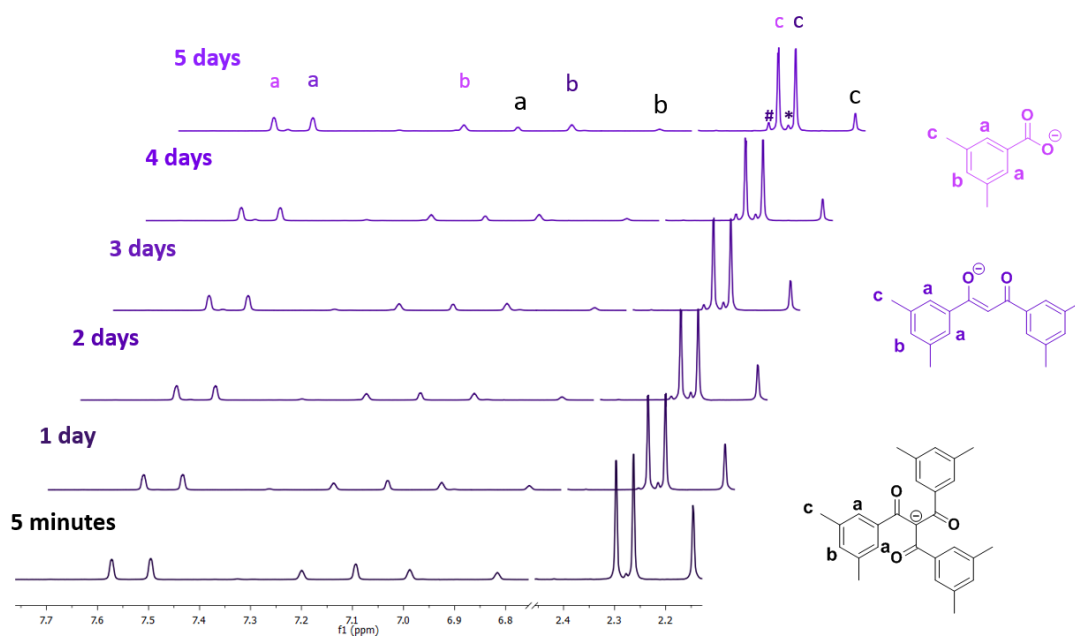


Figure 5.9 ^1H NMR of the **dmtbmH** molecule and one equivalent of KOH over 5 days in *d*-MeOH, where * and # highlight the enolate and ketone tautomers of **dmtbm** and **dmdbm**, respectively.

The **ettbmH** presented similar behaviour, where only β -triketonate was noted in the fresh solution, at 7.42 (6H) ppm, 6.97 (6H) ppm, 2.5 (6H) ppm and 1.08 (9H) ppm, but peaks consistent with both β -diketonate and benzoate were observed after one day (see Figure 5.10)^{225,250}

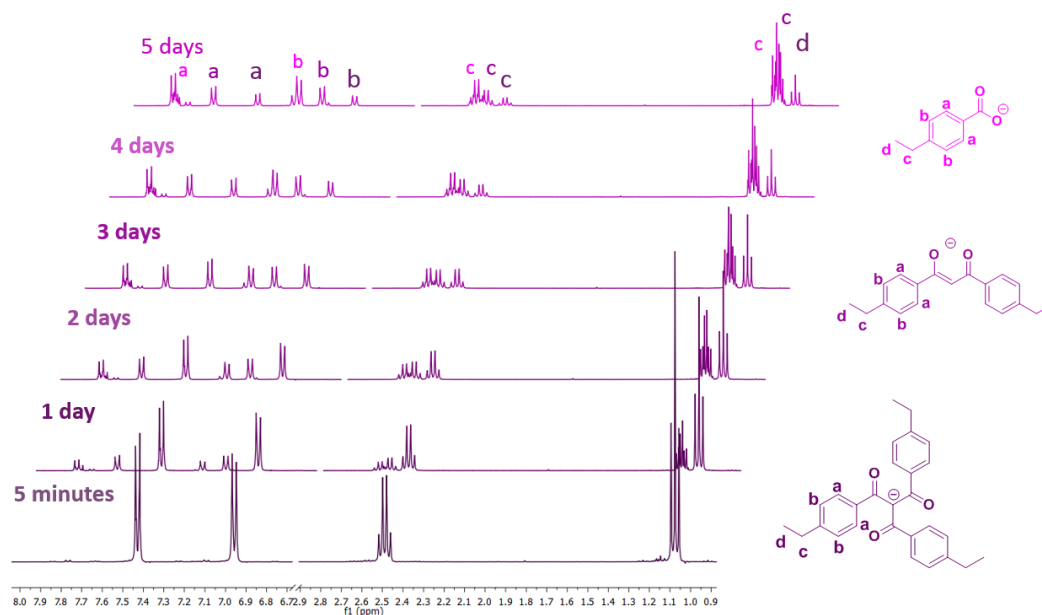


Figure 5.10 ^1H NMR of the **ettbmH** molecule and one equivalent of KOH over 5 days in *d*-MeOH.

Similar results were found in the case of the **butbmH** molecule, where only β -triketonate was seen at first at 7.48 (6H) ppm, 7.02 (6H) ppm, 2.58 (2H) ppm, 1.57 (2H) ppm, 1.30 (2H) ppm and 0.91 (2H) ppm while the β -diketonate and benzoate derivatives were present after 1 day (see Figure 5.11).^{225,250}

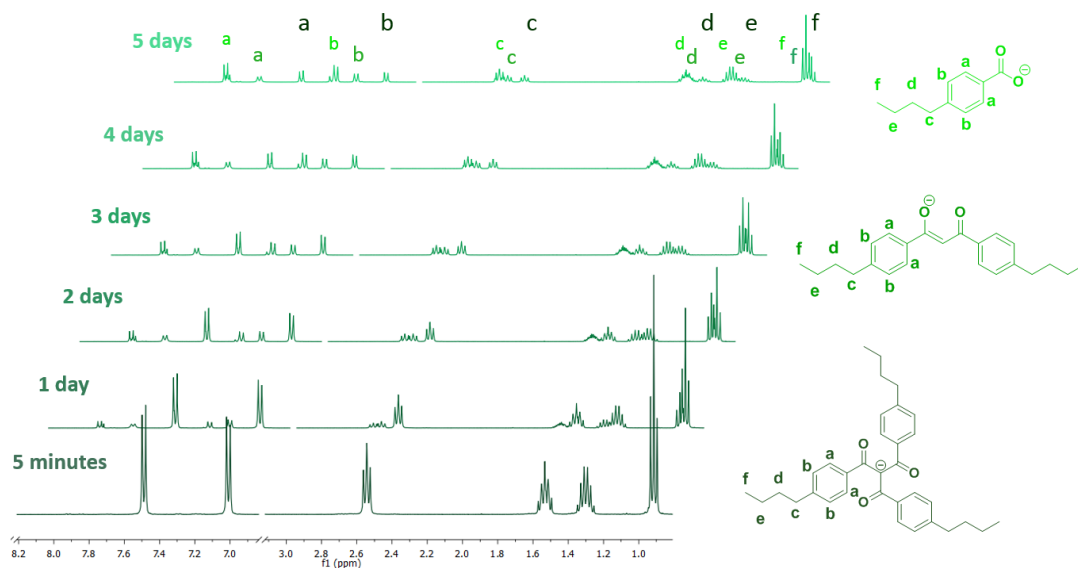


Figure 5.11 ^1H NMR of the **butbmH** molecule and one equivalent of KOH over 5 days in *d*-MeOH.

Finally, the **t-butbmH** molecule underwent the retro-Claisen condensation to a detectable extent within the first 5 minutes, such that traces of the β -diketonate and benzoate could be observed along with the β -triketonate at 7.53 (6H) ppm, 7.24 (6H) ppm and 1.25 (27H) ppm (see Figure 5.12).^{225,8}

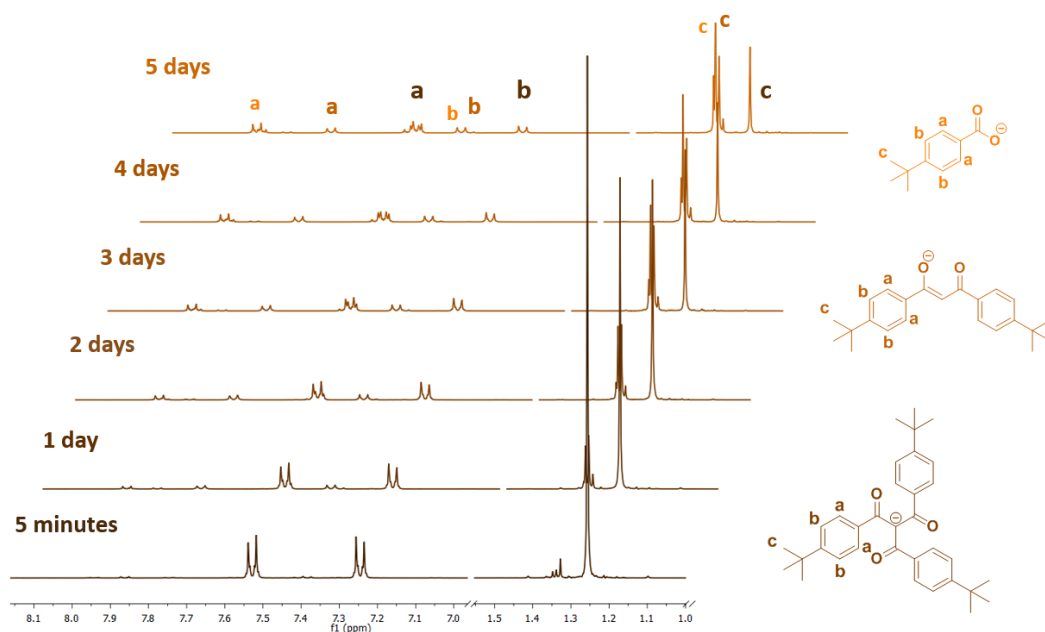


Figure 5.12 ^1H NMR of the *t*-butbmH molecule and one equivalent of KOH over 5 days in *d*-MeOH.

The ratio between the integration of the aromatic proton *a*, for the β -triketonate, and the constant integration of the solvent peak, was plotted against time to quantify the progression of the retro-Claisen condensation in these systems. High decomposition rates for all the molecules were noted, with almost 80% lost in the case of **ettbm** after 5 days (see Figure 5.13). The most stable β -triketonate is **tbm** with 30% lost after 5 days, which may explain why retro-Claisen condensation of this molecule was not observed in earlier work on the triketonates. Finally, these results show that **butbmH** and *t*-**butbmH** are impacted by the retro-Claisen condensation but to a lesser extent than **ettbmH**. Therefore, the fact that examples of complexes based on these ligands have yet to be isolated may be related to solubility of the resulting complexes rather than their initial formation.

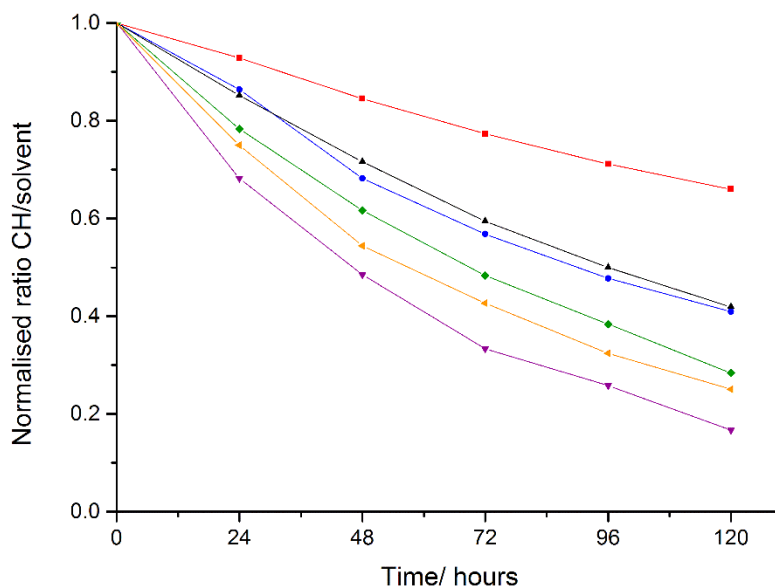


Figure 5.13 Retro-Claisen condensation ratio of the *tbm* (red trace), *mtbm* (blue trace), *dmtbm* (black trace), *ettbm* (purple trace), *butbm* (green trace), *t-butbm* (orange trace) molecules over the time.

As the least stable of the triketonates examined, **ettbmH** was then tested in d_6 -ethanol solution under similar conditions. In this case, it was found that the stability is significantly enhanced with only 2% of **ettbm** lost over the same time and therefore, negligible appearance of the retro-Claisen condensation products after 5 days (see Figure 5.14). These results are in agreement with the experimentally isolated structures from ethanol which all included unreacted β -triketonate either exclusively, or as part of the ligand mixture.

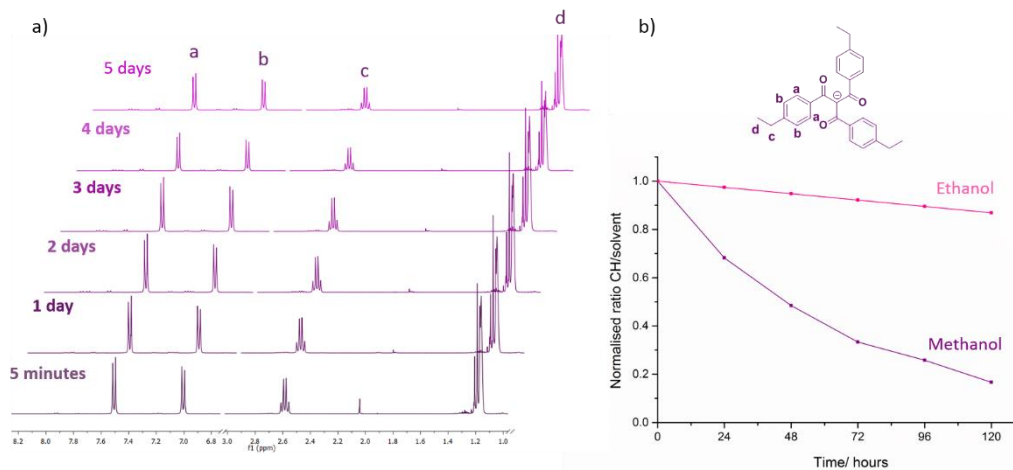


Figure 5.14. - ^1H NMR of the **ettbmH** molecule and one equivalent of KOH over 5 days in $d\text{-EtOH}$ (a) and comparison of the decomposition ratio of the **ettbm** in $d\text{-EtOH}$ (pink trace) and $d\text{-MeOH}$ (purple trace).

5.4 X-Ray Diffraction Studies

5.4.1 Products of the Reaction of **dmtbmH** with Lanthanoids

The structures for the $[\text{Ln}(\mu\text{-dmmba})(\text{dmdbm})(\text{dmtbm})(\text{HOEt})]_2 \text{Ln}^{3+} = \text{Eu}$ (**C15**), Tb (**C16**) are isomorphous and can be described as a dimer formed by two Ln^{3+} , two β -triketonates, two β -diketonates and two bridging benzoate anions. Each metal centre can be considered seven-coordinate, with one β -triketonate and one β -diketonate in a bidentate mode, two bridging O, O' -benzoate ligands linking the lanthanoid centres and one molecule of ethanol completing the coordination sphere (see Figure 5.15).

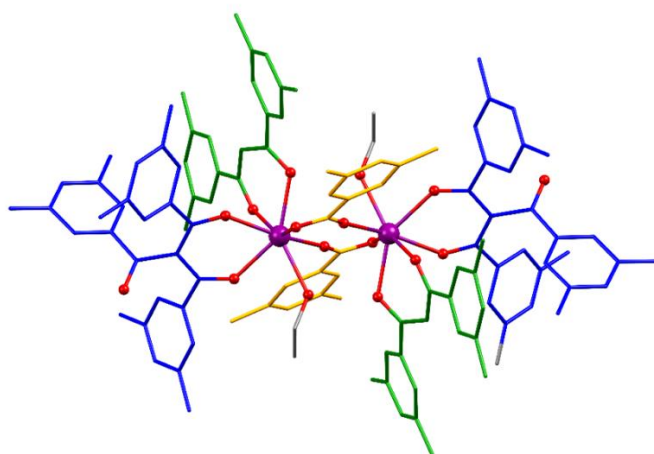


Figure 5.15 Representation of the X-Ray crystal structure of $[\text{Ln}(\mu\text{-dmmba})(\text{dmdbm})(\text{dmtbm})(\text{HOEt})]_2 \text{Ln}^{3+} = \text{Eu}^{3+}$ and Tb^{3+} where the coordination of β -triketonates (blue trace), β -diketonates (green trace) and benzoates (yellow trace) is highlighted.

The binding mode of the benzoate anions could be described as $\mu_2\text{-}\eta^2, \eta^1$ (chelating/bridging unidentate), leading to a description of the metal centres as eight-coordinate (Figure 5.16).²⁵¹ The $\text{Ln}\text{-O}31$ distance of 2.623 Å is, however, substantially longer than the other $\text{Eu}\text{-O}$ distances (2.316-2.448 Å). This suggests that the binding mode might be better described as $\mu_2\text{-}\eta^1, \eta^1$ *ZE* (bridging bidentate), with the metal ions being seven-coordinate. Binding modes of carboxylates that are intermediate between these two extremes have been discussed,²⁵² but given that the emission properties of the Eu^{3+} dimer suggests that the metal centre is, indeed, seven coordinated (see Section 5.5.1), the seven-coordinate description of the structure was preferred in this case (Figure 5.16). The two Ln^{3+} cations are symmetrically equivalent, being related by an inversion centre, and are at a distance of 4.0509(5) Å.

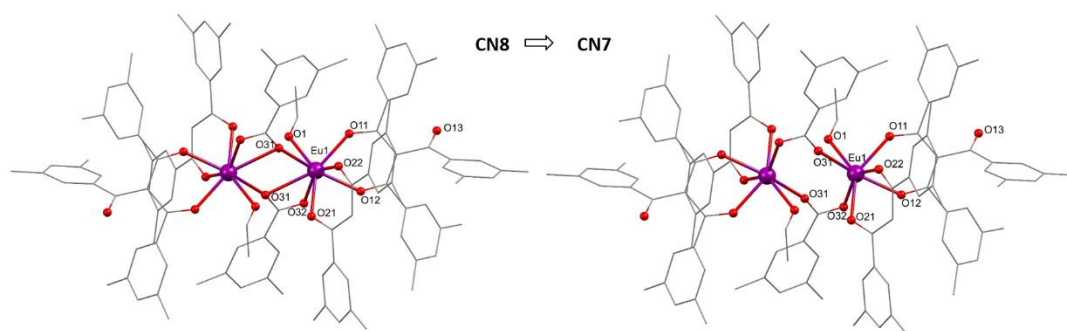


Figure 5.16 Representation of the X-Ray crystal structure of $[\text{Eu}(\mu\text{-dmba})(\text{dmdbm})(\text{dmdbm})(\text{HOEt})]_2$ showing the eight-coordinate and seven-coordinate, where hydrogens and molecules of solvent have been omitted for clarity.

A broadly similar structure was found in the case of $[\text{Yb}(\mu\text{-dmba})(\text{dmdbm})_2(\text{HOMe})]_2$ (**C17**), except that the triketonate ligands are replaced by additional diketonates (and solvent ethanol replaced by methanol). Again the metal centres are bridged by two benzoate ligands, and eight- or seven-coordination could be considered. Here the bond length distinctions are more extreme: Yb1-O42, 2.944 Å; Yb2-O31, 2.826 Å, compared to 2.207–2.383 Å (see Figure 5.17). This interaction becoming longer as the metal radius decreases is to be expected if this M–O interaction is weak or negligible²⁵², and further supports the description of these complexes as seven-coordinate. The dinuclear complex is not generated by an inversion centre, but is nevertheless *quasi*-symmetrical, with only slight differences in the coordination spheres of the two metals, which are situated at a distance of 4.235(1) Å.

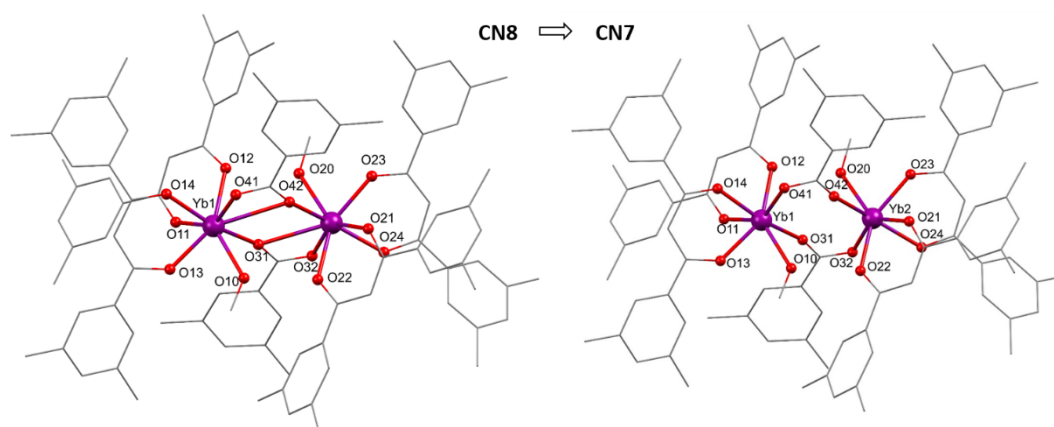


Figure 5.17 Representations of the X-Ray crystal structure of $[\text{Yb}(\mu\text{-dmba})(\text{dmdbm})_2(\text{HOMe})]_2$ as eight or seven-coordinate, where hydrogens and molecules of solvent have been omitted for clarity.

A different dinuclear complex was found for the $[\text{Yb}(\mu\text{-dmdbm})(\text{dmdbm})_2]$ (**C18**) where only the β -diketonate ligand is present in the structure (see Figure 5.18). This arrangement is

analogous to the previously published structure formed by Gd^{3+} and *t*-butylacetylacetonate.²⁵³ In this case, each Yb^{3+} is seven coordinate, with the Yb_2O_2 core supported by two $\mu_2\text{-}\eta^2,\eta^1$ (chelating/bridging unidentate) ligands, and the remainder of the coordination sphere comprising of chelating diketonate ligands. The dinuclear complex is generated by an inversion centre, with the $\text{Yb}^{3+}\cdots\text{Yb}^{3+}$ distance slightly shorter at 3.691 Å, in comparison to the mixed ligand dimers.

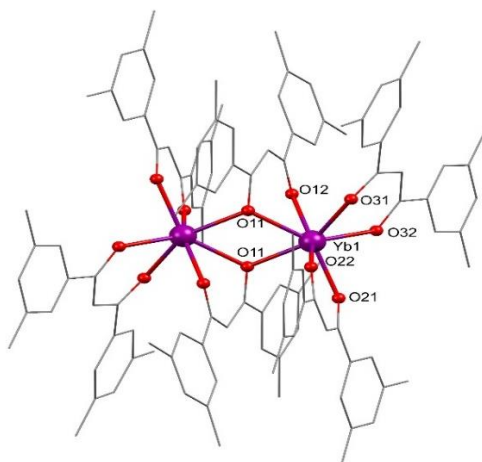


Figure 5.18 Representation of the X-Ray crystal structure of $[\text{Yb}(\mu\text{-dmbm})(\text{dmbm})_2]_2$ where hydrogens and molecules of solvent have been omitted for clarity.

Finally, complexes **C19**, $[\text{Eu}(\text{dmbm})_4(\text{Cs})]_n$ and **C20**, $([\text{Yb}(\text{dmbm})_4(\text{K})]_n)$ were identified as linear coordination polymers, following a similar formula to the previously reported structures with dibenzoylmethane (see Figure 5.19).²²⁶

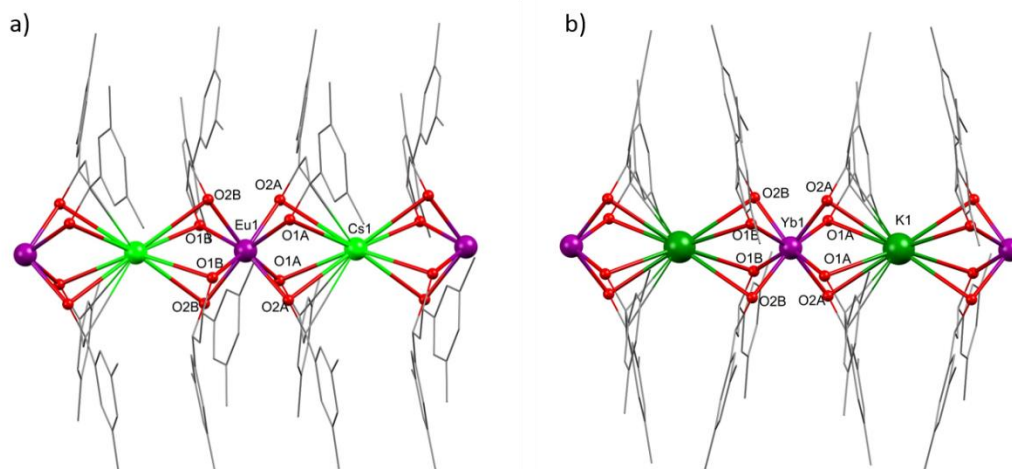


Figure 5.18 Representation of the X-Ray crystal structure of $[\text{Eu}(\text{dmbm})_4(\text{Cs})]_n$ (a) and $([\text{Yb}(\text{dmbm})_4(\text{K})]_n)$ (b) where hydrogens have been omitted for clarity.

5.4.2 Products of the Reaction of **ettbmH** with Lanthanoids

Complex **C21** crystallises as hydrogen bonded dimers involving only the β -diketonate ligand, formulated as $[\text{Yb}(\text{etdbm})_3(\text{HOMe})_2]$, where each Yb^{3+} is seven coordinate with three β -diketonates binding in a bidentate mode and an oxygen atom from a molecule of solvent methanol (see Figure 5.20). There are two symmetrically inequivalent but essentially identical dimers in the structure. Each dimer is situated about an inversion centre and is linked by hydrogen bonds between methanol O and keto-O atoms (O1...O22, 2.756 Å; O2...O51, 2.758 Å). The resulting pairs of lanthanoid ions are relatively close in distance (Yb1...Yb1', 5.704 Å; Yb2...Yb2', 5.759 Å), which could cause quenching by energy transfer between lanthanoid excited states. This structure is analogous to **C14** ($[\text{Yb}(\text{mtbm})_3(\text{OH}_2)_2]_2$) with **mtbmH** where the dimer was formed with molecules of water instead.

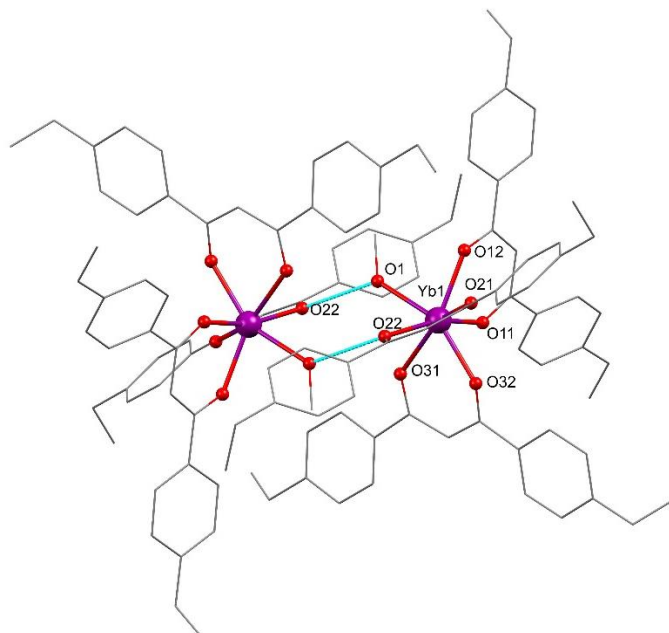


Figure 5.20 Representation of the X-Ray crystal structure, showing one of the hydrogen bonded dimers in $[\text{Yb}(\text{etdbm})_3(\text{HOMe})_2]$ where hydrogens and lattice solvent molecules have been omitted for clarity.

Complexes **C22** ($[\text{Yb}(\text{etdbm})_4(\text{Cs})]_n$) and **C23** ($[\text{Eu}(\text{ettbm})_4(\text{Cs}\cdot\text{OHET})]_2$) are analogous to the previously described linear diketonate polymers (**C19**, **C20**)²²⁶ and reported triketonate-supported tetranuclear assemblies²⁰⁹, respectively (see Figure 5.21).

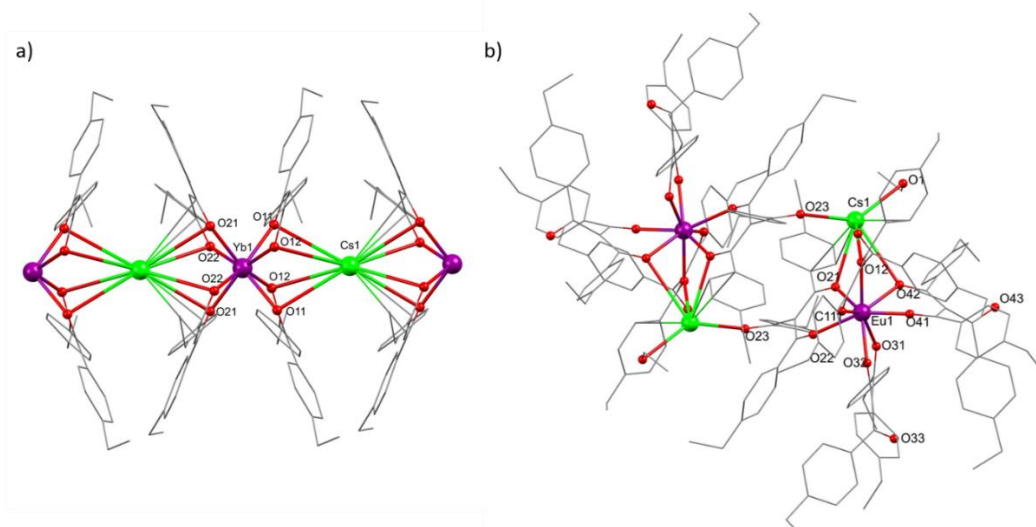


Figure 5.219 Representation of the X-Ray crystal structure of $[Yb(\text{etdbm})_4(\text{Cs})]_n$ (a) and $[\text{Eu}(\text{etdbm})_4(\text{Cs-OHEt})]_2$ (b) where hydrogens have been omitted for clarity.

5.4.3 Products of the Reaction of **butbmH** and *t*-**butbmH** with Lanthanoids

The $[\text{Eu}(\text{budbm})_4(\text{Cs})]_n$ (**24**) structure presents a similar linear polymeric structure to that already described for the **dmtbmH** and **etdbmH** complexes where $[\text{Eu}(\text{budbm})_4]$ were found to be linked by Cs^+ atoms (see Figure 5.22).

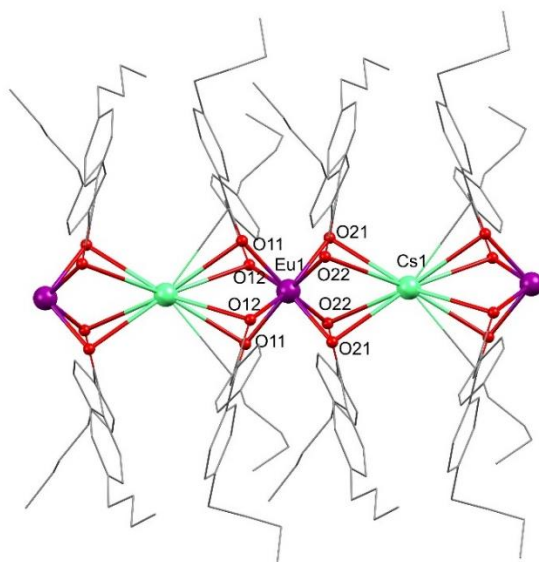


Figure 5.20 Representation of the X-Ray crystal structure of $[\text{Eu}(\text{budbm})_4(\text{Cs})]_n$ where hydrogens have been omitted for clarity.

No complexes containing the ***t*-butbm** or its corresponding retro-Claisen condensation products were able to be crystallised. In contrast, as previously explained in Section 5.2.2, when the $\text{Ln}(\text{NO}_3)_3 \cdot \text{DMSO}_n$ salts were used under less polar conditions, the ***t*-butbmH** molecule crystallised (see Figure 5.23).

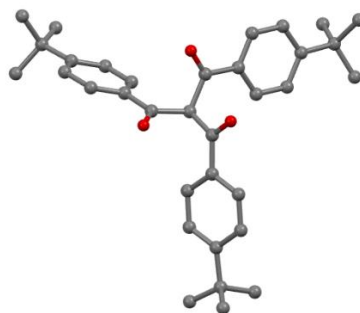


Figure 5.21 X-ray crystal structure of the ***t*-butbmH** molecule where the hydrogens are omitted for clarity.

5.4.4 Products of the Reaction of **mtbmH** with Lanthanoids

Finally, complex **C25**, with formula $[\text{Eu}(\mu\text{-mba})(\text{mdbm})(\text{OHEt})_2]_2$, crystallised as a dimer similar to **C17** ($[\text{Yb}(\mu\text{-dmba})(\text{dmdbm})_2(\text{HOME})_2]_2$) (see Figure 5.24). Here the additional bridging Eu–O interaction is more closely comparable to the other Eu–O bond lengths: Eu1–O31', 2.580 Å, compared to 2.307–2.483 Å for the keto and carboxylate O atoms. The solvent Eu–O1 distance is 2.507 Å. Thus this complex is reasonably described as having eight-coordinate metal centres, and in fact, shape analysis measurements showed the coordination sphere is best described as a triangular dodecahedron (eight coordinate) (see Section 5.4.5).

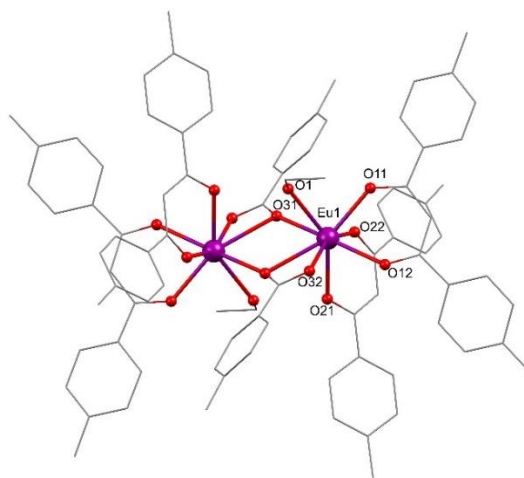


Figure 5.22 X-ray crystal structure of $[\text{Eu}(\mu\text{-mba})(\text{mdbm})(\text{OHEt})_2]_2$ where the hydrogens are omitted for clarity.

5.4.5 Shape Analysis

Shape analysis calculations were performed for the eleven complexes studied in this chapter (**C15-C25**) in two different groups: seven and eight coordinated.

The seven coordinate complexes (**C15-C18** and **C21**) were studied with respect to two ideal geometries; capped octahedron and capped trigonal prism. Three different coordination geometries were found and assigned to the three different families of complexes; with one (square), two (circle) or three (rectangle) different ligands coordinated to the lanthanoid centre (see Figure 5.25). The first family, corresponding to complexes containing the three different species of the retro-Claisen condensation, **C15** and **C16**, were best described as distorted capped octahedra with CShM values close to one in both cases. The second group corresponds to complex **C17** with two different ligands incorporated in the structure, benzoate and β -diketonate, being best described as distorted capped octahedron with a lower CShM value of 0.5. Finally, the third group was assigned to complexes **C18** and **C21**, with only β -diketonate present in their structure. The closest geometry in this case was, in contrast, a capped trigonal prism.

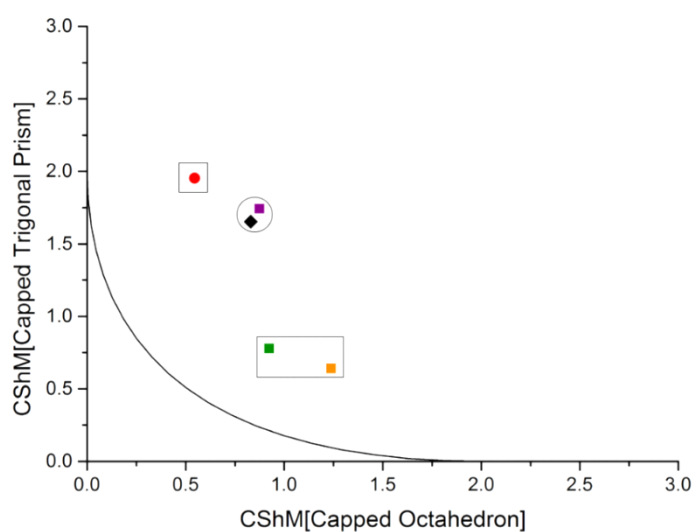


Figure 5.23 Shape Map representing the CShM values of the seven-coordinate complexes **C15** (purple), **C16** (black), **C17** (red), **C18** (green) and **C21** (orange) for Eu^{3+} (squares), Yb^{3+} (circles) and Tb^{3+} (diamonds).

Complexes **C15-C17** were also analysed as eight coordinate against the square antiprism and triangular dodecahedron ideal geometries. The CShM values were found to be 3.14, 3.06 and 4.25 for square antiprism and 1.60, 1.51 and 1.64 for triangular dodecahedron regarding complexes **C15**, **C16** and **C17**, respectively (see Figure 5.26). These values are certainly higher

than those found for the seven coordinate geometries, which further support the assignment as seven-coordinate.

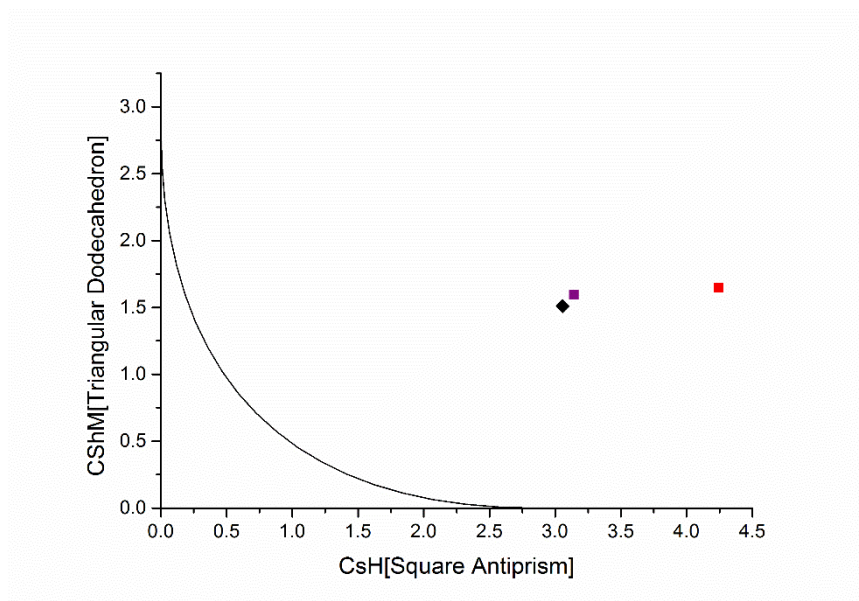


Figure 5.24 Shape Map representing the CShM values of complexes C15 (purple), C16 (black) and C17 (red) for Eu^{3+} (squares) and Tb^{3+} (diamonds) as eight-coordinate.

In contrast, complexes **C19**, **C20** and **C22-25**, assigned as eight-coordinate, were generally found to match more closely against the square antiprism and triangular dodecahedron geometries (see Figure 5.27). The polymer β -diketonate-based complexes **C19**, **C20** and **C22** were best described as distorted square antiprisms while complex **C24** for **butbmH** was assigned to a distorted triangular dodecahedron. This difference in geometry may be due to steric effects of the long butyl chains. The tetranuclear assembly formed in complex **C23** is best described as a distorted square antiprism as found for the analogous **tbmH** complexes formed with RbOH .²⁷ Finally, the dimer **C23**, is far from being described as a square antiprism but relatively well defined as a triangular dodecahedron with CShM value of ~1.5 (see Table 5.1)

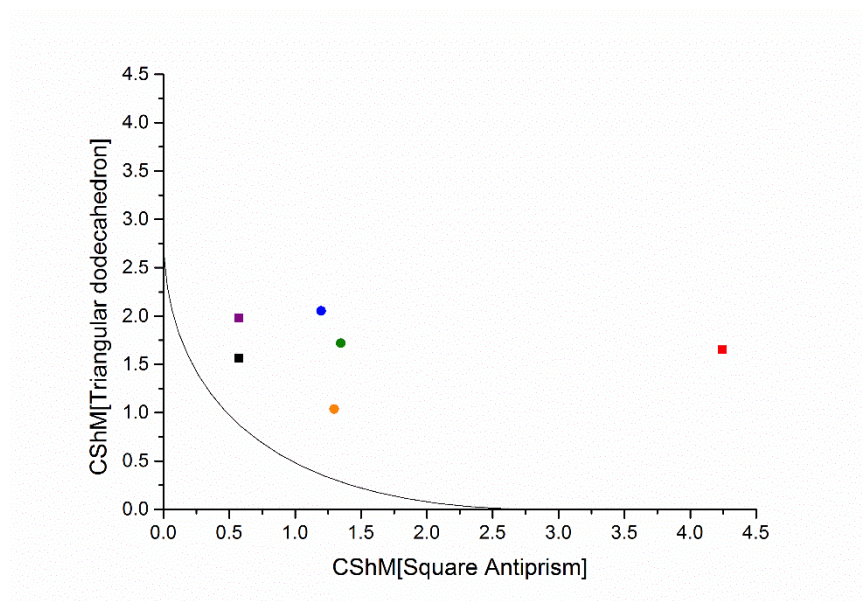


Figure 5.27 Shape Map representing the CShM values of the eight-coordinate complexes C19 (blue), C20 (black), C22 (purple), C23 (green), C24 (orange) and C25 (red) for Eu^{3+} (squares) and Yb^{3+} (circles).

Table 5.1 CShM values for the seven- (C15-C18, C21) and eight-coordinate (C19, C20, C22-C25) complexes.

Complex	COC-7	CTPR-7	Complex	TTD-8	SAPR-8
C15	0.8746	1.7434	C19	2.0531	1.1982
C16	0.8302	1.6540	C20	1.9782	0.8581
C17	0.5453	1.9529	C22	1.5610	0.5724
C18	0.9230	0.7781	C23	1.7169	1.3469
C21	1.2382	0.6393	C24	1.0359	1.2957
			C25	1.6494	4.2455

5.5 Photophysical Properties

The absorption spectra of **dmtbmH**, **ettbmH**, **buttbmH** and **t-butbmH** were recorded in ethanol in neutral and basic conditions at room temperature. The comparison of the deprotonated molecules can be seen in Figure 5.28. The main absorption bands lie at similar wavelengths, ~260 nm and ~350 nm, for the four different molecules, being attributed to $\pi\text{-}\pi^*$ transitions. These results suggest that the different substituents in the β -triketones do not significantly affect the energy level of the transitions involved. In the case of the **dmtbmH** a bathochromic shift is observed in both absorption bands. This may be the result of the substitution in meta position which forces the rotation of the benzene group, disturbing the

coplanarity and therefore, the conjugation of the system.²²⁵ While the molar absorptivity for **dmtbmH**, **ettbmH** and **t-butbmH** are of the same order than their analogous β -diketonates²²⁵, the intensity of **butbmH** is higher, which may suggest that the extra benzene group could be contributing at a higher degree in the absorption of this molecule.

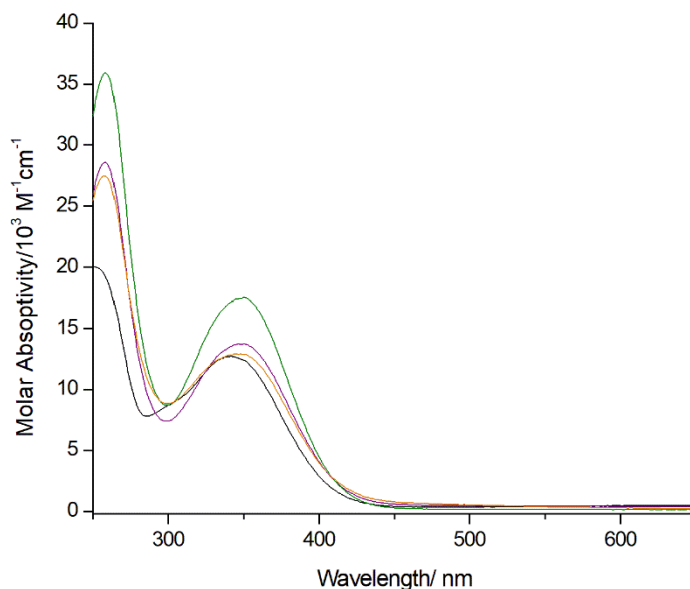


Figure 5.25 Absorption profiles of **dmtbm** (black trace), **ettbm** (purple trace), **butbm** (green trace) and **t-butbm** (orange trace) in ethanol with excess of KOH (ca. $10^{-5}M$).

The triplet state of the β -triketonates and their corresponding β -diketonates were measured at the 0-phonon transition of the phosphorescent emission at 77 K of their corresponding Gd^{3+} complexes and were found to lie close in energy independently of the substituent; 20,202 - 20,844 cm^{-1} (see Table 5.2 and Figure 5.29). In every case the energy of lowest triplet excited state of the β -triketonate is higher than the corresponding β -diketonate. This may be because when complexed, the loss in planarity of the phenyl rings of the β -triketonate causes a break on the system conjugation, destabilising the energy of the triplet state.

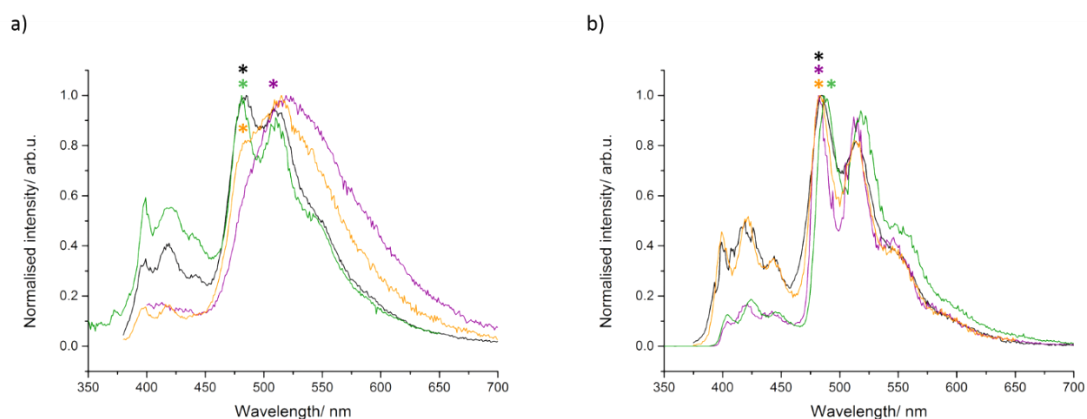


Figure 5.29 Emission of the *dmtbmH* (black trace), *ettbmH* (purple trace), *butbmH* (green trace) and *t-butbmH* (orange trace) Gd^{3+} complexes (a) and their β -diketonates analogues (b), where the * symbol indicates the 0-phonon transition for the triplet excited state.

Table 5.2 Energy values for the 0-phonon transition for the singlet and triplet excited state of ligands **L1H-L6H**.

Ligand	$^1\pi\pi^*(\text{cm}^{-1})$	$^3\pi\pi^*(\text{cm}^{-1})$	Ligand	$^1\pi\pi^*(\text{cm}^{-1})$	$^3\pi\pi^*(\text{cm}^{-1})$
tbm	25,575 ^a	20,620 ^a	dmtbm	24,509	20,790
dbm	26,110 ^a	20,580 ^a	dmdbm	25,974	20,633
mtbm	24,957	20,790	butbm	25,156	20,790
mdbm	25,974	20,576	budbm	25,840	20,537
ettbm	25,189	20,790	t-butbm	25,126	20,844
etdbm	25,445	20,202	t-budbm	26,007	20,709

^a Experimental data in accordance to literature^{26,175} (see Appendix for individual emission plots).

Based on these numbers, ligands **L3H-L6H** would effectively sensitise Eu^{3+} ($^5D_0 = \sim 17,200 \text{ cm}^{-1}$) and Yb^{3+} ($^2F_{5/2} = \sim 10,200 \text{ cm}^{-1}$) excited states.

The emission properties for complexes where the bulk of the sample was confirmed to be pure by elemental analysis (**C15**, **C17**, **C18**, **C19**, **C20**, **C21** and **C24**) were recorded in the solid state. In every case the emission was seen as a consequence of an efficient antenna effect, evidenced by the broad structureless excitation spectra similar to the absorption spectra of the ligands. The photophysical data, including excited state lifetime decay (τ_{obs}), calculated radiative decay (τ_R), intrinsic photoluminescence quantum yield ($\Phi_{\text{Ln}}^{\text{Ln}}$) and overall quantum

yield (Φ_{Ln}^L) are reported in Tables 5.3 and 5.4 at the beginning of Sections 5.51 and 5.52, respectively.

5.5.1 Europium Assemblies

Table 5.3 Photophysical data for the Eu^{3+} complexes in the solid state at 298K.

Complex	τ_{obs} (μ s)	τ_R (ms)	Φ_{Ln}^{Ln} (%)	Φ_{Ln}^L (%)
C15	47	0.79	6	2
C19	815	1.19	68	45
C24	485	0.96	50	43

The emission spectrum of complex **C15** shows the characteristic Eu^{3+} attributed to the ${}^7F_J \leftarrow {}^5D_0$ ($J = 0-4$) in the region 550-750 nm (see Figure 5.30).⁴⁶ The presence of the narrow ${}^7F_0 \leftarrow {}^5D_0$ peak at 580 nm (full width at half maximum ~ 40 cm^{-1}) is an indication of a unique low symmetry Eu^{3+} centre. This is in agreement with the crystal structure where the two Eu^{3+} cations present in the dimer are related by an inversion centre. The splitting of the magnetic dipole (${}^7F_1 \leftarrow {}^5D_0$) and the hypersensitive transition (${}^7F_2 \leftarrow {}^5D_0$) into two and three bands, respectively, is suggestive of trigonal fields. This result is supported by shape analysis where the geometry is best described as capped octahedron (trigonal, C_{3v}) (see Section 5.4.5). The excited state lifetime decay was satisfactorily fitted to a monoexponential function and was measured to be 47 μ s (see Figure 5.), shorter than analogous β -diketonate complexes, suggesting efficient non-radiative decay pathways of the 5D_0 excited level. These quenching processes may include multiphonon relaxation due to the EtO-H coordinated to the Eu^{3+} centre and energy transfer between the two lanthanoid centres laying at short distance (4.06 \AA). From the Eu^{3+} spectrum, the value of radiative lifetime can be calculated to be 0.78 ms, giving an intrinsic quantum yield value of 6%. The overall quantum yield was measured with help of an integrating sphere and was found to be 2%, which implies a poor sensitisation efficiency of 33%. In fact, some direct excitation can be observed in the excitation plot for emission recorded at 612 nm (see Figure 5.30).

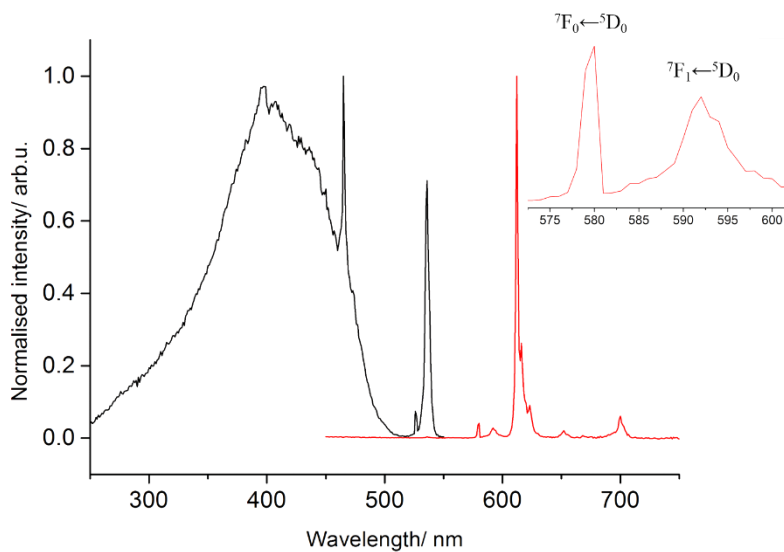


Figure 5.30 Normalised excitation (black) and emission ($\lambda_{exc}=350$ nm) (red) plots for complex **C15** in the solid state.

Complexes **C19**, **C24** show characteristic Eu^{3+} emission in the region 580-750 nm (see Figure 5.31). The ${}^7\text{F}_0 \leftarrow {}^5\text{D}_0$ transition is absent in both cases, suggesting that the Eu^{3+} ion occupies a site with higher symmetry than complex **C15**. The splitting of the magnetic dipole transition, ${}^7\text{F}_1 \leftarrow {}^5\text{D}_0$, and the hypersensitive band, ${}^7\text{F}_2 \leftarrow {}^5\text{D}_0$, is slightly different which indicates different degrees of distortion between the two coordination spheres. These trends are confirmed by the results found in the shape analysis (see Section 5.4.5). The excited state lifetimes decay values (τ_{obs}) were measured to be much longer than complex **1** with values of 815 and 485 μs , respectively (see Figure 5.32). These data suggest that lanthanoid cross relaxation quenching is not effective in the linear polymers (**C19**, **C24**) where the $\text{Eu}\cdots\text{Eu}$ distance is longer than 8 \AA . The intrinsic quantum yields (Φ_{Ln}^{Ln}) were found to be 68% and 50%, respectively, based on the radiative lifetimes calculated from the emission spectra. Overall quantum yields were measured to be 45% and 43%, respectively. The photophysical data for the two complexes are therefore comparable, showing high sensitisation efficiency in both cases.

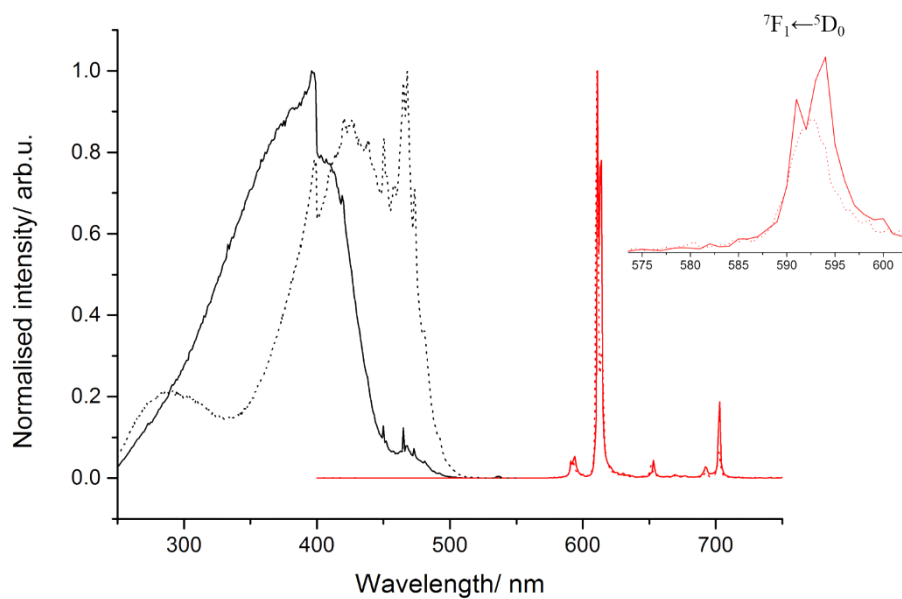


Figure 5.31 Normalised excitation (black) and emission ($\lambda_{exc}=350$ nm) (red) plots for complex **C19** (solid line) and **C24** (dashed line) in the solid state at 298K.

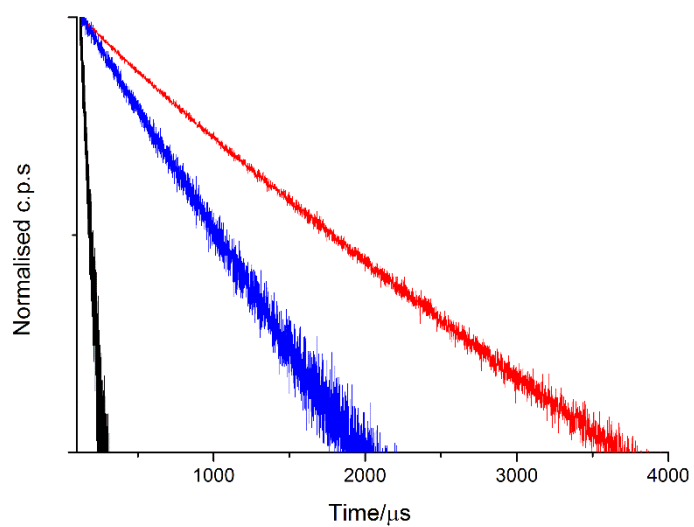


Figure 5.32 Lifetime decays of **C15** (black trace), **C19** (red trace) and **C24** (blue trace) in the solid state at 298K.

5.5.2 Ytterbium Assemblies

Table 5.4 Photophysical data for the Yb^{3+} complexes in the solid state at 298K.

Complex	τ_{obs} (μs)	τ_{R} (ms)	$\Phi_{\text{Ln}}^{\text{Ln}}$ (%)
C17	10.4	1.2	0.86
C18	12.7	1.2	1.1
C20	14.0	1.2	1.2
C21	8.0	1.2	0.7

Characteristic Yb^{3+} NIR emission for complexes **C17**, **C18**, **C19** and **C21** was observed in the 900-1100 nm region, corresponding to the ${}^2\text{F}_{7/2} \leftarrow {}^2\text{F}_{5/2}$ transition (see Figure 5.33). Different splitting of this transition is found in the case of the seven coordinate Yb^{3+} dimers (**C17**, **C18** and **C21**), suggestive of different coordination environments of the lanthanoid centres, which is in agreement with the shape analysis studies (see Section 5.4.5). In contrast, this transition is split into five main bands in the case of the 8-coordinate Yb^{3+} polymer (**C20**). In every case, emission from hot bands is present as a shoulder in the 930-960 nm region.⁶

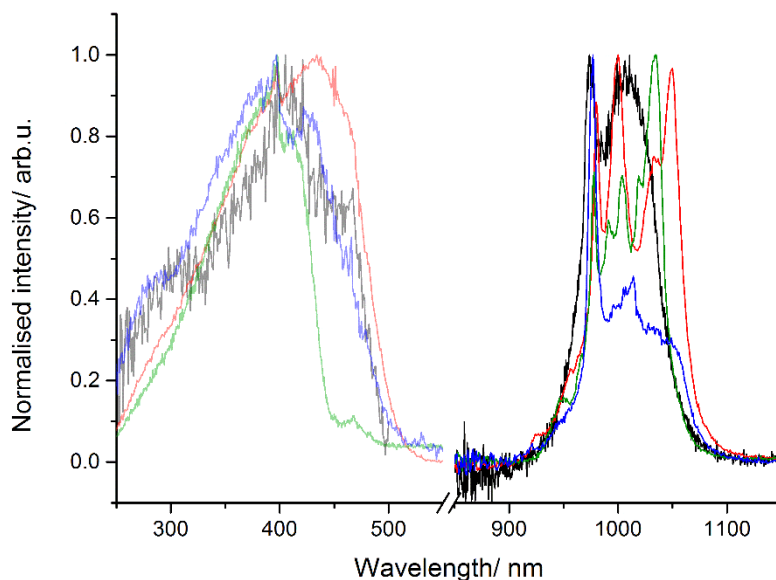


Figure 5.33 Normalised excitation (soft trace) and emission ($\lambda_{\text{exc}}=350$ nm) (dark trace) plot for complex **C17** (black trace), **C18** (red trace), **C19** (blue trace) and **C21** (green trace) in the solid state at 298K.

The observed lifetime decays (τ_{obs}) for all the Yb^{3+} complexes were monoexponential. The lifetime decay values for the Yb^{3+} dimers **C17**, **C18** and **C21**, are 10.4, 12.7, 8.0 μs , respectively (see Figure 5.). This suggests that the presence of a molecule of methanol coordinated to the lanthanoid cation in complexes **C17** and **C21** does not dramatically quench the NIR emission as might be expected, and only a small decrease in the lifetime value was found. The lifetime decay for the Yb^{3+} polymer (**C20**) was found to be slightly longer with a value of 14.0 μs . These data suggest that the MeO-H directly coordinated to the metal centre in complexes **3** and **7** may be causing multiphoton relaxation quenching resulting in of slightly shorter lifetimes. However, other quenching effects such as self-quenching could also be occurring, since the Yb^{3+} cations sit relatively close in distance of 4.24 Å, 3.69 Å and 5.70 Å for complexes **C17**, **C18** and **C21**, respectively.

3

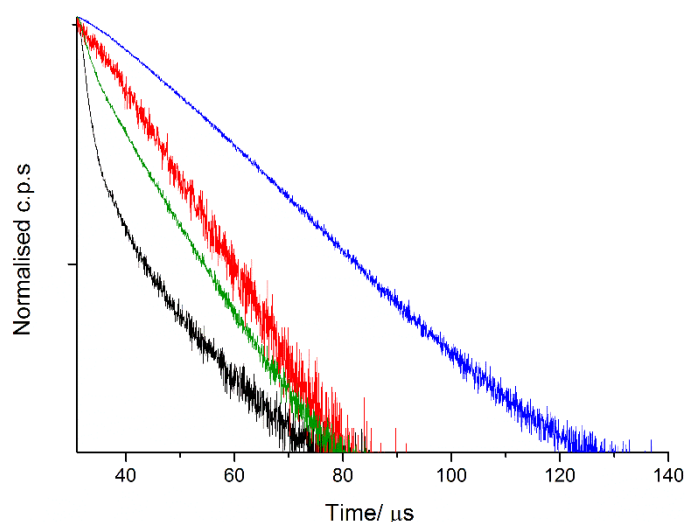


Figure 5.34 Lifetime decays of **C17** (black trace), **C18** (red trace), **C19** (blue trace) and **C21** (green trace) in the solid state at 298K.

5.6 Conclusions

In this chapter four new β -triketones, **L3H-L6H** were synthesised and fully characterised. Their complexation reaction under basic conditions in polar solvents, such as methanol or ethanol, yielded structures where their retro-Claisen condensation products were incorporated. Therefore, their stability under the same complexation conditions were studied, showing the retro-Claisen condensation reaction occurring to significant extents, and up to 80% completion for the **dmtbmH** molecule. The complexes formed, presented new structures where one, two

or even the all three retro-Claisen reactants and products were linked to the lanthanoid centres. These results, showed how the lability of the lanthanoid metal centres can give rise to novel complexes when reacted with a dynamically changing set of ligands. The photophysical study revealed that the majority of the mixed ligand complexes were emissive in the visible or NIR range.

Chapter 6 DMSO Solvated Complexes

6.1 Introduction

Chapters 3 and 4 described the synthesis of new β -triketones developed in order to expand the family of β -triketone assemblies and better understand their photophysical properties. However, in Chapter 5, it was reported that high retro-Claisen condensation rates of these ligands occurred in ethanolic or methanolic media. Therefore, an alternative synthetic pathway is needed where the use of alcoholic solvents for the complexation reaction is avoided. In this chapter, a set of mononuclear complexes with formula $[\text{Ln}(\mathbf{tnm})_3(\text{DMSO})_2]$ ($\text{Ln}^{3+} = \text{Nd}^{3+}$, Eu^{3+} , Gd^{3+} and Yb^{3+}), where **tnm** is tris(2-naphthoyl)methane, will be presented where DMSO was chosen as the complexation reaction medium. This more conjugated triketone was chosen with the aim of lowering the triplet state energy to favour the sensitisation process of the NIR lanthanoids such as Yb^{3+} . A photophysical study was performed, showing an enhancement of the luminescence properties for Yb^{3+} , where long lifetimes and high quantum yields were found in solution. These are the first examples of soluble β -triketone complexes, opening up an alternative pathway to further develop this area of research.

6.2 Synthesis

6.2.1 Ligand

The tris(2-naphthoyl)methane (**L7H**) was synthesised following the same procedure used for ligands **L1H-L6H**, according to scheme presented in Figure 6.1.

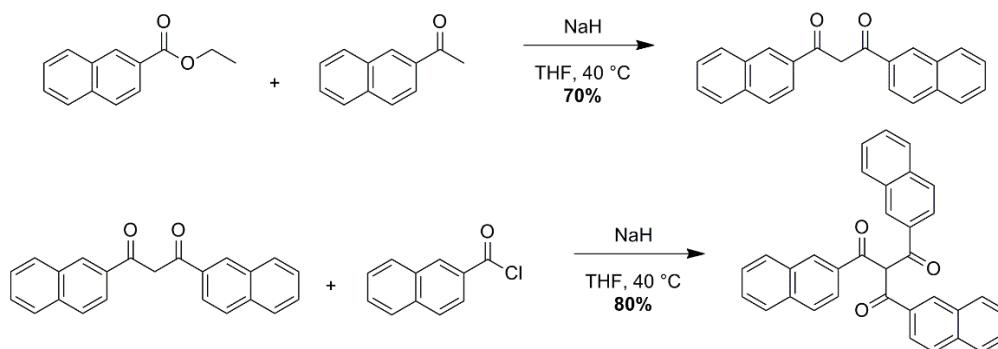


Figure 6.1 Synthetic scheme for the preparation of **tnmH**.

The **tnmH** was characterised by melting point, IR, $^1\text{H-NMR}$, $^{13}\text{C-NMR}$ and elemental analysis (see Experimental section). The $^1\text{H-NMR}$ in *d*-DMSO showed the presence of the keto

tautomer with the characteristic α -H at 8.57 ppm and small traces of the enol tautomer at 7.5 ppm and 7.85 ppm (see Figure 6.2).

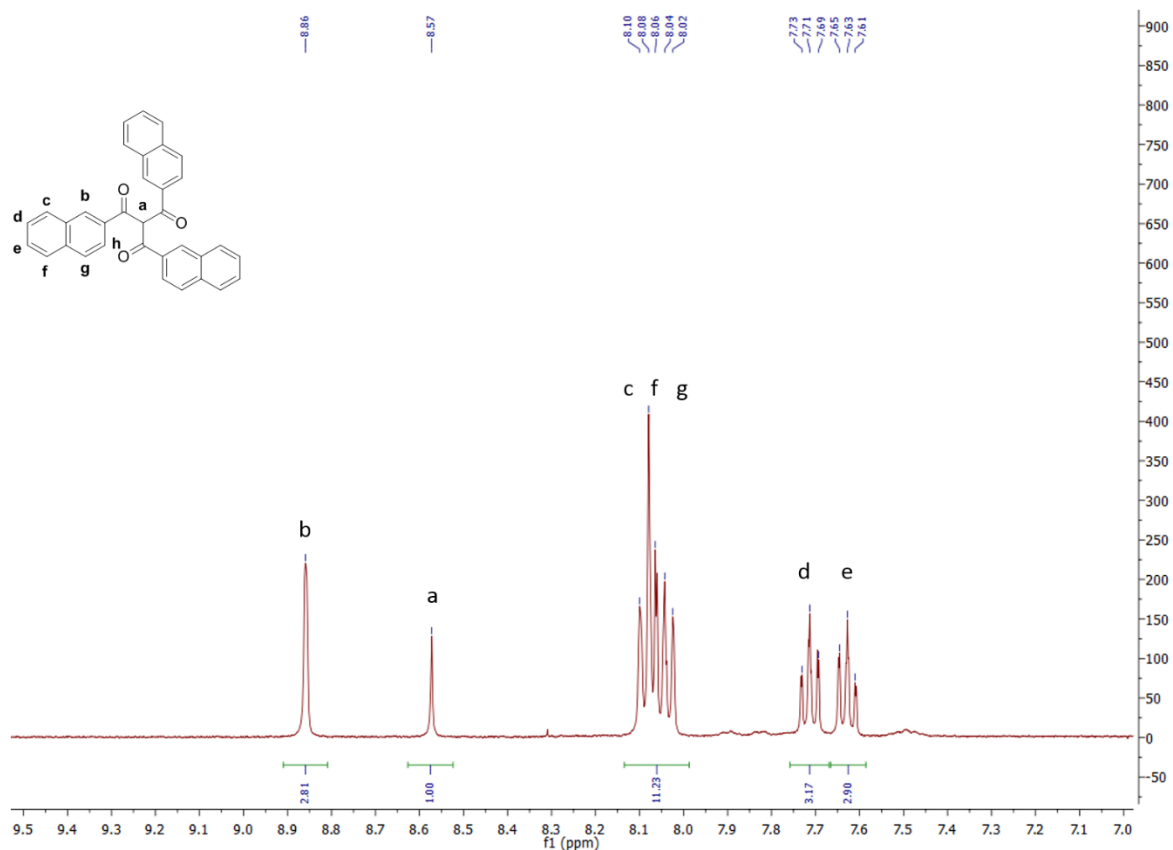


Figure 6.2 Portion of the $^1\text{H-NMR}$ spectrum of **tnmH** in *d*-DMSO.

The stability of **tnmH** in *d*-DMSO (10^{-2} M) under basic conditions (1eq. KOH) was studied by $^1\text{H-NMR}$. The spectra showed no change in the intensity of the bands and no presence of new peaks over 5 days (see Figure 6.3). These results clearly suggest high stability of the β -triketone in DMSO and therefore, no retro-Claisen condensation occurring under these conditions in contrast to what it was observed when the studies were carried out in methanol (see Section 5.3).

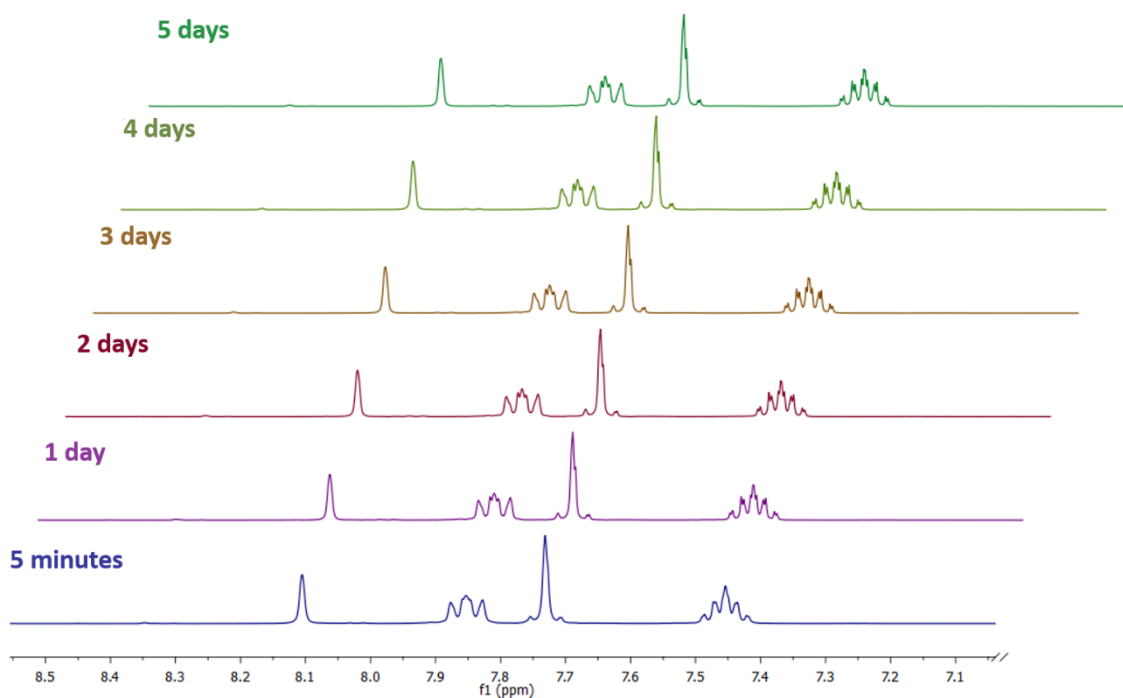


Figure 6.3 $^1\text{H-NMR}$ of the **tnmH** molecule and one equivalent of **KOH** over 5 days in *d*-DMSO.

6.2.2 Lanthanoid Assemblies

The lanthanoid complexes were made by reaction of three equivalents of **tnmH**, three equivalents of **KOH** and one equivalent of the hydrated LnCl_3 ($\text{Ln}^{3+} = \text{Nd}^{3+}, \text{Eu}^{3+}, \text{Gd}^{3+}, \text{Yb}^{3+}$) in dimethylsulfoxide (DMSO). Suitable crystals for X-Ray diffraction were collected by slow diffusion of ethanol into the DMSO solution, revealing the formation of monomeric species with formula $[\text{Ln}(\text{tnm})_3(\text{DMSO})_2]$ for $\text{Ln}^{3+} = \text{Nd}^{3+}$ (**C26**), Eu^{3+} (**C27**), Gd^{3+} (**C28**) and Yb^{3+} (**C29**). Although **KOH** was first employed in an attempt to form polynuclear assemblies, only the mononuclear complexes were isolated, probably due to steric hindrance of the bulky ligand. When NEt_3 was used instead, yields were slightly higher and therefore, triethylamine was chosen as the preferred base.

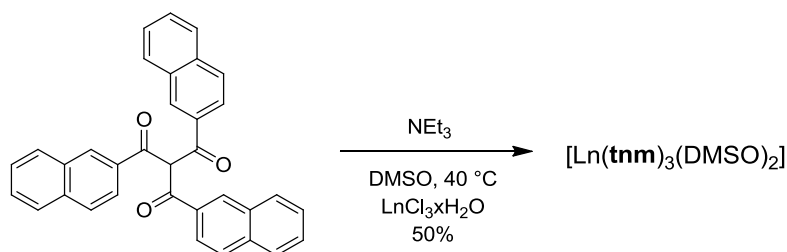


Figure 6.4 Reaction scheme for the synthesis of $[\text{Ln}(\text{tnm})_3(\text{DMSO})_2]$.

The same synthetic methods were followed for ligands **L1H-L6H** and their β -diketone analogues. Despite the fact that only the monomeric species for **dbmH** and *t*-**butbmH** have been isolated so far, this is still under investigation and it will be the focus of further research.

6.3 X-Ray Diffraction Studies

Complexes **C26-C29** crystallised as monomeric species with octacoordinate Ln^{3+} centres surrounded by 6 O-keto atoms from three **tnm** ligands and 2 O atoms from two coordinated DMSO molecules. Possible C-H...O intermolecular interactions are found between the uncoordinated keto O(22,32) atoms and methyl groups of DMSO molecules coordinated to neighbouring lanthanoid centres (O22...C1, 3.019; O32...C4, 3.187 Å). Moreover, π -stacked planes of the naphthoyl fragments of the **tnmH** ligands results in supramolecular dimers related by an inversion centre (see Figure 6.5 and Table 6.1). The distance between two adjacent lanthanoid centres was found to be longer than 10 Å (see Table 6.1), suggesting that direct energy transfer between Ln^{3+} should be minimal unless it is ligand-mediated.^{64,66}

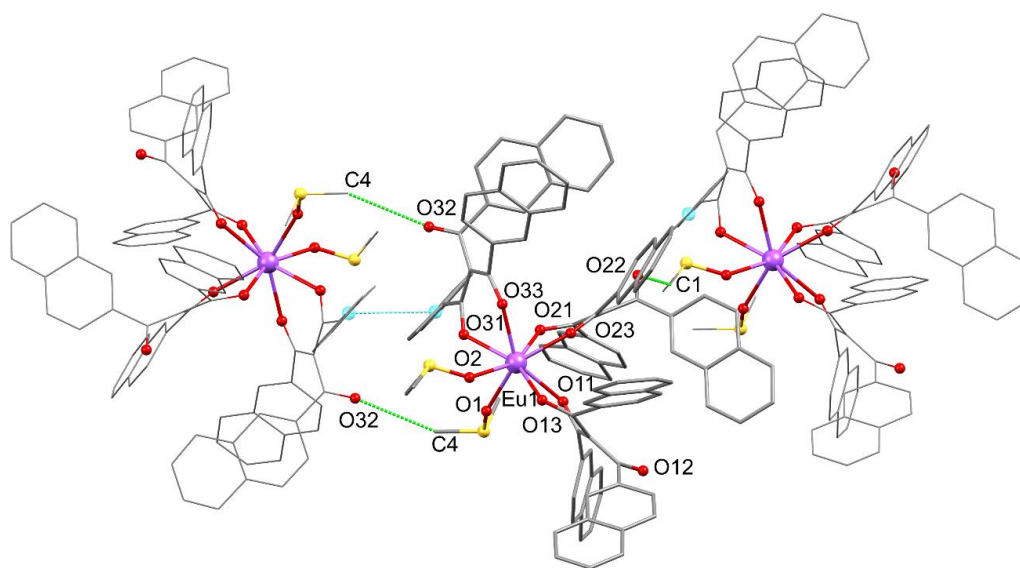


Figure 6.5 Representation of $[\text{Eu}(\text{tnm})_3(\text{DMSO})_2]$ where centroids are marked in blue and intermolecular interactions emphasised in green. Hydrogens and molecules of solvent are omitted for clarity.

As shown in Table 6.1 the length of Ln-O bonds decreases gradually from Nd^{3+} to Yb^{3+} , as expected due to the *lanthanoid contraction* phenomenon.

Table 6.1 Selected Ln-O bond lengths, Ln-Ln intermetallic distances, π - π interplanar spacings and centroid-centroid distances (Å), for the $[\text{Ln}(\text{tnm})_3(\text{DMSO})_2]$ complexes.

Complex	Ln-O	Ln-Ln	π - π	Centroid-Centroid
C26 $[\text{Nd}(\text{tnm})_3(\text{DMSO})_2]$	2.464(2)- 2.377(2)	10.4025(6)	2.238	5.017
C27 $[\text{Eu}(\text{tnm})_3(\text{DMSO})_2]$	2.431(2)- 2.344(2)	10.3749(6)	2.245	5.004
C28 $[\text{Gd}(\text{tnm})_3(\text{DMSO})_2]$	2.420(3)- 2.325(3)	10.3882(6)	2.285	5.007
C29 $[\text{Yb}(\text{tnm})_3(\text{DMSO})_2]$	2.369(3)- 2.265(2)	10.3784(6)	2.392	5.001

6.3.1 Shape Analysis

The coordination geometry of the four monomeric species, **C26-C29**, were studied against the 13 ideal eight-coordinate polyhedral, being closest to square antiprism (SAPR-8) and triangular dodecahedron (TDD-8), as found for the other eight-coordinate complexes presented in previous chapters (see Figure 6.6).

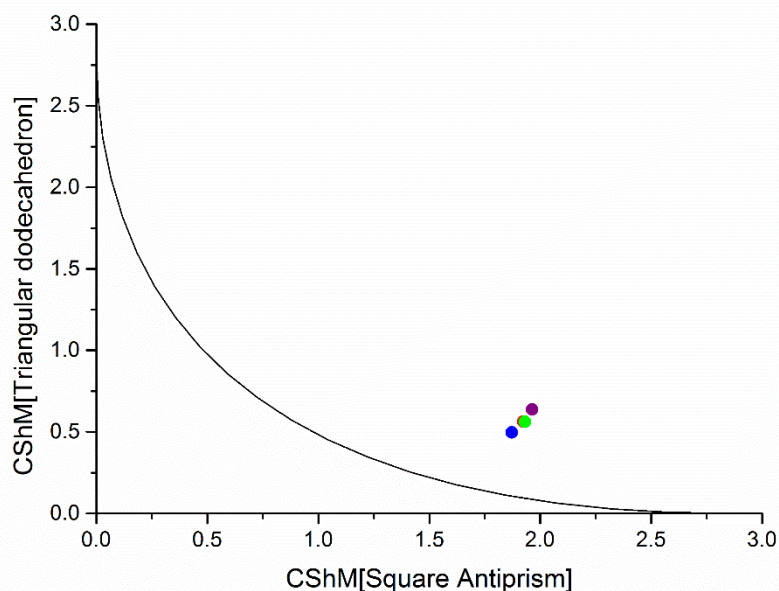


Figure 6.6 Shape Map representing the CshM values of the $[\text{Nd}(\text{tnm})_3(\text{DMSO})_2]$ (purple trace), $[\text{Eu}(\text{tnm})_3(\text{DMSO})_2]$ (red trace), $[\text{Gd}(\text{tnm})_3(\text{DMSO})_2]$ (green trace) and $[\text{Yb}(\text{tnm})_3(\text{DMSO})_2]$ (blue trace).

As can be observed in Figure 6.6, the four complexes were best described as triangular dodecahedra with slightly different degrees of distortion. The Nd^{3+} was found to be the most

distorted with a CShM value of 0.6363. In contrast, the Yb³⁺ was the least distorted with a CShM value of 0.4967. These numbers suggests that the bigger the lanthanoid ion the more distorted the coordination sphere geometry, which in accordance with what was previously cited by Kenneth *et al.* who explained that the shortening in the Ln-X (X=O, N) bond seems to be associated with a shrinking of the coordination sphere around the lanthanoid ion.³⁸

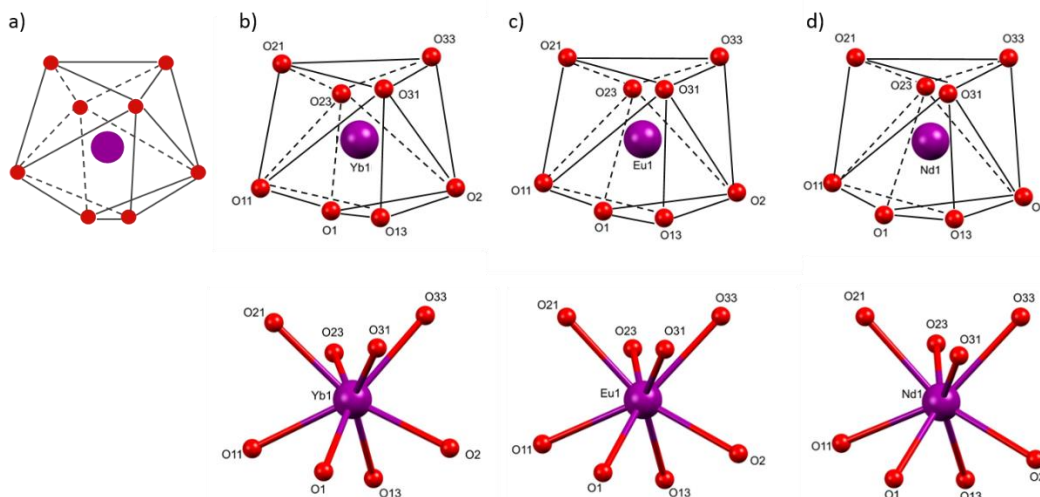


Figure 6.7 Coordination sphere of complexes $[Ln(\mathbf{tnm})_3(\text{DMSO})_2]$ in comparison with the ideal triangular dodecahedron polyhedron (a), for Yb³⁺(b), Eu³⁺(c), and Nd³⁺(d).

Table 6.2 CShM values for complexes **C26-C29**.

Complex	TTD-8	SAPR-8
C26 [Nd(tnm) ₃ (DMSO) ₂]	0.6363	1.9629
C27 [Eu(tnm) ₃ (DMSO) ₂]	0.5631	1.9233
C28 [Gd(tnm) ₃ (DMSO) ₂]	0.5615	1.9314
C29 [Yb(tnm) ₃ (DMSO) ₂]	0.4967	1.8718

6.4 Photophysical Properties

The photophysical data, which include excited state lifetime decay (τ_{obs}), calculated radiative decay (τ_{R}), intrinsic photoluminescence quantum yield ($\Phi_{\text{Ln}}^{\text{Ln}}$), overall photoluminescence quantum yield ($\Phi_{\text{Ln}}^{\text{L}}$), and calculated sensitisation efficiency (η_{sens}), are reported in Tables 6.3 and 6.4 at the beginning of each of sections 6.4.1 and 6.4.2, respectively. The photophysical measurements were performed in acetonitrile solution *ca.* 10⁻⁵ M at room temperature and 77K and in the solid state as powder. Acetonitrile was chosen as the preferred solvent as in every

case the lifetime decay at room temperature was maintained as monoexponential after 6 hours, which suggests stability of the complexes in such conditions.

The absorption spectra of **tmH/tm** is slightly different to the rest of ligands **L1H-L6H**, with three main absorption bands at 250 nm, 280 nm and 350 nm attributed to π - π^* transitions (see Figure 6.8). The band at 280 nm was not observed for the other ligands and it may be associated with the presence of both keto and enol form in ethanolic solution.²³³ As the conjugation is higher in the enol form, the band is red shifted compared to the keto tautomer.

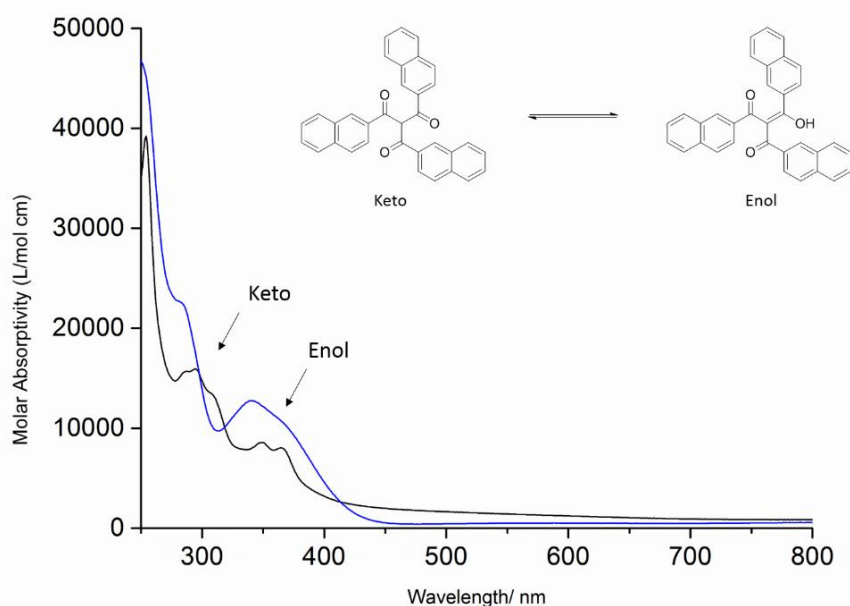


Figure 6.8 Absorption profiles of **tmH** (black trace) and **tm** (excess of KOH, blue trace) at 298K in $10^{-5}M$ ethanol.

The energy of the lowest singlet ($25,907\text{ cm}^{-1}$) and triplet excited states ($19,231\text{ cm}^{-1}$) of the **tm** ligand were determined at the 0-phonon transition from its corresponding $[\text{Gd}(\text{tm})_3(\text{DMSO})_2]$ complex in a frozen acetonitrile matrix (see Figure 6.9). The energy of the triplet state is the lowest found for the β -triketone molecules studied to date, which should assist in promoting near-infrared emission. However, by lowering the triplet state energy, the sensitisation of the $^5\text{D}_0$ of Eu^{3+} ($\sim 17,200\text{ cm}^{-1}$) may not be as efficient due to back energy transfer expected for ΔE lower than $3,500\text{ cm}^{-1}$.⁶¹ In each case, the emission of the complexes is the result of the antenna effect where the broad excitation spectra are analogous to the absorption profiles of the **tm** ligand (see Sections 6.4.1 and 6.4.2).

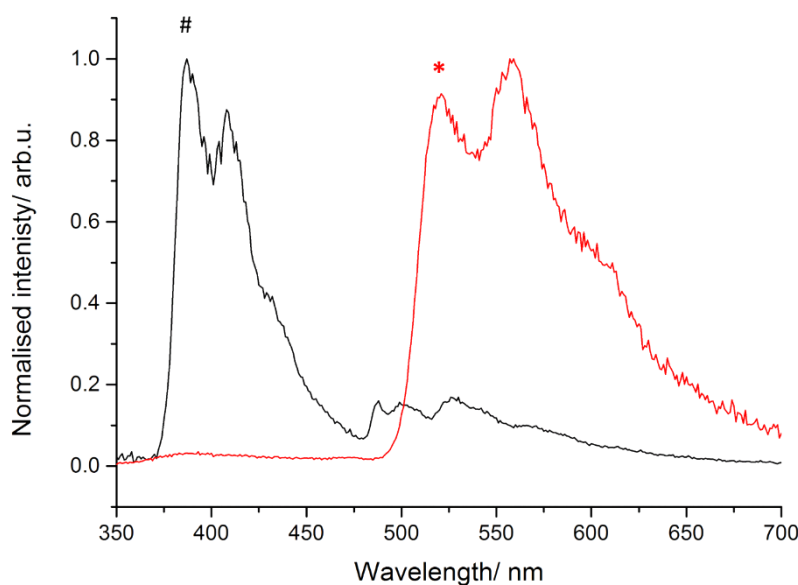


Figure 6.9 Emission of ligand **tnmH** (black trace) and $[Gd(\mathbf{tnm})_3(DMSO)_2]$ (red trace). The # and * symbols indicate de 0-phonon transitions for the singlet and triplet excited states, respectively.

6.4.1 Europium Emission

Table 6.3 Photophysical data for complex $[Eu(\mathbf{tnm})_3(DMSO)_2]$.

Sample	$\tau_{\text{obs}}(\mu\text{s})$	$\tau_{\text{R}}(\text{ms})$	$\Phi_{\text{Ln}}^{\text{Ln}}(\%)$	$\Phi_{\text{Ln}}^{\text{L}}(\%)^{\text{a}}$
MeCN (RT)	20	1.37	1.4	0.2
MeCN (77K)	394	0.88	45	-
Solid State	117	1.48	7.9	9

^a Measured with an integrating sphere.

The emission spectra of $[Eu(\mathbf{tnm})_3(DMSO)_2]$ in the three different conditions show the characteristic Eu^{3+} line-like bands attributed to the ${}^7\text{F}_J \leftarrow {}^5\text{D}_0$ ($J=0-4$) transition in the region 550-750 nm (see Figure 6.10). The ${}^7\text{F}_0 \leftarrow {}^5\text{D}_0$ peak appears narrow for the solid state and frozen matrix ($\sim 35 \text{ cm}^{-1}$) suggestive of the presence of a unique Eu^{3+} site.⁴⁶ The wider appearance ($\sim 70 \text{ cm}^{-1}$) of this peak in the acetonitrile solution at room temperature may be due to a higher degree of freedom where the complex could adopt different geometries. The slightly different splitting of the ${}^7\text{F}_1 \leftarrow {}^5\text{D}_0$ and the ${}^7\text{F}_2 \leftarrow {}^5\text{D}_0$ bands suggests different degrees of distortion between the different media. In the three cases the excited lifetime decays were satisfactorily

fitted to monoexponential functions, the radiative decay (τ_R) was determined from the emission spectra, and the intrinsic quantum yield were calculated as a ratio of τ_{obs}/τ_R and the overall quantum yield with the help of an integrating sphere.

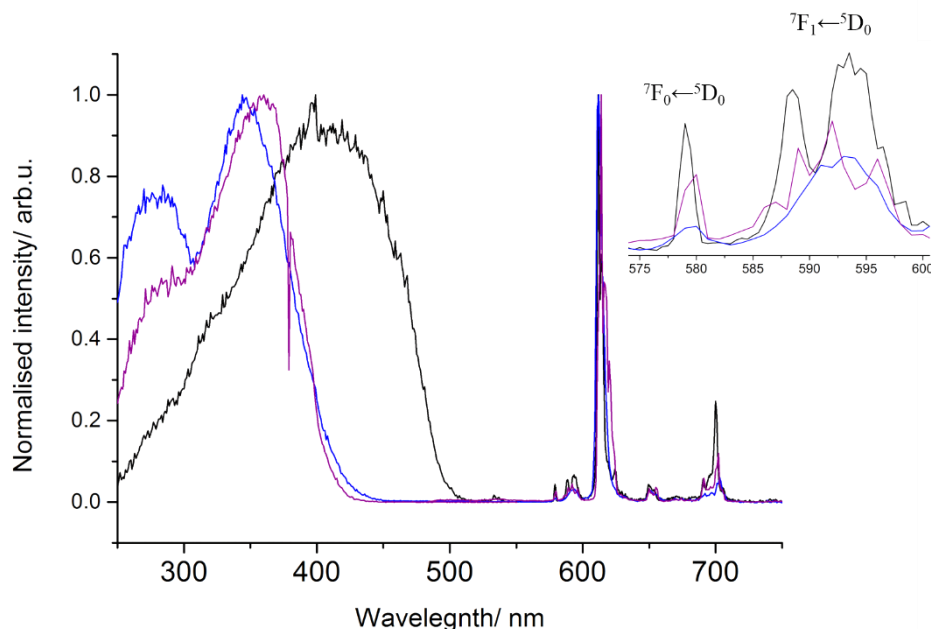


Figure 6.10 Normalised excitation and emission ($\lambda_{\text{exc}}=350$ nm) plot for $[\text{Eu}(\text{tnm})_3(\text{DMSO})_2]$ in the solid state at 298K (black trace), in MeCN at 298K (blue trace) and MeCN at 77K (purple trace). Inset: highlight of the peaks corresponding to the ${}^7F_0 \leftarrow {}^5D_0$ and ${}^7F_1 \leftarrow {}^5D_0$ transition.

In the case of the acetonitrile solution at room temperature, the values of the observable lifetime and radiative decay were found to be 20 μs and 1.37 ms, respectively, giving an intrinsic quantum yield of 1.4%. The short lifetime value and low quantum yield values suggest that the 5D_0 excited state is highly quenched, probably due to reversible energy transfer. The overall quantum yield was calculated to be 0.24% giving a low rate of sensitisation (17%) confirming that back energy transfer (BET) may be occurring from the 5D_0 to the lowest triplet state of the ligand.

When the same measurements were performed in the solid state, the values of lifetime (117 μs), intrinsic quantum yield (7.9%) and overall quantum yield (9%) were slightly improved, presumably due to the rigidity of the sample. Furthermore, the results in a frozen acetonitrile matrix at 77 K suggest BET to be restricted, where the observable lifetime was found to be 20 times longer, with a value of 394 μs , and the intrinsic quantum reached the 45%.

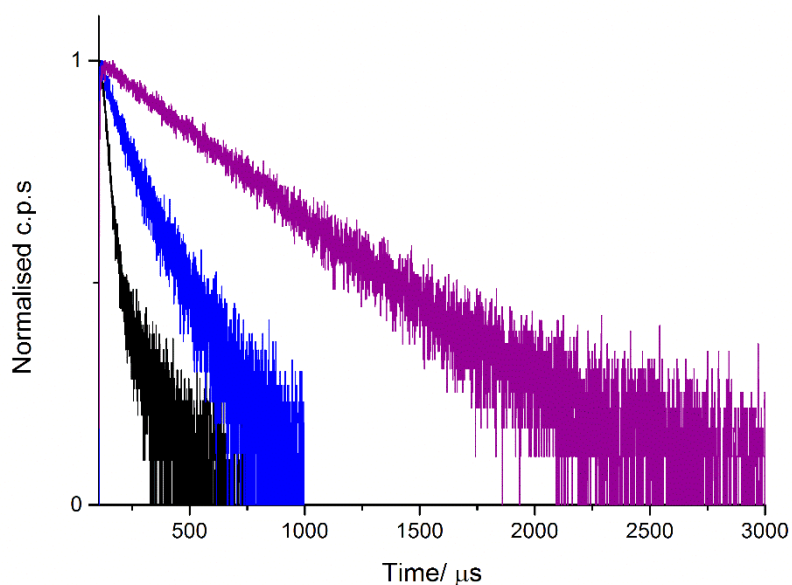


Figure 6.11 Lifetime decay plot at 612nm ($\lambda_{exc}=350$ nm) for $[Eu(tnm)_3(DMSO)_2]$ in the solid state at 298K (black trace), in MeCN at 298K (blue trace) and MeCN at 77K (purple trace).

Taken together, the photophysical data for the Eu^{3+} complex indicate that BET occurring in solution can be restricted in the frozen matrix. These data are in line with previous studies, which report that energy gaps between the lowest ligand triplet state and the lanthanoid excited state smaller than 3500 cm^{-1} can result in BET.⁶¹

6.4.2 Ytterbium and Neodymium Emission

Table 6.4- Photophysical data for complexes $[Yb(tnm)_3(DMSO)_2]$ (C26) and $[Nd(tnm)_3(DMSO)_2]$ (C29).

Complex	Sample	$\tau_{obs}(\mu s)$	$\Phi_{Ln}^{Ln}(\%)$	$\Phi_{Ln}^{Ln}(\%)^a$
C26	MeCN (RT)	39	-	3.6
	MeCN (77K)	44	-	-
	Solid State	18	-	4.2
C29	MeCN (RT)	10	-	0.4
	MeCN (77K)	10	-	-
	Solid State	11	-	1.2

^a Measured with an in-house modified integrating sphere

Characteristic Yb³⁺ NIR-centred emission was observed in the 900-1100 nm region from the [Yb(**tnm**)₃(DMSO)₂] in both the solid state and acetonitrile solution at room temperature (see Figure 6.12). For these spectra the spin allowed ²F_{7/2}←²F_{5/2} transition is split into three different bands due to crystal field effects and presents a shoulder in the 930-960 nm region corresponding to emission from hot bands. The differences in the fine splitting between the two media may be assigned to different degrees of distortion of the Yb³⁺ centres. In the frozen matrix, the emission band is more structured and the emission at 930-960 nm is absent, consistent with the attribution of the emission from “hot” excited states (see Figure 2.15).

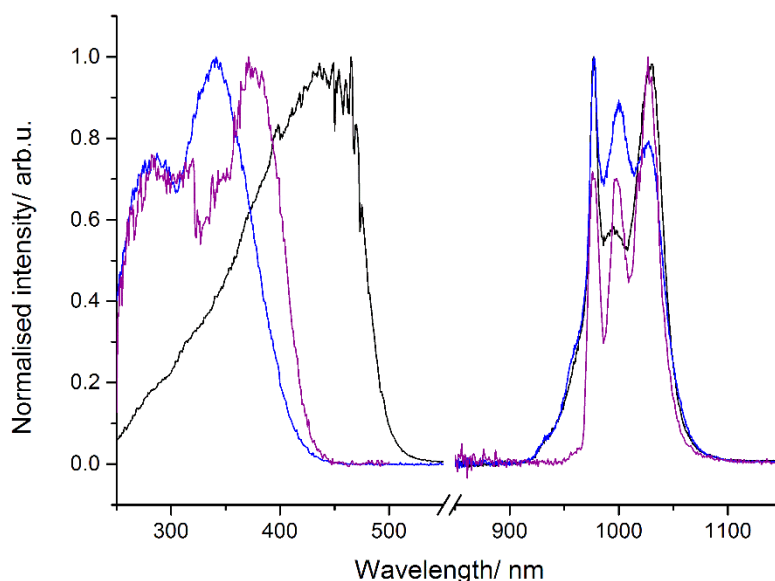


Figure 6.12 Normalised excitation and emission ($\lambda_{exc}=350$ nm) plot for [Yb(**tnm**)₃(DMSO)₂] in the solid state at 298K (black trace), in MeCN at 298K (blue trace) and MeCN at 77K (purple trace).

In the three cases the excited lifetime decays were fitted to monoexponential functions and the overall quantum yields were calculated by the diluted method relative to [Yb(phen)(**tta**)₃] with $\Phi_{Ln}^L = 1.6\%$, for solution measurements, and with the use of the in-house modified integrating sphere for the solid state.

In the case of the solution measurements at room temperature, the lifetime was found to be 39 μ s (see Figure 6.13) with an overall quantum yield of 3.6%. These numbers are much higher than the non-deuterated or non-perfluorinated β -diketonate based systems and in line with the β -triketonate assemblies, with the significant advantage that this complex is soluble in organic solvents such as acetonitrile. Therefore, this complex would be a promising candidate as an emitter in organic light emitting diodes (OLEDs).

In the case of the frozen matrix, the lifetime was found to be only slightly longer, 44 μs , which suggests that vibrational quenching does not seem to significantly affect the Yb^{3+} emission properties at room temperature.

The same photophysical studies were performed in the solid state where a shorter lifetime (18 μs) and comparable values of overall quantum yield (4.2%) were measured. The shorter lifetime may be explained by self-quenching processes occurring in the solid state, while the quantum yield is maintained probably due to a shorter radiative lifetime and/ or a higher sensitisation efficiency in the solid state, as has been previously reported²²⁹ and confirmed in Section 2.4.2.

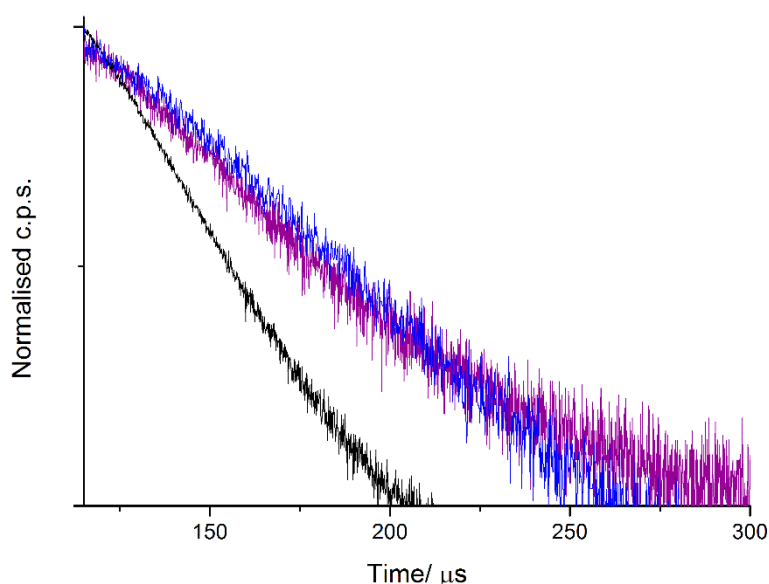


Figure 6.13 Lifetime decay plot at 980 nm ($\lambda_{\text{exc}}=350$ nm) for $[\text{Yb}(\text{tnm})_3(\text{DMSO})_2]$ in the solid state at 298K (black trace), in MeCN at 298K (blue trace) and MeCN at 77K (purple trace).

The Nd^{3+} complex characteristic emission peaks were attributed to the ${}^4\text{I}_J \leftarrow {}^4\text{F}_{3/2}$ ($J= 9/2, 11/2, 13/2$) transition in the 900-1400 region (see Figure 6.14). The structure and splitting of the bands is a consequence of the crystal field effects. The excited lifetime decay was found to be monoexponential in both media after deconvolution from instrumental response. The values of overall quantum yields were recorded in a similar manner to the Yb^{3+} complex.

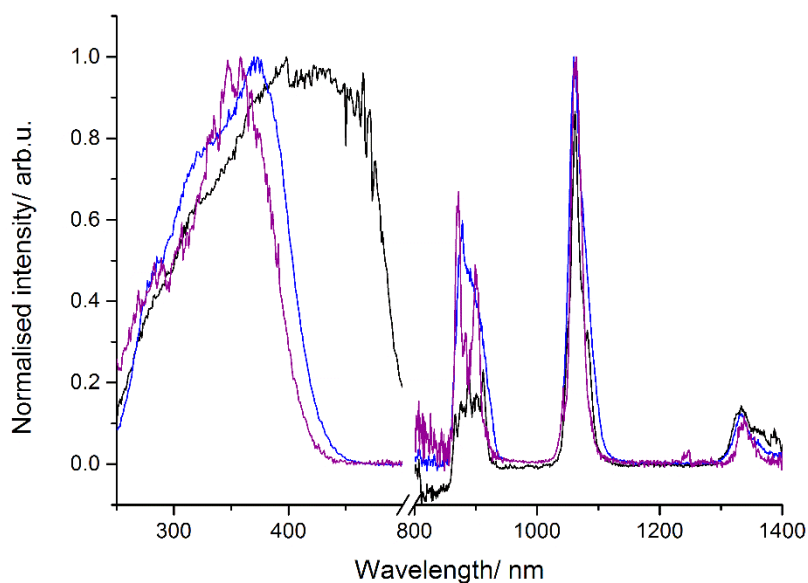


Figure 6.14 Normalised excitation and emission ($\lambda_{exc}=350$ nm) plot for $[Nd(tnm)_3(DMSO)_2]$ in the solid state at 298K (black trace), in MeCN at 298K (blue trace) and MeCN at 77K (purple trace).

In this case, the photophysical data is comparable in the systems at room temperature, with lifetimes of 10 μ s and 11 μ s (see Figure 6.15) and overall quantum yields of 0.4% and 1.2% for the acetonitrile solution and solid state, respectively. The small enhancement of the quantum yield in the solid state may be due to a more effective sensitisation process in the solid state, commonly occurring for the diketonate-based complexes as if was shown in Section 2.4.2. The emission bands at 77 K are visibly more structured, however, the lifetime (10 μ s) is comparable to the room temperature values, suggesting that vibrational modes do not significantly quench the Nd^{3+} emission in this system.

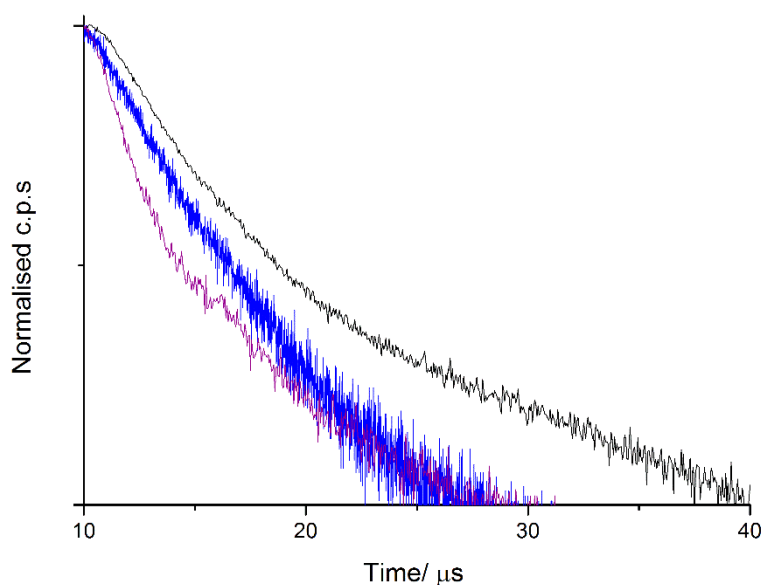


Figure 6.15 Lifetime decay plot at 1060 nm ($\lambda_{exc}=350$ nm) for $[Nd(\mathbf{tnm})_3(\text{DMSO})_2]$ in the solid state at 298K (black trace), in MeCN at 298K (blue trace) and MeCN at 77K (purple trace).

6.5 Conclusions

In this chapter a new synthetic pathway to make β -triketonate-based complexes that are stable in solution has been suggested, resulting in a new family of mononuclear complexes with formula $[\text{Ln}(\mathbf{tnm})_3(\text{DMSO})_2]$ for $\text{Ln}^{3+} = \text{Nd}^{3+}, \text{Eu}^{3+}, \text{Gd}^{3+}$ and Yb^{3+} . The NIR complexes present improved photophysical properties in comparison with their β -diketonates analogues and are comparable to the results achieved with the β -triketonate assemblies. However, these complexes are soluble in organic solvents, which make them good candidates for OLEDs. In contrast, the analogous Eu^{3+} complex was particularly poorly emissive due to efficient energy transfer between the triplet state of the ligand and the excited state of Eu^{3+} . This fact indicates that the emission of the lanthanoid ions can be promoted or quenched by modifying the ligands and consequently, tuning their triplet energy levels.

Chapter 7 Iridium Complexes Using β -Ketonates as Ancillary Ligands

7.1 Introduction

Since the observation of phosphorescence of tris(2,2'-bipyridyl)ruthenium(II) dichloride $[\text{Ru}(\text{bpy})_3]\text{Cl}_2$,²⁵⁴ phosphorescent transition metal complexes have garnered a great deal of attention^{255–259} due to their use in a wide range of applications such as emitters for electroluminescent devices,²⁶⁰ sensitizers for energy and electron transfer,^{96,261–263} photocatalysis^{259,264–267}, dyes for solar cells,²⁶⁸ imaging reagents as biological probes^{269–271} and sensors^{272,273}.

The photophysical properties of d-block metal complexes, such as those presented in Figure 7.1, can easily be tuned by modification of the ligand coordination sphere, in contrast to what occurs for f-metal complexes.²⁷⁴ Therefore, this photophysical tunability can be particularly useful for the sensitisation of the different lanthanoid ions.

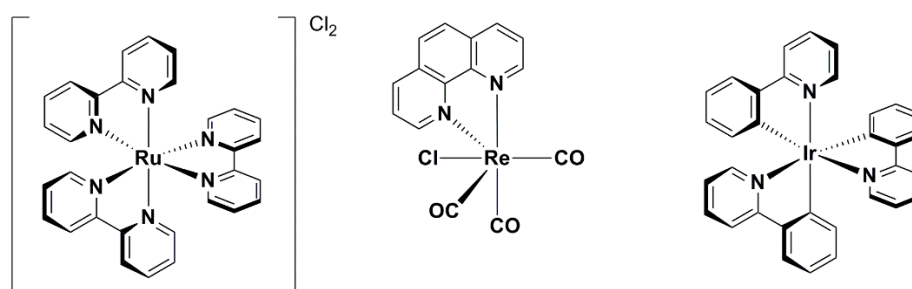


Figure 7.1 Examples of d-metal luminescent complexes: a) $\text{Ru}(\text{II})$ ²⁵⁴, b) $\text{Re}(\text{I})$ ²⁷⁵ and c) $\text{Ir}(\text{III})$ ²⁷⁶.

While centrosymmetric first row transition metal complexes often present metal-centred (MC) transitions as the lowest energy transition, second and third row complexes display low-lying symmetry-allowed transitions such as metal-to-ligand charge transfer (MLCT), ligand-to-metal charge transfer (LMCT) and ligand centred (LC) transitions. These features can easily be explained using molecular orbital (MO) theory.

One the simplest examples is $[\text{Fe}(\text{NH}_3)_6]^{2+}$, where the six coordinating ligands are purely σ -donating in nature. When the electron distribution is considered, the non-bonding t_{2g} orbitals of the metal constitute the HOMO, while the antibonding e_g^* orbitals comprise the LUMO (see Figure 7.2). The resulting transition can be classified as MC in nature. MC transitions in

centrosymmetric molecules are considered forbidden by the Laporte selection rule, which results in low molar absorptivities on the order of $100 \text{ M}^{-1}\text{cm}^{-1}$ or often lower.²⁷⁷ Moreover, the excited state involves the population of metal-based anti-bonding orbitals, which causes structural distortions about the metal leading to efficient non-radiative deactivation. This rapid non-radiative decay of the excited state normally implies a very low efficiency of any other competing emissive process.²⁶⁸ Therefore, these states are not desired and synthesis of phosphorescent transition metal complexes are often designed in order to suppress MC transitions.

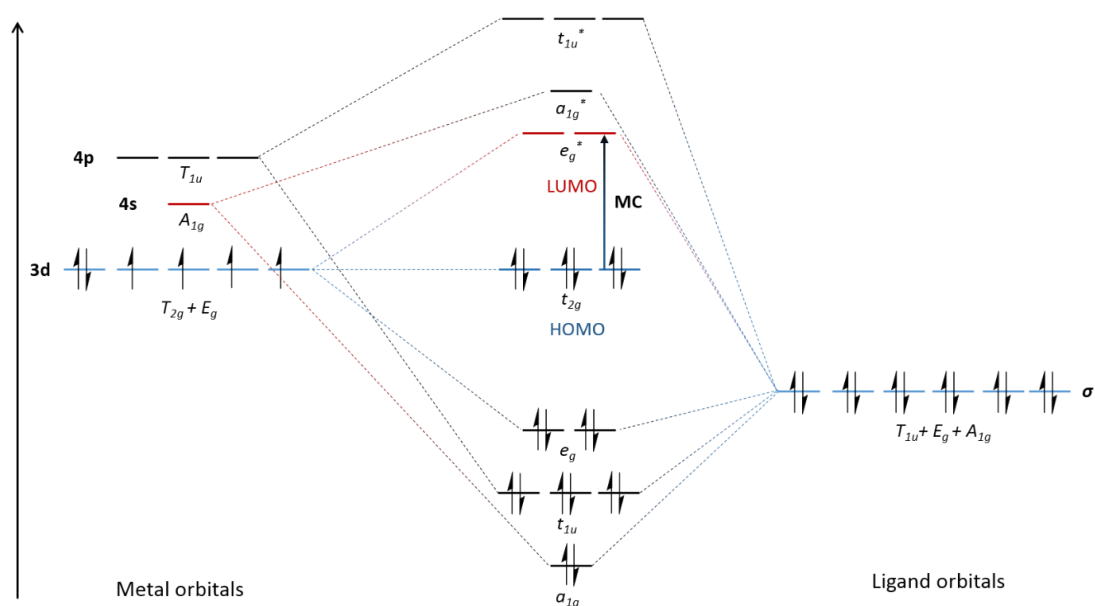


Figure 7.2 Simplified molecular orbital diagram for a first row transition metal containing purely σ -donating ligands such as $[\text{Fe}(\text{NH}_3)_6]^{2+}$.

A simplified molecular orbital (MO) of a low spin d^6 octahedral complex, such as $[\text{Ru}(\text{bpy})_3]^{2+}$, is shown in Figure 7.3. In this case, the frontier orbitals HOMO-LUMO correspond to t_{2g} and t_{2g}^* , respectively. The energy of the e_g^* is higher in energy with respect to the t_{2g}^* because of (1) the large crystal field splitting from the surrounding ligands, (2) the oxidation state of the metal, and (3) the specific position of the metal on the periodic table. The relative position of the t_{2g}^* orbitals is determined mainly by the energy of the $T_{2g} \pi^*$ orbital of the ligand. Therefore, depending on the nature of the ligands involved in the system, the relative energy of the t_{2g}^* orbitals can be modified. The transition involved between the HOMO and LUMO is formally considered MLCT in nature. Charge transfer states (CT) imply the movement of electron density from one site of the molecule to another, which generally translates into low extinction coefficients but covering low energies of the absorption

spectrum. The same behaviour is then expected, for ligand to metal charge transfer states (LMCT), found in this case from the t_{1u} (ligand base) to the e_g^* (metal centre base).

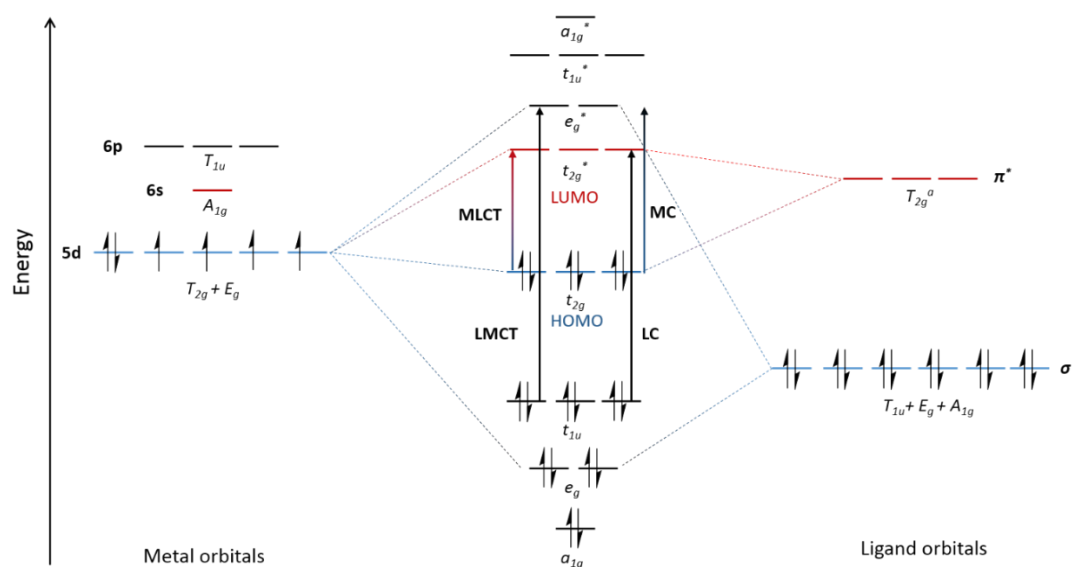


Figure 7.3 Simplified molecular orbital diagram for a d^6 metal complex coordinated to 6 equivalent π -accepting ligands, such as $[Ru(bpy)_3]^{2+}$. Non-bonding π^* orbitals (T_{2u} , T_{1g} , T_{1u}) are excluded for simplicity.

Apart from the CT and MC transitions, already described, ligand-centred (LC) transitions can also be found. These transitions are normally observed at high energy levels (blue to near ultraviolet region) with the highest absorptivity of all the different kinds of transitions as they are localised in the same π -network. CT transitions also include, ligand to ligand charge transfer (LLCT), when two different ligands are involved in the transition, and intraligand charge transfer (ILCT), when the electron is transferred from two different parts of the same ligand.

As explained in Chapter 1, after the absorption of light a singlet excited state gets promoted. In the presence of heavy atoms, such as second and third row d-block metals, ISC is favoured allowing efficient emission from the triplet state. Iridium in particular, has one of the highest SOC constants of $3,909 \text{ cm}^{-1}$ along with platinum ($4,480 \text{ cm}^{-1}$) and gold ($5,104 \text{ cm}^{-1}$).²⁷⁸

As an example, Figure 7.4 shows a diagram for an Ir(III) complex with formula $[Ir(C^{\wedge}N)_2(N^{\wedge}N)]PF_6$, where $C^{\wedge}N$ is a monoanionic cyclometalating ligand such as 2-phenylpyridine and $N^{\wedge}N$ is a chelating neutral diimine ligand such as 2,2'-bipyridine. In this case, the HOMO is usually a combination of the Ir(III) t_{2g} and the π phenyl of the $C^{\wedge}N$ ligand, while the LUMO is frequently localised on the π^* of the $N^{\wedge}N$ ancillary ligand.^{256,279} However,

as previously explained, by modifying the ligand system the relative energy of the HOMO-LUMO gap can be tuned, which would translate to a blue or red shift of the emission.

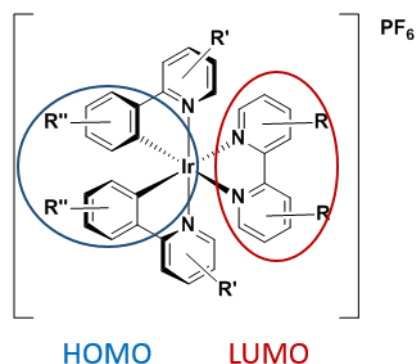


Figure 7.4 Schematic representation of the location of HOMO and LUMO on a cationic Ir(III) complex with R, R' and R'' as substituents.

While many reports can be found related to the tuning of the emission properties of Ir(III) complexes, only a few presenting energy transfer to lanthanoids are available.^{98,102,108,280–285} Indeed, the first bimetallic Ln^{III}-Ir^{III} complex was reported by de Cola *et al.* in 2005 (see structure **1** in Figure 7.5).¹⁰⁸ This complex presents emission from both iridium and europium, resulting in almost white light. The lifetime of iridium decreases from 1.4 μ s to 0.48 μ s, suggesting an efficiency of the iridium to europium energy transfer of 38%. A more efficient example of energy transfer to europium was later observed in complexes **2** and **3** in Figure 7.5.²⁸² In these two examples only emission from Eu³⁺ is observed with quantum yields of up to 17.7% in methanol for the latter complex. An interesting study was published in 2011 where the influence of the triplet state of the N[^]N,O[^]O bringing ligands was assessed (see structure **4** in Figure 7.5).²⁸³ The results suggested that only when the triplet state of the chelating linking ligand is lower than the ³MLCT of iridium and higher than the ⁵D₁ of europium, the energy transfer will be efficient and only europium emission will be observed. In 2014, Ward *et al.* presented a family of compounds based on pyrazoyl-pyridine bridging ligands.⁹⁶ This report presented the coexistence of a photo-induced electron transfer mechanism from the Ir-based excited state to the pyrazoyl-pyridine ligand and direct Dexter type energy transfer from the ³MLCT to the ⁵D₀ of Eu³⁺ or ⁵D₄ of Tb³⁺. Sensitisation of Eu³⁺ in these systems is almost quantitative (95% for **5e**) but poor in the case of Tb³⁺ due to the small energy difference between the ³MLCT and the ⁵D₄ (<1,800 cm⁻¹).

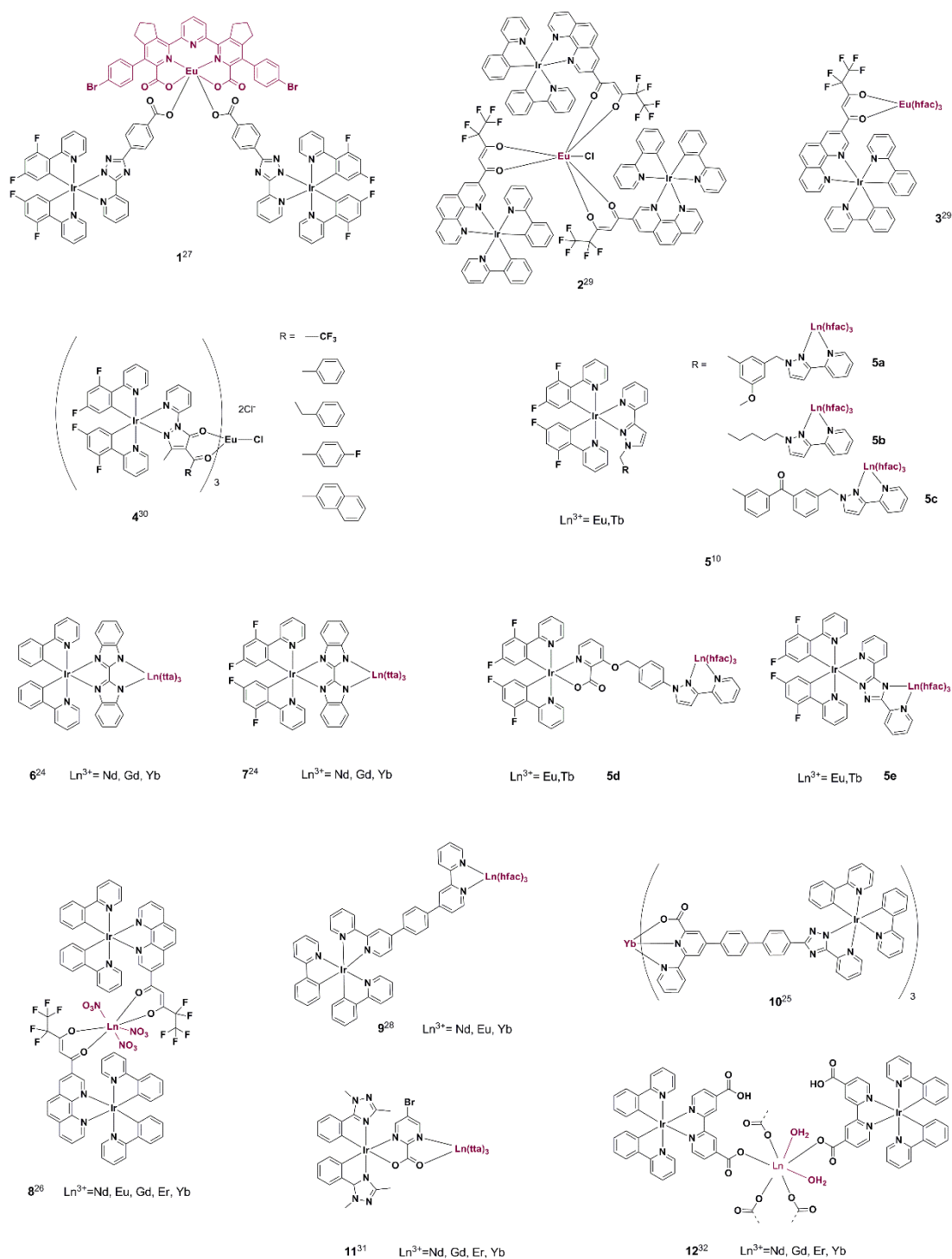


Figure 7.5 Representation of the main Ir-Ln complexes previously reported with the correspondent reference as superscripts.

Examples of NIR lanthanoid sensitisation via iridium excited states have also been reported. Since the first NIR-emitting complex reported in 2008 (structure **8** in Figure 7.5),²⁸¹ complexes have been designed in order to improve the energy transfer efficiency. The best example

presented so far is complex **10** in Figure 7.5, presenting 95% quenching of the iridium luminescence and an energy transfer efficiency of 65% for Yb^{3+} .⁹⁸

As can be observed in Figure 7.5, the majority of the complexes reported to date present ligands coordinated to iridium in a N[^]N coordination mode. In contrast, no examples of C[^]N bridging ligands have been found. In this chapter an attempt to synthesise a bimetallic Ln^{III} - Ir^{III} complex using C[^]N ligands will be presented.

In order to efficiently sensitise the visible-emitting lanthanoid ions, with excited states lying above $18,000\text{ cm}^{-1}$ for the case of Eu^{3+} and Tb^{3+} , the emissive state of the Ir(III) complex must lie at higher energies. Therefore, for this study, the cyclometalating ligand was chosen to be 2-(2,4-difluorophenyl)pyridine (**dFppy**) which, due to the presence of the two electron-withdrawing fluorine atoms, stabilises the energy of the HOMO. Furthermore, two new ancillary ligands, 1-phenyl-3-(4-(pyridin-2-yl)phenyl)propane-1,3-dione (**pydbmH**) and 2-benzoyl-1-phenyl-3-(4-(pyridin-2-yl)phenyl)propane-1,3-dione (**pytbnH**) were designed to simultaneously coordinate to Ir(III) and the lanthanoid ions. Finally, the previously reported **dbm** and **tbn** were employed as ancillary ligands to further probe effect of the extra carbonyl group present in β -triketones has on the optoelectronic properties.

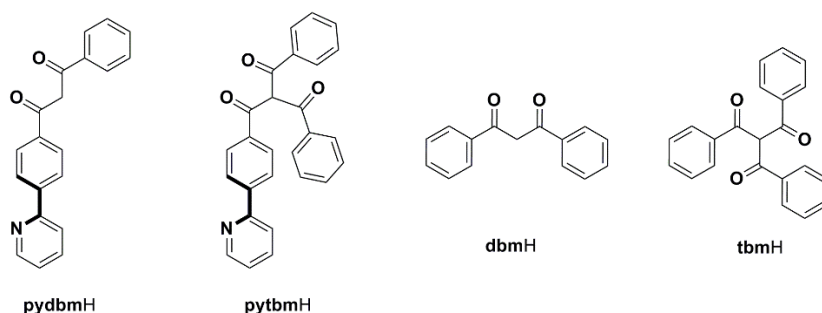


Figure 7.6 Structure of the ancillary ligands used in this chapter.

7.2 Synthesis

7.2.1 Ligands

The C[^]N ligand 2-(2,4-difluorophenyl)pyridine, **dFppyH**, was synthesised according to literature methods by Suzuki-Miyaura cross-coupling reactions.²⁸⁶

The 1-phenyl-3-(4-(pyridin-2-yl)phenyl)propane-1,3-dione (**pydbmH**, **L8H**) was synthesised in two steps via a Claisen condensation to make the intermediate 1-(4-bromophenyl)-3-phenylpropane-1,3-dione (**Br-dbmH**), followed by a Stille cross-coupling reaction to obtain the desired molecule (see Figure 7.7)

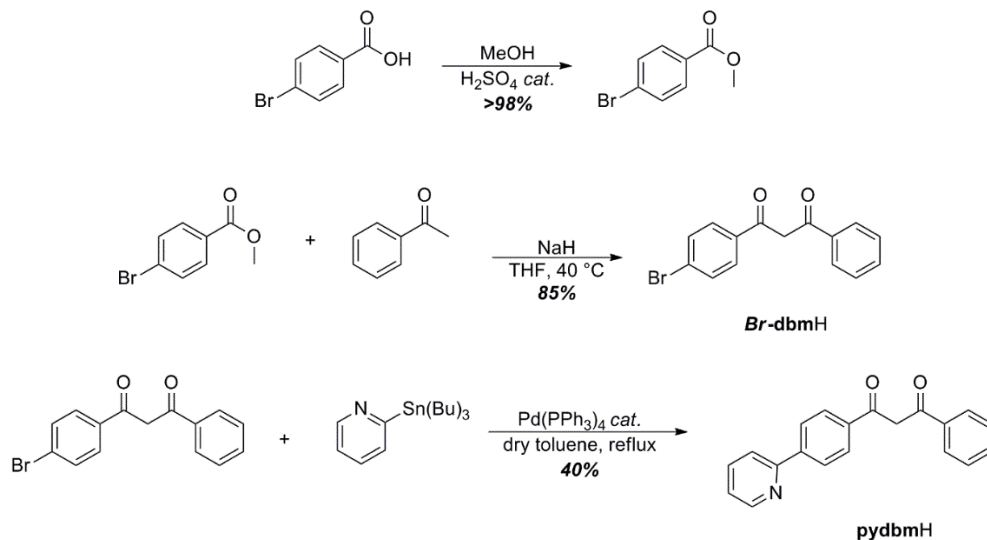


Figure 7.7 Reaction scheme for the synthesis of **pydbmH** (**L8H**).

The **pydbmH** was fully characterised by melting point, $^1\text{H-NMR}$, $^{13}\text{C-NMR}$ spectroscopy, mass spectrometry and elemental analysis (see Section 9.5.1.7). From the $^1\text{H-NMR}$ in chloroform, it can be seen that **L8H** is present as the enol form (see Figure 7.8). This form is the preferred tautomer found for other β -diketones due to the formation of an intramolecular hydrogen bond.²²⁵

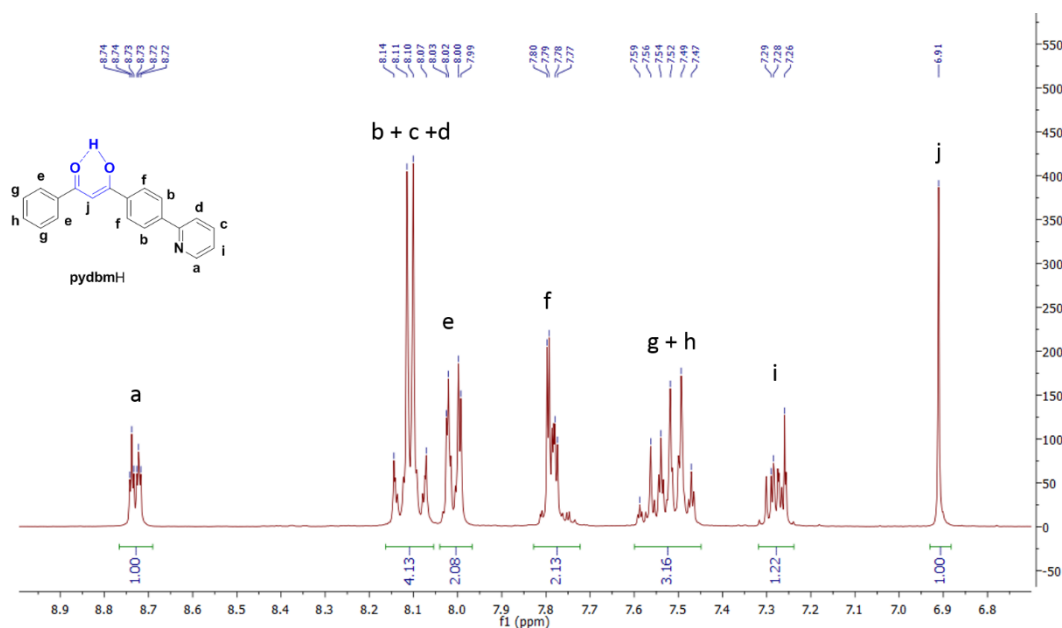


Figure 7.8 Portion of the $^1\text{H NMR}$ spectrum of **pydbmH** (**L8H**).

The 2-benzoyl-1-phenyl-3-(4-(pyridin-2-yl)phenyl)propane-1,3-dione molecule (**pyt**m**H**, **L9H**) was synthesised by reaction of the **pydbmH** and benzoylchloride (see Figure 7.9). This molecule was characterised by melting point, ¹H-NMR, ¹³C-NMR spectroscopy, mass spectrometry and elemental analysis (see Section 9.5.1.8).

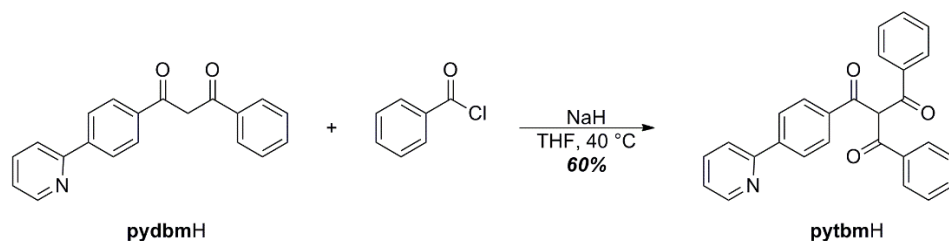


Figure 7.9 Reaction scheme for the synthesis of **pyt**m**H** (**L9H**).

In this case, the main tautomer form found by ¹H-NMR is the keto form as s-cis is not sterically favoured. Moreover the hydrogen bond can no longer be formed due to the longer distances between the oxygen atoms (see Figure 7.10). In fact, taking the **t**m**H** crystal structure as an example, it can be seen that the oxygen atoms do not lie in the same plane and are actually pointing in opposite directions (s-trans) as pointing in the same direction (s-cis) is not sterically favoured (see Figure 5.23).

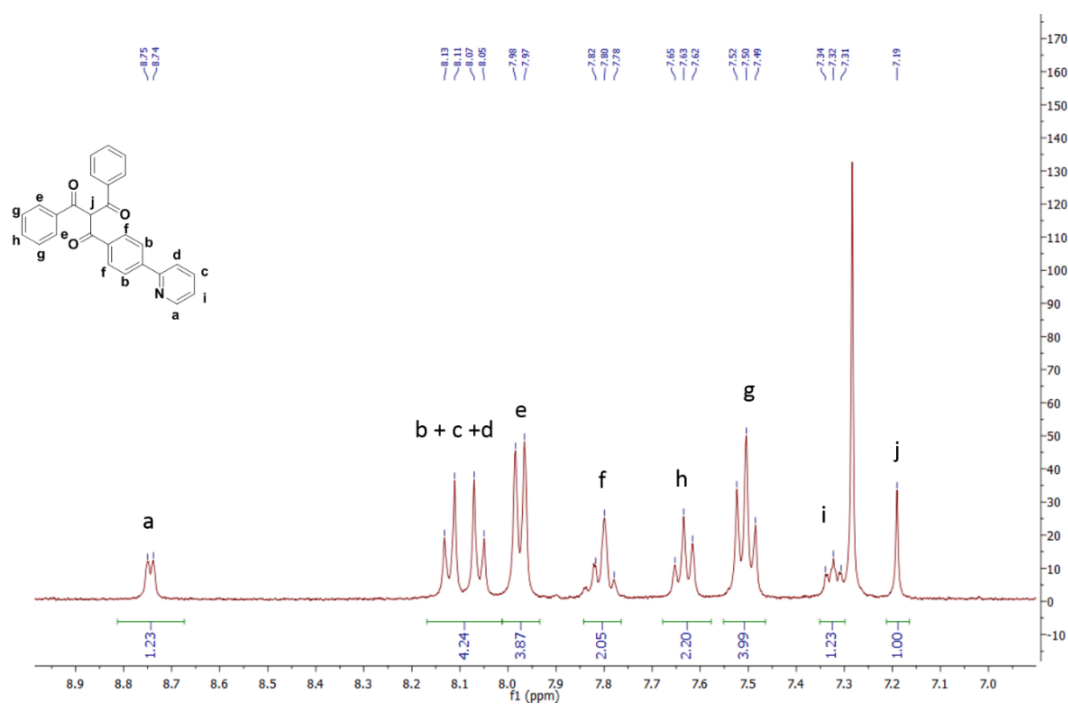


Figure 7.10 Portion of the ¹H-NMR spectrum of **pyt**m**H** (**L9H**).

7.2.2 Complexes

Synthesis of the chloro-bridged dimer, $[\text{Ir}(\text{dFppy})_2(\mu\text{-Cl})_2]$, was first performed by refluxing the dFppyH in 2-ethoxyethanol with IrCl_3 as the iridium source, giving the desired product in a 67% yield. The complexes with the formula $[\text{Ir}(\text{dFppy})_2(\text{L})]$ were then synthesised by cleaving the isolated crude iridium dimers with an excess of **tbmH**, **pydbmH** and **pytbmH**, giving complexes **C30**, **C31** and **C32**, respectively.

For the synthesis of the previously reported complex, $[\text{Ir}(\text{dFppy})_2(\text{dbm})]$, sodium carbonate in 2-ethoxyethanol was used, giving the reported product in 90% yield, where the characterisation matched with that reported (see Section 9.5.2.9).²⁸⁷

When this methodology was followed for the synthesis of **C30** using **tbmH**, the resulting retro-Claisen condensation product was obtained, $[\text{Ir}(\text{dFppy})_2(\text{dbm})]$. However, when triethylamine in a mixture of DCM/EtOH (80:20) was employed instead, the desired complex was isolated in 40% yield (see Figure 7.11). Complex **C30** was fully characterised by melting point, $^1\text{H-NMR}$, $^{13}\text{C-NMR}$, $^{19}\text{F-NMR}$, mass spectrometry and elemental analysis (see Section 9.5.2.9)

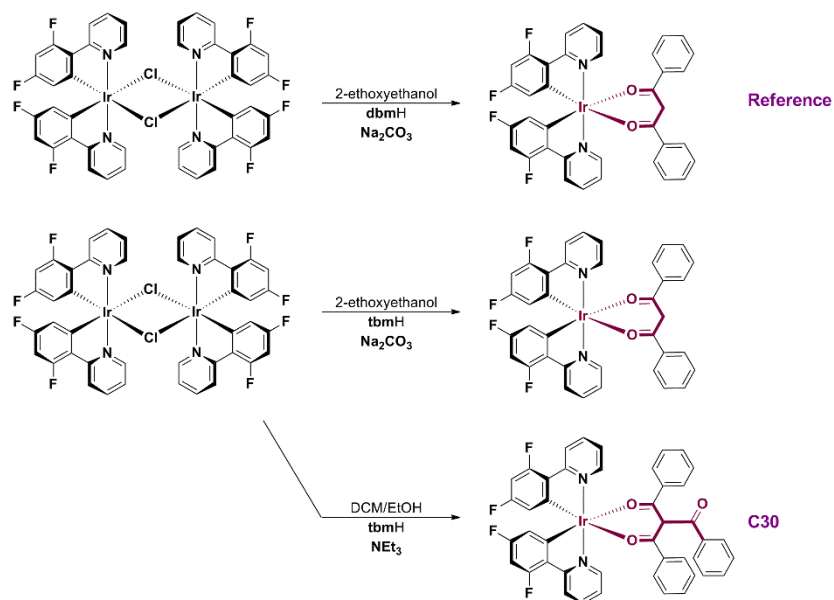


Figure 7.11 Reaction scheme for reference complex $[\text{Ir}(\text{dFppy})_2(\text{dbm})]$ and complex **C30**.

The synthesis of complex **C31** was first attempted without the presence of base in 2-ethoxyethanol. These conditions were chosen to favour the coordination of the **pydbm** in a C[^]N mode leaving the two ketone oxygens free for further lanthanoid coordination. Unfortunately, the crystal structure of the resulting purified product showed coordination of the ligand in a ketonate mode (see Figure 7.12). Therefore, this complex could not be used as a bridge molecule for d-f energy transfer. The conditions of the complexation reaction were then modified in an attempted to increase the yield of the reaction. In fact, when NEt₃ and a mixture of DCM/EtOH (80:20) were used, the complex [Ir(dFppy)₂(**pydbm**)] was synthesised in a high yield of 90%. This compound was fully characterised by melting point, ¹H-NMR, ¹³C-NMR, ¹⁹F-NMR, mass spectrometry and elemental analysis (see Section 9.5.2.9).

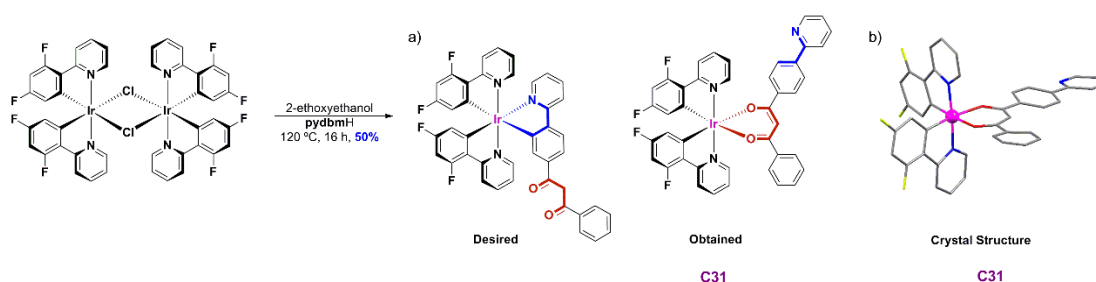


Figure 7.12 Reaction scheme highlighting the desired and obtained complex (a) and crystal structure (b) for complex **C31**.

Finally, complex **C32** was synthesised following the O[^]O coordination conditions. Unfortunately, the desired complex could not be isolated and only the retro-Claisen condensation complex, [Ir(dFppy)₂(**pydbm**)], was obtained as the main product of the reaction.

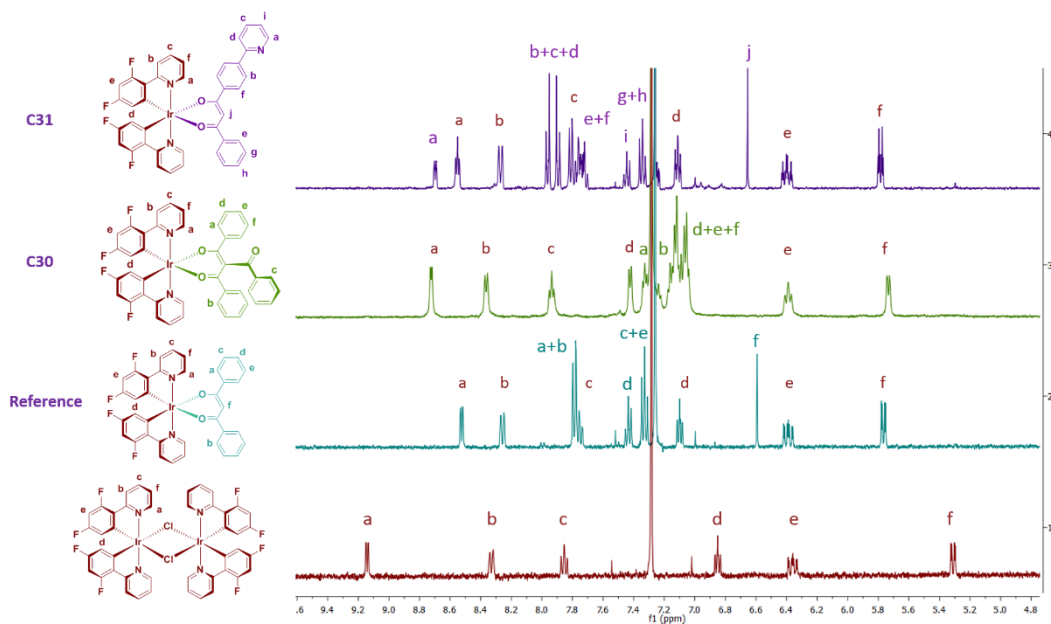


Figure 7.13 Portion of the ¹H-NMR spectrum of [Ir(dFppy)₂(μ-Cl)₂] (red trace), [Ir(dFppy)₂(dbm)] (turquoise trace), [Ir(dFppy)₂(tbm)] (green trace) and [Ir(dFppy)₂(pydbm)] (purple trace).

7.3 X-Ray diffraction Studies

The literature reports stated that the [Ir(dFppy)₂(dbm)] complex crystallised as two polymorphs, one in the space group $C_{2/c}$ and the other one in $P\bar{1}$.²⁸⁸ The main difference between the two is the presence of different π - π interactions between two neighbouring complexes, involving two dFppy, one dFppy and one dbm or two dbm ligands.

In contrast, in the case of complexes **C30** and **C31**, where crystals were obtained by slow diffusion of ether into a dichloromethane solution of the complex, only one crystal form was found. Complex **C31** crystallised in the triclinic $P\bar{1}$ space group. In each unit cell, two similar but symmetrically inequivalent Ir(III) units are found, with a Ir...Ir distance of 8.853 Å. The CShM values for the two centres were found to be 0.609 and 0.527 with respect to ideal octahedral geometry, which suggests slightly different degrees of distortion. These two Ir(III) complexes are connected by π - π interactions involving the offset pyridine group of the dFppy ligand and the phenyl ring of the phenylpyridine moiety of **pydbm**, with an interplanar distance of 3.315 Å, an interplanar angle of 7.33°, and a centroid-to-centroid distance of 3.803 Å (see Figure 7.14 and A.6). In the case of **C30**, the complex crystallised in the monoclinic $I_{2/a}$ space group, where the coordination of the Ir(III) can be best described as distorted octahedra with CShM value of 0.609. In contrast to the structure of complex **C31**, only one iridium centre and one kind of π - π interaction are found (see Figure 7.15). The π - π stacking is present between adjacent and offset dFppy fragments with interplanar and centroid to

centroid distances of 3.300 Å and 3.670 Å, respectively. Interactions involving the lone pair of the non-coordinating ketone oxygen and a phenyl ring of two adjacent **tbm** moieties with C...O distances of 3.217 Å can also be observed.

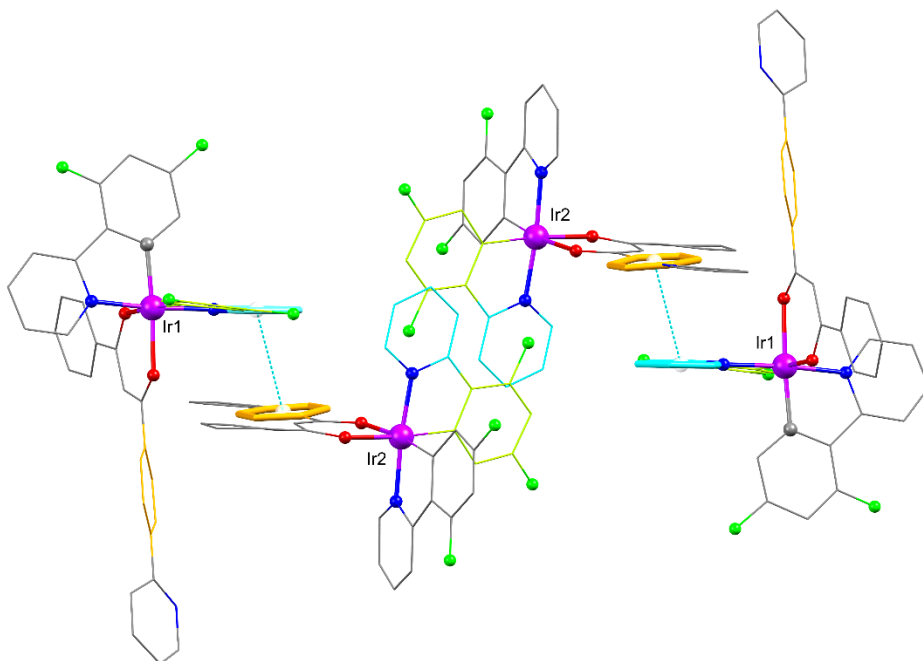


Figure 7.14 Representation of the X-ray crystal structure of $[\text{Ir}(\text{dFppy})_2(\text{pydbm})]$, emphasising the supramolecular composition formed by π - π stacking interactions. Hydrogen atoms and molecules of solvent have been omitted for clarity.

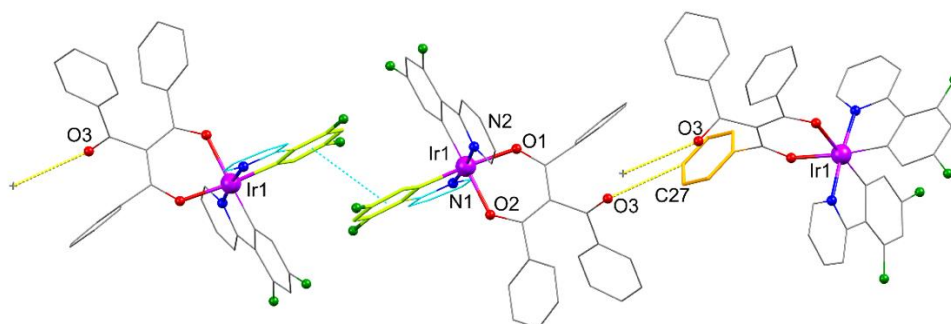


Figure 7.15 Representation of the X-ray crystal structure of $[\text{Ir}(\text{dFppy})_2(\text{tbm})]$, emphasising the supramolecular structure formed by intermolecular interactions. Hydrogen atoms and molecules of solvent have been omitted for clarity.

7.4 UV-VIS Studies

The absorption spectra in acetonitrile of the complexes **C30** and **C31** and the reference, $[\text{Ir}(\text{dFppy})_2(\text{dbm})]$, are presented in Figure 7.16. Complexes **C30** and **C31** present relatively

unstructured spectra comparable to the $[\text{Ir}(\text{dFppy})_2(\text{dbm})]$ which shows reproducible profile to that reported in the literature.²⁸⁸ Complexes **C30** and **C31**, however, show higher molar absorptivity likely due to the presence of the extra acyl group and pyridine ring, respectively. The high energy absorptions are assigned to $\pi\text{-}\pi^*$ transitions of the dFppy (250 - 350 nm)^{289,290} and LX ligands (LX= **tbm**, **pydbm**) (250 – 400 nm).^{291,292} The low energy band at 400 - 450 nm is attributed to the metal-to-ligand charge transfer transition ($^1\text{MLCT}$), while bands above 450 nm can be assigned to mixed $^3\text{MLCT}$.²⁸⁸ The onset of the CT bands is comparable for the three complexes which suggests that these bands are based on the π orbitals of the dFppy ligand and similar metal e_g^* orbitals.

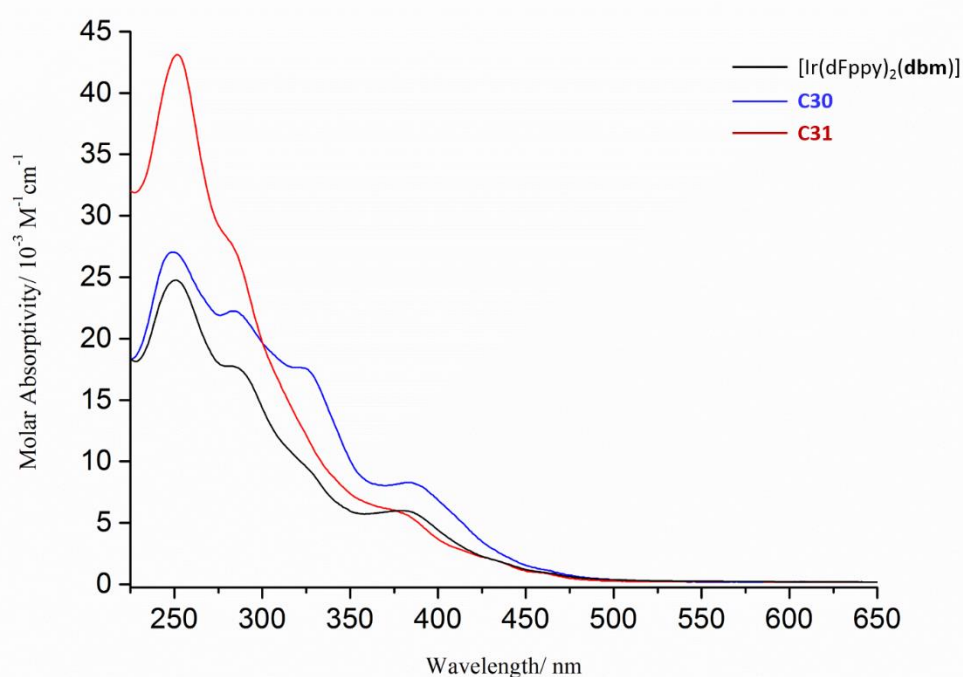


Figure 7.16 Absorption profiles of $[\text{Ir}(\text{dFppy})_2(\text{LX})]$ for LX=**dbm** (black trace), **tbm** (blue trace) and **pydbm** (red trace) in acetonitrile ($\text{ca.}10^{-5}\text{M}$).

7.5 Electrochemistry

The electrochemical properties were studied by cyclic voltammetry (CV) and differential pulse voltammetry (DPV) in de-aerated MeCN at 298K in order to measure the energies of the frontier molecular orbital of the synthesised complexes. $n\text{-NBu}_4\text{PF}_6$ was used as the supporting electrolyte and the ferrocene/ferrocenium (Fc/Fc^+) redox couple was employed as the internal standard. A summary of the redox potentials of the complexes, referenced with respect to the saturated calomel electrode (SCE, $\text{Fc}/\text{Fc}^+ = 0.38 \text{ V}$ in MeCN)²⁹³, is given in

Table 7.3. The HOMO and LUMO energy levels were determined following Equations 7.2 and 7.3²⁹⁴:

$$E_{HOMO} = - \left[E_{ox \text{ vs } \frac{Fc}{Fc^+}} + 4.8 \right] eV \quad (7.1)$$

$$E_{LUMO} = - \left[E_{red \text{ vs } \frac{Fc}{Fc^+}} + 4.8 \right] eV \quad (7.3)$$

Table 7.1 Electrochemical data for complexes **C30**, **C31** and the reference, [Ir(dFppy)₂dbm].

Complex	E _{ox} (V) ^a	HOMO (eV)	E _{red} (V) ^a	LUMO (eV)	Energy gap (eV)
<i>fac</i> -Ir(dFppy) ₃	0.76	-5.56	-2.49	-2.31	3.25
[Ir(dFppy) ₂ (acac)]	0.76	-5.56	-2.44	-2.36	3.20
[Ir(dFppy) ₂ dbm]	1.05	-5.85	-1.85	-2.95	2.90
C30 [Ir(dFppy) ₂ tbm]	1.30	-6.10	-1.67	-3.13	2.97
C31 [Ir(dFppy) ₂ pydbm]	1.10	-5.81	-1.60	-3.20	2.61

Measurements were performed in MeCN at 298K at a scan rate of 100 mV/s with Fc/Fc⁺ used as an internal standard.
^a Potential values were obtained from the DPV data.

The electrochemistry of the related tris-cyclometalated Ir(III) complexes, *fac*-Ir(dFppy)₃, has been previously studied.²⁹⁵ The reversible oxidation is considered to involve the iridium ion and π orbitals of the difluorophenyl (dFph) part of the dFppy ligands (Ir(III)/Ir(IV) + dFph) whereas the reduction is localised on the pyridyl ring of the dFppy ligands. Thus, if oxidation or reduction processes involving the ancillary ligand do not take part in these systems, these complexes will present a comparable behaviour to the *fac*-Ir(dFppy)₃. The electrochemical reported values for the *fac*-Ir(dFppy)₃ are E_{ox} = 0.76 V; E_{red} = -2.49 V vs SCE and energy gap = 3.25 eV. Indeed, some examples such as the well-studied [Ir(dFppy)₂(acac)],²⁹⁶ have been reported in literature suggesting comparable electrochemical properties (E_{ox} = 0.76 V; E_{red} = -2.44 V vs SCE) to the *fac*-Ir(dFppy)₃.

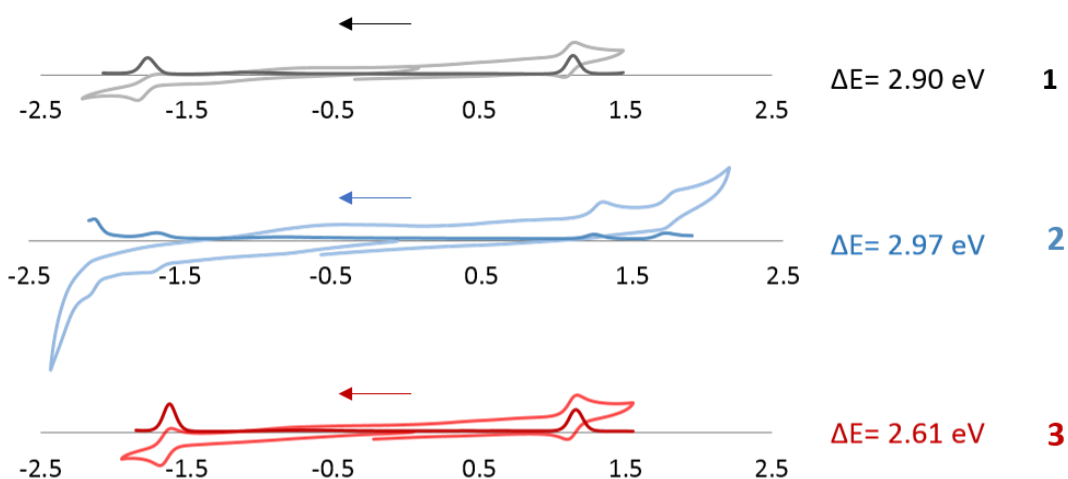


Figure 7.17 CV and DPV traces of reference (black trace), C30 (blue trace) and C31 (red trace), versus SCE ($Fc/Fc^+ = 0.38$ V in MeCN) redox couple. Scan rates were at 100 mVs^{-1} , in the negative direction.

The oxidation potentials of the complexes were found at 1.05 V, 1.30 V and 1.10 V for the reference, **C30**, and **C31**, respectively (see Figure 7.17). These numbers vary significantly from the oxidation value for the tris-cyclometalated complex ($E_{\text{ox}} = 0.76$ V), suggesting some contribution from the ancillary ligands. Indeed, the oxidation waves of the reference compound and **C31** are pseudo-reversible while **C30** is irreversible, which is another indication that the oxidation process in this latter case is not occurring on the metal centre. Furthermore, while the reference compound and complex **31** show similar oxidation potentials, complex **30** presents a more stabilised HOMO, which may be indicative of a stronger contribution of **tbm** in comparison to **dbm** or **pydbm**. When looking at the reduction potential values ($E_{\text{red(R)}} = -1.85$ V, $E_{\text{red(C30)}} = -1.67$ V and $E_{\text{red(C31)}} = -1.60$ V) a significant change with respect the reduction of *fac*-Ir(dFppy)₃ ($E_{\text{red}} = -2.49$ V) is representative of an ancillary-based LUMO in agreement with previous assignments in literature for the [Ir(dFppy)₂(**dbm**)].^{287,288} Surprisingly, significantly different values of the oxidation and reduction potentials as well as the energy gap were found in literature for this complex ($E_{\text{ox}}^{287} = 0.32$ V, $E_{\text{red}}^{287} = -2.02$ V and $\Delta E^{287} = 2.34$ eV vs. $E_{\text{ox}}^{36} = 0.73$ V, $E_{\text{red}}^{36} = -2.16$ V and $\Delta E^{36} = 2.64$ eV),^{287,288} being also different to the experimental data observed herein under similar conditions ($E_{\text{ox(R)}} = 1.05$ V, $E_{\text{red(R)}} = -1.85$ V and $\Delta E_{\text{(R)}} = 2.90$ eV). This may be due to the water content present in the system, as it can influence the energy of the electronic states.^{297,298} In the case presented here, anhydrous acetonitrile was used and the solution was degassed with solvent-saturated nitrogen bubbling for 10 min prior scanning.

The LUMO for complexes **C30** and **C31** are more stabilised than the reference compound, probably because of the electron withdrawing nature of the pendant acyl group and, to a higher degree, the pyridine ring, respectively. The HOMO-LUMO energy gap were thus calculated to be 2.90 eV, 2.97 eV and 2.61 eV for the reference compound, **C30** and **C31**, respectively (see Figure 7.18).

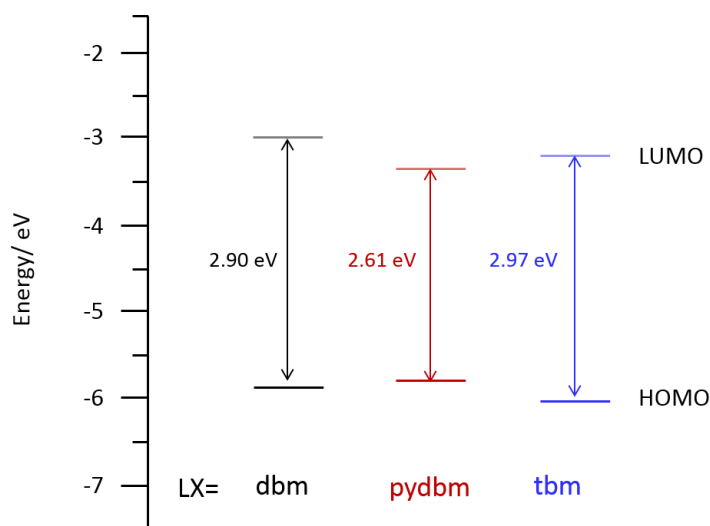


Figure 7.18 Energy gap representation for complexes $[Ir(dFppy)_2LX]$ according to the electrochemical experimental data.

7.6 Photophysical Properties

The photophysical properties of the three complexes were study in acetonitrile solution at room temperature and in a dichloromethane frozen matrix, in doped films (10 wt% in PMMA) and in the solid state as powdered samples. The photophysical data, including excited state lifetime decay (τ_{PL}) and photoluminescence quantum yield (Φ_{PL}), are reported in Table 7.2 and Table 7.3.

The room temperature emission spectra of the three complexes in deaerated acetonitrile show a very weak emission at 629 nm, 498 nm and 625 nm for the $[Ir(dFppy)_2(\mathbf{dbm})]$, **C30** and **C31**, respectively (see Figure 7.19). In the case of the reference and **C31**, the broad emission band is significantly red-shifted in comparison with the featured emission of *fac*- $Ir(dFppy)_3$ at 469 nm and previously assigned to mixed MLCT/LC transitions.²⁹⁵ Furthermore, the lifetimes were found to be on the order of nanoseconds ($\tau_R = 12$ ns and $\tau_{C30} = 7.5$ ns) and the quantum yields below 1%. This photophysical profile highly contrasts with the lifetime and quantum yields of the MLCT/LC of the *fac*- $Ir(dFppy)_3$ ($\tau = 1.64$ μ s, $\Phi_{PL} = 77\%$).²⁹⁵ Indeed, reported DFT calculations for **1** suggested that the emission had MLCT/ILCT character and the poor

emissive properties in solution were caused by efficient non-radiative decays promoted by strong vibrations of the **dbm** in the low frequency region.²⁹⁹ Therefore, comparable behaviour could be expected for complex **C31**. In the case of **C30**, although the emission peak is not significantly shifted with respect to the ³MLCT/LC found for *fac*-Ir(dFppy), the lifetime (30 ns), quantum yield ($\Phi_{PL} = 2\%$) and shape of the emission bands are not indicative of a charge transfer emission and are more characteristic of LC emission (LX).

The photoluminescence spectra were also studied in deaerated dichloromethane at room temperature in order to assess the impact of using nonpolar solvents. CT states are frequently found to be stabilised on increasing the solvent polarity.^{300–304} This effect is commonly known as positive solvatochromism. However, solvatochromism is an extremely complex phenomenon as many different interactions and dynamical processes can take place. Indeed, the experimental data for the reference and **C31** showed an unusual but not unprecedented^{305,306} negative solvatochromic shift (see Figure 7.19). This may indicate a decreased dipole moment in the excited state with respect to the ground state, which translates into a higher stabilisation of the ground state in more polar solvents as previously suggested.³⁰⁵ In any case, this hypsochromic shift is suggestive of charge-transfer character for these transitions. In contrast, the emission maximum was retained for complex **C30**, which confirms that this transition may be LC in nature.²⁸⁹

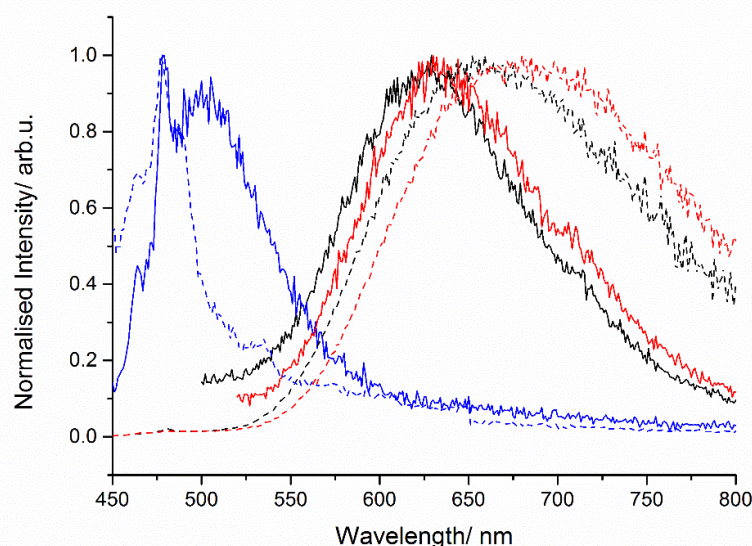


Figure 7.19 Normalised emission ($\lambda_{exc}=420$ nm) spectra for $[\text{Ir}(\text{dFppy})_2(\text{dbm})]$ (black trace), $[\text{Ir}(\text{dFppy})_2(\text{tbm})]$ (red trace) and $[\text{Ir}(\text{dFppy})_2(\text{pydbm})]$ (blue trace) in acetonitrile solution (10^{-5}M) at RT (dark trace) and dichloromethane at RT (dashed trace).

When the emission properties were studied in a dichloromethane frozen matrix, a clear blue-shift was identified in the reference and complex **C31**, while the emission of **C30** remained constant (see Figure 7.20). The fact that non rigidochromic shift was found in the emission maximum in **C30** can be explained as a function of the ^3LC nature of the emission. In contrast, the blue-shifted emission of the reference and **C31** suggests $^3\text{MLCT}$ character, in agreement with the literature and previous experimental results presented herein.²⁸⁷ The three complexes in the frozen matrix presented improved lifetime values of 800 ns, 3.77 μs and 630 ns for the reference, **C30** and **C31**, respectively. This improvement in lifetime can be explained by a reduction of the vibrational motions at 77 K, which makes quenching of radiated transitions less likely. While the reference and **C31** present similar values of lifetimes, **C30** is much longer, which is another indication that in this case, the transition seems to be LC in nature.

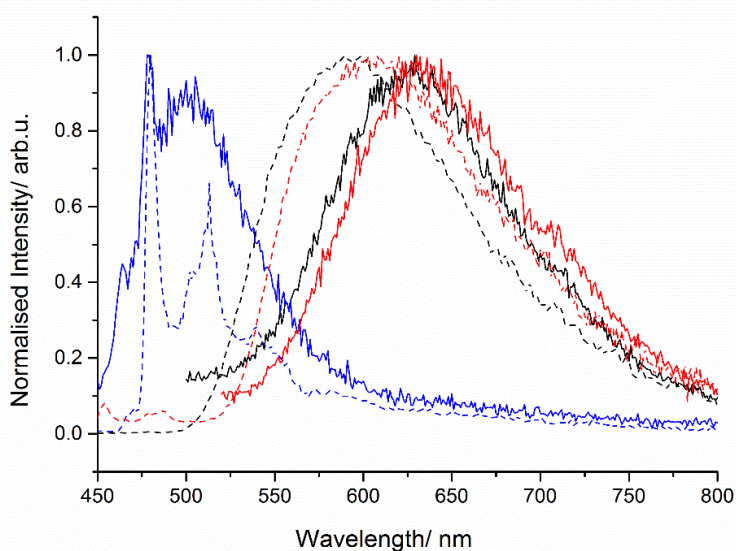


Figure 7.20 Normalised emission ($\lambda_{\text{exc}}=420$ nm) spectra for $[\text{Ir}(\text{dFppy})_2(\text{dbm})]$ (black trace), $[\text{Ir}(\text{dFppy})_2(\text{tbm})]$ (blue trace) and $[\text{Ir}(\text{dFppy})_2(\text{pydbm})]$ (red trace) in acetonitrile solution (10^{-5}M) at RT (dark trace) and dichloromethane 77K (dashed trace).

In order to better elucidate the nature of each emission spectrum, the triplet state of the three ancillary ligands were estimated at the 0-phonon transition of the phosphorescence spectra of their gadolinium complexes, finding values of 487 nm, 183 nm and 504 nm for the **dbm**, **tbm** and **pydbm**, respectively (see Figure 7.21). The triplet state values of **dbm** and **tbm** were in accordance with previously reported data.^{26,173,175} In fact, the emission profile and lifetime value of complex **C30** at 77 K seems to be consistent with the ligand phosphorescence spectrum of **tbm** in the frozen matrix, confirming that this transition is localised almost exclusively in the **tbm** moiety. In the case of **dbm** and **pydbm**, the emission wavelength and feature of the bands are different to what it was observed for reference and **C31**, respectively.

However, the fact that their triplet excited state level lies lower in energy than the ³MLCT indicates possible contribution of the LC state based on the ancillary ligands.

Table 7.2 Photophysical data of the synthesised complexes in solution (ca. 10⁻⁵M) at RT and 77K.

Complex	Sample	λ_{PL} (nm)	Φ_{PL} (%) ^a	τ (ns)
[Ir(dFppy) ₂ dbm]	MeCN-RT	629	1.02	12
	DCM-RT	660	-	18
	DCM-77K	595	-	800
C30 [Ir(dFppy) ₂ tbm]	MeCN-RT	498	2.1	2(35%), 30(65%)
	DCM-RT	477	-	17
	DCM-77K	478	-	3770
C31 [Ir(dFppy) ₂ pydbm]	MeCN-RT	625	0.5	7.5
	DCM-RT	679	-	10
	DCM-77K	607	-	630

^a quantum yield in MeCN solution relative to [Ru(bpy)₃](PF₆)₂ in MeCN (Φ_{PLref} = 9.5%).³⁰⁷

Table 7.3 Photophysical data of the synthesised complexes doped films and powder.

Complex	Sample	λ_{PL} (nm)	Φ_{PL} (%) ^a	τ_{PL} (ns)	k_r (10 ⁻⁶ s ⁻¹)	k_{nr} (10 ⁻⁶ s ⁻¹)
[Ir(dFppy) ₂ dbm]	Film ^b	542	8.2	3 (71%), 140 (17%), 425 (12%)	-	-
	Powder	578	21	360	5.78	21.94
C30 [Ir(dFppy) ₂ tbm]	Film ^b	542	8.9	1 (34%), 3 (37%), 11 (28%)	-	-
	Powder	644	3.0	13	22.58	727.70
C31 [Ir(dFppy) ₂ pydbm]	Film ^b	550	6.3	4 (33%), 116 (42%), 358 (26%)	-	-
	Powder	612	5.9	97	6.20	97.21

^a Photoluminescence quantum yield measured with an integrating sphere. ^b Films were prepared by doping 10 wt% of the complex in PMMA.

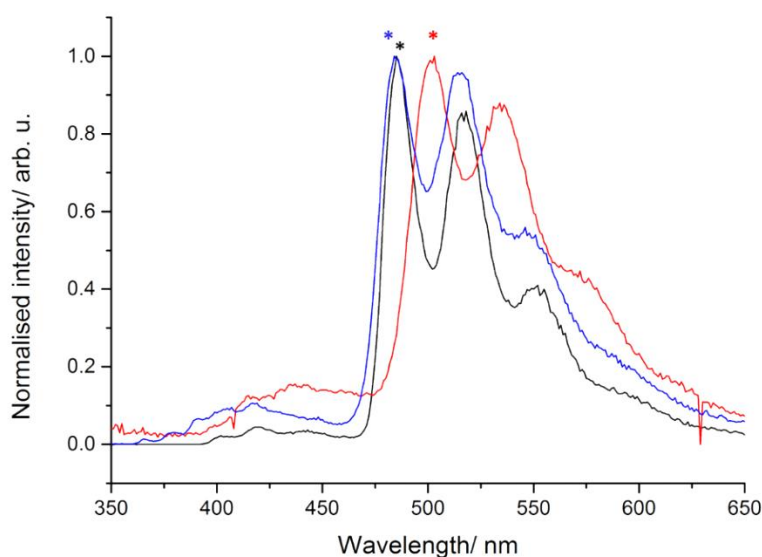


Figure 7.21 Normalised emission ($\lambda_{exc}=300$ nm) of the **dbmH** (black trace), **tbmH** (blue trace) and **pydbmH** (red trace) Gd^{3+} complexes where the * symbol indicates the 0-phonon transition for the triplet excited state.

In contrast to the weak emission found for the three complexes in solution, intense luminescence was produced at ~ 550 nm when the complexes were doped into films (10 wt% in PMMA), with improved photoluminescence quantum yields of 8.2%, 8.9% and 6.3% for the reference, complexes **C30** and **C31**, respectively. As observed for $[Ir(dFppy)_2\mathbf{dbm}]$,^{287,288} the mechanism of phosphorescence emission for complexes **C30** and **C31** is altered by intermolecular interactions. These interactions promote the formation of new lower energy states that seem to present reduced non-radiative decays. Interestingly, the maximum emission wavelength is similar for the three cases at ~ 550 nm, which may indicate the presence of delocalised transitions between the ancillary and cyclometalating ligands, as previously suggested for $[Ir(dFppy)_2\mathbf{dbm}]$.²⁹²

Furthermore, when the same study was performed with the crystalline sample, where there can be a different set of intermolecular interactions, a red-shift in the emission maximum was found in every case (see Figure 7.22). These data suggest that possible excited states of different nature, formed due to the different intermolecular interactions and probably involving the ancillary ligands, may be also taking place. Interestingly, the largest shift was found for complex **C30**, which happened to present the strongest ancillary ligand-based interactions as assessed by the relatively shorter distance of 3.2 Å, against 3.4 Å for the **dbm** and **pydbm** ligands. Photoluminescence quantum yields and excited state lifetimes in the solid state were measured to be 21 %, 3 % and 6 % and 361 ns, 13 ns and 97 ns for the reference, **C30** and **C31**, respectively. These data suggest that the **dbm** complex is a more efficient

emitter in the powder. Indeed, while radiative decays (k_r), calculated following Equation 7.1, were comparable for reference and **C31** and significantly faster in the case of **C30**, non-radiative decay rates (k_{nr}), for **C30** and **C31** were found to be 30 and 4 times large than the reference ($22 \cdot 10^6 \text{ s}^{-1}$).

$$\Phi = \frac{k_r}{k_r + k_{nr}} \quad 7.2$$

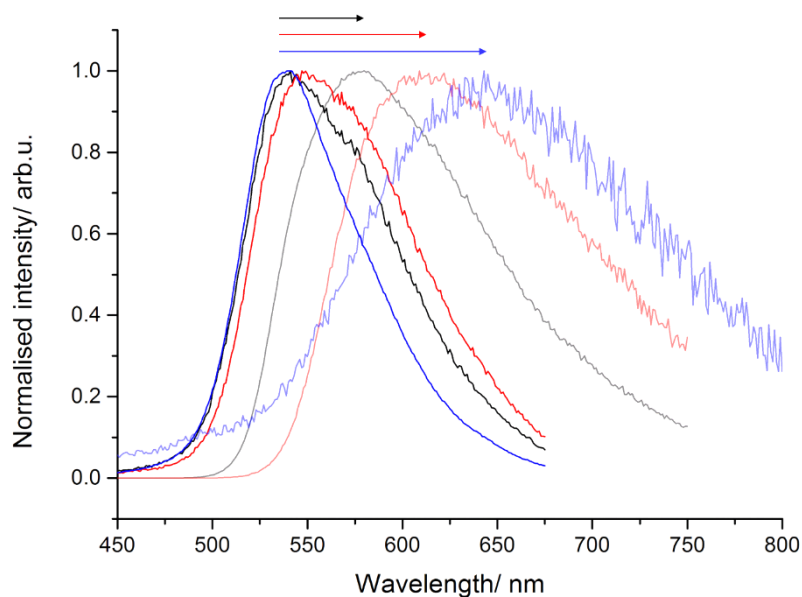


Figure 7.22 Normalised emission ($\lambda_{exc} = 420 \text{ nm}$) spectra for $[\text{Ir}(\text{dFppy})_2(\text{dbm})]$ (black trace), $[\text{Ir}(\text{dFppy})_2(\text{tbn})]$ (blue trace) and $[\text{Ir}(\text{dFppy})_2(\text{pydbm})]$ (red trace) in doped films (10 wt% in PMMA) (dark trace) and powder (soft trace).

Aggregation-induced emission (AIE) is a photophysical phenomenon, first formulated in 2001, where non-emissive luminogens are induced to emit light after the formation of aggregates.³⁰⁸ Its discovery provided a new platform of research that quickly motivated the science community because of its potential applications particularly in life science and biomedical engineering.^{309–313} Solid state phosphorescence emission has been often found in platinum (II) complexes. Owing to their planar structures, Pt-Pt interactions in the solid state are possible allowing efficient metal-metal-to-ligand charge transfer (MMLCT) transitions to occur.^{314–316} In contrast, octahedral iridium complexes cannot interact in a similar manner and therefore MMLCT transitions are not possible. It was not until 2008 when the first AIE cyclometalated iridium(III) complex was presented.²⁹² The molecular packing of the reported complex $[\text{Ir}(\text{ppy})_2(\text{dbm})]$, showed strong π - π interactions between the offset pyridine ring of two adjacent ppy ligands with a distance of $\sim 3.37 \text{ \AA}$ in a similar manner to the complexes

presented herein. Moreover, some examples of (dFppy) based iridium complexes have also shown AIE properties.^{288,317}

With this in mind, AIE studies were performed on the three complexes presented in this chapter. Indeed, addition of water into the dilute acetonitrile solutions turned on the photoluminescence emission of the three complexes with large enhancement in the emission intensity for the **dbm** and **pydbm** complexes and modest enhancement for the **tbm** analogue when the water content was 70%, 80% and 60% for the reference, **C30** and **C31**, respectively (see Figures 7.23-7.25). The PL intensity then decreased with higher percentages of water in every case, probably for two different reasons: Firstly, because after aggregation, the molecules covered with other nanoparticles do not emit light³¹⁸ and secondly, because in the process of aggregation amorphous particles are simultaneously formed, which do not enhance the emission intensity.³¹⁹

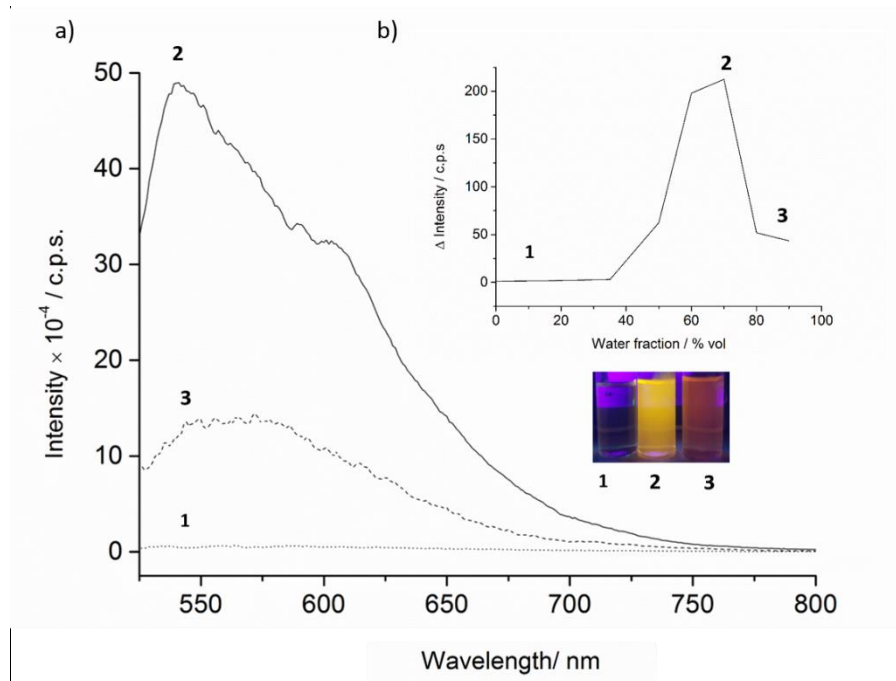


Figure 7.23 a) Emission spectra ($\lambda_{exc}= 420$ nm) of complex $[Ir(dFppy)_2(dbm)]$ (ref) in dilute MeCN (1), MeCN- H_2O (3:7 v/v) (2) and MeCN- H_2O (1:9 v/v) (3) and b) Variation of intensity according to water content.

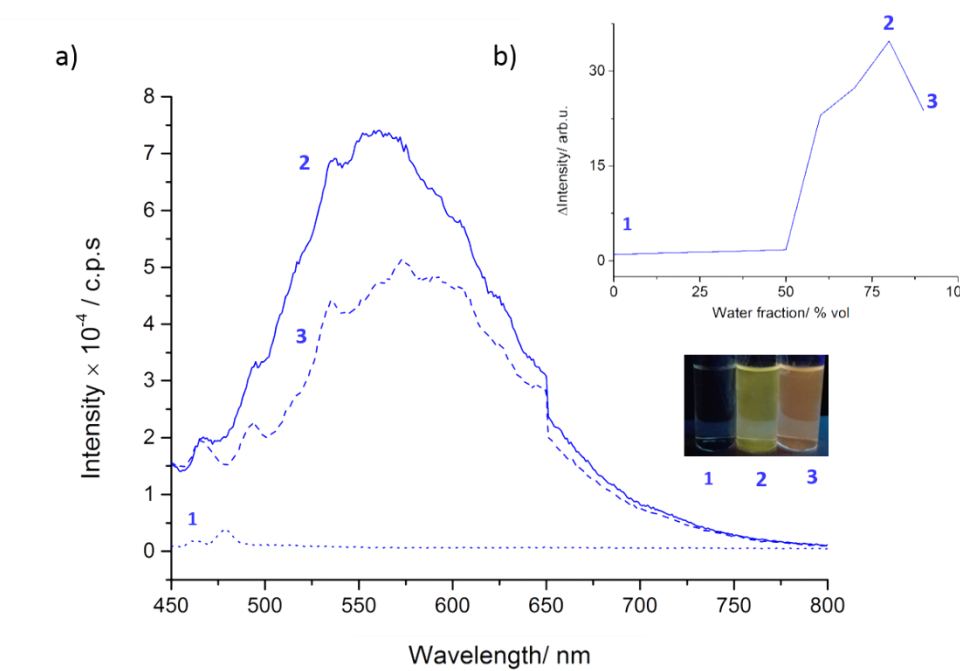


Figure 7.24 a) Emission spectra ($\lambda_{exc}=420$ nm) of complex $[Ir(dFppy)_2(tbm)]$ (C30) in dilute MeCN (1), MeCN- H_2O (2:8 v/v) (2) and MeCN- H_2O (1:9 v/v) (3) and b) Variation of intensity according to water content.

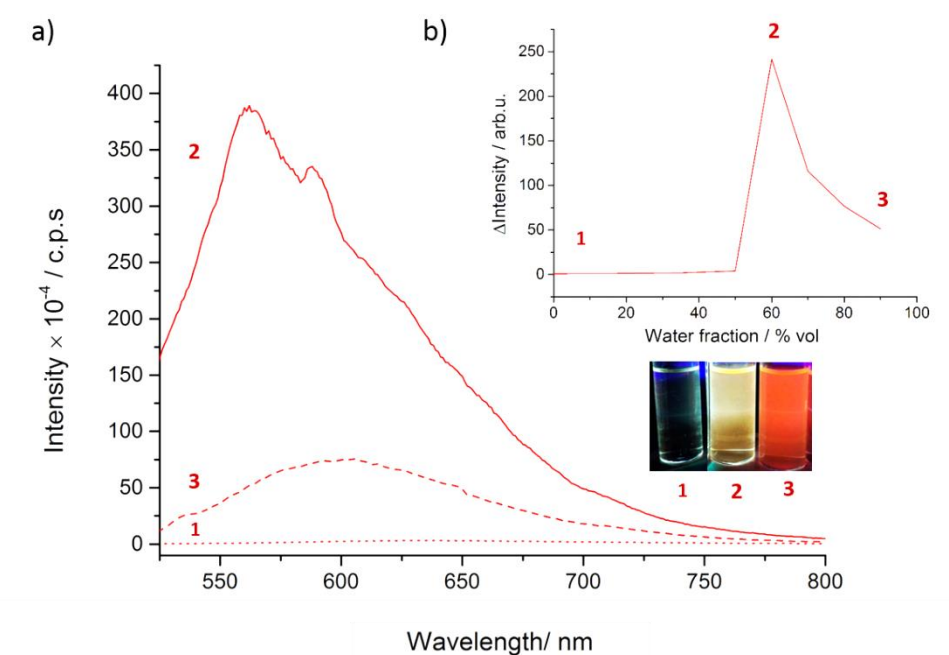


Figure 7.25 a) Emission spectra ($\lambda_{exc}=420$ nm) of complex $[Ir(dFppy)_2(pydbm)]$ (C31) in dilute MeCN (1), MeCN- H_2O (4:6 v/v) (2) and MeCN- H_2O (1:9 v/v) (3) and b) Variation of intensity according to water content.

7.7 Conclusions

This chapter presented two novel iridium complexes, $[\text{Ir}(\text{dFppy})_2(\text{pydbm})]$ and $[\text{Ir}(\text{dFppy})_2(\text{tbn})]$, bearing β -diketonate/triketones ligands respectively. Both complexes are poorly emissive in acetonitrile solution but their emission properties are remarkably enhanced in the solid state in a similar manner to the previously reported $[\text{Ir}(\text{dFppy})_2(\text{dbm})]$. By analysing the molecular packing in the crystal structure, the aggregation-induced emission (AIE) could be explained by a change in the nature of the emission to a mixed metal-to-ligand charge transfer and ligand-to-ligand charge transfer formed in the solid state, involving the dFppy and the ancillary ligands. These results showed that the addition of different substituents within the dbm moiety, a pyridyl group in the case of $[\text{Ir}(\text{dFppy})_2(\text{pydbm})]$, or a benzoate group in $[\text{Ir}(\text{dFppy})_2(\text{tbn})]$, do not block the π - π stacking and in contrast, favour different intermolecular interactions in the solid state, which modify the excited properties of the iridium complexes.

Chapter 8 Conclusion and Future Work

The research presented in this thesis was intended to further explore the chemistry of lanthanoid β -triketonate complexes. Indeed, the synthesis of nine new ligand systems opened up the formulation of a variety of lanthanoid complexes, from monomers or dimers to assemblies and polymers. A total of 29 crystal structures were presented and their structural and photophysical properties investigated.

While neutral discrete β -triketonate tetranuclear assemblies of formula $[\text{Ln}(\text{Ae}\cdot\text{HOEt})(\mathbf{tbm})_4]_2$ ($\text{Ae}^+ = \text{Na}^+, \text{K}^+$ and Rb^+), were previously studied with \mathbf{tbmH} , this thesis extended the study to reactions with CsOH , obtaining polymeric structures of general formula $[\text{Ln}(\text{Cs})(\mathbf{tbm})_4]_n$ ($\text{Ln}^{3+} = \text{Eu}^{3+}, \text{Er}^{3+}, \text{Yb}^{3+}$). Analogous structures were also found for the \mathbf{mtbmH} molecule for Eu^{3+} and Er^{3+} , $[\text{Ln}(\text{Cs})(\mathbf{mtbm})_4]_n$. In contrast, in the case of Yb^{3+} , a different structure with formula $[\text{Yb}(\text{Cs}\cdot\text{HOEt})(\mathbf{mtbm})_4]_n$, was obtained. A range of conditions were investigated in an effort to synthesise the first neodymium-based β -triketonate complexes, with positive results using RbOH as the base. In fact, isomorphous polymeric structures with formula $[\text{Ln}(\text{Rb})(\mathbf{mtbm})_4]_n$ ($\text{Ln}^{3+} = \text{Eu}^{3+}, \text{Nd}^{3+}$) were obtained for the \mathbf{mtbmH} ligand, while the regular tetranuclear assembly $[\text{Nd}(\text{Ae}\cdot\text{HOEt})(\mathbf{tbm})_4]_2$ was preserved for the \mathbf{tbmH} ligand. Interestingly, two structures showing the analogous β -diketonate ligands were obtained under similar synthetic conditions: $[\text{Eu}(\text{Cs})(\text{EtOH})_2(\mathbf{mdbm})_4]_n$ and $[\text{Nd}(\text{Cs}\cdot 2\text{HOEt})(\mathbf{dbm})_4]_n$ which showed possible retro-Claisen condensation reactivity occurring in solution. To further study these results, four new ligands were synthesised: \mathbf{dmtbmH} , \mathbf{ettbmH} , \mathbf{butbmH} and $\mathbf{t-butbmH}$ and their complexes studied. A wide variety of structures were found, showing retro-Claisen reactivity in the majority of them. The most remarkable example is $[\text{Ln}(\mu\text{-dmba})(\mathbf{dmdbm})(\mathbf{dmtbm})(\text{HOEt})]_2$ ($\text{Ln}^{3+} = \text{Eu}^{3+}, \text{Tb}^{3+}$), where the lanthanoid ion is simultaneously coordinated to the β -triketonate moiety and their retro-Claisen condensation products: β -diketonate and benzoate. When NMR studies were performed for all the synthesised ligands in basic ethanolic conditions, high rates of decompositions were found with almost 80% loss of the triketonate in the case of \mathbf{dmtbmH} . Therefore, alternative complexation routes needed to be found. Indeed, stable complexes with formula $[\text{Ln}(\mathbf{tnm})_3(\text{DMSO})_2]$ were found using DMSO as the solvent, which showed a possible pathway to further study the chemistry of β -triketonate complexes. Therefore, the logical progression for this field of work is the complexation of the other synthesised ligands under the same or similar conditions. A summary of all the synthesised structure is reported in Figure 8.1.

Because of the lack of quantitative photophysical data reported for the NIR lanthanoid complexes, a new method was developed to calculate overall quantum yields in the NIR. This method consists of the use of an integrating sphere with two detectors calibrated with [Yb(tta)₃(phen)] in toluene ($\Phi_{Ln}^L=1.6\%$) as reference. This method offers the possibility to fully characterise the photophysical properties of the NIR lanthanoid complexes and set this family of compounds in context. Indeed, the photophysical study of the NIR β -triketonate complexes showed enhanced emission properties in comparison to the β -diketonate retro-Claisen products and analogous previously reported β -diketonate complexes. In the case of the [Ln(**tbm**)₃(phen)] however, only a modest luminescence enhancement was achieved, which suggests that the removal of the α -CH oscillator is not the only cause for the improved emission properties of the NIR complexes and structural factors may also have an impact. Indeed, the assemblies and polymeric structures present an environment strongly protected from multiphonon relaxation pathways. Finally, the emission properties of the complexes [Ln(**tnm**)₃(DMSO)₂] (Ln³⁺= Nd³⁺, Eu³⁺ and Yb³⁺), synthesised under DMSO conditions and soluble in organic solvents, were studied. The results in the case of the Yb³⁺ complex showed long lifetime values and high overall quantum yields which suggests that this complex may be a good candidate for the fabrication of OLEDs.

Finally, **tbm** and **pydbm** were used as ancillary ligand for iridium (III) complexes, showing poor emissive properties in solution medium while their emission properties were remarkably enhanced in the solid state. Their crystal structure showed different π - π stacking that effectively modified the excitation properties of the iridium complexes. Although the synthesis of the desired iridium-lanthanoid complex was not achieved due to the unexpected O[^]O coordination mode of the **pydbm** ligand, these results showed two new examples of AIE and the correlation between their photophysical and structural properties.

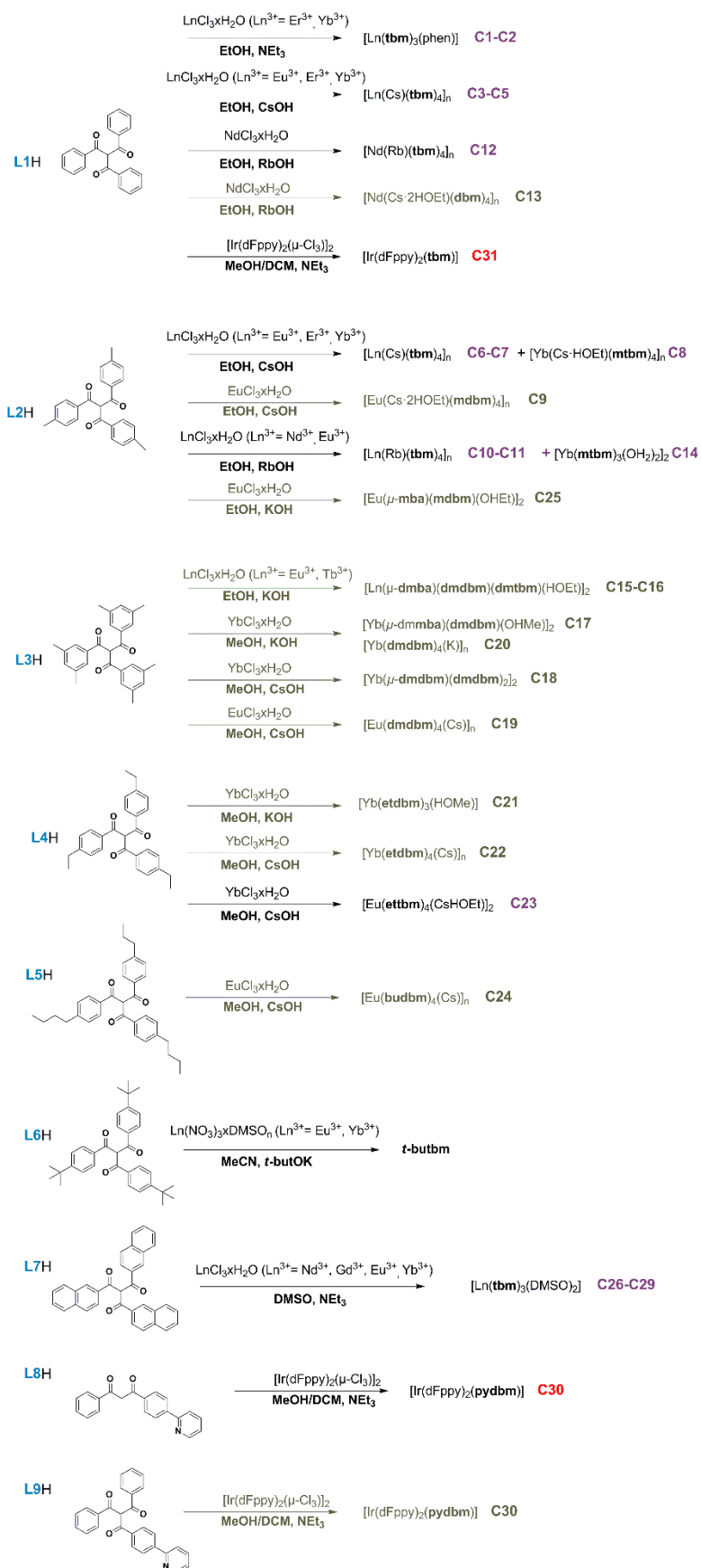


Figure 8.1 Summary of synthetic conditions for the isolated complexes studied in this thesis where the β -triketonate based lanthanoid complexes are presented in black, the retro-Claisen condensation products in grey and the iridium(III) complexes in red.

Chapter 9 Experimental

9.1 General Procedures

All reagents and solvents were purchased from chemical suppliers and used as received without further purification. The following molecules were previously reported: tribenzoylmethane (**tbmH**, **L1H**)²⁶, di(4-methylbenzoyl)methane (**mdbmH**)²²⁵, di(3,5-methylbenzoyl)methane (**dmdbmH**)²⁴⁹, di(4-ethylbenzoyl)methane (**etdbmH**)²²⁵, di(4-butylbenzoyl)methane (**budbmH**)²²⁵, di(4-tert-butylbenzoyl)methane (**t-budbmH**)²²⁵, dinaphthoylmethane (**dnmH**)¹⁷³ and 2-(2,4-difluorophenyl)pyridine (**dFppy**).³²⁰ Hydrated LnCl_3 ($\text{Ln} = \text{Eu}^{3+}, \text{Er}^{3+}, \text{Yb}^{3+}$) was prepared by the reaction of Ln_2O_3 with hydrochloric acid (5 M), followed by evaporation of the solvent under reduced pressure.

Infrared spectra (IR) were recorded on solid-state samples using an attenuated total reflectance Perkin Elmer Spectrum 100 FT-IR. IR spectra were recorded from 4000 to 650 cm^{-1} ; the intensities of the IR bands are reported as strong (s), medium (m), or weak (w), with broad (br) bands also specified.

Melting points were determined using a BI Barnsted Electrothermal 9100 apparatus.

Elemental analyses were performed by Robert Herman at Curtin University (Perth, Australia) and by Mr. Stephen Boyer, London Metropolitan University (London, UK).

Nuclear magnetic resonance (NMR) spectra were recorded using a Bruker Avance 400 spectrometer (400.1 MHz for ^1H ; 100 MHz for ^{13}C ; 376 MHz for ^{19}F) at 300 K. The data were acquired and processed by the MestNeNova software. All of the NMR spectra were calibrated to residual solvent signals. The following abbreviations have been used for multiplicity assignments: 's' for singlet, 'd' for doublet and 't' for triplet.

High-resolution mass spectra were recorded at the EPSRC UK National Mass Spectrometry Facility at Swansea University on a quadrupole time-of-flight (ESI-Q-TOF), model ABSciex 5600 Triple TOF in positive electrospray ionisation mode and spectra were recorded using sodium formate solution as the calibrant.

9.2 Photophysical Measurements

Collaborations with Dr. Stefano Stagni at University of Bologna, Italy were established for the measurements of the photophysical properties of the erbium complexes.

Absorption spectra were recorded at room temperature using a Perkin Elmer Lambda 35 UV/Vis spectrometer. Molar absorptivity determination was verified by linear least-squares fit of values obtained from at least three independent solutions at varying concentrations with absorbance of less than 1.0 for each absorption band.

Uncorrected steady state emission and excitation spectra were recorded using an Edinburgh FLSP980-stm spectrometer equipped with a 450 W xenon arc lamp, double excitation and emission monochromators, a Peltier cooled Hamamatsu R928P photomultiplier (185–850 nm) and a Hamamatsu R5509-42 photomultiplier for detection of NIR radiation (800–1400 nm). Emission and excitation spectra were corrected for source intensity (lamp and grating) and emission spectral response (detector and grating) by a calibration curve supplied with the instrument. Quantum yields in the solid state were measured with the use of an integrating sphere coated with BenFlect.⁴⁸ For the overall quantum yield of Yb³⁺ complexes the use of two different detectors, visible and NIR, is required. Therefore, a correction factor, as the ratio of the measured quantum yield to the reported value for a known sample, needs to be applied. To do that, [Yb(phen)(tta)₃], where tta is thenoyltrifluoroacetone, with an overall quantum yield of 1.6% in toluene was used as the reference.¹⁵⁰ Overall quantum yields in solution were determined by the optically dilute method proposed by Crosby and Demas¹¹¹, following Equation 8.1:

$$\Phi_s = \Phi_r \left(\frac{I_s}{I_r} \right) \left(\frac{A_r}{A_s} \right) \left(\frac{n_s}{n_r} \right)^2 \quad 9.1$$

where Φ_r is the photoluminescence quantum yield of the reference, I is the integrated area under the emission spectrum, A is the absorbance and n the refractive index. The subscripts s and r refer to the sample and reference, respectively. In Chapter 2, absorption and emission spectra were measured in 10⁻⁵M dichloromethane solutions by excitation at 350 nm under the same experimental conditions as the standard; air-equilibrated water solution of [Ru(**bpy**)₃]Cl₂, where bpy is bipyridine, ($\Phi=2.8\%$)²²³ for Eu³⁺ and [Yb(**phen**)(tta)₃] in toluene ($\Phi_{Ln}^L=1.6\%$)¹⁵⁰ for the Yb³⁺ complexes. In chapter 6 and chapter 8, same methodology was followed in 10⁻⁵ M acetonitrile solutions using the same standard conditions for [Ru(**bpy**)₃]Cl₂ in water ($\Phi = 2.8\%$)²²³ and acetonitrile ($\Phi = 9.5\%$)³⁰⁷, respectively.

Experimental uncertainties are estimated to be $\pm 15\%$ for quantum yields.

Excited-state decays (τ) for the lanthanoids were recorded using a microsecond flashlamp while the emission lifetimes for the iridium complexes were determined with the single photon counting technique (TCSPC) using pulsed picosecond LEDs (EPLD 375, FWHM<800ps) as the excitation source, with repetitions rates between 10kHz and 1 MHz, on the same Edinburgh FLSP980-stm spectrometer. The goodness of fit was assessed by minimizing the

reduced χ^2 function and by visual inspection of the weighted residuals. Experimental uncertainties are estimated to be $\pm 8\%$ for lifetime determinations.

To record the luminescence spectra at 77 K, the samples were placed in quartz tubes (2 mm diameter) and inserted in a special quartz Dewar filled with liquid nitrogen. All the solvents used in the preparation of the solutions for the photophysical investigations were of spectrometric grade.

Thy hybrid materials used for photophysical analysis were synthesised as described previously by swelling the lanthanoid complexes into PMMA monoliths.¹²³ The [Ln(phen)(t**bm**)₃] and [Ln(phen)(t**bm**)₃] were dissolved in dichloromethane, and the polymer matrix monoliths were added to the resulting solution, allowing incorporation of the complexes into the polymeric matrix. To make the polymer monoliths, lauroyl peroxide (0.005 g, 0.012 mmol) and ethylene glycol dimethacrylate (25 μ L, 0.13 mmol) was dissolved in methyl methacrylate (5.3 mL, 49 mmol). 1 mL aliquots of this solution were added into separate reaction containers. The reaction mixture was initiated by heating at 70 °C for 3 min and then quenched in an ice-water bath. Polymerisation progressed by heating at 60 °C for 2 days, then 70 °C for 24 h. Post-polymerisation was carried out at 100 °C for 1 h. Once separated from the reaction vessels the tubes of polymers were cut into 3–5 mm sections. The cut sections were immersed in a 10^{-3} M solution of the [Ln(phen)(t**bm**)₃] or [Ln(phen)(d**bm**)₃] in dichloromethane for 2 days. The solution was then removed and the polymer monoliths allowed to deswell at atmospheric pressure.

9.3 Transient Absorption Measurements

Transient Absorption measurements were carried out by Dr. Evan Moore at University of Queensland.

The excitation source utilized for femtosecond transient absorption measurements was an amplified laser system (Spitfire ACE, Spectra Physics) delivering 800 nm laser pulses of 110 fs duration and a 1 kHz repetition rate. Approximately 0.1 mJ of this output was attenuated and focused onto a 15 mm CaF₂ window mounted on an automated z-stage translation mount to generate a white light continuum probe pulse from 350-650 nm. The remainder of the laser fundamental was coupled to an OPA system (Topas Prime, Light Conversion) which was tuned to deliver excitation pulses at 340 nm. The pump pulse polarisation was set to magic angle with respect to the probe, and ground and excited state difference spectra (Δ OD) at various delay times were measured using a femtosecond TA spectrometer (Helios, Ultrafast

Systems) incorporating two 512 pixel CCD sensors as the sample and reference channel. Sample absorbance were *ca* 0.4 over the 2 mm path-length cell used, and these were continuously stirred mechanically. No detectable changes were observed in the UV-Vis absorption spectrum of the complex at the completion of transient absorption studies, indicating no decomposition. The instrument response function (IRF) had a full width at half maximum (FWHM) of *ca* 200 fs, measured experimentally by a Gaussian fit to the scattered laser excitation profile, and spectra were corrected for the chirp of the probe pulses. The resulting time traces were analysed globally using commercially available software (Igor, Version 6.1.2.1, Wavemetrics). Experimental uncertainties are estimated to be $\pm 10\%$ for lifetime determinations.

9.4 Electrochemical Measurements

Cyclic voltammetry (CV) and differential pulse voltammetry (DPV) measurements were performed on an Electrochemical Analyzer potentiostat model 600D from CH Instruments. Solutions for were prepared in MeCN and degassed with solvent-saturated nitrogen by bubbling for *ca.* 10 min prior to scanning. Tetra(*n*-butyl)ammoniumhexafluorophosphate (TBAPF₆; *ca.* 0.1 M in MeCN) was used as the supporting electrolyte. Two Ag/Ag⁺ electrode (silver wire in a solution of 0.1 M KCl in H₂O) were used as the pseudoreference electrode and counter electrode, respectively; a platinum electrode was used for the working electrode. The redox potentials are reported relative to a saturated calomel electrode (SCE) electrode with a ferrocenium/ferrocene (Fc⁺/Fc) redox couple as an internal reference (0.38 V vs SCE).²⁹³

9.5 Synthetic Procedures

9.5.1 Synthesis of Ligands

9.5.1.1 tri(4-methylbenzoyl)methane (**mtbmH**, **L2H**)

4-Methylbenzoic acid (625 mg, 4.8 mmol) was added to thionyl chloride (5 mL) and heated at reflux for 2 hours. After this time, the solvent was removed under reduced pressure and the remaining solid 4-methylbenzoyl chloride was immediately added to diethyl ether (20 mL). NaH (60% in mineral oil, 144 mg, 3.6 mmol) and **dmdbmH** (300 mg, 1.2 mmol) were combined in 20 mL diethyl ether and the suspension was maintained at 0 °C. To this suspension, the solution of 4-methylbenzoyl chloride in diethyl ether was added dropwise. After the addition, the mixture was stirred under nitrogen atmosphere at 40 °C for 16 hours. The formed precipitate was filtered and washed with a HCl solution (1 M). The solid was then dried under reduced pressure for several hours, and afforded the target compound as a white solid. Yield 60%. M.p. 233-234 °C. Elemental analysis calcd (%) for C₂₅H₂₂O₃: C, 80.67; H, 6.01; found: C, 80.61; H, 5.93. IR (ATR): ν = 2920 w, 1685 s, 1669 s, 1605 s, 1574 w, 1509 w, 1446 w, 1406 w, 1376 w, 1316 m, 1284 s, 1260 m, 1218 m, 1192 m, 1181 s, 1123 w, 1020m, 1011 m, 957 w, 906 w, 859 s, 841 w, 815 s, 783 w, 711 m. ¹H-NMR (400 MHz, DMSO-d₆): δ = 7.95 (s, 1H, α CH), 7.89 (d, J = 8.0 Hz, 6H, Hortho), 7.35 (d, J = 8.0 Hz, 6H, Hmeta), 2.38 (s, 9H, CH₃) ppm. ¹³C-NMR(101 MHz, DMSO-d₆) δ = 193.3 (CO), 144.9 (α CH), 133.3 (C1), 129.7 (Cortho), 128.9 (Cmeta), 65.1 (Cpara), 21.4 (CH₃) ppm.

Unless stated otherwise, a similar procedure was followed for the other ligands (**L3H-L7H**), substituting in the appropriate ester and ketone.

9.5.1.2 tri(3,5-dimethylbenzoyl)methane (**dmtbmH**, **L3H**)

Yield 88%. M.p. 194-196 °C. Elemental analysis calcd (%) for C₂₈H₂₈O₃: C, 81.52; H, 6.84; found: C, 81.66; H, 6.77. IR (ATR): ν = 2918 w, 2863 w, 1735 s, 1661 s, 1640 s, 1596 m, 1444 m, 1381 m, 1357 w, 1326 m, 1298 s, 1242 m, 1197 w, 1175 s, 1161 s, 1125 m, 1100 s, 1082 m, 1067 m, 1039 m, 1011 w, 995 w, 947 w, 929 m, 895 m, 867 m, 848 m, 812 m, 772 m, 748 m, 713 m. ¹H-NMR (400 MHz, CDCl₃) δ 7.54 (dt, J = 1.6, 0.8 Hz, 6H), 7.24 (tt, J = 1.6, 0.8 Hz, 3H), 7.08 (s, 1H), 2.36 (s, 18H). ¹³C-NMR (101 MHz, CDCl₃) δ 192.67, 138.61, 135.59, 126.46, 66.14, 21.27.

9.5.1.3 tri(4-ethylbenzoyl)methane (**ettbmH**, **L4H**)

Yield 60%. M.p. 210-212 °C. Elemental analysis calcd (%) for C₂₈H₂₈O₃: C, 81.52; H, 6.84; found: C, 81.59; H, 6.84. IR (ATR): ν = 3058 w, 2967 w, 1668 s, 1629 m, 1603 s, 1571 m, 1509 w, 1464 m, 1412 m, 1355 m, 1287 s, 1214 m, 1181 s, 1122 m, 1059 w, 1019 w, 1007 m, 961 w, 928 w, 909 w, 863 s, 822 s, 741 m. ¹H-NMR (400 MHz, CDCl₃) δ 7.86 (d, *J* = 8.4 Hz, 6H), 7.27 (d, *J* = 8.6 Hz, 6H), 7.08 (s, 1H), 2.70 (q, *J* = 7.6 Hz, 6H), 1.24 (t, *J* = 7.6 Hz, 9H). ¹³C-NMR (101 MHz, CDCl₃) δ 191.97, 151.19, 133.71, 129.16, 128.61, 77.16, 66.41, 29.13, 15.20.

9.5.1.4 tri(4-buthylbenzoyl)methane (**butbmH**, **L5H**)

Yield 55%. M.p. 260-262 °C. Elemental analysis calcd (%) for C₃₄H₄₀O₃·H₂O: C, 79.34; H, 8.22; found: C, 79.44; H, 7.89. IR (ATR): ν = 2929 m, 2957 m, 2859 m, 1930 w, 1688 s, 1667 s, 1604 s, 1571 m, 1508 w, 1459 w, 1433 w, 1412 m, 1377 w, 1038 m, 1284 s, 1261 m, 1213 m, 1181 s, 1120 w, 1006 s, 1011 m, 960 w, 931 w, 910 w, 860 s, 832 m, 819 w, 778 w, 730 w, 743 w. ¹H-NMR (400 MHz, CDCl₃) δ 7.85 (d, *J* = 8.3 Hz, 6H), 7.08 (s, 1H), 2.73 – 2.57 (m, 6H), 1.67 – 1.54 (m, 7H), 1.44 – 1.29 (m, 6H), 0.92 (t, *J* = 7.3 Hz, 9H). ¹³C-NMR (101 MHz, CDCl₃) δ 191.79, 149.78, 133.55, 128.98, 66.25, 35.72, 33.10, 22.31, 13.87.

9.5.1.5 tri(4-*tert*-buthylbenzoyl)methane (***t*-butbmH**, **L6H**)

Yield 88%. M.p. 267-269 °C. Elemental analysis calcd (%) for C₃₄H₄₀O₃: C, 82.22; H, 8.12; found: C, 81.91; H, 8.15. IR (ATR): ν = 2961 w, 2919w, 2866 w, 1736 m, 1697 m, 1661 m, 1639m, 1600 s, 1473 m, 1406 w, 1380 w, 1357 w, 1298 s, 1242 s, 1188 m, 1176 m, 1161 m, 1125 m, 1102 s, 1067 w, 1008 m, 948 w, 929 w, 909 w, 895 w, 861 s, 847 m, 812 m, 748 m, 713 m. ¹H-NMR (400 MHz, CDCl₃) δ 7.88 (d, *J* = 8.7 Hz, 1H), 7.47 (d, *J* = 8.7 Hz, 1H), 7.13 (s, 0H), 1.32 (s, 5H). ¹³C-NMR (101 MHz, CDCl₃) δ 191.91, 157.92, 133.35, 130.80, 128.92, 126.10, 125.40, 77.16, 66.25, 35.37, 31.14.

9.5.1.6 tri(naphthoyl)methane (**tnmH**, **L7H**)

A similar procedure was followed but using THF instead of diethylether as solvent. The reaction was stirred under nitrogen at 40 °C for 16 hours. Yield 80%. M.p. 289- 291 °C. Elemental analysis calcd (%) for C₃₄H₂₂O₃: C, 85.34; H, 4.63; found: C, 84.91; H, 4.53. IR (ATR): ν = 3059 w, 1671 s, 1656 s, 1626 s, 1597 m, 1581 m, 1507 w, 1469 m, 1438 w, 1393 w, 1371 w, 1353 m, 1290 s, 1239 m, 1178 s, 1221 s, 1020 w, 1007 m, 947 m, 907 m, 860 m, 812 s, 764 w, 740 s. ¹H NMR (400 MHz, DMSO-*d*₆) δ 8.86 (s, 3H), 8.57 (s, 1H), 8.06 (dt, *J* = 14.3, 7.8 Hz, 12H), 7.71 (ddd, *J* = 8.2, 6.9, 1.2 Hz, 3H), 7.63 (ddd, *J* = 8.1, 7.0, 1.2 Hz, 3H). ¹³C

NMR (101 MHz, DMSO) δ 193.79, 135.38, 133.02, 132.08, 130.89, 129.75, 129.25, 128.79, 127.77, 127.28, 123.79, 65.45, 39.52.

9.5.1.7 1-phenyl-3-(4-(pyridin-2-yl)phenyl)propane-1,3-dione
(**pydbmH**, **L8H**)

4-bromobenzoic acid (1g, 4.9 mmol) was dissolved in MeOH in the presence of a catalytic amount of H₂SO₄ and refluxed for 16 hours. MeOH was then removed at reduced pressure and the reaction mixture neutralised with saturated Na₂CO₃ and extracted with ethylacetate (3 x 15 mL). The organic layer was then dried and evaporated under reduced pressure giving the corresponding methyl 4-bromobenzoate as a white solid in quantitative yield. A suspension of NaH (60% in mineral oil, 468 mg, 11.7 mmol) was prepared in 15 mL of THF and stirred for 30 min. at 0 °C. After this time, a solution of acetophenone (465 mg, 3.9 mmol) in 7 mL of THF was added dropwise at 0 °C. The same step was then performed with the previously prepared methyl 4-bromobenzoate (1g, 4.65 mmol). The suspension was kept at room temperature for an hour and then heated at 40 °C for 16 more hours. After this time, the solvent was removed and the crude product was neutralised with a HCl solution (1 M) and extracted with ethylacetate (3 x 15 mL). The compound was purified by recrystallisation in EtOH giving a white solid corresponding to 1-(4-bromophenyl)-3-phenylpropane-1,3-dione (*Br*-dbmH) with 85% yield, whose characterisation matched with literature.³²¹ Finally, 2-(tributylstannyl)pyridine (607 mg, 1.65 mmol) was reacted with the previously formed *Br*-dbmH (500 mg, 1.65 mmol) following a conventional Stille Coupling reaction catalysed by tetrakis(triphenylphosphine)palladium(0), Pd(PPh₃)₄ (92 mg, 0.082 mmol) in dry toluene. The reaction mixture was refluxed for 32 hours at 120 °C. The crude product was purified by silica gel chromatography (hexanes/ethylacetate 90:10), giving the pure compound as a light brown solid. Yield 40%. M.p. 83-85 °C. Elemental analysis calcd (%) for C₂₀H₁₅NO₂·0.5 H₂O: C, 77.40; H, 5.20; N, 4.51; found: C, 77.80; H, 5.35; N, 4.27. ¹H NMR (500 MHz, CDCl₃) δ 8.77 (dt, *J* = 4.7, 1.4 Hz, 1H), 8.15 (q, *J* = 8.6 Hz, 4H), 8.07 – 8.02 (m, 2H), 7.86 – 7.80 (m, 2H), 7.63 – 7.57 (m, 1H), 7.56 – 7.50 (m, 2H), 7.33 (ddd, *J* = 6.2, 4.8, 2.6 Hz, 1H), 6.95 (s, 1H). ¹³C NMR (126 MHz, CDCl₃) δ 186.13, 184.88, 156.16, 149.93, 143.06, 135.71, 135.59, 132.54, 128.72, 127.65, 127.40, 127.12, 122.89, 120.97, 93.36, 77.28, 77.03, 76.77. Mass Spect: *m/z*: 301.11, Found: [M+H]⁺: 302.12.

9.5.1.8 2-benzoyl-1-phenyl-3-(4-(pyridin-2-yl)phenyl)propane-1,3-dione (**pytbnH**, **L9H**)

NaH (60% in mineral oil, 40 mg, 0.99 mmol) and **pydbmH** (100 mg, 0.33 mmol) were combined in 10 mL of THF and the suspension was maintained at 0 °C. To this suspension, the benzoyl chloride (93mg, 0.66 mmol) in 5 mL of THF was added dropwise. After the addition, the mixture was stirred under nitrogen atmosphere at 40 °C for 24 hours. The crude was neutralised with an acetic acid solution (1 M) and extracted with ethylacetate (3 x 10 mL). The organic layers were dried under vacuum and the resulted solid washed with diethylether in order to remove the excess of benzoic acid formed in the reaction mixture. The pure compound was isolated as a pale brown solid. Yield 50%. M.p. 197-199 °C. Elemental analysis calcd (%) for C₂₇H₁₉NO₃ (0.75·H₂O): C, 77.40; H, 4.93; N, 3.34; found: C, 77.40; H, 4.57; N, 3.35. ¹H NMR (400 MHz, CDCl₃) δ 8.81 – 8.67 (m, 1H), 8.17 – 8.01 (m, 4H), 8.01 – 7.93 (m, 4H), 7.84 – 7.76 (m, 2H), 7.63 (t, *J* = 7.4 Hz, 2H), 7.50 (t, *J* = 7.7 Hz, 4H), 7.32 (ddd, *J* = 6.6, 4.8, 1.7 Hz, 1H), 7.19 (s, 1H). ¹³C NMR (101 MHz, CDCl₃) δ 192.03, 191.71, 136.17, 135.69, 134.06, 129.54, 129.39, 129.05, 128.80, 128.49, 128.31, 128.12, 127.69, 114.98, 66.50. Mass Spect: m/z: 405.44, Found: [M+H]⁺: 406.14.

9.5.2 Synthesis of the Lanthanoid Complexes

9.5.2.1 [Ln(phen)(**dbm**)₃]

The [Ln(phen)(**dbm**)₃] were synthesised accordingly to literature methods, where **dbm** (32 mg, 0.15 mmol), phen (9 mg, 0.05 mmol) and the hydrated LnCl₃ (18 mg, 0.05 mmol) were reacted in EtOH (10 mL) in presence of base (triethylamine, 3eq.) for 30 min at 40°C.^{127,134,212} The slow evaporation of the solvent resulted in yellow crystalline powder, which was filtered and dried under vacuum to give the desired complexes.

[Eu(phen)(**dbm**)₃]: 35 mg (67%). M.p. 141-143 °C, ATR-IR: $\nu = 3057$ w, 1593 s, 1545 s, 1476 s, 1404 s, 1306 m, 1283 m, 1218 m, 1177 w, 1067 m, 1023 m, 840 w, 782 w, 743 m, 719 s, 684 s, 659 m cm⁻¹. Elemental analysis calcd (%) for C₅₇H₄₁N₂O₆Eu·H₂O: C, 67.12; H, 4.25; N, 2.75; found: C, 66.74; H, 3.90; N, 2.68. The characterisation matched with reported literature.¹²⁷

[Er(phen)(**dbm**)₃]: 28 mg (53%). M.p. 153-155 °C, ATR-IR: $\nu = 3057$ w, 1594 s, 1548 s, 1513 s, 1477 m, 1456 s, 1411 s, 1286 w, 1177 w, 1065 m, 1023 m, 941 w, 837 m, 741 m, 718 s, 685 s cm⁻¹. Elemental analysis calcd (%) for C₅₇H₄₁N₂O₆Er·H₂O: C, 66.13; H, 4.19; N, 2.71; found: C, 66.33; H, 3.95; N, 2.68. The characterisation matched with reported literature.²¹²

[Yb(phen)(**dbm**)₃]: 40 mg (75%). M.p. 172-174 °C, ATR-IR: $\nu = 3058$ w, 1594 m, 1549 s, 1514 s, 1477 m, 1455 s, 1412 s, 1393 s, 1311 m, 1286 m, 1219 m, 1177 m, 1023 m, 942 w, 784 w, 740 m, 718 s, 685 s cm⁻¹. Elemental analysis calcd (%) for C₅₇H₄₁N₂O₆Yb·H₂O: C, 65.77; H, 4.16; N, 2.69; found: C, 65.79; H, 3.67; N, 2.67. The characterisation matched with reported literature.¹³⁴

9.5.2.2 [Ln(phen)(**tbm**)₃]

The [Ln(phen)(**tbm**)₃] were prepared in a similar manner to the previously reported [Eu(phen)(**tbm**)₃]²¹⁰ by reaction of **tbmH** (54 mg, 0.15 mmol), phen (10 mg, 0.05 mmol) and hydrated LnCl₃ (0.05 mmol) in ethanol (10 mL). Triethylamine (23 μ L, 0.15 mmol) was added and the mixture was heated at 50°C for 30 minutes. The resulting mixture was hot filtered and the filtrate left to stand at ambient temperature. Slow evaporation of the solvent over several days afforded yellow crystals.

[Eu(phen)(**tbm**)₃]: 20 mg (30%). M.p. 200-202 °C, ATR-IR: $\nu = 3082$ w, 1590 s, 1557 m, 1520 s, 1477 m, 1400 s, 1291 m, 1242 m, 1161 m, 1100 m, 986 m, 854 m, 828 s, 782 m, 720m, 712 m, 688 m, 641 m, 567 m, 526 m, 458 w cm⁻¹. The characterisation matched with reported literature.²¹⁰

C1 [Er(phen)(**tbm**)₃]: 18 mg (28%). M.p. 248-249 °C; elemental analysis calcd (%) for C₇₈H₅₃N₂O₉Er·H₂O: C, 69.52; H, 4.11; N, 2.08; found: C, 69.94; H, 3.65; N, 2.17; ATR-IR: $\nu = 3058$ w, 1642 m, 1565m, 1583 m, 1538 s, 1448 m, 1427 w, 1368 s, 1310 m, 1276 m, 1222 w, 1176 w, 1154 m, 1102 w, 1072 w, 1027 w, 1013 w, 1000 w, 968 w, 920 w, 896 m, 863 w, 843 w, 824 w, 810 w, 779 w, 742 m, 728 w, 722 w, 692 s, 666 w cm⁻¹.

C2 [Yb(phen)(**tbm**)₃]: 30 mg (45%). M.p. 256-257 °C; elemental analysis calcd (%) for C₇₈H₅₃N₂O₉Yb·H₂O: C, 69.23; H, 4.1; N, 2.01; found: C, 69.28; H, 3.75; N, 2.01; ATR-IR: $\nu = 3060$ w, 1669 w, 1643 m, 1583 m, 1538 s, 1448 m, 1427 w, 1369 s, 1310 w, 1277 m, 1177 w, 1155 m, 1102 w, 1073 w, 1027 w, 1013 w, 1000 w, 968 w, 921 w, 896 m, 864 w, 844 w, 824 w, 811 w, 780 w, 759 m, 729 m, 723 m, 692 s, 667 w cm⁻¹.

9.5.2.3 {[Ln(Ae)(**L**)₄]₂}_n

For the synthesis of {[Ln(Ae)(**L**)₄]₂}_n, AeOH (4 eq.) (Ae⁺=Rb⁺,Cs⁺) was added to a mixture containing **LH** (4 eq.) and hydrated LnCl₃ (ca. 18 mg) in ethanol (10 mL). The mixture was heated at reflux for 30 minutes and filtered over a glass frit while still hot. The filtered solution was then left undisturbed at ambient temperature and slow evaporation of the solvent over several days afforded crystals suitable for X-ray diffraction.

C3 {[Eu(Cs)(**tbm**)₄]₂]_n: 18 mg (23%). M.p. 271-272 °C. Elemental analysis calcd (%) for C₈₈H₆₀CsO₁₂Eu: C, 66.30; H, 3.79; found: C, 65.93; H, 3.31. IR (ATR): ν = 3057 w, 1646 w, 1584 m, 1545 s, 1446 m, 1368 s, 1273 m, 1153 m, 1073 w, 1027 w, 1013 w, 924 w, 896 s, 823 m, 780 m, 744 m, 693 s, 666 m cm⁻¹.

C4 {[Er(Cs)(**tbm**)₄]₂]_n: 24 mg (30%). M.p. 260-261 °C. Elemental analysis calcd (%) for C₈₈H₆₀CsO₁₂Er·(1.6H₂O): C, 64.51; H, 3.89; found: C, 64.00; H, 3.31. IR (ATR): ν = 3056 w, 1646 w, 1585 m, 1548 s, 1446 m, 1371 s, 1275 m, 1153 m, 1073 w, 1027 w, 1013 w, 924 w, 896 s, 823 m, 780 m, 743 m, 693 s, 667 m cm⁻¹.

C5 {[Yb(Cs)(**tbm**)₄]₂]_n: 22 mg (28%). M.p. 252-253 °C. Elemental analysis calcd (%) for C₈₈H₆₀CsO₁₂Er·(0.3H₂O): C, 65.18; H, 3.37; found: C, 64.70; H, 3.36. IR (ATR): ν = 3056 w, 3026 w, 1646 w, 1585 m, 1550 s, 1446 m, 1372 s, 1313 m, 1274 m, 1177 w, 1154 m, 1103 w, 1073 w, 1027 w, 1013 w, 1000 w, 973 w, 924 w, 896 s, 823 m, 811 w, 780 m, 743 m, 693 s, 667 m cm⁻¹.

C6 {[Eu(Cs)(**mtbm**)₄]₂]_n: 27 mg (31%). M.p. 291-290 °C. Elemental analysis calcd (%) for C₁₀₀H₈₄O₁₂EuCs·(2H₂O): C, 66.78; H, 4.93; found: C, 66.36; H, 4.49. IR (ATR): ν = 3058 w, 3024 w, 1642 m, 1583 s, 1537 s, 1448 m, 1428 m, 1366 s, 1310 m, 1292 m, 1275 m, 1176 w, 1154 m, 1101 w, 1072 w, 1027 w, 1013 w, 1000 w, 968 w, 920 w, 895 m, 863 w, 844 w, 823 w, 810 w, 780 w, 743 m, 729 w, 721 w, 692 m, 667 w cm⁻¹.

C7 {[Er(Cs)(**mtbm**)₄]₂]_n: 30 mg (34%) M.p. 298-299 °C. Elemental analysis calcd (%) for C₁₀₀H₈₄CsO₁₂Er: C, 66.54; H, 4.86; found: C, 66.43; H, 4.46. IR (ATR): ν = 3057 w, 3027 w, 1646 w, 1595 m, 1585 m, 1549 s, 1447 m, 1373 s, 1312 m, 1276 m, 1219 w, 1178 w, 1154 m, 1073 w, 1000 w, 972 w, 924 w, 896 m, 847 w, 823 w, 781 w, 743 m, 692 s, 668 m cm⁻¹.

C10 {[Eu(Rb)(**mtbm**)₄]₂]_n: 24 mg (15%). M.p. 267-269 °C. Elemental analysis calcd (%) for C₂₀₀H₁₆₈Rb₂Eu₂O₂₄ (1.75·H₂O): C, 68.53; H, 5.05; found: C, 68.53; H, 4.74. IR (ATR): ν = 2919 w, 1634 w, 1602 m, 1577 m, 1538 s, 1408 m, 1360 s, 1275 m, 1183 m, 1151 m, 1115 w, 1021 w, 899 s, 837 m, 7836 s, 721 m, 694 w cm⁻¹.

C11 {[Nd(Rb)(**mtbm**)₄]₂]_n: 18 mg (10%). M.p. 289-291 °C. Elemental analysis calcd (%) for C₁₀₀H₈₄RbNdO₁₂ (1.5·H₂O): C, 66.49; H, 5.30; found: C, 66.24; H, 4.93. IR (ATR): ν = 2920 w, 2164 w, 1634 m, 1602 m, 1574 m, 1529 s, 1405 m, 1342 s, 1273 m, 1184 m, 1151 m, 1112 w, 1034 w, 899 s, 825 m, 780 s, 763 s, 721 m cm⁻¹.

9.5.2.4 [Ln(Ae·HOEt)(L)₄]₂

Complexes with formula, {[Ln(Ae)(L)₄]₂}_n, were synthesised by addition of AeOH (4 eq.) (Ae⁺=Rb⁺,Cs⁺) to a mixture containing LH (4 eq.) and hydrated LnCl₃ (ca. 18 mg) in ethanol (10 mL). The mixture was heated at reflux for 30 minutes and filtered over a glass frit while still hot. The filtered solution was then left undisturbed at ambient temperature and slow evaporation of the solvent over several days afforded crystals suitable for X-ray diffraction.

C12 [Nd(Rb·HOEt)(**tbm**)₄]₂: 20 mg (12%). M.p. 259-261 °C. Elemental analysis calcd (%) for C₁₈₀H₁₃₂Rb₂Nd₂O₂₆: C, 68.19; H, 4.20; found: C, 67.70; H, 3.78. IR (ATR): $\nu = 3065$ w, 1739 w, 1644 w, 1645w, 1597 w, 1583 m, 1540 m, 1491 w, 1448 m, 1374 s, 1297 s, 1277 s, 1181 w, 1151 m, 1073 w, 1012 w, 897 s, 823 m, 779 w, 747 s cm⁻¹.

C23 [Eu(Cs·HOEt)(**ettbm**)₄]₂: 30 mg (15%). MP. 267-269. Elemental analysis calcd (%) for C₂₂₈H₂₂₈Cs₂Eu₂O₂₆(5H₂O): C, 67.72; H, 5.93; found: C, 67.19; H, 5.40, the elemental analysis is slightly off due to co-precipitation of multiple species as explained in chapter 5. M.p. 267-269 °C. IR (ATR): $\nu = 2964$ w, 1637 w, 1604 w, 1577 m, 1540 s, 1452 w, 1412 m, 1365 s, 1307 m, 1277 m, 1184 w, 1152 m, 1116 w, 1080 w, 1020 w, 964 w, 900 s, 837 m, 796 m, 772 w cm⁻¹.

9.5.2.5 Other β -triketonate based complexes

C8 [Yb(Cs)(**mtbm**)₄]_n: 29 mg (32%). M.p. 278-279 °C. Elemental analysis calcd (%) for C₁₀₀H₈₄O₁₂Yb·(4.5H₂O): C, 64.41; H, 5.03; found: C, 64.09; H, 4.53. IR (ATR): $\nu = 3023$ w, 2920 w, 1635 m, 1603 m, 1577 m, 1538 s, 1452 w, 1407 m, 1360 s, 1316 m, 1308 m, 1281 m, 1183 m, 1154 m, 1113 w, 1033 w, 1013 w, 961 w, 900 s, 850 m, 824 m, 781 s, 762 m, 734 w, 723 m, 690 w cm⁻¹.

C14 [Yb(**mtbm**)₃(OH₂)₂]₂: 40 mg (60%). M.p. 277-279 °C. Elemental analysis calcd (%) for C₇₅H₆₅O₁₀Yb(2.75·H₂O): C, 66.78; H, 5.27; found: C, 66.53; H, 4.84. IR (ATR): $\nu = 2917$ w, 1590 m, 1520 s, 1486 s, 1424 m, 1296, 1203 w, 1181 m, 1018 m, 937 w, 834 w, 770 s, 728 m, 623 m, 500 s, 479 m cm⁻¹.

9.5.2.6 Retro-Claisen condensation complexation products

AeOH (Ae = K, Cs) (4 eq.) was added to a mixture containing ligands L1H-L6H (4 eq.) and hydrated LnCl₃ (ca. 18 mg) in ethanol or methanol (10 mL). The mixture was heated at reflux for 30 minutes and filtered over a glass frit while still hot. The filtered solution was then left undisturbed at ambient temperature and slow evaporation of the solvent over several days afforded crystals suitable for X-ray diffraction.

C15 [Eu(**dmdba**)(**dmdbm**)(**dmtbm**)HOEt]₂: 21 mg (19%). M.p. 147-149 °C. Elemental analysis calcd (%) for C₁₁₆H₁₂₂Eu₂O₁₆·1.5H₂O: C, 66.25; H, 5.99; found: C, 65.88; H, 5.80. IR (ATR): $\nu = 2916$ w, 1534 s, 1505 s, 1426 m, 1349 s, 1318 s, 1269 m, 1213 m, 1161 w, 1131 w, 1089 w, 1038 w, 959 w, 860 m, 790 s, 765 m cm⁻¹.

C16 [Tb(μ -**dmdba**)(**dmdbm**)(**dmtbm**)HOEt]₂: 16 mg (14%). M.p. 146-148 °C. The elemental analysis is off due to co-precipitation of multiple species as explained in chapter 5 IR (ATR): $\nu = 2916$ w, 1535 s, 1507 s, 1425 m, 1351 s, 1320 s, 1269 m, 1212 m, 1161 w, 1131 m, 1021 w, 946 w, 859 m, 789 s, 765 m cm⁻¹.

C17 [Yb(μ -**dmdba**)(**dmdbm**)₂HOME]₂: 12 mg (13%). M.p. 288-290 °C. Elemental analysis calcd (%) for C₉₇H₁₀₆O₁₅Yb₂·3.5H₂O: C, 60.78; H, 5.73; found: C, 60.49; H, 5.38. IR (ATR): $\nu = 2914$ w, 1505 s, 1372 s, 1326 m, 1270 m, 1216 m, 998 w, 946 w, 859 w, 788 s, 750 m cm⁻¹.

C18 [Yb(μ -**dmdbm**)(**dmdbm**)₂]₂: 20 mg (20%). M.p. 310-312 °C. Elemental analysis calcd (%) for C₁₁₄H₁₁₄O₁₂Yb₂: C, 67.71; H, 5.68; found: C, 67.29; H, 5.46. IR (ATR): $\nu = 2914$ w, 1552 s, 1508 s, 1459 s, 1373 s, 1312 m, 1271 m, 1210 m, 1160 m, 1103 w, 997 w, 946 w, 856 m, 783 s, 730 w cm⁻¹.

C19 [Eu(**dmdbm**)₄(Cs)]_n: 28 mg (40%). M.p. 267-269 °C. Elemental analysis calcd (%) for C₇₆H₇₆CsEuO₈: C, 65.10; H, 5.46; found: C, 4.77; H, 5.08. IR (ATR): $\nu = 2912$ w, 1551 s, 1503 s, 1459 s, 1402 s, 1362 m, 1317 m, 1211 m, 1157 m, 944 w, 857 w, 781 s cm⁻¹.

C20 [Yb(**dmdbm**)₄(K)]_n: 31 mg (47%). M.p. 243-245 °C. Elemental analysis calcd (%) for C₇₆H₇₆KO₈Yb·H₂O: C, 67.74; H, 5.83; found: C, 67.53; H, 5.73. IR (ATR): $\nu = 2914$ w, 1551 m, 1508 s, 1459 m, 1384 m, 1323 m, 1210 m, 1159 m, 1103 w, 996 w, 856 m, 782 s, 730 w cm⁻¹.

C21 [Yb(**etdbm**)₃(HOME)]₂: 16 mg (31%). M.p. 249-251 °C. Elemental analysis calcd (%) for C₅₈H₆₁O₇Yb·2.5H₂O: C, 64.02; H, 6.11; found: C, 63.73; H, 5.84. IR (ATR): $\nu = 2965$ w, 1586 m, 1520 s, 1489 s, 1422 s, 1379 s, 1309 s, 1225 m, 1182 s, 1112 w, 1063 s, 1016 w, 937 w, 849 w, 792 m, 717 w cm⁻¹.

C22 [Yb(**etdbm**)₄(Cs)]_n: 21 mg (30%). M.p. 211-213 °C. The elemental analysis is off due to co-precipitation of multiple species as explained in chapter 5. IR (ATR): $\nu = 2966$ w, 1590 s, 1541 m, 1523 s, 1489 s, 1447 s, 1390 m, 1308 m, 1224 m, 1182 m, 1110 m, 11063 m, 1017 m, 941 w, 850 m, 792 m, 715 w cm⁻¹.

C24 [Eu(**budbm**)₄Cs]_n: 29 mg (36%). M.p. 214-216 °C. Elemental analysis calcd (%) for C₉₂H₁₀₈CsEuO₈: C, 67.93; H, 6.69; found: C, 67.63; H, 6.75. IR (ATR): $\nu = 2925$ w, 1590s,

1520 s, 1496 s, 1441 s, 1397 m, 1303 m, 1223 m, 1183 m, 1110 w, 1018 w, 939 w, 850 m, 772 s, 710 w cm^{-1} .

C25 [Eu(μ -mba)(mdbm)(OHEt)]₂: 18 mg (22%). M.p. 266-268 °C. Elemental analysis calcd (%) for C₈₈H₈₆Eu₂O₁₄: C, 65.17; H, 5.78; found: C, 64.77; H, 5.55. IR (ATR): $\nu = 2920$ w, 1634 w, 1603 m, 1578 m, 1538 s, 1408 m, 1361 s, 1275 m, 1184 m, 1151 m, 1113 w, 900 s, 826 m, 782 s, 721 m cm^{-1} .

9.5.2.7 [Ln(tnm)₃(DMSO)₂]

Triethylamine (3 eq) was added to a mixture containing tnmH (3 eq) and hydrated LnCl₃ (ca. 18 mg) in DMSO (5 mL). The mixture was heated at 60°C for 30 minutes and left at ambient temperature. When cooled down, EtOH was double layered carefully. Slow diffusion of the EtOH over several days afforded crystals suitable for X-ray diffraction.

C26 [Nd(tnm)₃(DMSO)₂]: 50 mg (27%) M.p. 220-222 °C. Elemental analysis calcd (%) for C₁₀₆H₇₅S₂O₁₁Nd·2SOC₂H₆: C, 69.89; H, 4.45; found: C, 69.93; H, 4.64. IR (ATR): $\nu = 3053$ w, 2918 w, 1619 w, 1596 m, 1539 s, 1505 w, 1375 s, 1308 m, 1242 w, 1204 w, 1112 m, 1020 m, 961 w, 909 m, 861 m, 819 s, 794 s, 757 m, 748 m, 730 m cm^{-1} .

C27 [Eu(tnm)₃(DMSO)₂]: 65 mg (36%). M.p. 210-212 °C. Elemental analysis calcd (%) for C₁₀₆H₇₅S₂O₁₁Eu·2SOC₂H₆: C, 69.64; H, 4.62; found: C, 70.02; H, 4.38. IR (ATR): $\nu = 3054$ w, 1623 m, 1576 m, 1543 s, 1465 m, 1433 m, 1372 s, 1333 s, 1309 s, 1242 m, 1204 w, 1151 m, 1111 m, 1023 m, 962 m, 906 m, 863 m, 818 m, 793 s, 756 m, 731 m cm^{-1} .

C28 [Gd(tnm)₃(DMSO)₂]: 58 mg (32%). M.p. 204-206 °C. Elemental analysis calcd (%) for C₁₀₆H₇₅S₂O₁₁Gd·4SOC₂H₆: C, 66.51; H, 4.854; found: C, 66.81; H, 4.60. IR (ATR): $\nu = 3053$ w, 1624 m, 1577 m, 1543 s, 1505 w, 1466 w, 1433 w, 1374 s, 1335 s, 1301 s, 1242 m, 1204 w, 1112 m, 1020 m, 961 m, 863 m, 818 s, 792 s, 763 m, 731 m cm^{-1} .

C29 [Yb(tnm)₃(DMSO)₂]: 68 mg (37%). M.p. 186-188 °C. Elemental analysis calcd (%) for C₁₀₆H₇₅S₂O₁₁Yb·2.5SOC₂H₆: C, 68.12; H, 4.63; found: C, 68.44; H, 4.28. IR (ATR): $\nu = 3054$ w, 1625 m, 1597 m, 1578 m, 1547 s, 1505 w, 1466 w, 1434 w, 1376 s, 1336 s, 1302 s, 1243 m, 1152 w, 1112 m, 1022 m, 961 w, 906 m, 863 w, 818 s, 792 s, 763 m, 732 m cm^{-1} .

9.5.2.8 μ -Chloro-Bridged Iridium Dimers

A modified version of the originally reported procedure by Nonoyama *et al.* was followed.³²² IrCl₃·3H₂O (1 eq.) and the C⁻N ligand (2.2 eq.) were dissolved in 2-ethoxyethanol and distilled water (3:1 v/v) to give a concentration of ca. 0.2 M. The mixture was degassed by three cycles of vacuum/ N₂ and heated to reflux for 18h. After an hour a yellow precipitate was formed. The system was cooled to room temperature follow by addition of water to favour the

precipitation of the dimer. The solid formed was washed with a mixture of water and ethanol (1:1 v/v) and mixture of hexanes and diethyl ether (1:1 v/v), before drying to give the title compound.

Tetrakis[2-(4',6'-difluorophenyl)-pyridinato-N,C2']-bis(μ -chloro)diiridium(III),

[Ir(dFppy)₂(μ -Cl)]₂: 67%. ¹H-NMR (400 MHz, CDCl₃) (ppm) δ 9.12 (d, *J* = 6.7 Hz, 1H), 8.31 (d, *J* = 9.3 Hz, 1H), 7.87 – 7.78 (m, 1H), 6.83 (t, *J* = 7.2 Hz, 1H), 6.38 – 6.31 (m, 1H), 5.29 (d, *J* = 9.1 Hz, 1H). ¹⁹F-NMR (377 MHz, CDCl₃) (ppm) δ -107.72 (d, *J* = 10.3 Hz), -110.32 (d, *J* = 10.3 Hz). The characterisation matched with reported literature.

9.5.2.9 [Ir(dFppy)₂(L)]

To a round bottom flask containing the [Ir(dFppy)₂(μ -Cl)]₂ dimer (100 mg, 0.082 mmol, 1 eq.) and the LH (LH= **dbmH**, **tbmH**, **pydbmH** and **pytbmH**) (0.18 mmol, 2.2 eq.) and NEt₃ (0.18 mmol) were added in a mixture DCM/MeOH (80:20 v/v) to give a suspension with a concentration of *ca.* 0.02 M. The mixture was degassed via bubbling with N₂ for 10 min, before the reaction vessel was sealed. The reaction mixture was heated to 40 for 19 h. The solution was cooled to room temperature, and the solvent evaporated. The crude product was purified by silica gel chromatography in Hexanes/DCM (70:30) giving the pure compound as a yellow solid.

[Ir(dFppy)₂(**dbm**)]: Yield 90%. M.p. 307-309 °C. ¹H NMR (500 MHz, DMSO-*d*₆) δ 8.50 (dd, *J* = 6.0, 1.5 Hz, 2H), 8.26 (d, *J* = 8.5 Hz, 2H), 8.06 – 8.01 (m, 1H), 7.85 – 7.77 (m, 4H), 7.54 – 7.43 (m, 4H), 7.39 (t, *J* = 7.7 Hz, 4H), 6.76 (ddd, *J* = 12.2, 9.4, 2.4 Hz, 2H), 6.71 (s, 1H), 5.65 (dd, *J* = 8.7, 2.4 Hz, 2H). ¹⁹F NMR (470 MHz, DMSO-*d*₆) δ -108.88, -110.64 (d, *J* = 9.9 Hz). The characterisation matched with reported literature.²⁸⁷

C30 [Ir(dFppy)₂(**tbm**)]: Yield 40%. M.p. 317-319 °C. . Elemental analysis calcd (%) for C₄₄H₂₇O₃N₂Ir: C, 58.73; H, 3.02; N, 3.11; found: C, 58.74; H, 3.12; N, 3.12. ¹H NMR (500 MHz, CDCl₃) δ 8.52 (d, *J* = 5.8 Hz, 2H), 8.26 (d, *J* = 8.3 Hz, 2H), 7.76 (m, *J* = 17.1, 8.2 Hz, 6H), 7.43 (t, *J* = 7.3 Hz, 2H), 7.33 (t, *J* = 7.6 Hz, 4H), 7.10 (t, *J* = 7.3 Hz, 2H), 6.59 (s, 1H), 6.39 (ddd, *J* = 11.7, 9.4, 2.4 Hz, 2H), 5.77 (dd, *J* = 8.8, 2.3 Hz, 2H). ¹⁹F NMR (471 MHz, Chloroform-*d*) δ -108.52 – -108.68 (m), -110.69 – -110.88 (m). ¹³C NMR (126 MHz, CDCl₃) δ 186.24, 148.06, 138.46, 129.44, 129.11, 127.71, 127.04, 77.28, 77.03, 76.77, 65.89. Mass Spect: *m/z*: 900.16, Found: [M+H]⁺: 901.17.

C31 [Ir(dFppy)₂(**pydbm**)]: Yield 90%. M.p. 313-315 °C. Elemental analysis calcd (%) for C₄₂H₂₆O₂N₃Ir: C, 57.59; H, 3.00; N, 4.81; found: C, 57.78; H, 2.91; N, 5.00. ¹H NMR (500

MHz, CDCl₃) δ 8.72 (d, $J = 4.3$ Hz, 1H), 8.57 (t, $J = 4.9$ Hz, 2H), 8.29 (d, $J = 8.2$ Hz, 2H), 8.03 – 7.86 (m, 4H), 7.86 – 7.70 (m, 6H), 7.42 (dt, $J = 51.5, 7.5$ Hz, 3H), 7.14 (ddt, $J = 7.5, 5.9, 1.6$ Hz, 2H), 6.67 (s, 1H), 6.42 (ddt, $J = 12.4, 9.3, 3.0$ Hz, 2H), 5.80 (dt, $J = 8.7, 2.9$ Hz, 2H). ¹⁹F NMR (377 MHz, CDCl₃) δ -109.13 (dd, $J = 9.9, 4.6$ Hz), -111.33 (dd, $J = 10.1, 3.2$ Hz). ¹³C NMR (126 MHz, Chloroform-*d*) δ 207.07, 179.39, 178.63, 165.28, 163.59, 161.69, 159.75, 156.64, 151.56, 149.85, 148.02, 140.95, 138.00, 130.60, 128.77, 127.33, 126.89, 122.52, 121.76, 120.69, 115.18, 97.25, 95.20. Mass Spect: m/z : 873.16, Found: [M+H]⁺: 874.16.

9.6 X-Ray Crystallography

Crystallographic data for the structures *t*-butbmH, **C1- C29** were collected at the University of Western Australia by Prof. Brian Skelton and Dr. Alexandre Sovolev, at 100(2) K on an Oxford Diffraction Gemini or Xcalibur diffractometer fitted using Mo K α or Cu K α radiation. Following absorption corrections and solution by direct methods, the structures were refined against F^2 with full-matrix least-squares using the program SHELXL-97 or SHELX-2014.³²³ Unless stated below, anisotropic displacement parameters were employed for the non-hydrogen atoms and hydrogen atoms were added at calculated positions and refined by use of a riding model with isotropic displacement parameters based on those of the parent atom. Suitable crystals of **C30** and **C31** were mounted in silicone oil and were measured using a Rigaku FR-X Ultrahigh brilliance Microfocus RA generator/confocal optics and Rigaku XtaLAB P200 diffractometer using the CrystalClear program suite at University of St Andrews by Dr. David Cordes. Structures were solved by Patterson (PATTY)³²⁴ methods and refined by full-matrix least-squares against F^2 using SHELXL-2018/3.³²³ All non-hydrogen atoms were refined anisotropically. Hydrogen atoms were placed in calculated positions (riding model). Structure solution and refinement were carried out using the CrystalStructure interface. Details on selected individual crystal structure determinations and refinements are given below.

t-butbmH: Empirical formula C₃₄H₄₀O₃, $MW = 496.66$, $\lambda = 1.54178$ Å. Monoclinic, space group $P2_1/n$ (No. 14), $a = 12.7501(3)$, $b = 10.0565(2)$, $c = 22.7503(5)$ Å, $\beta = 97.672(2)^\circ$, $V = 2890.96(11)$ Å³ $Z = 4$, crystal size $0.28 \times 0.08 \times 0.03$ mm³, $\rho_c = 1.141$ g/cm³, $\mu = 0.553$ mm⁻¹. $F_{000} = 1072$, CuK α radiation, $\lambda = 1.54178$ Å, $T = 100(2)$ K, $2\theta_{\max} = 134.6^\circ$, 25300 reflections collected, 5149 unique ($R_{\text{int}} = 0.0570$). Final $Goof = 1.002$. $R1 = 0.0438$, $wR2 = 0.11048$, R indices based on 3870 reflections with $I > 2\sigma(I)$ (refinement on F^2), $|\Delta\rho|_{\max} = 0.21(4)$ e Å⁻³, 343 parameters, 0 restraints. CCDC-1846435.

C1 Er(phen)(t**bm**)₃: Empirical formula C₇₈H₅₃ErN₂O₉; *MW* = 1329.48. Triclinic, Space group *P*1, *a* = 10.6127(3), *b* = 13.4533(4), *c* = 21.3672(7) Å, α = 93.073(2)°, β = 102.241(2)°, γ = 96.098(2)°, *V* = 2955.38(16) Å³, *Z* = 2; ρ_c = 1.493 Mg/m³, μ = 3.169 mm⁻¹, crystal size 0.15 x 0.07 x 0.05 mm³; *F*₀₀₀ = 1354, CuK α radiation, λ = 1.54178, *T* = 100(2)K, $2\theta_{\max}$ = 134.5°, 26571 reflections collected, 10450 unique reflections (*R*_{int} = 0.0484). Final *Goof* = 1.000, *R*1 = 0.0460, *wR*2 = 0.1261, *R* indices based on 9023 reflections with *I* > 2 σ (*I*) (refinement on *F*²), $|\Delta\rho|_{\max}$ = 1.4(1) e Å⁻³. 811 parameters, 0 restraints. CCDC-1587888.

C2 [Yb(phen)(t**bm**)₃]: Empirical formula C₇₈H₅₃YbN₂O₉; *MW* = 1335.26. Triclinic, space group *P*1, *a* = 10.6346(4), *b* = 13.4190(4), *c* = 21.3553(7) Å, α = 93.181(2)°, β = 102.149(3)°, γ = 96.363(3)°, *V* = 2951.16(18) Å³, *Z* = 2; ρ_c = 1.503 Mg/m³, μ = 1.651 mm⁻¹, crystal size 0.39 x 0.19 x 0.105 mm³; *F*₀₀₀ = 1350, Mo-K α radiation, λ = 0.71073 Å, *T* = 100(2) K, $2\theta_{\max}$ = 29.9°, 31459 reflections collected, 17169 unique reflections (*R*_{int} = 0.0370). Final *Goof* = 1.037, *R*1 = 0.0389, *wR*2 = 0.0758, *R* indices based on 14909 reflections with *I* > 2 σ (*I*) (refinement on *F*²), $|\Delta\rho|_{\max}$ = 1.00(2) e Å⁻³. 812 parameters, 0 restraints. CCDC-1587889.

C3 {[Eu(Cs)(t**bm**)₄]₂}: Empirical formula C₈₈H₆₀CsEuO₁₂, C₂H₆O; *MW* = 1640.29. Triclinic, space group *P*1, *a* = 14.6063(4), *b* = 16.8300(4), *c* = 17.6843(4) Å, α = 74.721(2), β = 77.698(2), γ = 83.202(2)°, *V* = 4088.34(17) Å³, *Z* = 2, ρ_c = 1.332 g/cm³, μ = 1.266 mm⁻¹, crystal size 0.32 x 0.28 x 0.02 mm³, *F*₀₀₀ = 1656, Mo-K α radiation, λ = 0.71073 Å, *T* = 100(2)K, $2\theta_{\max}$ = 64.5°, 90077 reflections collected, 26973 unique (*R*_{int} = 0.0599). Final *Goof* = 1.005, *R*1 = 0.0485, *wR*2 = 0.1002, *R* indices based on 20172 reflections with *I* > 2 α (*I*) (refinement on *F*²), $|\Delta\rho|_{\max}$ = 1.3(1) e Å⁻³, 944 parameters, 6 restraints. CCDC-1539972.

C4 {[Er(Cs)(t**bm**)₄]₂}: Empirical formula C₈₈H₆₀O₁₂CsEr, C₂H₆O; *MW* = 1655.59. Triclinic, space group *P*1, *a* = 14.6999(2), *b* = 16.6792(3), *c* = 17.5946(3) Å, α = 75.643(2), β = 76.758(2), γ = 83.394(1)°, *V* = 4060.28(11) Å³, *Z* = 2, ρ_c = 1.354 g/cm³, μ = 1.536 mm⁻¹, crystal size 0.30 x 0.26 x 0.10 mm³. *F*₀₀₀ = 1666, Mo-K α radiation, λ = 0.71073 Å, *T* = 100(2) K, $2\theta_{\max}$ = 69.2°, 108898 reflections collected, 32735 unique (*R*_{int} = 0.0359). Final *Goof* = 1.004, *R*1 = 0.0415, *wR*2 = 0.1026, *R* indices based on 26538 reflections with *I* > 2 σ (*I*) (refinement on *F*²), $|\Delta\rho|_{\max}$ = 1.9(1) e Å⁻³, 946 parameters, 24 restraints. CCDC-1539973.

C5 {[Yb(Cs)(t**bm**)₄]₂}: Empirical formula C₈₈H₆₀CsO₁₂Yb, C₂H₆O; *MW* = 1661.37. Triclinic, space group *P*1, *a* = 14.7042(3), *b* = 16.6321(3), *c* = 17.6009(4) Å, α = 75.677(2), β = 76.631(2), γ = 83.400(2)°, *V* = 4050.07(14) Å³, *Z* = 2, ρ_c = 1.362 g/cm³, μ = 1.658 mm⁻¹, crystal size 0.29 x 0.17 x 0.06 mm³, *F*₀₀₀ = 1670, Mo-K α radiation, λ = 0.71073 Å, *T* = 100(2) K, $2\theta_{\max}$ = 64.6°, 84523 reflections collected, 26691 unique (*R*_{int} = 0.0437). Final *Goof* = 1.010,

$RI = 0.0426$, $wR2 = 0.1041$, R indices based on 21048 reflections with $I > 2\sigma(I)$ (refinement on F^2), $|\Delta\rho|_{\max} = 1.8(1) \text{ e } \text{\AA}^{-3}$, 948 parameters, 12 restraints. CCDC-1539974.

C6 $\{[\text{Eu}(\text{Cs})(\text{mtbm})_4]_2\}_n$: Empirical formula $\text{C}_{100}\text{H}_{84}\text{CsEuO}_{12}$; $MW = 1762.54$. Triclinic, space group $P1$, $a = 14.8674(5)$, $b = 16.1731(5)$, $c = 18.0171(6) \text{ \AA}$, $\alpha = 84.406(2)$, $\beta = 74.987(3)$, $\gamma = 87.816(2)^\circ$, $V = 4164.1(2) \text{ \AA}^3$, $Z = 2$, $\rho_c = 1.406 \text{ g/cm}^3$, $\mu = 9.255 \text{ mm}^{-1}$, crystal size $0.13 \times 0.05 \times 0.03 \text{ mm}^3$, $F_{000} = 1796$, Cu-K α radiation, $\lambda = 1.54178 \text{ \AA}$, $T = 100(2) \text{ K}$, $2\theta_{\max} = 134.9^\circ$, 40590 reflections collected, 14792 unique ($R_{\text{int}} = 0.0490$). Final $Goof = 1.001$, $RI = 0.0370$, $wR2 = 0.0833$, R indices based on 12187 reflections with $I > 2\sigma(I)$ (refinement on F^2), $|\Delta\rho|_{\max} = 1.05(9) \text{ e } \text{\AA}^{-3}$, 1027 parameters, 0 restraints. CCDC-1539975.

C7 $\{[\text{Er}(\text{Cs})(\text{mtbm})_4]_2\}_n$: Empirical formula $\text{C}_{100}\text{H}_{84}\text{CsErO}_{12}$; $MW = 1777.84$. Triclinic, space group $P1$, $a = 14.8243(3)$, $b = 16.1860(4)$, $c = 17.9760(4) \text{ \AA}$, $\alpha = 83.768(2)$, $\beta = 75.176(2)$, $\gamma = 87.485(2)^\circ$, $V = 4144.49(17) \text{ \AA}^3$, $Z = 2$, $\rho_c = 1.425 \text{ g/cm}^3$, $\mu = 1.509 \text{ mm}^{-1}$, crystal size $0.28 \times 0.12 \times 0.05 \text{ mm}^3$, $F_{000} = 1806$, Mo-K α radiation, $\lambda = 0.71073 \text{ \AA}$, $T = 100(2) \text{ K}$, $2\theta_{\max} = 64.4^\circ$, 92120 reflections collected, 27193 unique ($R_{\text{int}} = 0.0591$). Final $Goof = 1.003$, $RI = 0.0455$, $wR2 = 0.0998$, R indices based on 20682 reflections with $I > 2\sigma(I)$ (refinement on F^2), $|\Delta\rho|_{\max} = 2.6(1) \text{ e } \text{\AA}^{-3}$, 1027 parameters, 6 restraints. CCDC-1539976.

C8 $[\text{Yb}(\text{Cs}\cdot\text{HOEt})(\text{mtbm})_4]_n$: Empirical formula $\text{C}_{102}\text{H}_{90}\text{CsO}_{13}\text{Yb}$; $MW = 1829.68$. Triclinic, space group $P1$, $a = 11.5606(2)$, $b = 16.2195(3)$, $c = 26.5428(5) \text{ \AA}$, $\alpha = 81.060(2)$, $\beta = 83.329(2)$, $\gamma = 81.209(2)^\circ$, $V = 4836.93(15) \text{ \AA}^3$, $Z = 2$, $\rho_c = 1.256 \text{ g/cm}^3$, $\mu = 1.395 \text{ mm}^{-1}$, crystal size $0.23 \times 0.15 \times 0.13 \text{ mm}^3$, $F_{000} = 1862$, Mo-K α radiation, $\lambda = 0.71073 \text{ \AA}$, $T = 100(2) \text{ K}$, $2\theta_{\max} = 52.7^\circ$, 81814 reflections collected, 19778 unique ($R_{\text{int}} = 0.0415$). Final $Goof = 1.005$, $RI = 0.0336$, $wR2 = 0.0810$, R indices based on 17759 reflections with $I > 2\sigma(I)$ (refinement on F^2), $|\Delta\rho|_{\max} = 1.26(8) \text{ e } \text{\AA}^{-3}$, 1066 parameters, 6 restraints. CCDC-1539977.

C9 $[\text{Eu}(\text{Cs})(\text{EtOH})_2(\text{mdbm})_4]_n$: Empirical formula $\text{C}_{72}\text{H}_{72}\text{CsEuO}_{10}$; $MW = 1382.16$. Monoclinic, space group $C2/c$, $a = 29.9314(14)$, $b = 8.4707(3)$, $c = 26.1484(11) \text{ \AA}$, $\alpha = 105.325(5)^\circ$, $V = 6393.9(5) \text{ \AA}^3$, $Z = 4$, $\rho_c = 1.436 \text{ g/cm}^3$, $\mu = 11.859 \text{ mm}^{-1}$, crystal size $0.18 \times 0.15 \times 0.06 \text{ mm}^3$, $F_{000} = 2808$, Cu-K α radiation, $\lambda = 1.54178 \text{ \AA}$, $T = 100(2) \text{ K}$, $2\theta_{\max} = 134.3^\circ$, 15957 reflections collected, 5670 unique ($R_{\text{int}} = 0.0398$). Final $Goof = 1.022$, $RI = 0.0650$, $wR2 = 0.1834$, R indices based on 4887 reflections with $I > 2\sigma(I)$ (refinement on F^2), $|\Delta\rho|_{\max} = 2.8(2) \text{ e } \text{\AA}^{-3}$, 397 parameters, 4 restraints. CCDC-1539978.

C10 $\{[\text{Eu}(\text{Rb})(\text{mtbm})_4]_2\}_n$: $\text{C}_{200}\text{H}_{168}\text{Eu}_2\text{O}_{24}\text{Rb}_2\cdot(\text{H}_2\text{O})$, $MW = 3448.20$. Triclinic, space group $P\bar{1}$ (No. 2), $a = 14.9383(5)$, $b = 15.9699(4)$, $c = 17.9990(7) \text{ \AA}$, $\alpha = 84.625(2)$, $\beta = 74.799(3)$, $\gamma = 88.086(2)^\circ$, $V = 4125.3(2) \text{ \AA}^3$, $Z = 1$, $\rho_c = 1.388 \text{ g/cm}^3$, $\mu = 6.673 \text{ mm}^{-1}$, crystal size $0.23 \times 0.07 \times 0.05 \text{ mm}^3$. $F_{000} = 1770$, Cu K α radiation, $\lambda = 1.54178 \text{ \AA}$, $2\theta_{\max} = 134.8^\circ$, 44958

reflections collected, 14682 unique ($R_{\text{int}} = 0.0549$). Final $Goof = 1.059$, $RI = 0.0386$, $wR2 = 0.0890$, R indices based on 13164 reflections with $I > 2\sigma(I)$, $|\Delta\rho|_{\text{max}} = 0.67 \text{ e } \text{\AA}^{-3}$, 1054 parameters, 3 restraints. The water molecule hydrogen atoms were refined with geometries restrained to ideal values. CCDC-1829212.

C11 $\{[\text{Nd}(\text{Rb})(\text{mtbm})_4]_2\}_n$: $\text{C}_{200}\text{H}_{168}\text{Nd}_2\text{O}_{24}\text{Rb}_2 \cdot (\text{H}_2\text{O})$, $MW = 3432.77$. Triclinic, space group $P\bar{1}$ (No. 2), $a = 14.9907(3)$, $b = 15.9632(3)$, $c = 17.9930(4) \text{ \AA}$, $\alpha = 84.954(2)$, $\beta = 74.674(2)$, $\gamma = 88.124(2)^\circ$, $V = 4136.30(15) \text{ \AA}^3$, $Z = 1$, $\rho_c = 1.378 \text{ g cm}^{-3}$, $\mu = 6.017 \text{ mm}^{-1}$, crystal size $0.167 \times 0.044 \times 0.028 \text{ mm}^3$. $F_{000} = 1764$, Cu $K\alpha$ radiation, $\lambda = 1.54178 \text{ \AA}$, $2\theta_{\text{max}} = 134.6^\circ$, 89010 reflections collected, 14738 unique ($R_{\text{int}} = 0.0665$). Final $Goof = 1.001$, $RI = 0.0335$, $wR2 = 0.0787$, R indices based on 13047 reflections with $I > 2\sigma(I)$, $|\Delta\rho|_{\text{max}} = 0.84 \text{ e } \text{\AA}^{-3}$, 1054 parameters, 9 restraints. The water molecule hydrogen atoms were refined with geometries restrained to ideal values. CCDC-1829213.

C12 $[\text{Nd}(\text{Rb} \cdot \text{HOEt})(\text{tbm})_4]_2$: $\text{C}_{180}\text{H}_{132}\text{Nd}_2\text{O}_{26}\text{Rb}_2 \cdot 2(\text{C}_2\text{H}_6\text{O})$, $MW = 3262.40$. Triclinic, space group $P\bar{1}$ (No. 2), $a = 14.0539(2)$, $b = 14.7835(3)$, $c = 19.7708(4) \text{ \AA}$, $\alpha = 99.829(2)$, $\beta = 107.431(2)$, $\gamma = 90.137(2)^\circ$, $V = 3855.27(13) \text{ \AA}^3$, $Z = 1$, $\rho_c = 1.405 \text{ g/cm}^3$, $\mu = 1.367 \text{ mm}^{-1}$, crystal size $0.31 \times 0.21 \times 0.12 \text{ mm}^3$. $F_{000} = 1666$, Mo $K\alpha$ radiation, $\lambda = 0.71073 \text{ \AA}$, $2\theta_{\text{max}} = 64.7^\circ$, 84599 reflections collected, 25545 unique ($R_{\text{int}} = 0.0650$). Final $Goof = 1.002$, $RI = 0.0496$, $wR2 = 0.0959$, R indices based on 19518 reflections with $I > 2\sigma(I)$, $|\Delta\rho|_{\text{max}} = 1.1 \text{ e } \text{\AA}^{-3}$, 961 parameters, 13 restraints. One phenyl ring and two solvent ethanol molecules were modelled as being disordered over two sets of sites with occupancies constrained to 0.5 and with the non-hydrogen atoms refined with isotropic displacement parameters. Geometries of the disordered atoms were restrained to ideal values. CCDC-1829214.

C13 $[\text{Nd}(\text{Cs} \cdot 2\text{HOEt})(\text{dbm})_4]_n$: $\text{C}_{64}\text{H}_{56}\text{CsNdO}_{10}$, $MW = 1262.23$. Monoclinic, space group $C2/c$, $a = 27.4726(6)$, $b = 8.29060(10)$, $c = 25.4388(6) \text{ \AA}$, $\alpha = 108.315(2)^\circ$, $V = 5500.5(2) \text{ \AA}^3$, $Z = 4$, $\rho_c = 1.524 \text{ g/cm}^3$, $\mu = 12.772 \text{ mm}^{-1}$, crystal size $0.26 \times 0.084 \times 0.053 \text{ mm}^3$. $F_{000} = 2540$, Cu $K\alpha$ radiation, $\lambda = 1.54178 \text{ \AA}$, $2\theta_{\text{max}} = 134.6^\circ$, 29516 reflections collected, 4906 unique ($R_{\text{int}} = 0.0436$). Final $Goof = 1.090$, $RI = 0.0386$, $wR2 = 0.1095$, R indices based on 4314 reflections with $I > 2\sigma(I)$, $|\Delta\rho|_{\text{max}} = 2.5 \text{ e } \text{\AA}^{-3}$, 349 parameters, 0 restraints. CCDC-1829216.

C14 $[\text{Yb}(\text{mtbm})_3(\text{OH}_2)]_2$: $\text{C}_{75}\text{H}_{65}\text{O}_{10}\text{Yb} \cdot 0.5(\text{C}_2\text{H}_6\text{O})$, $MW = 1322.34$. Monoclinic, space group $P2_1/n$, $a = 10.5065(12)$, $b = 22.8219(3)$, $c = 26.2567(3) \text{ \AA}$, $\alpha = 90.116(2)^\circ$, $V = 6295.8(7) \text{ \AA}^3$, $Z = 4$, $\rho_c = 1.395 \text{ g/cm}^3$, $\mu = 3.245 \text{ mm}^{-1}$, crystal size $0.31 \times 0.042 \times 0.038 \text{ mm}^3$. $F_{000} = 2712$, Cu $K\alpha$ radiation, $\lambda = 1.54178 \text{ \AA}$, $2\theta_{\text{max}} = 134.9^\circ$, 66086 reflections collected, 11254 unique ($R_{\text{int}} = 0.0839$). Final $Goof = 1.069$, $RI = 0.0486$, $wR2 = 0.1117$, R indices based on 8726 reflections with $I > 2\sigma(I)$, $|\Delta\rho|_{\text{max}} = 1.7 \text{ e } \text{\AA}^{-3}$, 820 parameters, 17 restraints. The solvent was

modelled as an ethanol molecule disordered about a crystallographic inversion centre. Geometries were restrained to ideal values. Water molecule hydrogen atoms were located and refined with geometries restrained to ideal values. CCDC 1829215.

[Cs(**mtbm**)]_n: C₂₅H₂₁CsO₃, *MW* = 502.33. Monoclinic, space group *P2₁/c*, *a* = 8.41028(14), *b* = 31.2556(4), *c* = 8.01519(14) Å, σ = 102.777(2)°, *V* = 2054.77(6) Å³, *Z* = 4, ρ_c = 1.624 g/cm³, μ = 14.245 mm⁻¹, crystal size 0.240 x 0.057 x 0.042 mm³. *F*₀₀₀ = 1000, Cu K α radiation, λ = 1.54178 Å, $2\theta_{\max}$ = 134.6°, 17616 reflections collected, 3671 unique (*R*_{int} = 0.0558). Final *Goof* = 1.037, *RI* = 0.0455, *wR2* = 0.1174, *R* indices based on 3361 reflections with *I* > 2 σ (*I*), $|\Delta\rho|_{\max}$ = 2.4 e Å⁻³, 265 parameters, 0 restraints. CCDC-1829217.

C15 [Eu(μ -**dmba**)(**dmdbm**)(**dmtbm**)HOEt]₂ : C₁₁₆H₁₂₂Eu₂O₁₆₄(C₂H₆O), *MW* = 2260.32. Monoclinic, space group *P2₁/n* (No. 14), *a* = 15.0498(1), *b* = 20.7837(1), *c* = 19.1261(2) Å, α = 110.583(1)°, *V* = 5600.56(7) Å³, *Z* = 2, ρ_c = 1.340 g/cm³, μ = 8.475 mm⁻¹, crystal size 0.16 x 0.11 x 0.08 mm³. *F*₀₀₀ = 2352, CuK σ radiation, λ = 1.54178 Å, *T* = 100(2)K, $2\theta_{\max}$ = 134.6°, 61717 reflections collected, 10001 unique (*R*_{int} = 0.0485). Final *Goof* = 1.000, *RI* = 0.0289, *wR2* = 0.0667, *R* indices based on 8766 reflections with *I* > 2 σ (*I*) (refinement on *F*²), $|\Delta\rho|_{\max}$ = 0.68(6) e Å⁻³, 697 parameters, 14 restraints. CCDC-1846430.

C16 [Tb(μ -**dmba**)(**dmdbm**)(**dmtbm**)HOEt]₂: C₁₁₆H₁₂₂Tb₂O₁₆₄(C₂H₆O), *MW* = 2274.25. Monoclinic, space group *P2₁/n* (No. 14), *a* = 15.0467(1), *b* = 20.8306(1), *c* = 19.1237(2) Å, α = 110.933(1)°, *V* = 5598.36(7) Å³, *Z* = 2, ρ_c = 1.349 g/cm³, μ = 6.671 mm⁻¹, crystal size 0.17 x 0.14 x 0.10 mm³. *F*₀₀₀ = 2360, CuK σ radiation, λ = 1.54178 Å, *T* = 100(2)K, $2\theta_{\max}$ = 134.6°, 55865 reflections collected, 9972 unique (*R*_{int} = 0.0311). Final *Goof* = 1.002, *RI* = 0.0241, *wR2* = 0.0607, *R* indices based on 9188 reflections with *I* > 2 σ (*I*) (refinement on *F*²), $|\Delta\rho|_{\max}$ = 0.46(5) e Å⁻³, 715 parameters, 8 restraints. CCDC-1846434.

C17 [Yb(μ -**dmba**)(**dmdbm**)₂HOMe]₂: C₉₇H₁₀₆O₁₅Yb₂, *MW* = 1857.90, monoclinic, space group *P2₁/c* (No. 14), *a* = 18.0271(3), *b* = 14.4367(2), *c* = 34.8079(3) Å, α = 102.091(1)°, *V* = 8857.9(2) Å³, *Z* = 4, ρ_c = 1.393 g/cm³, μ = 4.306 mm⁻¹, crystal size 0.30 x 0.27 x 0.12 mm³, *F*₀₀₀ = 3792, CuK α radiation, λ = 1.54178 Å, *T* = 100(2)K, $2\theta_{\max}$ = 135.4°, 26738 reflections collected, 26738 unique (*R*_{int} = 0.0000). Final *Goof* = 1.251, *RI* = 0.0696, *wR2* = 0.1772, *R* indices based on 25451 reflections with *I* > 2 σ (*I*) (refinement on *F*²), $|\Delta\rho|_{\max}$ = 2.0(1) e Å⁻³, 1050 parameters, 7 restraints. CCDC-1846437.

C18 [Yb(μ -**dmdbm**)(**dmdbm**)₂]₂: C₁₁₄H₁₁₄O₁₂Yb₂, *MW* = 2022.13. Monoclinic, space group *P2₁/n* (No. 14), *a* = 17.1570(2), *b* = 14.8841(1), *c* = 19.6698(2) Å, α = 108.494(1)°, *V* = 4763.60(8) Å³, *Z* = 2, ρ_c = 1.410 g/cm³, μ = 2.014 mm⁻¹, crystal size 0.38 x 0.25 x 0.08 mm³. *F*₀₀₀ = 2068, MoK α radiation, λ = 0.71073 Å, *T* = 100(2)K, $2\theta_{\max}$ = 75.3°, 161830 reflections

collected, 24607 unique ($R_{\text{int}} = 0.0543$). Final $Goof = 1.003$, $RI = 0.0391$, $wR2 = 0.0841$, R indices based on 18359 reflections with $I > 2\sigma(I)$ (refinement on F^2), $|\Delta\rho|_{\text{max}} = 5.0(1) \text{ e } \text{\AA}^{-3}$, 589 parameters, 0 restraints. CCDC-1846431.

C19 [Eu(**dmdbm**)₄(Cs)]_n: C₇₆H₇₆CsEuO₈, $MW = 1402.2$. Orthorhombic, space group $Pccn$ (No. 56), $a = 14.7842(3)$, $b = 29.7258(5)$, $c = 7.5735(2) \text{ \AA}$, $V = 3328.34(12) \text{ \AA}^3$, $Z = 2$, $\rho_c = 1.399 \text{ g/cm}^3$, $\mu = 1.536 \text{ mm}^{-1}$, crystal size $0.25 \times 0.20 \times 0.15 \text{ mm}^3$, $F_{000} = 1428$, MoK α radiation, $\lambda = 0.71073 \text{ \AA}$, $T = 100(2)\text{K}$, $2\theta_{\text{max}} = 64.9^\circ$, 65961 reflections collected, 5842 unique ($R_{\text{int}} = 0.0393$). Final $Goof = 1.002$, $RI = 0.0505$, $wR2 = 0.1589$, R indices based on 4609 reflections with $I > 2\sigma(I)$ (refinement on F^2), $|\Delta\rho|_{\text{max}} = 6.1(2) \text{ e } \text{\AA}^{-3}$, 222 parameters, 13 restraints. CCDC-1846431.

C20 [Yb(**dmdbm**)₄(K)]_n: C₇₆H₇₆KO₈Yb, $MW = 1329.51$. Orthorhombic, space group $Pccn$ (No. 56), $a = 14.6365(7)$, $b = 29.8941(14)$, $c = 7.4973(7) \text{ \AA}$, $V = 3280.4(4) \text{ \AA}^3$, $Z = 2$, $\rho_c = 1.346 \text{ g/cm}^3$, $\mu = 3.641 \text{ mm}^{-1}$, crystal size $0.07 \times 0.03 \times 0.02 \text{ mm}^3$. $F_{000} = 1370$, CuK α radiation, $\lambda = 1.54178 \text{ \AA}$, $T = 100(2)\text{K}$, $2\theta_{\text{max}} = 134.6^\circ$, 22647 reflections collected, 2928 unique ($R_{\text{int}} = 0.1196$). Final $Goof = 1.009$, $RI = 0.0851$, $wR2 = 0.2296$, R indices based on 1781 reflections with $I > 2\sigma(I)$ (refinement on F^2), $|\Delta\rho|_{\text{max}} = 3.8(2) \text{ e } \text{\AA}^{-3}$, 222 parameters, 13 restraints. CCDC-1846432.

C21 [Yb(**etdbm**)₃(HOME)]₂: C₅₈H₆₁O₇Yb, $MW = 1043.10$. Monoclinic, space group $P2_1/c$ (No. 14), $a = 27.6844(3)$, $b = 12.2823(1)$, $c = 30.1388(3) \text{ \AA}$, $\alpha = 105.316(1)^\circ$, $V = 9884.06(17) \text{ \AA}^3$, $Z = 8$, $\rho_c = 1.402 \text{ g/cm}^3$, $\mu = 1.945 \text{ mm}^{-1}$, $0.31 \times 0.23 \times 0.17 \text{ mm}^3$. $F_{000} = 4280$, MoK α radiation, $\lambda = 0.71073 \text{ \AA}$, $T = 100(2)\text{K}$, $2\theta_{\text{max}} = 64.9^\circ$, 204134 reflections collected, 33939 unique ($R_{\text{int}} = 0.0415$). Final $Goof = 1.002$, $RI = 0.0450$, $wR2 = 0.1147$, R indices based on 28533 reflections with $I > 2\sigma(I)$ (refinement on F^2), $|\Delta\rho|_{\text{max}} = 4.0(1) \text{ e } \text{\AA}^{-3}$, 1204 parameters, 13 restraints. CCDC-1846438.

C22 [Yb(**etdbm**)₄(Cs)]_n: C₇₆H₇₆CsO₈Yb, $MW = 1423.31$. Monoclinic, space group $C2$ (No. 5), $a = 30.1708(10)$, $b = 8.3962(1)$, $c = 14.9290(9) \text{ \AA}$, $\alpha = 118.445(4)^\circ$, $V = 3325.3(2) \text{ \AA}^3$, $Z = 2$, $\rho_c = 1.422 \text{ g/cm}^3$, $\mu = 2.001 \text{ mm}^{-1}$, crystal size $0.24 \times 0.19 \times 0.08 \text{ mm}^3$. $F_{000} = 1442$, MoK α radiation, $\lambda = 0.71073 \text{ \AA}$, $T = 100(2)\text{K}$, $2\theta_{\text{max}} = 65.4^\circ$, 18749 reflections collected, 18749 unique ($R_{\text{int}} = 0.0000$). Final $Goof = 1.004$, $RI = 0.0495$, $wR2 = 0.1494$, R indices based on 17754 reflections with $I > 2\sigma(I)$ (refinement on F^2), $|\Delta\rho|_{\text{max}} = 5.5(2) \text{ e } \text{\AA}^{-3}$, 394 parameters, 1 restraint. Lp and absorption corrections applied. Absolute structure parameter = $0.010(7)$ (Flack, H. D. *Acta Cryst.* **1983**, *A39*, 876-881). The structure refined as a 2-component twin. Component 2 rotated by -179.9953° around $[1.00 \ 0.00 \ 0.01]$ (reciprocal) or $[0.71 \ 0.00 \ 0.71]$ (direct) direction. CCDC-1846429.

C23 [Eu(**ettbm**)₄(Cs·HOEt)]₂: C₂₂₈H₂₂₈Cs₂Eu₂O₂₆, *MW* = 3953.84. Triclinic, space group *P*-1 (No. 2), *a* = 17.1680(5), *b* = 17.4332(4), *c* = 18.4379(3) Å, α = 88.513(2), β = 80.968(2), γ = 65.713(2)°, *V* = 4963.0(2) Å³, *Z* = 1, ρ_c = 1.323 g/cm³, μ = 7.829 mm⁻¹, crystal size 0.25 x 0.09 x 0.06 mm³, *F*₀₀₀ = 2040, CuK α radiation, λ = 1.54178 Å, *T* = 100(2)K, $2\theta_{\max}$ = 134.6°, 109457 reflections collected, 17676 unique (*R*_{int} = 0.0557). Final *Goof* = 1.034, *R**I* = 0.0707, *wR*₂ = 0.1979, *R* indices based on 14055 reflections with *I* > 2 σ (*I*) (refinement on *F*²), $|\Delta\rho|_{\max}$ = 1.57(9) e Å⁻³, 1049 parameters, 732 restraints. CCDC-1846436.

C24 [Eu(**budbm**)₄Cs]_{*n*}: C₉₂H₁₀₈CsEuO₈, *MW* = 1626.65. Monoclinic, space group *I*2 (No. 5), *a* = 21.3014(2), *b* = 8.0066(1), *c* = 23.7700(3) Å, α = 99.984(1)°, *V* = 3992.62(8) Å³, *Z* = 2, ρ_c = 1.353 g/cm³, μ = 1.291 mm⁻¹, crystal size 0.38 x 0.25 x 0.18 mm³. *F*₀₀₀ = 1684, MoK α radiation, λ = 0.71073 Å, *T* = 100(2)K, $2\theta_{\max}$ = 64.1°, 42702 reflections collected, 13119 unique (*R*_{int} = 0.0238). Final *Goof* = 1.004, *R**I* = 0.0277, *wR*₂ = 0.0688, *R* indices based on 12624 reflections with *I* > 2 σ (*I*) (refinement on *F*²), $|\Delta\rho|_{\max}$ = 1.89(8) e Å⁻³, 465 parameters, 1 restraint. *Lp* and absorption corrections applied. Absolute structure parameter = 0.014(3) (Parsons P., Flack H. D. and Wagner T., *Acta Cryst.*, **2013**, *B69*, 249-259). CCDC-1846428.

C25 [Eu(μ -**mba**)(**mdbm**)(OHEt)]₂: C₈₈H₈₆Eu₂O₁₄, *MW* = 1671.48. Triclinic, space group *P*-1 (No. 2), *a* = 12.3967(3), *b* = 12.4774(3), *c* = 15.2425(4) Å, α = 77.570(2), β = 66.211(2), γ = 60.554(2)°, *V* = 1878.26(8) Å³, *Z* = 1, ρ_c = 1.478 g/cm³, μ = 1.721 mm⁻¹, crystal size 0.16 x 0.15 x 0.07 mm³. *F*₀₀₀ = 852, MoK α radiation, λ = 0.71073 Å, *T* = 100(2)K, $2\theta_{\max}$ = 65.4°, 41454 reflections collected, 12690 unique (*R*_{int} = 0.0378). Final *Goof* = 1.004, *R**I* = 0.0285, *wR*₂ = 0.0620, *R* indices based on 11231 reflections with *I* > 2 σ (*I*) (refinement on *F*²), $|\Delta\rho|_{\max}$ = 1.2(1) e Å⁻³, 479 parameters, 1 restraint.

C26 [Nd(**tnm**)₃(DMSO)₂]: 2(C₁₀₆H₇₅NdO₁₁S₂), C₂H₆OS, 1.5(C₂H₆O, H₂O), *MW* = 3640.28. Triclinic, space group *P*-1 (No. 2), *a* = 13.2128(4), *b* = 17.3769(4), *c* = 20.8146(4) Å, α = 89.837(2), β = 75.481(2), γ = 85.908(2)°, *V* = 4614.0(2) Å³, *Z* = 1, ρ_c = 1.310 g cm⁻³, μ = 0.683 mm⁻¹, crystal size 0.416 x 0.200 x 0.070 mm³. *F*₀₀₀ = 1878, MoK radiation, λ = 0.71073 Å, *T* = 100(2) K, $2\theta_{\max}$ = 64.7°, 100011 reflections collected, 30417 unique (*R*_{int} = 0.0583). Final *Goof* = 1.002, *R**I* = 0.0561, *wR*₂ = 0.1389, *R* indices based on 23101 reflections with *I* > 2 σ (*I*) (refinement on *F*²), $|\Delta\rho|_{\max}$ = 1.1(1) e Å⁻³, 1444 parameters, 378 restraints.

C27 [Eu(**tnm**)₃(DMSO)₂]: 2(C₁₀₆H₇₅EuO₁₁S₂), C₂H₆OS, 1.5(C₂H₆O, H₂O), *MW* = 3655.72, pale yellow plate, 0.26 x 0.22 x 0.04 mm³, triclinic, space group *P*-1 (No. 2), *a* = 13.2024(3), *b* = 17.3493(4), *c* = 20.7471(5) Å, α = 89.687(2), β = 75.677(2), γ = 85.672(2)°, *V* = 4590.90(19) Å³, *Z* = 1, ρ_c = 1.322 g/cm³, μ = 5.933 mm⁻¹. *F*₀₀₀ = 1884, CuK α radiation, λ = 1.54178 Å, *T* = 100(2)K, $2\theta_{\max}$ = 134.7°, 46811 reflections collected, 16278 unique (*R*_{int} =

0.0426). Final $Goof = 1.005$, $R1 = 0.0411$, $wR2 = 0.1068$, R indices based on 14775 reflections with $I > 2\sigma(I)$ (refinement on F^2), $|\Delta\rho|_{\max} = 0.77(7) \text{ e } \text{\AA}^{-3}$, 1444 parameters, 360 restraints.

C28 [Gd(**tnm**)₃(DMSO)₂]: 2(C₁₀H₇S₂O₁₁Gd), C₂H₆OS, 1.5(C₂H₆O, H₂O), $MW = 3666.30$. Triclinic, space group $P-1$ (No. 2), $a = 13.2123(4)$, $b = 17.3707(5)$, $c = 20.7312(5) \text{ \AA}$, $\alpha = 89.738(2)$, $\beta = 75.704(2)$, $\gamma = 85.603(2)^\circ$, $V = 4596.5(2) \text{ \AA}^3$, $Z = 1$, $\rho_c = 1.324 \text{ g cm}^{-3}$, $\mu = 5.708 \text{ mm}^{-1}$, crystal size $0.166 \times 0.102 \times 0.021 \text{ mm}^3$. $F_{000} = 1886$, CuK α radiation, $\lambda = 1.54178 \text{ \AA}$, $T = 100(2) \text{ K}$, $2\theta_{\max} = 133.2^\circ$, 126377 reflections collected, 16220 unique ($R_{\text{int}} = 0.1306$). Final $Goof = 1.000$, $R1 = 0.0516$, $wR2 = 0.1237$, R indices based on 12817 reflections with $I > 2\sigma(I)$ (refinement on F^2), $|\Delta\rho|_{\max} = 0.83(8) \text{ e } \text{\AA}^{-3}$, 1446 parameters, 366 restraints.

C29 [Yb(**tnm**)₃(DMSO)₂]: 2(C₁₀H₇S₂O₁₁Yb), C₂H₆OS, 1.5(C₂H₆O, H₂O), $MW = 3697.88$. Triclinic, space group $P-1$ (No. 2), $a = 13.2004(3)$, $b = 17.3176(4)$, $c = 20.6645(5) \text{ \AA}$, $\alpha = 89.505(2)$, $\beta = 75.711(2)$, $\gamma = 85.494(2)^\circ$, $V = 4563.32(19) \text{ \AA}^3$, $Z = 1$, $\rho_c = 1.346 \text{ g cm}^{-3}$, $\mu = 1.146 \text{ mm}^{-1}$, crystal size $0.322 \times 0.248 \times 0.074 \text{ mm}^3$. $F_{000} = 1898$, MoK α radiation, $\lambda = 0.71073 \text{ \AA}$, $T = 100(2) \text{ K}$, $2\theta_{\max} = 64.7^\circ$, 98398 reflections collected, 29997 unique ($R_{\text{int}} = 0.0548$). Final $Goof = 1.003$, $R1 = 0.0568$, $wR2 = 0.1451$, R indices based on 25610 reflections with $I > 2\sigma(I)$ (refinement on F^2), $|\Delta\rho|_{\max} = 2.1(1) \text{ e } \text{\AA}^{-3}$, 1446 parameters, 366 restraints. Lp and absorption corrections applied.

C30 [Ir(dFppy)₂(**tbm**)]: C₄₄H₂₇F₄IrN₂O₃, $MW = 899.92$. Monoclinic, space group $I2/a$ (No. 15), $a = 18.766(2)$, $b = 7.9098(9)$, $c = 47.242(5) \text{ \AA}$, $\beta = 99.366(4)^\circ$, $V = 6918.8(13) \text{ \AA}^3$, $Z = 8$, $\rho_c = 1.728 \text{ g cm}^{-3}$, $\mu = 3.938 \text{ mm}^{-1}$, crystal size $0.20 \times 0.17 \times 0.02 \text{ mm}^3$. $F_{000} = 3536$, Mo-K α radiation, $\lambda = 0.71075 \text{ \AA}$, $T = 173(2) \text{ K}$, $2\theta_{\max} = 50.8^\circ$, 40414 reflections collected, 6361 unique ($R_{\text{int}} = 0.0455$). Final $Goof = 1.059$, $R1 = 0.0241$, $wR2 = 0.0519$, R indices based on 5453 reflections with $I > 2\sigma(I)$ (refinement on F^2), $|\Delta\rho|_{\max} = 1.14 \text{ e } \text{\AA}^{-3}$, 487 parameters, 0 restraints. Lp and absorption corrections applied.

C31 [Ir(dFppy)₂(**pydbm**)]: C₄₃H₂₈Cl₂F₄IrN₃O₂, $MW = 957.83$. Triclinic, space group $P\bar{1}$ (No. 2), $a = 11.7141(17)$, $b = 18.089(3)$, $c = 19.339(3) \text{ \AA}$, $\alpha = 98.282(3)$, $\beta = 93.158(3)$, $\gamma = 105.434(4)^\circ$, $V = 3890.1(11) \text{ \AA}^3$, $Z = 4$, $\rho_c = 1.635 \text{ g cm}^{-3}$, $\mu = 3.639 \text{ mm}^{-1}$, crystal size $0.08 \times 0.04 \times 0.02 \text{ mm}^3$. $F_{000} = 1880$, Mo-K α radiation, $\lambda = 0.71075 \text{ \AA}$, $T = 173(2) \text{ K}$, $2\theta_{\max} = 50.7^\circ$, 45449 reflections collected, 13854 unique ($R_{\text{int}} = 0.1067$). Final $Goof = 1.041$, $R1 = 0.0684$, $wR2 = 0.1277$, R indices based on 7605 reflections with $I > 2\sigma(I)$ (refinement on F^2), $|\Delta\rho|_{\max} = 2.44 \text{ e } \text{\AA}^{-3}$, 1018 parameters, 0 restraints. Lp and absorption corrections applied.

Chapter 10 References

- 1 S. V. Eliseeva and J.-C. G. Bünzli, *New J. Chem.*, 2011, **35**, 1165.
- 2 S. V. Eliseeva and J.-C. G. Bünzli, *Chem. Soc. Rev.*, 2010, **39**, 189–227.
- 3 J.-C. G. Bünzli, *Eur. J. Inorg. Chem.*, 2017, **2017**, 5058–5063.
- 4 J.-C. G. Bünzli, *Luminescence Bioimaging with Lanthanide Complexes*, 2014, vol. 1st.
- 5 J. Kido and Y. Okamoto, *Chem. Rev.*, 2002, **102**, 2357–2368.
- 6 J. C. G. Bünzli and S. V. Eliseeva, *Photophysics of Lanthanoid Coordination Compounds*, 2013, vol. 8.
- 7 S. Shuvaev, M. Starck and D. Parker, *Chem. - Eur. J.*, 2017, **23**, 9974–9989.
- 8 J. C. G. Bünzli and K. L. Wong, *J. Rare Earths*, 2018, **36**, 1–41.
- 9 J.-L. Liu, Y.-C. Chen and M.-L. Tong, *Chem. Soc. Rev.*, 2018, **47**, 2431–2453.
- 10 A. de Bettencourt-Dias, *Dalton Trans.*, 2007, **22**, 2229–2241.
- 11 S. Faulkner, S. J. A. Pope and B. P. Burton- Pye, *Appl. Spectrosc. Rev.*, 2005, **40**, 1–31.
- 12 J.-C. G. Bünzli, *Coord. Chem. Rev.*, 2015, **293–294**, 19–47.
- 13 J.-C. G. Bünzli and S. V. Eliseeva, *J. Rare Earths*, 2010, **28**, 824–842.
- 14 Bünzli, *Mater. Sci.*, 2005, **83**, 25.
- 15 A. J. Amoroso and S. J. a Pope, *Chem. Soc. Rev.*, 2015, **44**, 4723–42.
- 16 J.-C. G. Bünzli, *J. Lumin.*, 2015, **170**, 866–878.
- 17 J. Frangioni, *Curr. Opin. Chem. Biol.*, 2003, **7**, 626–634.
- 18 G. A. Crosby and R. E. Whan, *J. Chem. Phys.*, 1960, **32**, 614–615.
- 19 G. A. Crosby, R. E. Whan and R. M. Alire, *J. Chem. Phys.*, 1961, **34**, 743–748.
- 20 L. R. Melby, N. J. Rose, E. Abramson and J. C. Caris, *J. Am. Chem. Soc.*, 1964, **86**,

- 5117–5125.
- 21 H. Bauer, J. Blanc and D. Ross, *J. Am. Chem. Soc.*, 1964, **86**, 5125–5131.
 - 22 L. G. Hubert-Pfalzgraf, N. Miele-Pajot, R. Papiernik and J. Vaissermann, *J. Chem. Soc. Dalton Trans.*, 1999, **9**, 4127–4130.
 - 23 P. W. Roesky, G. Canseco-Melchor and A. Zulys, *Chem. Commun.*, 2004, **0**, 738–739.
 - 24 P. C. Andrews, W. J. Gee, P. C. Junk and M. Massi, *New J. Chem.*, 2013, **37**, 35–48.
 - 25 D. T. Thielemann, A. T. Wagner, E. Rösch, D. K. Kölmel, J. G. Heck, B. Rudat, M. Neumaier, C. Feldmann, U. Schepers, S. Bräse and P. W. Roesky, *J. Am. Chem. Soc.*, 2013, **135**, 7454–7457.
 - 26 B. L. Reid, S. Stagni, J. M. Malicka, M. Cocchi, G. S. Hanan, M. I. Ogden and M. Massi, *Chem. Commun.*, 2014, **50**, 11580–11582.
 - 27 B. L. Reid, S. Stagni, J. M. Malicka, M. Cocchi, A. N. Sobolev, B. W. Skelton, E. G. Moore, G. S. Hanan, M. I. Ogden and M. Massi, *Chem. - Eur. J.*, 2015, **21**, 18354–18363.
 - 28 S. Cotton, *Lanthanide and Actinide Chemistry*, John Wiley & Sons, Ltd, Chichester, UK, 2005.
 - 29 M. R. Macdonald, J. E. Bates, J. W. Ziller, F. Furche and W. J. Evans, *J. Am. Chem. Soc.*, 2013, **135**, 9857–9868.
 - 30 J. Andrez, G. Bozoklu, G. Nocton, J. Pécaut, R. Scopelliti, L. Dubois and M. Mazzanti, *Chem. - Eur. J.*, 2015, **21**, 15188–15200.
 - 31 W. J. Evans, *Coord. Chem. Rev.*, 2000, **206–207**, 263–283.
 - 32 I. V. Basalov, V. Dorcet, G. K. Fukin, J.-F. Carpentier, Y. Sarazin and A. A. Trifonov, *Chem. - A Eur. J.*, 2015, **21**, 6033–6036.
 - 33 I. V. Basalov, O. S. Yurova, A. V. Cherkasov, G. K. Fukin and A. A. Trifonov, *Inorg. Chem.*, 2016, **55**, 1236–1244.
 - 34 J. A. Bogart, A. J. Lewis, S. A. Medling, N. A. Piro, P. J. Carroll, C. H. Booth and E. J. Schelter, *Inorg. Chem.*, 2013, **52**, 11600–11607.

- 35 N. A. Piro, J. R. Robinson, P. J. Walsh and E. J. Schelter, *Coord. Chem. Rev.*, 2014, **260**, 21–36.
- 36 Z. Dan, C. Ji and L. Deqian, *J. Rare Earths*, 2014, **32**, 681–685.
- 37 M. E. Fieser, C. T. Palumbo, H. S. La Pierre, D. P. Halter, V. K. Voora, J. W. Ziller, F. Furche, K. Meyer and W. J. Evans, *Chem. Sci.*, 2017, **8**, 7424–7433.
- 38 M. Seitz, A. G. Oliver and K. N. Raymond, *J. Am. Chem. Soc.*, 2007, **129**, 11153–11160.
- 39 M. Seth, P. Schwerdtfeger, M. Dolg and P. Fulde, *J. Am. Chem. Soc.*, 1995, **117**, 6597–6598.
- 40 W. T. Carnall, *J. Chem. Phys.*, 1968, **49**, 4443.
- 41 A. de Bettencourt-Dias, *Luminescence of Lanthanide ions in Coordination Compounds and Nanomaterials*, John Wiley & Sons, Ltd, Chichester, UK, 2014.
- 42 H. Kramers, *Proc ASTM*, 1957, **57**, 1259–1272.
- 43 L. F. Chibotaru, L. Ungur and A. Soncini, *Angew. Chemie - Int. Ed.*, 2008, **47**, 4126–4129.
- 44 R. J. Blagg, L. Ungur, F. Tuna, J. Speak, P. Comar, D. Collison, W. Wernsdorfer, E. J. L. McInnes, L. F. Chibotaru and R. E. P. Winpenny, *Nat. Chem.*, 2013, **5**, 673–678.
- 45 N. J. Turro, V. Ramamurthy and J. C. Scaiano, *Photochem. Photobiol.*, 2012, **88**, 1033–1033.
- 46 K. Binnemans, *Coord. Chem. Rev.*, 2015, **295**, 1–45.
- 47 C. E. Schäffer and C. K. Jørgensen, *J. Inorg. Nucl. Chem.*, 1958, **8**, 143–148.
- 48 E. Condon, *Phys. Rev.*, 1926, **28**, 1182–1201.
- 49 M. Kasha, *Discuss. Faraday Soc.*, 1950, **9**, 14–19.
- 50 C. M. Rudzinski, D. S. Engebretson, W. K. Hartmann and D. G. Nocera, *J. Phys. Chem. A*, 1998, **102**, 7442–7446.
- 51 S. I. Klink, G. A. Hebbink, L. Grave, P. G. B. Oude Alink, F. C. J. M. van Veggel and

- M. H. V. Werts, *J. Phys. Chem. A*, 2002, **106**, 3681–3689.
- 52 J. B. Lamture, Z. Hong Zhou, A. Suresh Kumar and T. G. Wensel, *Inorg. Chem.*, 1995, **34**, 864–869.
- 53 M. K. Nah, H. G. Cho, H. J. Kwon, Y. J. Kim, C. Park, H. K. Kim and J. G. Kang, *J. Phys. Chem. A*, 2006, **110**, 10371–10374.
- 54 M. H. Ha-Thi, J. A. Delaire, V. Michelet and I. Leray, *J. Phys. Chem. A*, 2010, **114**, 3264–3269.
- 55 C. Yang, L. M. Fu, Y. Wang, J. P. Zhang, W. T. Wong, X. C. Ai, Y. F. Qiao, B. S. Zou and L. L. Gui, *Angew. Chemie - Int. Ed.*, 2004, **43**, 5010–5013.
- 56 M. Kleinerman, *J. Chem. Phys.*, 1969, **51**, 2370–2381.
- 57 D. L. Dexter, *J. Chem. Phys.*, 1953, **21**, 836–850.
- 58 T. Forster, *Naturwissenschaften*, 1948, **33**, 166–175.
- 59 C. Reinhard and H. U. Güdel, *Inorg. Chem.*, 2002, **41**, 1048–1055.
- 60 S. J. A. Pope, B. P. Burton-Pye, R. Berridge, T. Khan, P. J. Skabara and S. Faulkner, *Dalton Trans.*, 2006, **23**, 2907–2912.
- 61 F. J. Steemers, W. Verboom, D. N. Reinhoudt, E. B. Vandertol and J. W. Verhoeven, *J. Am. Chem. Soc.*, 1995, **117**, 9408–9414.
- 62 S. Omagari, T. Nakanishi, Y. Hirai, Y. Kitagawa, T. Seki, K. Fushimi, H. Ito and Y. Hasegawa, *Eur. J. Inorg. Chem.*, 2017, 1–8.
- 63 F. Auzel, *Chem. Rev.*, 2004, **104**, 139–173.
- 64 N. M. Shavaleev, R. Scopelliti, F. Gumy and J. C. G. Bünzli, *Inorg. Chem.*, 2009, **48**, 7937–7946.
- 65 A. Nonat, M. Regueiro-Figueroa, D. Esteban-Gómez, A. De Blas, T. Rodríguez-Blas, C. Platas-Iglesias and L. J. Charbonnière, *Chem. - Eur. J.*, 2012, **18**, 8163–8173.
- 66 A. Zam, S. V. Eliseeva, L. Guø̃nø̃e, H. Nozary, S. Petoud and C. Piguet, *Chem. - Eur. J.*, 2014, **20**, 12172–12182.

- 67 E. A. Mikhalyova, A. V. Yakovenko, M. Zeller, M. A. Kiskin, Y. V. Kolomzarov, I. L. Eremenko, A. W. Addison and V. V. Pavlishchuk, *Inorg. Chem.*, 2015, **54**, 3125–3133.
- 68 S. Omagari, T. Nakanishi, Y. Kitagawa, T. Seki, K. Fushimi, H. Ito, A. Meijerink and Y. Hasegawa, *Sci. Rep.*, 2016, **6**, 1–11.
- 69 S. Lis, M. Elbanowski, B. Makowska and Z. Hnatejko, *J. Photochem. Photobiol. A Chem.*, 2002, **150**, 233–247.
- 70 C. Piguet, A. F. Williams, J. C. G. Bünzli, G. Bernardinelli and G. Hopfgartner, *J. Am. Chem. Soc.*, 1993, **115**, 8197–8206.
- 71 C. M. Andolina and J. R. Morrow, *Eur. J. Inorg. Chem.*, 2010, **2011**, 154–164.
- 72 M. Elhabiri, R. Scopelliti, J. C. G. Bünzli and C. Piguet, *J. Am. Chem. Soc.*, 1999, **121**, 10747–10762.
- 73 X. Rao, T. Song, J. Gao, Y. Cui, Y. Yang, C. Wu, B. Chen and G. Qian, *J. Am. Chem. Soc.*, 2013, **135**, 15559–64.
- 74 L. Song, Q. Wang, D. Tang, X. Liu and Z. Zhen, *New J. Chem.*, 2007, **31**, 506–511.
- 75 D. T. De Lill, A. De Bettencourt-Dias and C. L. Cahill, *Inorg. Chem.*, 2007, **46**, 3960–3965.
- 76 S. Freslon, Y. Luo, G. Calvez, C. Daignebonne, O. Guillou, K. Bernot, V. Michel and X. Fan, *Inorg. Chem.*, 2014, **53**, 1217–1228.
- 77 T. Shimanouchi, H. Matsuura, Y. Ogawa and I. Harada, *Tables of molecular vibrational frequencies*, 1972, vol. 1.
- 78 T. Shimanouchi, *J. Phys. Chem. Ref. Data*, 1977, **6**, 993–1102.
- 79 L. Winkless, R. H. C. Tan, Y. Zheng, M. Motevalli, P. B. Wyatt and W. P. Gillin, *Appl. Phys. Lett.*, 2006, **89**, 210–213.
- 80 R. H. C. Tan, M. Motevalli, I. Abrahams, P. B. Wyatt and W. P. Gillin, *J. Phys. Chem. B*, 2006, **110**, 24476–24479.
- 81 A. D'Aléo, F. Pointillart, L. Ouahab, C. Andraud and O. Maury, *Coord. Chem. Rev.*, 2012, **256**, 1604–1620.

- 82 W.-S. Lo, W.-T. Wong and G.-L. Law, *RSC Adv.*, 2016, **6**, 74100–74109.
- 83 A. T. Bui, A. Roux, A. Grichine, A. Duperray, C. Andraud and O. Maury, *Chem. - Eur. J.*, 2018, **24**, 3408–3412.
- 84 J. W. Walton, A. Bourdolle, S. J. Butler, M. Soulie, M. Delbianco, B. K. McMahon, R. Pal, H. Puschmann, J. M. Zwier, L. Lamarque, O. Maury, C. Andraud and D. Parker, *Chem. Commun.*, 2013, **49**, 1600–1602.
- 85 L. N. Puntus, K. A. Lyssenko, I. S. Pekareva and J. G. Bu, *J. Phys. Chem B*, 2009, **3**, 9265–9277.
- 86 D. Nie, Z. Chen, Z. Bian, J. Zhou, Z. Liu, F. Chen, Y. Zhao and C. Huang, *New J. Chem.*, 2007, **31**, 1639–1646.
- 87 S. Sivakumar, M. L. P. Reddy, A. H. Cowley and K. V Vasudevan, *Dalton Trans.*, 2010, **39**, 776–786.
- 88 F. R. Gonc, R. Longo and C. Piguet, *Phys. Chem. Chem. Phys.*, 2000, **2**, 5400–5403.
- 89 V. Vicinelli, P. Ceroni, M. Maestri, V. Balzani, M. Gorka and F. Vögtle, *J. Am. Chem. Soc.*, 2002, **124**, 6461–6468.
- 90 L. M. Fu, X. C. Ai, M. Y. Li, X. F. Wen, R. Hao, Y. S. Wu, Y. Wang and J. P. Zhang, *J. Phys. Chem. A*, 2010, **114**, 4494–4500.
- 91 W. D. Horrocks, J. P. Bolender, W. D. Smith and R. M. Supkowski, *J. Am. Chem. Soc.*, 1997, **4**, 5972–5973.
- 92 G. K. Liu, M. P. Jensen and P. M. Almond, *J. Phys. Chem. A*, 2006, **110**, 2081–2088.
- 93 Y. Zhong, L. Si, H. He and A. G. Sykes, *Dalton Trans.*, 2011, **40**, 11389–11395.
- 94 R. Janicki, P. Starynowicz and A. Mondry, *Eur. J. Inorg. Chem.*, 2008, **2008**, 3075–3082.
- 95 M. D. Ward, *Coord. Chem. Rev.*, 2010, **254**, 2634–2642.
- 96 D. Sykes, A. J. Cankut, N. M. Ali, A. Stephenson, S. J. P. Spall, S. C. Parker, J. a Weinstein and M. D. Ward, *Dalton Trans.*, 2014, **43**, 6414–28.
- 97 L. J. Charbonnière, S. Faulkner, C. Platas-Iglesias, M. Regueiro-Figueroa, A. Nonat,

- T. Rodríguez-Blas, A. de Blas, W. S. Perry and M. Tropicano, *Dalton Trans.*, 2013, **42**, 3667–81.
- 98 M. Mehlstäubl, G. S. Kottas, S. Colella and L. De Cola, *Dalton Trans.*, 2008, **2**, 2385.
- 99 T. Lazarides, D. Sykes, S. Faulkner, A. Barbieri and M. D. Ward, *Chem. - Eur. J.*, 2008, **14**, 9389–9399.
- 100 F. Kennedy, N. M. Shavaleev, T. Koullourou, Z. R. Bell, J. C. Jeffery, S. Faulkner and M. D. Ward, *Dalton Trans.*, 2007, **0**, 1492–1499.
- 101 F. C. J. M. Klink, Stephen.I.; Keizer, Henk; Van Veggel, *Angew. Chemie - Int. Ed.*, 2000, **39**, 4319–4321.
- 102 F. Chen, Z. Bian, Z. Liu, D. Nie, Z. Chen and C. Huang, *Inorg. Chem.*, 2008, **47**, 2507–2513.
- 103 H.-B. Xu, X.-L. Chen, J.-G. Deng, Z.-H. Deng, S.-L. Huang, M. Kurmoo and M.-H. Zeng, *Dalton Trans.*, 2018, **47**, 2073–2078.
- 104 N. M. Shavaleev, G. Accorsi, D. Virgili, Z. R. Bell, T. Lazarides, G. Calogero, N. Armaroli and M. D. Ward, *Inorg. Chem.*, 2005, **44**, 61–72.
- 105 N. M. Shavaleev, L. P. Moorcraft, S. J. a Pope, Z. R. Bell, S. Faulkner and M. D. Ward, *Chem. Commun.*, 2003, **0**, 1134–5.
- 106 K. Sénéchal-David, S. J. A. Pope, S. Quinn, S. Faulkner and T. Gunnlaugsson, *Inorg. Chem.*, 2006, **45**, 10040–10042.
- 107 L. Moriggi, A. Aebischer, C. Cannizzo, A. Sour, A. Borel, J.-C. G. Bünzli and L. Helm, *Dalton Trans.*, 2009, **0**, 2088–2095.
- 108 P. Coppo, M. Duati, V. N. Kozhevnikov, J. W. Hofstraat and L. De Cola, *Angew. Chemie - Int. Ed.*, 2005, **44**, 1806–1810.
- 109 P. A. Brayshaw, J. C. Bünzli, P. Froidevaux, J. M. Harrowfield, Y. Kim and A. N. Sobolev, *Inorg. Chem.*, 1995, **34**, 2068–2076.
- 110 N. M. Shavaleev, S. V. Eliseeva, R. Scopelliti and J.-C. G. Bünzli, *Inorg. Chem.*, 2014, **53**, 5171–5178.
- 111 G. a. Crosby and J. N. Demas, *J. Phys. Chem.*, 1971, **75**, 991–1024.

- 112 M. Massi, S. Stagni and M. I. Ogden, *Coord. Chem. Rev.*, 2017, <https://doi.org/10.1016/j.ccr.2017.11.017>.
- 113 H. Li, J. Sun, M. Yang, Z. Sun, J. Tang, Y. Ma and L. Li, *Inorg. Chem.*, 2018, 10.1021/acs.inorgchem.7b03186.
- 114 W. Wu, X. Zhang, A. Y. Kornienko, G. A. Kumar, D. Yu, T. J. Emge, R. E. Riman and J. G. Brennan, *Inorg. Chem.*, 2018, **57**, 1912–1918.
- 115 E. S. Andreiadis, D. Imbert, J. Pécaut, R. Demadrille and M. Mazzanti, *Dalton Trans.*, 2012, **41**, 1268.
- 116 M. Albrecht, O. Osetska, J. Klankermayer, R. Fröhlich, F. Gumy and J.-C. G. Bünzli, *Chem. Commun.*, 2007, **0**, 1834–1836.
- 117 T. Chuasaard, A. Ngamjarurojana, S. Surinwong, T. Konno, S. Bureekaew and A. Rujiwatra, *Inorg. Chem.*, 2018, 10.1021/acs.inorgchem.7b03016.
- 118 A. K. Jassal, B. S. Sran, Y. Suffren, K. Bernot, F. Pointillart, O. Cadour and G. Hundal, *Dalton Trans.*, 2018, **47**, 4722–4732.
- 119 M. Massi and M. I. Ogden, *Materials (Basel)*, 2017, **10**, 1369.
- 120 A. Nonat, T. Liu, O. Jeannin, F. Camerel and L. J. Charbonnière, *Chem. - Eur. J.*, 2018, **24**, 3784–3792.
- 121 Y. Ning, Y.-W. Liu, Y.-S. Meng and J.-L. Zhang, *Inorg. Chem.*, 2018, **57**, 1332–1341.
- 122 D. D'Alessio, S. Muzzioli, B. W. Skelton, S. Stagni, M. Massi and M. I. Ogden, *Dalton Trans.*, 2012, **41**, 4736–4739.
- 123 C. R. Driscoll, B. L. Reid, M. J. McIldowie, S. Muzzioli, G. L. Nealon, B. W. Skelton, S. Stagni, D. H. Brown, M. Massi and M. I. Ogden, *Chem. Commun.*, 2011, **47**, 3876–3878.
- 124 C. Lincheneau, E. Quinlan, J. a. Kitchen, T. McCabe, S. E. Matthews and T. Gunnlaugsson, *Supramol. Chem.*, 2013, **25**, 869–880.
- 125 J. Hamacek and A. Vuillamy, *Eur. J. Inorg. Chem.*, 2018, **2018**, 1155–1166.
- 126 M. G. Urbain, *Comp. Rend.*, 1897, **124**, 618 – 621.

- 127 J.-G. Bünzli, E. Moret, V. Foiret, K. J. Schenk, W. Mingzhao and Jin Linpei, *J. Alloys Compd.*, 1994, **207–208**, 107–111.
- 128 K. Binnemans, *Rare-earth beta-diketonates*, Elsevier B.V, 2005, vol. 35.
- 129 T. Anderson, M. Neuman and G. Melson, *Inorg. Chem.*, 1973, **111**, 927–930.
- 130 V. Lorenz, A. Fischer, K. Jacob, W. Brüser and F. T. Edelmann, *Chem. - Eur. J.*, 2001, **7**, 848–857.
- 131 P. Martín-Ramos, M. Ramos Silva, F. Lahoz, I. R. Martín, P. Chamorro-Posada, M. E. S. Eusebio, V. Lavín and J. Martín-Gil, *J. Photochem. Photobiol. A Chem.*, 2014, **292**, 16–25.
- 132 P. Martín-Ramos, P. S. Pereira da Silva, V. Lavín, I. R. Martín, F. Lahoz, P. Chamorro-Posada, M. R. Silva and J. Martín-Gil, *Dalton Trans.*, 2013, **42**, 13516–26.
- 133 P. B. Glover, A. P. Bassett, P. Nockemann, B. M. Kariuki, R. Van Deun and Z. Pikramenou, *Chem. - Eur. J.*, 2007, **13**, 6308–6320.
- 134 L. N. Sun, H. J. Zhang, Q. G. Meng, F. Y. Liu, L. S. Fu, C. Y. Peng, J. B. Yu, G. L. Zheng and S. Bin Wang, *J. Phys. Chem. B*, 2005, **109**, 6174–6182.
- 135 H. Wang, P. He, S. Liu, J. Shi and M. Gong, *Appl. Phys. B*, 2009, **97**, 481–487.
- 136 M. Ramos Silva, P. Martín-Ramos, J. T. Coutinho, L. C. J. Pereira and J. Martín-Gil, *Dalton Trans.*, 2014, **43**, 6752–61.
- 137 S. Biju, R. O. Freire, Y. K. Eom, R. Scopelliti, J. C. G. Bünzli and H. K. Kim, *Inorg. Chem.*, 2014, **53**, 8407–8417.
- 138 F. Albert Cotton, L. M. Daniels and P. Huang, *Inorg. Chem. Commun.*, 2001, **4**, 319–321.
- 139 J. P. Martins, P. Martín-Ramos, C. Coya, A. L. Álvarez, L. C. Pereira, R. Díaz, J. Martín-Gil and M. Ramos Silva, *Mater. Chem. Phys.*, 2014, **147**, 1157–1164.
- 140 A. Mech, M. Karbowski, C. Görrler-Walrand and R. Van Deun, *J. Alloys Compd.*, 2008, **451**, 215–219.
- 141 S. Akerboom, M. S. Meijer, M. a. Siegler, W. T. Fu and E. Bouwman, *J. Lumin.*, 2014, **145**, 278–282.

- 142 J. C. G. Bünzli, S. Comby, A. S. Chauvin and C. D. B. Vandevyver, *J. Rare Earths*, 2007, **25**, 257–274.
- 143 W. Q. Fan, J. Feng, S. Y. Song, Y. Q. Lei, Y. Xing, R. P. Deng, S. Dang and H. J. Zhang, *Eur. J. Inorg. Chem.*, 2008, **35**, 5513–5518.
- 144 X. Guo, H. Guo, L. Fu, L. D. Carlos, R. A. S. Ferreira, L. Sun, R. Deng and H. Zhang, *J. Phys. Chem. C*, 2009, **113**, 12538–12545.
- 145 T.-S. Kang, B. S. Harrison, M. Bouguettaya, T. J. Foley, J. M. Boncella, K. S. Schanze and J. R. Reynolds, *Adv. Funct. Mater.*, 2003, **13**, 205–210.
- 146 A. Shahalizad, A. D'Aléo, C. Andraud, M. H. Sazzad, D. H. Kim, Y. Tsuchiya, J. C. Ribierre, J. M. Nunzi and C. Adachi, *Org. Electron. physics, Mater. Appl.*, 2017, **44**, 50–58.
- 147 S. Comby and J. C. G. Bünzli, *Handb. Phys. Chem. Rare Earths*, 2007, **37**, 217–470.
- 148 S. B. Meshkova, Z. M. Topilova, D. V Bolshoy, S. V Beltyukova, M. P. Tsvirko and V. Y. Venchikov, *Acta Phys. Pol., A*, 1999, **95**, 983–990.
- 149 M. Iwamuro, Y. Wada, T. Kitamura and N. Nakashima, *Phys. Chem. Chem. Phys.*, 2000, **2**, 2291–2296.
- 150 M. P. Tsvirko, S. B. Meshkova, V. Y. Venchikov, Z. M. Topilova and D. V. Bol'shoi, *Opt. Spectrosc.*, 2001, **90**, 669–673.
- 151 N. M. Shavaleev, S. J. A. Pope, Z. R. Bell and M. D. Ward, *Dalton Trans.*, 2003, **0**, 808–814.
- 152 A. Bellusci, G. Barberio, A. Crispini, M. Ghedini, M. La Deda and D. Pucci, *Inorg. Chem.*, 2005, **44**, 1818–1825.
- 153 L. N. Sun, J. B. Yu, G. L. Zheng, H. J. Zhang, Q. G. Meng, C. Y. Peng, L. S. Fu, F. Y. Liu and Y. N. Yu, *Eur. J. Inorg. Chem.*, 2006, **19**, 3962–3973.
- 154 Q. Zhong, H. Wang, G. Qian, Z. Wang, J. Zhang, J. Qiu and M. Wang, *Inorg. Chem.*, 2006, **45**, 4537–4543.
- 155 A. I. Voloshin, N. M. Shavaleev and V. P. Kazakov, *J. Photochem. Photobiol. A Chem.*, 2000, **131**, 61–65.

- 156 A. Monguzzi, R. Tubino, F. Meinardi, A. O. Biroli, F. Demartin, F. Quochi, F. Cordella, M. A. Loi and M. Pizzotti, *Chem. Mater.*, 2009, **21**, 128–135.
- 157 Z. Ahmed and K. Iftikhar, *Inorg. Chim. Acta*, 2010, **363**, 2606–2615.
- 158 S. Dang, J. B. Yu, X. F. Wang, Z. Y. Guo, L. N. Sun, R. P. Deng, J. Feng, W. Q. Fan and H. J. Zhang, *J. Photochem. Photobiol. A Chem.*, 2010, **214**, 152–160.
- 159 R. Ilmi and K. Iftikhar, *Inorg. Chem. Commun.*, 2010, **13**, 1552–1557.
- 160 Z. Ahmed and K. Iftikhar, *Inorg. Chem. Commun.*, 2010, **13**, 1253–1258.
- 161 M. Irfanullah and K. Iftikhar, *Inorg. Chem. Commun.*, 2010, **13**, 1234–1238.
- 162 P. Martín-Ramos, V. Lavín, M. Ramos Silva, I. R. Martín, F. Lahoz, P. Chamorro-Posada, J. A. Paixão and J. Martín-Gil, *J. Mater. Chem. C*, 2013, **1**, 5701.
- 163 P. Martín-Ramos, P. S. Pereira da Silva, V. Lavín, I. R. Martín, F. Lahoz, P. Chamorro-Posada, M. Ramos Silva and J. Martín-Gil, *Dalton Trans.*, 2013, **42**, 13516.
- 164 P. Martín-Ramos, M. Ramos Silva, J. T. Coutinho, L. C. J. Pereira, P. Chamorro-Posada and J. Martín-Gil, *Eur. J. Inorg. Chem.*, 2014, **3**, 511–517.
- 165 P. S. Pereira da Silva, P. Martín-Ramos, M. R. Silva, V. Lavín, P. Chamorro-Posada and J. Martín-Gil, *Polyhedron*, 2014, **81**, 485–492.
- 166 Z. Ahmed and K. Iftikhar, *Polyhedron*, 2015, **85**, 570–592.
- 167 P. Martín-Ramos, P. Chamorro-Posada, M. Ramos Silva, P. S. Pereira da Silva, I. R. Martín, F. Lahoz, V. Lavín and J. Martín-Gil, *Opt. Mater. (Amst.)*, 2015, **41**, 139–142.
- 168 Z. Ahmed, R. E. Aderne, J. Kai, J. A. L. C. Resende and M. Cremona, *Polyhedron*, 2016, **117**, 518–525.
- 169 Z. Ahmed, R. E. Aderne, J. Kai, H. I. P. Chavarria and M. Cremona, *Thin Solid Films*, 2016, **620**, 34–42.
- 170 B. Li, H. Li, P. Chen, W. Sun, C. Wang, T. Gao and P. Yan, *Dalton Trans.*, 2016, **45**, 11459–11470.
- 171 O. Sun, P. Chen, H.-F. Li, T. Gao, W.-B. Sun, G.-M. Li and P.-F. Yan, *CrystEngComm*, 2016, **18**, 4627–4635.

- 172 Z. Ahmed, R. E. Aderne, J. Kai, J. A. L. C. Resende, H. I. Padilla-Chavarría and M. Cremona, *RSC Adv.*, 2017, **7**, 18239–18251.
- 173 L. Yang, Z. Gong, D. Nie, B. Lou, Z. Bian, M. Guan, C. Huang, H. J. Lee and W. P. Baik, *New J. Chem.*, 2006, **30**, 791.
- 174 R. Van Deun, P. Nockemann, T. N. Parac-Vogt, K. Van Hecke, L. Van Meervelt, C. Görrler-Walrand and K. Binnemans, *Polyhedron*, 2007, **26**, 5441–5447.
- 175 G. Zucchi, O. Maury, P. Thuéry and M. Ephritikhine, *Inorg. Chem.*, 2008, **47**, 10398–10406.
- 176 N. M. Shavaleev, R. Scopelliti, F. Gumy and J. C. G. Bünzli, *Eur. J. Inorg. Chem.*, 2008, **9**, 1523–1529.
- 177 N. S. Baek, Y. H. Kim, Y. K. Eom, J. H. Oh, H. K. Kim, A. Aebischer, F. Gumy, A.-S. Chauvin and J.-C. G. Bünzli, *Dalton Trans.*, 2010, **39**, 1532–1538.
- 178 S. Biju, Y. K. Eom, J.-C. G. Bünzli and H. K. Kim, *J. Mater. Chem. C*, 2013, **1**, 6935.
- 179 W. Li, J. Li, H. Li, P. Yan, G. Hou and G. Li, *J. Lumin.*, 2014, **146**, 205–210.
- 180 A. W. Woodward, A. Frazer, A. R. Morales, J. Yu, A. F. Moore, A. D. Campiglia, E. V. Jucov, T. V. Timofeeva and K. D. Belfield, *Dalton Trans.*, 2014, **43**, 16626–16639.
- 181 C. Yu, Z. Zhang, L. Liu, W. Feng, X. Lü, W. K. Wong and R. A. Jones, *Inorg. Chem. Commun.*, 2014, **49**, 30–33.
- 182 P. Martín-Ramos, I. R. Martín, F. Lahoz, S. Hernández-Navarro, P. S. Pereira da Silva, I. Hernández, V. Lavín and M. Ramos Silva, *J. Alloys Compd.*, 2015, **619**, 553–559.
- 183 Z. Zhang, C. Yu, L. Liu, H. Li, Y. He, X. Lü, W. K. Wong and R. A. Jones, *J. Photochem. Photobiol. A Chem.*, 2016, **314**, 104–113.
- 184 T. M. George, S. Varughese and M. L. P. Reddy, *RSC Adv.*, 2016, **6**, 69509–69520.
- 185 G. a Hebbink, D. N. Reinhoudt and F. C. J. M. Van Veggel, *European J. Org. Chem.*, 2001, **21**, 4101–4106.
- 186 J. R. Lakowicz, *Principles of Fluorescence Spectroscopy Principles of Fluorescence Spectroscopy*, 2006.

- 187 S. I. Klink, G. A. Hebbink, L. Grave, F. Van Veggel, D. N. Reinhoudt, L. H. Slooff, A. Polman and J. W. Hofstraat, *J. Appl. Phys.*, 1999, **86**, 1181–1185.
- 188 A. de Bettencourt-Dias, *Luminescence of lanthanide ions in coordination compounds and nanomaterials*, John Wiley & Sons, Ltd, Chichester, UK, 2014.
- 189 E. Deiters, B. Song, A. S. Chauvin, C. D. B. Vandevyver, F. Gumy and J. C. G. Bünzli, *Chem. - Eur. J.*, 2009, **15**, 885–900.
- 190 S. Swavey, A. Fratini, J. Grewal and A. Hutchinson, *Inorg. Chim. Acta*, 2015, **428**, 27–31.
- 191 E. E. S. Teotonio, G. M. Fett, H. F. Brito, W. M. Faustino, G. F. de Sá, M. C. F. C. Felinto and R. H. A. Santos, *J. Lumin.*, 2008, **128**, 190–198.
- 192 D. Niedzwiedzki and J. Sullivan, *J. Phys. Chem. B*, 2006, **110**, 22872–2285.
- 193 V. Divya, R. O. Freire and M. L. P. Reddy, *Dalton Trans.*, 2011, **40**, 3257–3268.
- 194 J. H. S. K. Monteiro, R. D. Adati, M. R. Davolos, J. R. M. Vicenti and R. A. Burrow, *New J. Chem.*, 2011, **35**, 1234.
- 195 K. Singh, R. Boddula and S. Vaidyanathan, *Inorg. Chem.*, 2017, **56**, 9376–9390.
- 196 O. L. Malta, H. F. Brito, J. F. S. Menezes, F. R. G. E. Silva, C. D. Donega and S. Alves, *Chem. Phys. Lett.*, 1998, **282**, 233–238.
- 197 O. Moudam, B. C. Rowan, M. Alamiry, P. Richardson, B. S. Richards, A. C. Jones and N. Robertson, *Chem. Commun.*, 2009, **43**, 6649–6651.
- 198 P. He, H. H. Wang, H. G. Yan, W. Hu, J. X. Shi and M. L. Gong, *Dalton Trans.*, 2010, **39**, 8919.
- 199 M. H. V. Werts, M. a. Duin, J. W. Hofstraat and J. W. Verhoeven, *Chem. Commun.*, 1999, **9**, 799–800.
- 200 M. L. P. Reddy, V. Divya and R. Pavithran, *Dalton Trans.*, 2013, **42**, 15249–15262.
- 201 K. Binnemans, *Chem. Rev.*, 2009, **109**, 4283–4374.
- 202 R. Van Deun, P. Nockemann, P. Fias, K. Van Hecke, L. Van Meervelt and K. Binnemans, *Chem. Commun.*, 2005, **3**, 590–592.

- 203 P. He, H. H. Wang, S. G. Liu, J. X. Shi, G. Wang and M. L. Gong, *Inorg. Chem.*, 2009, **48**, 11382–11387.
- 204 A. Bril, *J. Electrochem. Soc.*, 1976, **123**, 396–398.
- 205 W. H. Melhuish, *J. Phys. Chem.*, 1961, **65**, 229–235.
- 206 C. Yang, J. Xu, J. Ma, D. Zhu, Y. Zhang, L. Liang and M. Lu, *Photochem. Photobiol. Sci.*, 2013, **12**, 330–338.
- 207 M. Ismail, S. J. Lyle and J. E. Newbery, *J. Inorg. Nucl. Chem.*, 1969, **31**, 2091–2093.
- 208 B. L. Reid, R. C. Woodward, R. O. Fuller, A. N. Sobolev, B. W. Skelton, M. I. Ogden and M. Massi, *J. Coord. Chem.*, 2016, **69**, 1852–1863.
- 209 B. L. Reid, S. Stagni, J. M. Malicka, M. Cocchi, G. S. Hanan, M. I. Ogden and M. Massi, *Chem. Commun.*, 2014, **50**, 11580–11582.
- 210 B. L. Reid, PhD thesis, Curtin University, 2015.
- 211 C. Janiak, *J. Chem. Soc. Dalton Trans.*, 2000, **0**, 3885–3896.
- 212 L.-N. Sun, H.-J. Zhang, L.-S. Fu, F.-Y. Liu, Q.-G. Meng, C.-Y. Peng and J.-B. Yu, *Adv. Funct. Mater.*, 2005, **15**, 1041–1048.
- 213 C. F. Macrae, I. J. Bruno, J. A. Chisholm, P. R. Edgington, P. McCabe, E. Pidcock, L. Rodriguez-Monge, R. Taylor, J. Van De Streek and P. A. Wood, *J. Appl. Crystallogr.*, 2008, **41**, 466–470.
- 214 D. Casanova, M. Llunell, P. Alemany and S. Alvarez, *Chem. - Eur. J.*, 2005, **11**, 1479–1494.
- 215 H. Zabrodsky, S. Peleg and D. Avnir, *J. Am. Chem. ...*, 1992, **4**, 7843–7851.
- 216 D. Casanova, J. Cirera, M. Llunell, P. Alemany, D. Avnir and S. Alvarez, *J. Am. Chem. Soc.*, 2004, **126**, 1755–1763.
- 217 A. Ruiz-Martínez, D. Casanova and S. Alvarez, *Chem. - Eur. J.*, 2010, **16**, 6567–6581.
- 218 S. Alvarez, P. Alemany, D. Casanova, J. Cirera, M. Llunell and D. Avnir, *Coord. Chem. Rev.*, 2005, **249**, 1693–1708.

- 219 A. Ruiz-Martínez, D. Casanova and S. Alvarez, *Chemistry*, 2008, **14**, 1291–303.
- 220 K. Zhuravlev, V. Tsaryuk, V. Kudryashova, I. Pekareva, J. Sokolnicki and Y. Yakovlev, *J. Lumin.*, 2010, **130**, 1489–1496.
- 221 N. Armaroli, L. De Cola, V. Balzani, J.-P. Sauvage, C. O. Dietrich-Buchecker and J.-M. Kern, *J. Chem. Soc. Faraday Trans.*, 1992, **88**, 553–556.
- 222 S. Sato and M. Wada, *Bull. Chem. Soc. Jpn.*, 1970, **43**, 1955–1962.
- 223 K. Nakamaru, *Bull. Chem. Soc. Jpn.*, 1982, **55**, 2697–2705.
- 224 L. Abad Galán, B. L. Reid, S. Stagni, A. N. Sobolev, B. W. Skelton, M. Cocchi, J. M. Malicka, E. Zysman-colman, E. G. Moore, M. I. Ogden and M. Massi, *Inorg. Chem.*, 2017, **56**, 8975–8985.
- 225 J. Zawadiak and M. Mrzyczek, *Spectrochim. Acta - Part A Mol. Biomol. Spectrosc.*, 2012, **96**, 815–819.
- 226 D. T. Thielemann, M. Klinger, T. J. a Wolf, Y. Lan, W. Wernsdorfer, M. Busse, P. W. Roesky, A. N. Unterreiner, A. K. Powell, P. C. Junk and G. B. Deacon, *Inorg. Chem.*, 2011, **50**, 11990–12000.
- 227 M. Cametti, M. Nissinen, A. Dalla Cort, L. Mandolini and K. Rissanen, *J. Am. Chem. Soc.*, 2005, **127**, 3831–3837.
- 228 A. S. Mahadevi and G. N. Sastry, *Chem. Rev.*, 2013, **113**, 2100–2138.
- 229 N. M. Shavaleev, R. Scopelliti, F. Gumy and J. C. G. Bü nzli, *Inorg. Chem.*, 2009, **48**, 2908–2918.
- 230 L. Poisson, P. Roubin, S. Coussan, B. Soep and J. M. Mestdagh, *J. Am. Chem. Soc.*, 2008, **130**, 2974–2983.
- 231 B. L. Reid, A. E. G. Moore, D. B. W. Skelton, M. I. Ogden and M. M. A, *Aust. J. Chem.*, 2015, **68**, 1392–1398.
- 232 P. K. Verma, A. Steinbacher, F. Koch, P. Nuernberger and T. Brixner, *Phys. Chem. Chem. Phys.*, 2015, **17**, 8459–8466.
- 233 C. Paris, V. Lhiaubet-Vallet, O. Jiménez, C. Trullas and M. Á. Miranda, *Photochem. Photobiol.*, 2009, **85**, 178–184.

- 234 B. W. Gung, Y. Zou, Z. Xu, J. C. Amicangelo, D. G. Irwin, S. Ma and H. C. Zhou, *J. Org. Chem.*, 2008, **73**, 689–693.
- 235 H. Y. Zhuo, L. X. Jiang, Q. Z. Li, W. Z. Li and J. B. Cheng, *Chem. Phys. Lett.*, 2014, **608**, 90–94.
- 236 L. Hu, J. Zhang, Q. Yin, P. Li and K. Du, *Opt. Commun.*, 2014, **324**, 26–29.
- 237 S. S. Dudar', V. L. Ermolaev and a. V. Shablya, *Opt. Spectrosc.*, 2007, **102**, 533–544.
- 238 E. J. Sharp, M. J. Weber and G. Cleek, *J. Appl. Phys.*, 1970, **41**, 364–369.
- 239 J. Bunzli and F. Ihringer, *Inorg. Chim. Acta*, 1996, **246**, 195–205.
- 240 S. T. Frey, M. L. Gong and W. D. Horrocks, *Inorg. Chem.*, 1994, **33**, 3229–3234.
- 241 J.-C. G. Bünzli and C. Piguet, *Chem. Soc. Rev.*, 2005, **34**, 1048–1077.
- 242 R. S. Rasmussen, D. D. Tunnicliff and R. R. Brattain, *J. Am. Chem. Soc.*, 1949, **71**, 1068–1072.
- 243 F. Xie, F. Yan, M. Chen and M. Zhang, *RSC Adv.*, 2014, **4**, 29502–29508.
- 244 C. B. Rao, D. C. Rao, D. C. Babu and Y. Venkateswarlu, *European J. Org. Chem.*, 2010, **0**, 2855–2859.
- 245 S. L. Bartlett and C. M. Beaudry, *J. Org. Chem.*, 2011, **76**, 9852–9855.
- 246 A. K. C. Schmidt and C. B. W. Stark, *Org. Lett.*, 2011, **13**, 5788–5791.
- 247 A. K. C. Schmidt and C. B. W. Stark, *Org. Lett.*, 2011, **13**, 4164–4167.
- 248 N. Taha, M. Chidambaram, J. Dakka and Y. Sasson, *Catal. Letters*, 2009, **129**, 358–362.
- 249 J. Ishida, H. Ohtsu, Y. Tachibana, Y. Nakanishi, K. F. Bastow, M. Nagai, H. K. Wang, H. Itokawa and K. H. Lee, *Bioorganic Med. Chem.*, 2002, **10**, 3481–3487.
- 250 B. Wang, H. X. Sun, Z. H. Sun and G. Q. Lin, *Adv. Synth. Catal.*, 2009, **351**, 415–422.
- 251 Z. Zheng, *Lanthanides: Amino Acid Compounds*, John Wiley & Sons, Ltd, Chichester, UK, 2012.

- 252 H. Sawase, Y. Koizumi, Y. Suzuki, M. Shimoi and A. Ouchi, *Bull. Chem. Soc. Jpn.*, 1984, **57**, 2730–2737.
- 253 I. Baxter, S. R. Drake, M. B. Hursthouse, K. M. Abdul Malik, J. McAleese, D. J. Otway and J. C. Plakatouras, *Inorg. Chem.*, 1995, **34**, 1384–1394.
- 254 J. P. Paris and W. W. Brandt, *J. Am. Chem. Soc.*, 1959, **81**, 5001–5002.
- 255 I. M. Dixon, J.-P. Collin, J.-P. Sauvage, L. Flamigni, S. Encinas and F. Barigelletti, *Chem. Soc. Rev.*, 2000, **29**, 385–391.
- 256 A. F. Henwood and E. Zysman-Colman, *Chem. Commun.*, 2017, **53**, 807–826.
- 257 J. A. Gareth Williams, S. Develay, D. L. Rochester and L. Murphy, *Coord. Chem. Rev.*, 2008, **252**, 2596–2611.
- 258 V. W.-W. Yam and K. M.-C. Wong, *Chem. Commun.*, 2011, **47**, 11579–11592.
- 259 C. K. Prier, D. A. Rankic and D. W. C. MacMillan, *Chem. Rev.*, 2013, **113**, 5322–5363.
- 260 R. D. Costa, E. Ortí, H. J. Bolink, F. Monti, G. Accorsi and N. Armaroli, *Angew. Chemie - Int. Ed.*, 2012, **51**, 8178–8211.
- 261 D. Sykes and M. D. Ward, *Chem. Commun.*, 2011, **47**, 2279–81.
- 262 J. R. Piper, L. Cletheroe, C. G. P. Taylor, A. J. Metherell, J. A. Weinstein, I. V. Sazanovich and M. D. Ward, *Chem. Commun.*, 2017, **53**, 408–411.
- 263 H. Tsubaki, A. Sekine, Y. Ohashi, K. Koike, H. Takeda and O. Ishitani, *J. Am. Chem. Soc.*, 2005, **127**, 15544–15555.
- 264 J. H. Montoya, L. C. Seitz, P. Chakthranont, A. Vojvodic, T. F. Jaramillo and J. K. Nørskov, *Nat. Mater.*, 2016, **16**, 70–81.
- 265 J. J. Concepcion, J. W. Jurss, M. K. Brennaman, P. G. Hoertz, A. O. T. Patrocinio, N. Y. Murakami Iha, J. L. Templeton and T. J. Meyer, *Acc. Chem. Res.*, 2009, **42**, 1954–1965.
- 266 J. W. Tucker and C. R. J. Stephenson, *J. Org. Chem.*, 2012, **77**, 1617–1622.
- 267 G. Sahara, R. Abe, M. Higashi, T. Morikawa, K. Maeda, Y. Ueda and O. Ishitani,

- Chem. Commun.*, 2015, **51**, 10722–10725.
- 268 M. K. Nazeeruddin and M. Gratzel, *Photofunctional Transition Metal Complexes*, 2007, vol. 123.
- 269 A. J. Amoroso, M. P. Coogan, J. E. Dunne, V. Fernández-Moreira, J. B. Hess, A. J. Hayes, D. Lloyd, C. Millet, S. J. A. Pope and C. Williams, *Chem. Commun.*, 2007, **29**, 3066–3068.
- 270 K. K. W. Lo, M. W. Louie and K. Y. Zhang, *Coord. Chem. Rev.*, 2010, **254**, 2603–2622.
- 271 C. Caporale, C. A. Bader, A. Sorvina, K. D. M. MaGee, B. W. Skelton, T. A. Gillam, P. J. Wright, P. Raiteri, S. Stagni, J. L. Morrison, S. E. Plush, D. A. Brooks and M. Massi, *Chem. - Eur. J.*, 2017, **23**, 15666–15679.
- 272 V. Guerschais and J. L. Fillaut, *Coord. Chem. Rev.*, 2011, **255**, 2448–2457.
- 273 M. Keefe, K. D. Benkstein and J. T. Hupp, *Coord. Chem. Rev.*, 2000, **205**, 201–228.
- 274 J. V. Caspar and T. J. Meyer, *J. Phys. Chem.*, 1983, **87**, 952–957.
- 275 J. C. Luong, R. A. Faltynek and M. S. Wrighton, *J. Am. Chem. Soc.*, 1980, **102**, 7892–7900.
- 276 M. A. Baldo, S. Lamansky, P. E. Burrows, M. E. Thompson and S. R. Forrest, *Appl. Phys. Lett.*, 1999, **75**, 4–6.
- 277 P. S. Wagenknecht and P. C. Ford, *Coord. Chem. Rev.*, 2011, **255**, 591–616.
- 278 A. Barbieri, G. Accorsi and N. Armaroli, *Chem. Commun.*, 2008, **19**, 2185–2193.
- 279 R. D. Costa, E. Ortí, H. J. Bolink, S. Graber, S. Schaffner, M. Neuburger, C. E. Housecroft and E. C. Constable, *Adv. Funct. Mater.*, 2009, **19**, 3456–3463.
- 280 L. Zhang, Y. Hou, M. Pan, L. Chen, Y. Zhu and S. Yin, *Dalton Trans.*, 2015, **44**, 15212–15219.
- 281 F. F. Chen, Z. Q. Bian, B. Lou, E. Ma, Z. W. Liu, D. B. Nie, Z. Q. Chen, J. Bian, Z. N. Chen and C. H. Huang, *Dalton Trans.*, 2008, **2**, 5577–5583.
- 282 N. M. Tart, D. Sykes, I. Sazanovich, I. S. Tidmarsh and M. D. Ward, *Photochem.*

- Photobiol. Sci.*, 2010, **9**, 886.
- 283 W. Jiang, B. Lou, J. Wang, H. Lv, Z. Bian and C. Huang, *Dalton Trans.*, 2011, **40**, 11410–11418.
- 284 F. F. Chen, H. B. Wei, Z. Q. Bian, Z. W. Liu, E. Ma, Z. N. Chen and C. H. Huang, *Organometallics*, 2014, **33**, 3275–3282.
- 285 L. Li, S. Zhang, L. Xu, Z.-N. Chen and J. Luo, *J. Mater. Chem. C*, 2014, **2**, 1698.
- 286 Y. You and S. Y. Park, *J. Am. Chem. Soc.*, 2005, **127**, 12438–12439.
- 287 X. Gu, T. Fei, H. Zhang, H. Xu, B. Yang, Y. Ma and X. Liu, *Eur. J. Inorg. Chem.*, 2009, **16**, 2407–2414.
- 288 C. H. Shin, J. O. Huh, M. H. Lee and Y. Do, *Dalton Trans.*, 2009, **33**, 6476–9.
- 289 S. Lamansky, P. Djurovich, D. Murphy, F. Abdel-Razzaq, H. E. Lee, C. Adachi, P. E. Burrows, S. R. Forrest and M. E. Thompson, *J. Am. Chem. Soc.*, 2001, **123**, 4304–4312.
- 290 S. Lamansky, P. Djurovich, D. Murphy, F. Abdel-Razzaq, R. Kwong, I. Tsyba, M. Bortz, B. Mui, R. Bau and M. E. Thompson, *Inorg. Chem.*, 2001, **40**, 1704–1711.
- 291 A. P. Bassett, S. W. Magennis, P. B. Glover, D. J. Lewis, N. Spencer, S. Parsons, R. M. Williams, L. De Cola and Z. Pikramenou, *J. Am. Chem. Soc.*, 2004, **126**, 9413–9424.
- 292 Q. Zhao, L. Li, F. Li, M. Yu, Z. Liu, T. Yi and C. Huang, *Chem. Commun.*, 2008, **3**, 685–687.
- 293 V. V. Pavlishchuk and A. W. Addison, *Inorg. Chim. Acta*, 2000, **298**, 97–102.
- 294 C. M. Cardona, W. Li, A. E. Kaifer, D. Stockdale and G. C. Bazan, *Adv. Mater.*, 2011, **23**, 2367–2371.
- 295 K. Dedeian, J. Shi, N. Shepherd, E. Forsythe and D. C. Morton, *Inorg. Chem.*, 2005, **44**, 4445–4447.
- 296 E. Baranoff, B. F. E. Curchod, J. Frey, R. Scopelliti, F. Kessler, I. Tavernelli, U. Rothlisberger, M. Grätzel and M. K. Nazeeruddin, *Inorg. Chem.*, 2012, **51**, 215–224.

- 297 P. Suppan, *J. Photochem. Photobiol. A Chem.*, 1990, **50**, 293–330.
- 298 X. G. Zhang, Y. L. Shi and H. L. Li, *J. Colloid Interface Sci.*, 2002, **246**, 296–301.
- 299 Y. Wang, P. Bao, J. Wang, R. Jia, F. Bai and H. Zhang, *Inorg. Chem.*, 2018, **57**, 6561–6570.
- 300 A. Marini, A. Mun, A. Biancardi and B. Mennucci, *J. Phys. Chem. B*, 2010, **114**, 17128–17135.
- 301 J. M. Fernández-Hernández, J. I. Beltrán, V. Lemauro, M. D. Gálvez-López, C. H. Chien, F. Polo, E. Orselli, R. Fröhlich, J. Cornil and L. De Cola, *Inorg. Chem.*, 2013, **52**, 1812–1824.
- 302 A. Onder, M. Turkyilmaz and Y. Baran, *Inorg. Chim. Acta*, 2012, **391**, 28–35.
- 303 M. A. Chagas and W. R. Rocha, *Chem. Phys. Lett.*, 2014, **612**, 78–83.
- 304 J. Jayabharathi, V. Thanikachalam, N. Srinivasan and M. V. Perumal, *J. Fluoresc.*, 2011, **21**, 1585–1597.
- 305 S. Fantacci, F. De Angelis and A. Selloni, *J. Am. Chem. Soc.*, 2003, **125**, 4381–4387.
- 306 D. Chen, K. Li, X. Guan, G. Cheng, C. Yang and C. M. Che, *Organometallics*, 2017, **36**, 1331–1344.
- 307 K. Suzuki, A. Kobayashi, S. Kaneko, K. Takehira, T. Yoshihara, H. Ishida, Y. Shiina, S. Oishi and S. Tobita, *Phys. Chem. Chem. Phys.*, 2009, **11**, 9850.
- 308 J. Luo, Z. Xie, J. W. Y. Lam, L. Cheng, B. Z. Tang, H. Chen, C. Qiu, H. S. Kwok, X. Zhan, Y. Liu and D. Zhu, *Chem. Commun.*, 2001, **381**, 1740–1741.
- 309 R. Hu, N. L. C. Leung and B. Z. Tang, *Chem. Soc. Rev.*, 2014, **43**, 4494–4562.
- 310 Y. Hong, J. W. Y. Lam and B. Z. Tang, *Chem. Soc. Rev.*, 2011, **40**, 5361–5388.
- 311 J. Mei, N. L. C. Leung, R. T. K. Kwok, J. W. Y. Lam and B. Z. Tang, *Chem. Rev.*, 2015, **115**, 11718–11940.
- 312 Y. Liu, C. Deng, L. Tang, A. Qin, R. Hu, J. Z. Sun and B. Z. Tang, *J. Am. Chem. Soc.*, 2011, **133**, 660–663.

- 313 Y. Hong, J. W. Y. Lam and B. Z. Tang, *Chem. Commun.*, 2009, **29**, 4332–4353.
- 314 W. Lu, B. X. Mi, M. C. W. Chan, Z. Hui, C. M. Che, N. Zhu and S. T. Lee, *J. Am. Chem. Soc.*, 2004, **126**, 4958–4971.
- 315 Y. Sun, K. Ye, H. Zhang, J. Zhang, L. Zhao, B. Li, G. Yang, B. Yang, Y. Wang, S. W. Lai and C. M. Che, *Angew. Chemie - Int. Ed.*, 2006, **45**, 5610–5613.
- 316 V. W. W. Yam, K. H. Y. Chan, K. M. C. Wong and B. W. K. Chu, *Angew. Chemie - Int. Ed.*, 2006, **45**, 6169–6173.
- 317 P. Alam, S. Dash, C. Climent, G. Kaur, A. R. Choudhury, D. Casanova, P. Alemany, R. Chowdhury and I. R. Laskar, *RSC Adv.*, 2017, **7**, 5642–5648.
- 318 Y. Jiang, G. Li, W. Che, Y. Liu, B. Xu, G. Shan, D. Zhu, Z. Su and M. R. Bryce, *Chem. Commun.*, 2017, **53**, 3022–3025.
- 319 Q. Lu, X. Li, J. Li, Z. Yang, B. Xu, Z. Chi, J. Xu and Y. Zhang, *J. Mater. Chem. C*, 2015, **3**, 1225–1234.
- 320 J. C. Xiao and J. M. Shreeve, *J. Org. Chem.*, 2005, **70**, 3072–3078.
- 321 Z. He, X. Qi, Z. She, Y. Zhao, S. Li, J. Tang, G. Gao, Y. Lan and J. You, *J. Org. Chem.*, 2017, **82**, 1403–1411.
- 322 M. Nonoyama, *Bull. Chem. Soc. Jpn.*, 1974, **47**, 767–768.
- 323 G. M. Sheldrick, *Acta Crystallogr. Sect. C-Struct. Chem.*, 2015, **71**, 3–8.
- 324 P. T. Beurskens, G. Beurskens, R. de Gelder, S. Garcia-Granda, R. Israel and J. M. Smits, *M.DIRDIF-99*, The DIRDIF99 Program System, Technical Report of the University of Nijmegen, The Netherlands, 1999.
- 325 N. M. Shavaleev, S. J. A. Pope, Z. R. Bell, S. Faulkner and M. D. Ward, *Dalton Trans.*, 2003, **5**, 808–814.
- 326 M. H. Baker, J. D. Dorweiler, A. N. Ley, R. D. Pike and S. M. Berry, *Polyhedron*, 2009, **28**, 188–194.
- 327 A. I. Voloshin, N. M. Shavaleev and V. P. Kazakov, *J. Lumin.*, 2001, **93**, 115–118.
- 328 A. A. Ansari, M. Irfanullah and K. Iftikhar, *Spectrochim. Acta - Part A Mol. Biomol.*

Spectrosc., 2007, **67**, 1178–1188.

Every reasonable effort has been made to acknowledge the owners of copyright material. I would be pleased to hear from any copyright owner who has been omitted or incorrectly acknowledged.

Appendix

Table A.1 Recently reported (1999-2017) Yb^3 systems including β -diketonate ligands.

Complex	Sample	τ_{obs} (μs)	Φ_{Ln}^{Ln} (%)	Φ_{Ln}^L (%)	Ref	Year
[Yb(tta) ₃ (OH ₂) ₂]	Toluene	5.7	-	0.35 ^e	148	1999
	CCl ₄	4.3	-	-		
	PMMA	9.7	-	0.55 ^e		
[Yb(tta) ₃ (phen)]	Toluene	10.4	-	1.10 ^e	148	1999
	CCl ₄	11.9	-	-		
	PMMA	10.7	-	1.10 ^e		
[Yb(hfth) ₃ (OH ₂) ₂]	Toluene	8.6	-	0.26 ^e	148	1999
	CCl ₄	5.4	-	-		
	PMMA	11	-	0.37 ^e		
[Yb(hfth) ₃ (phen)]	Toluene	11.7	-	1.20 ^e	148	1999
	CCl ₄	11.9	-	-		
	PMMA	11.1	-	1.20 ^e		
[Yb(nfth) ₃ (OH ₂) ₂]	Toluene	9.2	-	0.24 ^e	148	1999
	CCl ₄	5.6	-	-		
	PMMA	11.4	-	0.42 ^e		
[Yb(nfth) ₃ (phen)]	Toluene	11.8	-	0.88 ^e	148	1999
	CCl ₄	11.3	-	-		
	PMMA	11.0	-	1.00 ^e		
[Yb(D5) ₃ (OH ₂) ₂]	Toluene	1.8	-	0.11 ^e	148	1999
[Yb(D5) ₃ (phen)]	Toluene	10.4	-	0.65 ^e	148	1999
[Yb(D6) ₃ (OH ₂) ₂]	Toluene	2.5	-	0.15 ^e	148	1999
[Yb(D6) ₃ (phen)]	Toluene	10.7	-	0.88 ^e	148	1999
[Yb(D7) ₃ (OH ₂) ₂]	Toluene	2.6	-	0.17 ^e	148	1999
[Yb(D7) ₃ (phen)]	Toluene	11.0	-	0.98 ^e	148	1999
[Yb(D8) ₃ (OH ₂) ₂]	Toluene	2.5	-	0.19 ^e	148	1999
[Yb(D8) ₃ (phen)]	Toluene	10.5	-	0.92 ^e	148	1999
[Yb(tta)(tppo) ₂]	DMSO	-	-	Emissive no data reported	150	2001

[Yb(tta) ₃ (OH ₂) ₂]	Toluene	1.16	-	0.12 ^e	150	2001
[Yb(tta-D) ₃ (OH ₂) ₂]	Toluene	1.25	-	0.15 ^e	150	2001
[Yb(tta) ₃ (DMSO- <i>d</i> ⁶) _n]	DMSO- <i>d</i> ⁶	27.3	-	2.14 ^e	150	2001
[Yb(tta-D) ₃ (DMSO- <i>d</i> ⁶) _n]	DMSO- <i>d</i> ⁶	71.8	-	6.1 ^e	150	2001
[Yb(tta) ₃ (phen)]	Toluene	15.8	-	1.6 ^e	150	2001
[Yb(tta-D) ₃ (phen)]	Toluene	18.6	-	1.86 ^e	150	2001
	CCl ₄	22.8	-	2.14 ^e		
[Yb(dbm) ₃ (OH ₂) ₂]	Toluene	1.0	-	0.02 ^e	150	2001
[Yb(dbm-D) ₃ (OH ₂) ₂]	Toluene	1.0	-	0.02 ^e	150	2001
[Yb(dbm) ₃ (DMSO- <i>d</i> ⁶) _n]	DMSO- <i>d</i> ⁶	17.4	-	0.73 ^e	150	2001
[Yb(dbm-D) ₃ (DMSO- <i>d</i> ⁶) _n]	DMSO- <i>d</i> ⁶	30.1	-	1.26 ^e	150	2001
[Yb(dbm) ₃ (phen)]	Toluene	10.3	-	0.59 ^e	150	2001
[Yb(dbm-D) ₃ (phen)]	Toluene	12.1	-	0.69 ^e	150	2001
	CCl ₄	13.6	-	0.69 ^e		
[Yb(tta) ₃ (OH ₂) ₂]	CH ₂ Cl ₂	0.85	-	-	325	2003
[{Yb(tta) ₃ } ₂ (BPTZ)]	CH ₂ Cl ₂	14.5	0.70 ^a	-	325	2003
	Solid	14.1	-	-		
[Yb(acac) ₃ (A1)]		-	-	No emissive	152	2005
[Yb(acac) ₃ (A2)]		-	-	No emissive	152	2005
[Yb(hfth) ₃ (phen)]	Powder	14.7	-	-	153	2006
	Toluene	-	-	1.28 ^d		
[Yb(hfth) ₃ (bipy)]	Powder	13.8	-	-	153	2006
	Toluene	-	-	1.24 ^d		
Ybn(hfth) ₃ (OH ₂) ₂]	Powder	0.97	-	-	153	2006
	Toluene	-	-	0.37 ^d		
Cs[Yb(hfaa) ₄]	Powder	21.6	-	-	80	2006
Cs[Yb(hfaa-D) ₄]	Powder	289	-	-	80	2006

[Yb(hfaa) ₃ (TPPO) ₂]	Powder	89.1	4.5 ^a		154	2006
R1[Yb(D13) ₄]	MeCN	46.4	-	-	174	2007
[Yb(D12) ₃ (phen)]	Powder	8.6	0.43 ^a	0.2 ^e	176	2008
[Yb(D12) ₃ (DMSO) _n]	DMSO	12	0.6 ^a	0.04 ^e	176	2008
[Yb(tmhd) ₃] ₂ (bpm)	CHCl ₃ (RT)		-	No emissive	326	2009
[Yb(hfaa) ₃ (OP(C ₆ F ₅) ₃)]	CCl ₄	2.4	-	-	156	2009
[Yb(hfaa-F) ₃ (OP(C ₆ F ₅) ₃)]	CCl ₄	16.8	-	-	156	2009
[Yb(hfaa) ₃ (phen)]	CHCl ₃ (RT)	-	-	Emissive no data reported	157	2010
[Yb(tfnb) ₃ (daf)]	Powder	8.77	-	-	158	2010
[Yb(hfth) ₃ (daf)]	Powder	10	-	-	158	2010
[Yb(pfnd) ₃ (daf)]	Powder	10	-	-	158	2010
[Yb(D9)](NBu ₄)	Powder	12.1	-	2.6 ^d	178	2013
	DMF	12.3	-	1.8 ^d		
	PMMA film	9.7	-	-		
	PMMA wires	9.8	-	-		
[Yb(h) ₃ (5-NO ₂ Phen)]	Powder	5.2	-	-	163	2013
[Yb(tta) ₃ (5-NO ₂ Phen)]	Powder	5.8	-	-	163	2013
[Yb(dmh) ₃ (5-NO ₂ Phen)]	Powder	5.0	-	-	163	2013
[Yb(tfac) ₃ (5-NO ₂ Phen)]	Powder	4.7	-	-	163	2013
[Yb(tmp) ₃ (5-NO ₂ Phen)]	Powder	3.6	-	-	163	2013
[Yb(fhd) ₃ (5-NO ₂ Phen)]	Powder	3.3	-	-	163	2013
[Yb(tfnb) ₃ (5-NO ₂ Phen)]	Powder	7.2	-	-	163	2013
[Yb(TFI) ₃ (OH ₂) ₂]	Powder	10.85	3.24 (τ _r =0.34ms) ^b		179	2014
[Yb(TFI) ₃ (bipy)]	Powder	19.92	4.44(τ _r =0.45ms) ^b	-	179	2014

[Yb(TFI) ₃ (bipy)]	Powder	24.31	4.24($\tau_r=0.58\text{ms}$) ^b		179	2014
[Yb(hfaa) ₃ (bpy)]	CHCl ₃ (RT)	47	-	3.3 ^c	166	2014
[Yb(D10) ₃ (phen)]	Cyclohexane	-	-	0.29 ^f	180	2014
	THF	13	-	0.05 ^f		
[Yb(D10) ₃ (OH ₂) ₂]	MeCN	15.8	0.79 ^a	-	181	2014
	PMMA	19.4	-	-		
[Yb(D10) ₃ (bipy)]	MeCN	16.17	1.35 ^a	1.12 ^c	183	2016
	PMMA	19.33	-	1.24 ^e		
[Yb(tta) ₃ (tppo)]H ₂ O	CHCl ₃ (RT)	-	-	1.92 ^c	168	2016
[Yb(tta) ₃ (tppo)]H ₂ O	Film	-	-	-	168	2016
[Yb(tta) ₃ (dpsO)]	CHCl ₃ (RT)	-	-	2.40 ^c	169	2016
[Yb(tta) ₃ (dbso)]	CHCl ₃ (RT)	-	-	1.41 ^c	169	2016
[Yb(tta) ₃ (bga)]	CHCl ₃ (RT)	-	-	1.33 ^c	169	2016
[Yb(hfpYr) ₃ (OH ₂) ₂]	Powder	6.88	0.34 ^a	1.69 ^e	184	2016
[Yb(hfpYr) ₃ (bath)]	Powder	13.45	0.67 ^a	3.08 ^e	184	2016
(A3)[Yb(dbm) ₃] ₂	Powder	10.1	0.5 ^a	-	171	2016

^a Assuming literature τ_R of 2 ms. ^b Radiative lifetime calculated from absorbance spectra following Eq. 1.6. ^c Calculated following diluted methods with [Yb(tta)₃(H₂O)₂] as reference ($\Phi_{Ln}^L = 0.35\%$).¹⁴⁸ ^d Calculated following diluted methods with [Yb(tta)₃(phen)] as reference ($\Phi_{Ln}^L = 1.1\%$).¹⁴⁸ ^e Measured with an integrating sphere. ^f Calculated following diluted methods with 9,10-diphenylanthracene as reference ($\Phi = 0.95\%$).¹⁸⁶

Table A.2 Recently reported (1999-2017) Er³⁺ systems including β -diketonate ligands.

Complex	Sample	τ_{obs} (μs)	$\Phi_{\text{Ln}}^{\text{Ln}}$ (%)	$\Phi_{\text{Ln}}^{\text{L}}$ (%)	Ref	Year
[Er(tta) ₃] ₂ (BPTZ)]	CH ₂ Cl ₂	1.69	0.01 ^a		325	2003
	Powder	2.0	-			
[Er(tta) ₃ (OH ₂) ₂]	CH ₂ Cl ₂	0.20			325	2003
[Er(acac) ₃ (A1)]		-	-	No emissive	152	2005
[Er(acac) ₃ (A2)]		-	-	No emissive	152	2005
[Er(hfth) ₃ (phen)]	Powder	2.73		-	171	2006
	Toluene	-		0.019 ^c		
[Er(hfth) ₃ (bipy)]	Powder	2.27		-	171	2006
	Toluene	-		0.014 ^c		
Cs[Er(hfaa) ₄]	Powder	1.8			80	2006
Cs[Er(hfaa-D) ₄]	Powder	106		-	80	2006
[Er(hfaa) ₃ (TPPO) ₂]	Powder	60.8	0.43 ^a	-	154	2006
R1[Er(D13) ₄]	MeCN	3.2		-	174	2007
[Er(D12) ₃ (phen)]	Powder	1.4		-	176	2008
[Er(D12) ₃ (DMSO) _n]	DMSO	DMSO		-	176	2008
[Er(hfaa) ₃ (phen)]	CHCl ₃ (RT)	-	-	Emissive no data reported	157	2010
[Er(CNPD) ₃ (tpy)]	MeCN	1.44	-	-	177	2010
	Powder	-	-	0.008 ^d		
[Er(tfnb) ₃ (daf)]	Powder	2.0	-	-	158	2010
[Er(hfth) ₃ (daf)]	Powder	2.26	-	-	158	2010
[Er(pfnd) ₃ (daf)]	Powder	2.08	-	-	158	2010
[Er(acac) ₃] ₂ bpm]	CHCl ₃ (RT)	-	-	No emissive	161	2010

[Er(D9)](NBu ₄)	Powder	1.6	-	-	178	2013
	DMF	1.5	-	-		
	PMMA film	1.6	-	-		
	PMMA wires	1.3	-	-		
[Er(tmp) ₃ (bipy)]	MeOH	1.77	-	0.012 ^e	178	2013
[Er(tmp) ₃ (bath)]	MeOH	1.55	-	No emissive	178	2013
[Er(tmp) ₃ (5-NO ₂ Phen)]	MeOH	1.53	-	No Emissive	178	2013
[Er(fod) ₃ (bipy)]	MeOH	1.50	-	Emissive no data reported	131	2014
[Er(fod) ₃ (bath)]	MeOH	1.34	-	Emissive no data reported	131	2014
[Er(tmhd) ₃] ₂ (bath)]	Powder	1.38	-	-	164	2014
[Er(od) ₃] ₂ (bath)]	Powder	1.09	-	-	165	2014
[Er(od) ₃] ₂ (bipy)]	Powder	1.26	-	-	165	2014
[Er(od) ₃] ₂ (5-NO ₂ Phen))	Powder	1.02	-	-	165	2014
[Er(D10) ₃ (phen)]	Cyclohexane	-	-	0.09 ^f	180	2014
	THF	2.5	-	0.11 ^f		
[Er(D11) ₃ (OH ₂) ₂]	MeCN	-	-	-	181	2014
	PMMA	-	-	-		
[Er(dnm) ₃ (5-NO ₂ Phen)]	Powder	1.57	-	-	182	2015
[Er(nd) ₃ (bipy)]	Powder	1.22	-	-	167	2015
[Er(D11) ₃ (bipy)]	MeCN	5.90	0.13 ^b	0.002 ^g	183	2016
	PMMA	8.14	-	0.004 ^d		
[Er(tta) ₃ (tppo)]	CHCl ₃ (RT)	-	-	-	172	2017
[Er(tta) ₃ (tppo)]	PMMA	-	-	-	172	2017

^a Assuming literature τ_R of 14 ms.¹⁸⁵ ^a Assuming literature τ_R of 4.5 ms. ⁶ ^c Calculated following diluted methods with [Yb(tta)₃(phen)] as reference ($\Phi_{Ln}^L = 1.1\%$).¹⁴⁸ ^d Measured with an integrating sphere ^e Calculated following diluted methods with perylene as reference ($\Phi = 92\%$).^f Calculated following diluted methods with 9,10-diphenylanthracene as reference ($\Phi = 95\%$).¹⁸⁶ ^g Calculated following diluted methods with [Yb(tta)₃(H₂O)₂] as reference ($\Phi_{Ln}^L = 0.35\%$).¹¹⁶

Table A.3 Recently reported (1999-2017) Nd³⁺ systems including β -diketonate ligands.

Complex	Sample	τ_{obs} (μs)	$\Phi_{\text{Ln}}^{\text{Ln}}$ (%)	$\Phi_{\text{Ln}}^{\text{L}}$ (%)	Ref	Year
[Nd(hfaa) ₃]	THF-d ⁸	2.1	1.51 ^a	0.30 ^e	149	2000
[Nd(D1) ₃]	THF-d ⁸	2.7	1.34 ^a	0.30 ^e	149	2000
[Nd(D2) ₃]	THF-d ⁸	2.4	1.29 ^a	0.30 ^e	149	2000
[Nd(D3) ₃]	THF-d ⁸	4.5	1.70 ^a	0.42 ^e	149	2000
[Nd(D4) ₃]	THF-d ⁸	2.8	1.44 ^a	0.52 ^e	149	2000
[Nd(tta)(tppo) ₂]	DMSO	-	-	Emissive, no data reported	327	2001
[Nd(tta) ₃ (BPTZ)]	CH ₂ Cl ₂	0.76	0.30 ^b	-	151	2003
	Powder	1.25	-	-		
[Nd(hfth) ₃ (bipy)]	Powder	1.27	-	-	153	2006
	Toluene	-	-	0.072 ^d		
[Nd(hfth) ₃ (OH) ₂]	Powder	0.15	-	-	153	2006
	Toluene	-	-	0.0085 ^d		
Cs[Nd(hfaa) ₄]	Powder	1.65	-	-	80	2006
Cs[Nd(hfaa-D) ₄]	Powder	4.2	-	-	80	2006
[Nd(dbm) ₃ (phen)]	Powder	21.5(37%)	8.6 ^b	-	173	2006
[Nd(dbm) ₃ (bath)]	Powder	20.2(48%)	8.1 ^b	-	173	2006
[Nd(cbo-dbm) ₃ (bath)]	Powder	14.0(71%)	5.6 ^b	-	173	2006
[Nd(dnm) ₃ (bath)]	Powder	24.5(88%)	9.81 ^b	-	173	2006
[Nd(carz-dbm) ₃ (bath)]	Powder	24.2(92%)	9.69 ^b	-	173	2006
[Nd(t-onbm) ₃ (bath)]	Powder	24.9(93%)	9.95 ^b	-	173	2006

[Nd(acac) ₃ (phen)(OH ₂) ₂]	MeOH	-	-	Emissive, no	328	2007
	i-prOH	-	-	data		
	EtOH	-	-	reported		
	DMSO	-	-			
	Pyridine	-	-			
	CHCl ₃	-	-			
	MeCN	-	-			
	NitroBenzene	-	-			
	-	-	-			
[Nd(acac) ₃ (bipy)]	MeOH	-	-	Emissive,	328	2007
	i-prOH	-	-	no data		
	EtOH	-	-	reported		
	DMSO	-	-			
	Pyridine	-	-			
	CHCl ₃	-	-			
	MeCN	-	-			
	NitroBenzene	-	-			
	-	-	-			
R1[Nd(D13) ₄]	MeCN	1.0	-	-	174	2007
[Nd(D12) ₃ (phen)]	Powder	0.71	0.17 ^c	-	176	2008
[Nd(D12) ₃ (DMSO) _n]	DMSO	1.2	0.29 ^c	0.008 ^e	176	2008
{Nd(dbm) ₃ (THF)} ₂ (bpm)	-	-	-	Emissive,	175	2008
				no data		
				reported		
{Nd(D5) ₃ (MeOH)} ₂ (bpm)	-	-	-	Emissive,	175	2008
				no data		
				reported		
[Nd(tta) ₃ (μ-bpm)] _n	-	-	-	Emissive,	175	2008
				no data		
				reported		
[Nd(tfnb) ₃ (μ-bpm)] _n	-	-	-	Emissive,	175	2008
				no data		
				reported		
[Nd(hfaa) ₃ (phen)]	CHCl ₃ (RT)	-	-	Emissive,	157	2010
				no data		
				reported		

[Nd(CTPD) ₃ (tpy)]	MeCN	0.95	-	-	177	2010
	Powder	-	-	0.1 ^e		
[Nd(CNPD) ₃ (tpy)]	MeCN	0.85	-	-	177	2010
	Powder	-	-	0.05 ^e		
[Nd(tfnb) ₃ (daf)]	Powder	1.21	-	-	158	2010
[Nd(hfth) ₃ (daf)]	Powder	1.69	-	-	158	2010
[Nd(pfnd) ₃ (daf)]	Powder	1.26	-	-	158	2010
[Nd(hfaa) ₃ (tptz)]	CHCl ₃	-	-	Emissive, no data reported	160	2010
[Nd(acac) ₃] ₂ bpm	CHCl ₃	-	-	No emissive	159	2010
[Nd(fod) ₃] ₂ pyz	CHCl ₃	-	-	No emissive	161	2010
[Nd(TFI) ₃ (OH ₂)]	Powder	2.62	1.1 ^b	-	179	2013
[Nd(TFI) ₃ (bpy)]	Powder	9.95	4.0 ^b	-	179	2013
[Nd(TFI) ₃ (phen)]	Powder	13.3	4.6 ^b	-	179	2013
[Nd(hfaa) ₃ (bpy)]	CHCl ₃	1.5	-	0.19 ^f	166	2014
[Nd(hfaa) ₃ (bpy)(OH ₂)]	CHCl ₃	1.3	-	0.12 ^f	166	2014
[Nd(D10) ₃ (phen)]	Cyclohexane	-		0.35 ^g	180	2014
	THF	1.6		0.09 ^g		
[Nd(D11) ₃ (OH ₂) ₂]	MeCN	1.33	0.53 ^b	-	181	2014
	PMMA	2.38	-	-		
[Nd(hfpvr) ₃ (OH ₂)]	Powder	2.8	1.04 ^b	0.45 ^e	184	2016
[Nd(hfpvr) ₃ (bath)]	Powder	6.16	2.28 ^b	1.07 ^e	184	2016
[Nd(tta) ₃ (DMSO) ₂]	DMSO	-	-	0.22 ^f	170	2016
[Nd ₂ (BDT) ₃ (DMSO) ₆]	DMSO	-	-	0.49 ^f	170	2016
[Nd ₂ (BTT) ₃ (DMSO) ₄]	DMSO	-		0.33 ^f	170	2016
[Nd(D11) ₃ (bipy)]	MeCN	5.34	1.27 ^c	0.068 ^f	183	2016
	PMMA	7.21		0.075 ^e		

^a Measured with an integrating sphere after direct excitation. ^b Assuming literature τ_R of 0.25 ms. ¹⁸⁷ ^c Assuming literature τ_R of 0.42ms. ^d Calculated following diluted methods with [Yb(tta)₃(phen)] as reference ($\Phi_{Ln}^L = 1.1\%$).¹⁴⁸ ^e Measured with an integrating sphere. ^f Calculated following diluted methods with [Yb(tta)₃(H₂O)₂] as reference ($\Phi_{Ln}^L = 0.35\%$).¹⁴⁸ ^g Calculated following diluted methods with 9,10-diphenylanthracene as reference ($\Phi = 0.95\%$).¹⁸⁶

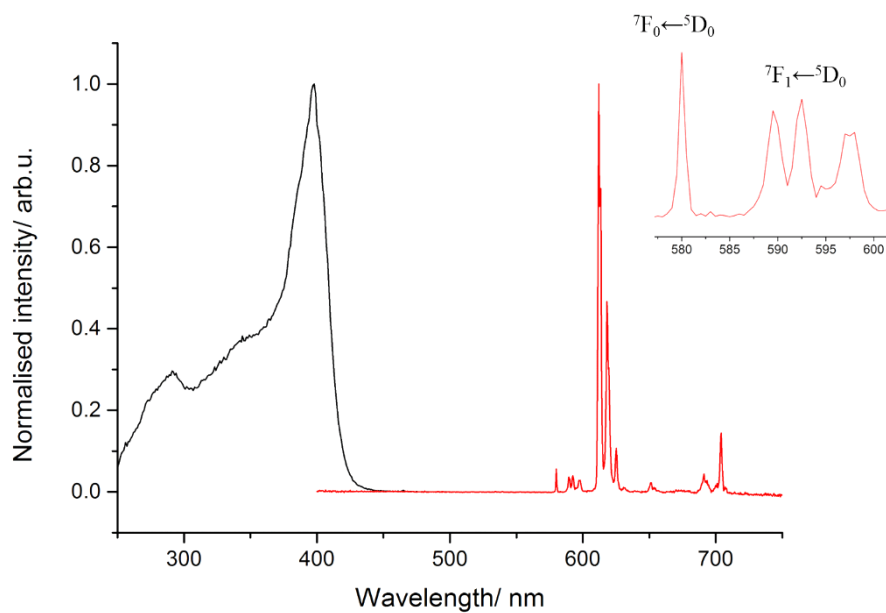


Figure A.1 Normalised excitation and emission ($\lambda=350$ nm) of $[\text{Eu}(\text{phen})(\text{dbm})_3]$ in PMMA.

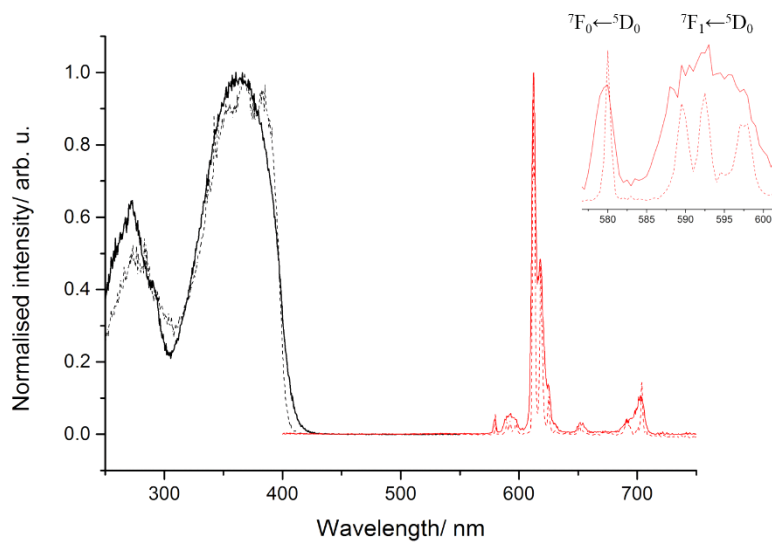


Figure A.2 Normalised excitation and emission ($\lambda=350$ nm) of $[\text{Eu}(\text{phen})(\text{dbm})_3]$ in 10^{-5} M DCM at room temperature (solid line) and 77K (dashed line).

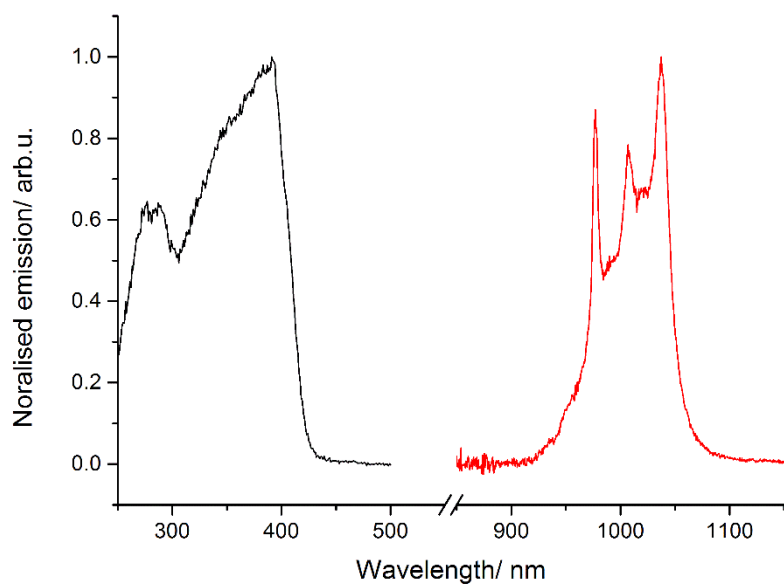


Figure A.3 Normalised excitation and emission ($\lambda=350$ nm) of $[Yb(phen)(dbm)_3]$ in the solid state.

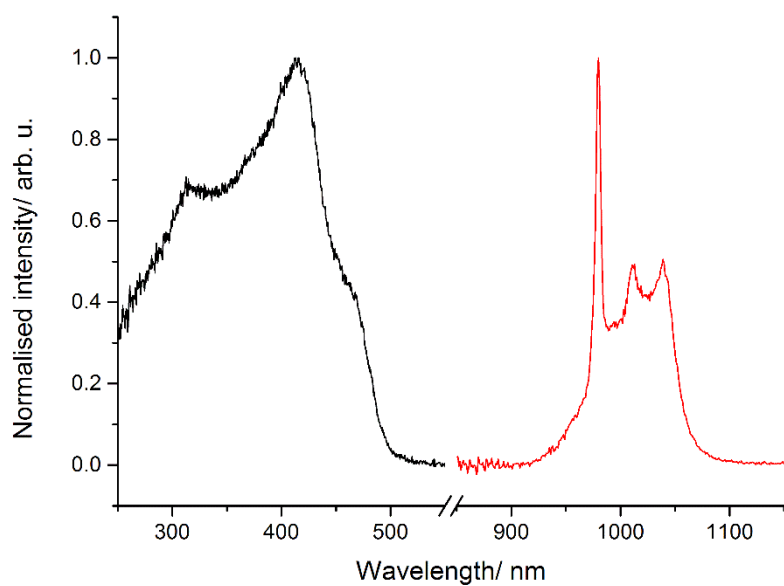


Figure A.4 Normalised excitation and emission ($\lambda=350$ nm) of $[Yb(phen)(dbm)_3]$ in PMMA.

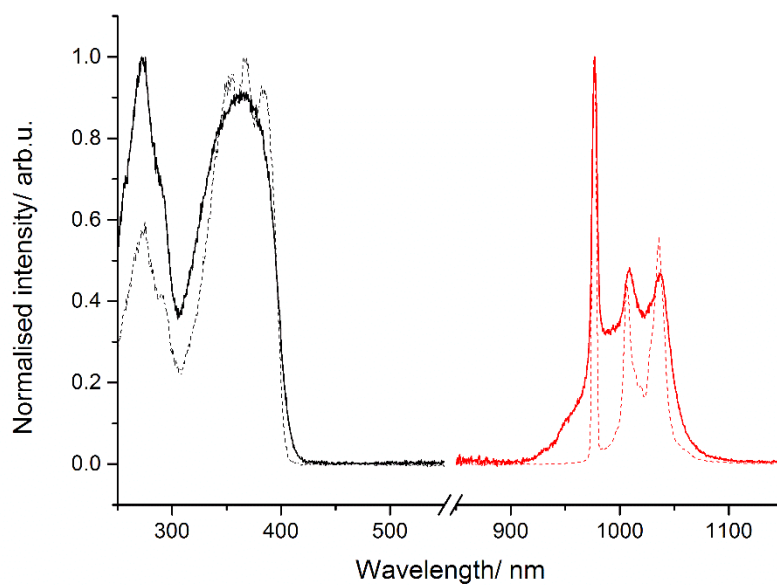


Figure A.5 Normalised excitation and emission ($\lambda=350$ nm) of $[\text{Yb}(\text{phen})(\text{dbm})_3]$ in 10^{-5}M DCM at room temperature (solid line) and 77K (dashed line).

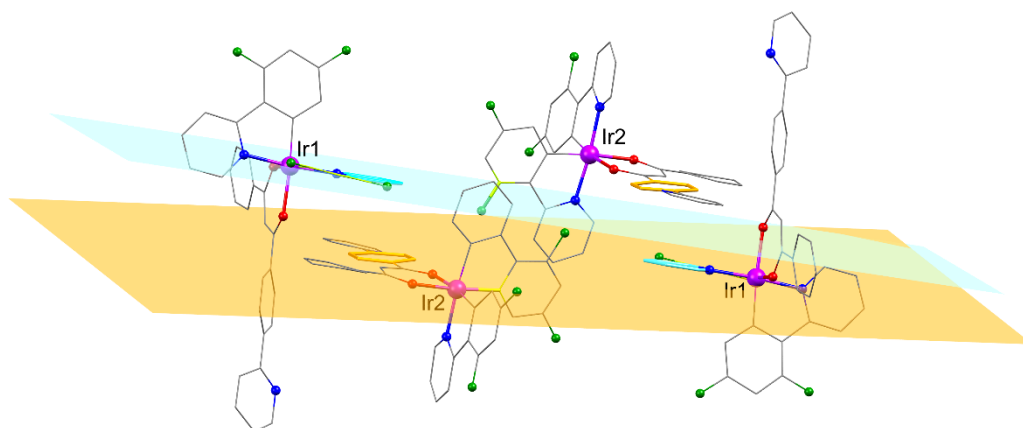


Figure A.6 Representation of the X-ray crystal structure of $[\text{Ir}(\text{dFppy})_2(\text{pydbm})]$, emphasising the planes containing the offset pyridine group of dFppy (light blue) and the phenyl ring of the phenylpyridine moiety of **pydbm** (orange).